UNIVERSITY OF LJUBLJANA
FACULTY OF MATHEMATICS AND PHYSICS
DEPARTMENT OF PHYSICS

Jure Beričič

Measurement of Generalized Polarizabilities of the Proton by Virtual Compton Scattering

Doctoral thesis

ADVISER: assoc. prof. dr. Simon Širca

Ljubljana, 2015

UNIVERZA V LJUBLJANI
FAKULTETA ZA MATEMATIKO IN FIZIKO
ODDELEK ZA FIZIKO

Jure Beričič

Meritev posplošenih polarizirnosti protona z virtualnim comptonskim sipanjem

Doktorska disertacija

MENTOR: izred. prof. dr. Simon Širca

Ljubljana, 2015

Izjava o avtorstvu in objavi elektronske oblike

Izjavljam:

- da sem doktorsko disertacijo z naslovom Meritev posplošenih polarizirnosti protona z virtualnim comptonskim sipanjem izdelal kot rezultat lastnega raziskovalnega dela pod mentorstvom izred. prof. dr. Simona Širce,
- da je tiskani izvod dela identičen z elektronskim izvodom in
- da Fakulteti za matematiko in fiziko Univerze v Ljubljani dovoljujem objavo elektronske oblike svojega dela na spletnih straneh.

Ljubljana, 4. 6. 2015 Podpis:

Acknowledgements

I would like to take a few lines to thank everyone who helped me get here.

Many thanks go to my mentor assoc. prof. dr. Simon Širca who took me under his wing. He was always there to offer me help when help was needed, but otherwise gave me a complete freedom to explore the world of physics as I saw fit.

I am also very grateful to dr. Helene Fonvieille for all insightful conversations we had about physics and in particular about virtual Compton scattering, and for all the helpful memos she wrote.

I would also like to thank the helpful members of the A1 collaboration, especially to dr. Harald Merkel, dr. Michael O. Distler, dr. Björn Sören Schlimme and dr. Miha Mihovilovič for their support during the experiment and analysis.

A special thanks go to my colleagues and friends for all the fun we had during this time.

Last but not least, I would like to send my thanks to my family for all the support they have given me. And to Saša, for everything.

Povzetek

Proces elektroprodukcije fotona omogoča vpogled v virtualno comptonsko sipanje $\gamma^* + \mathrm{p} \to \gamma + \mathrm{p}'$. Sipalno amplitudo lahko opišemo kot koherentno vsoto treh prispevkov: Bethe-Heitlerjevega, Bornovega in ne-Bornovega. Prva dva dela ne vsebujeta nobene nove informacije in jih je možno natančno izračunati v okviru kvantne elektrodinamike, v kolikor so znani elastični oblikovni faktorji. Ne-Bornov del pa nosi nove informacije o strukturi protona. Pri nizkih energijah ga lahko opišemo s šestimi posplošenimi polarizirnostmi, ki so razširitve polarizirnosti realnega comptonskega sipanja. Analogno temu so elastični oblikovni faktorji, ki posplošijo celoten naboj in magnetni moment protona. V pravilnem koordinatnem sistemu jih lahko obravnavamo kot Fourierevo transformacijo radialne porazdelitve polarizirnosti.

V tem delu opišem analizo podatkov pri $Q^2 = 0.1\,\mathrm{GeV}^2$, ki smo jih izmerili pri meritvi sipalnega preseka za nepolariziran proces elektroprodukcije fotona $\mathrm{e} + \mathrm{p} \to \mathrm{e}' + \mathrm{p}' + \gamma$. Sipalni presek smo merili na tri-dimenzionalni mreži, razpeti na $(\mathrm{q}'_{\mathrm{cm}}, \cos(\theta'_{\mathrm{cm}}), \phi'_{\mathrm{cm}})$ pri konstantni vrednosti Q^2 in ϵ. Podatke sem analiziral v okviru nizkoenergijskega razvoja in disperzijskih relacij. Uporaba nizkoenergijskega razvoja mi je omogočila modelsko neodvisno določitev dveh strukturnih funkcij $P_{\mathrm{LL}} - P_{\mathrm{TT}}/\epsilon$ in P_{LT}, vendar izbira faznega prostora ni bila modelsko neodvisna. Model disperzijskih relacij pa sem uporabil za neposredno določitev posplošenih polarizirnosti α_{E} in β_{M}.

Ključne besede: elektronsko sipanje, virtualno comptonsko sipanje, posplošene polarizirnosti, nizko energijski razvoj, disperzijske relacije

PACS (2010): 13.40.Gp, 13.60.Fz, 14.20.Dh, 11.55.Fv

Abstract

The photon electro-production reaction is a window to the virtual Compton scattering $\gamma^* + \mathrm{p} \to \gamma + \mathrm{p}'$. The scattering amplitude can be described as a coherent sum of Bethe-Heitler, Born and non-Born contributions. The first two are exactly calculable in quantum electrodynamic if the proton elastic form factors are known. On the other hand, the non-Born contribution carries new information about the proton structure which, at low energies, can be parametrized by six generalized polarizabilities. They are a generalization of polarizabilities that are measured in real Compton scattering. They are analogous to the generalization of the total charge and magnetic moment to elastic form factors. In an appropriate frame the generalized polarizabilities can be interpreted as a Fourier transform of the radial distribution of the polarizabilities.

This work describes the analysis of a part of data at $Q^2 = 0.1\,\mathrm{GeV}^2$ from the measurement of the cross section of the unpolarized photon electro-production process $\mathrm{e} + \mathrm{p} \to \mathrm{e}' + \mathrm{p}' + \gamma$. The cross sections were measured on a three-dimensional grid of $(\mathrm{q}'_{\mathrm{cm}}, \cos(\theta'_{\mathrm{cm}}), \phi'_{\mathrm{cm}})$ and constant values of Q^2 and ϵ. The data was then analyzed within two frameworks, low energy expansion and dispersion relation model. The low energy expansion was used for model independent extraction of two structure functions $P_{\mathrm{LL}} - P_{\mathrm{TT}}/\epsilon$ and P_{LT}, albeit using model dependent bin selection. The dispersion relation model allowed for a direct extraction of the generalized polarizabilities α_{E} and β_{M}.

Keywords: electron scattering, virtual Compton scattering, generalized polarizabilities, low energy expansion, dispersion relations

PACS (2010): 13.40.Gp, 13.60.Fz, 14.20.Dh, 11.55.Fv

Contents

List of Figures

List of Tables

Chapter 1

Introduction

People have always wondered what the world is made of, what are its building blocks. In the nineteenth century it was already clear that everything was built of atoms. The fact that Mendeleev managed to sort them into a periodic table hinted at an internal structure of the atoms, though at the time it was still unclear what it might be. The first confirmation of smaller particles came from Thomson, who in 1896 discovered electrons [1]. Further insight into atomic structure was provided by Rutherford [2]. First he proved that the atoms have a heavy nucleus in 1909 and later in 1919 he discovered that the hydrogen nucleus - the proton - is a building block of other nuclei. He also predicted the existence of neutrons, which were later discovered by Chadwick in 1932 [3]. To explain the energy conservation in beta decay, Pauli in 1930 postulated the existence of another particle called neutrino [4]. The first confirmed detection of neutrinos only came much later, in 1956 [5].

For a time these four particles were enough to describe all known phenomena of atomic and nuclear physics. But the advent of more powerful particle accelerators brought with it a whole plethora of new particles. The proton and the neutron were now just a part of a big family of particles called hadrons. In 1961 Gell-Mann and Nishijima proposed a classification scheme for hadrons [6] which again hinted that an underlying structure exists. This structure was elegantly described again by Gell-Mann by postulating three quarks [7]. All the different particles were joined into a standard model in the middle of 1970s which is also dubbed *The theory of almost everything*. Recently also the elusive Higgs boson was found [8] and with it all of the particles predicted by the standard model. But this does not mean that the search for new particles is now over!

According to the standard model there are twenty-five elementary particles. First there are six leptons arranged in three generations: electron and electron neutrino; muon and muon neutrino; and tau and tau neutrino, each with its antiparticle. The neutrinos interact only via weak interaction while other three leptons interact also electromagnetically. Then there are six quarks also arranged in three generations: up and down; charm and strange; and top and bottom, each with its antiparticle. Each quark carries also a color charge and thus can interact via electroweak and strong interaction. Both leptons and quarks are fermions. Then

there are twelve gauge bosons that mediate the interactions between particles. For the weak interaction there are two W bosons and a Z boson. Electromagnetic interaction is carried by a photon and strong interaction by eight gluons. The final particle in the standard model is the Higgs boson that is responsible for giving mass to other particles.

Just knowing all the elementary particles is not enough, also a precise knowledge of their interactions is necessary. The electromagnetic interaction is described by a quantum electrodynamics. This theory gives extremely accurate predictions of physics phenomena like the electron's anomalous magnetic moment [9]. This is why it earned the title "the jewel of physics" from Feynman. At higher energies it unifies with the theory of weak interaction (also sometimes called quantum flavordynamics) into the electroweak interaction. The description of the strong interaction is made within the quantum chromodynamics that describes the interaction of quarks and gluons. This theory has two interesting properties called asymptotic freedom and confinement. Asymptotic freedom means that at high energies, the coupling constant diminishes. This allows for a perturbative approach in this high energy region. On the other hand, the confinement tells us that the force between the quarks grows (linearly) with the separation. This is the reason why no free quark has yet been observed. They are always bound in colorless hadrons, either three quarks in baryons or a quark anti-quark pair in mesons.

Confinement is described by the growth of the coupling constant at low energies. This means that a the typical hadron scales the perturbative approach to quantum chromodynamics is not possible. There are several approaches to treating the quantum chromodynamics, some more some less reliable (e.g., QCD sum rules [10], ChPT [11], lattice QCD [12]). However, these are all active fields of study. For an illustrative example of the importance of the quantum chromodynamics interactions, let us take a look at the proton. It is composed of three valence quarks uud, however their rest masses contribute only about 1% to the total mass. The other mass comes from the energy of the gluons that bind the quarks. And the interactions of the gluons also gives rise to the sea quarks which have been taken into account recently in lattice simulations [13].

The description of the inner structure of the hadrons, for example, the spatial charge distribution in nuclei is given by their form factors, or more precisely, by their Fourier transform. The response to the external perturbation is described by the polarizabilities. The spatial distribution of these polarizabilities is parametrized by generalized polarizabilities, which are the main topic of this work.

Generalized polarizabilities are interesting for several reasons. Since they can be interpreted as Fourier transforms of spatial distributions of polarizabilities, they provide insight into hadronic structure, complementary to the information gained from form factors. This also gives information about quantum chromodynamics at non-perturbative scales. The generalized polarizabilities also enter the calculation of the muonic hydrogen Lamb shift and with that the calculation of the proton radius. The proton charge radius is currently a very debated topic, since recent results from muonic hydrogen measurements [14, 15] show a 7σ deviation from the 2010-CODATA value, that is based on hydrogen spectroscopy and electron scattering results. The modern calculations of proton-neutron mass difference also rely on generalized

polarizabilities, namely on the difference in behavior of magnetic polarizability for proton and neutron [16, 17].

The generalized polarizabilities can be accessed via a virtual Compton scattering, that is, a scattering of a virtual photon off a target nucleus. Experimentally this is done by a photon electro-production reaction, where an electron is scattered off a target and a photon is present in the final state. The electron and the target exchange a virtual photon. Looking only at the hadronic side of the reaction, this is precisely the virtual Compton scattering reaction. The photon electro-production reaction can naively be seen as an elastic scattering off a target put into an electro-magnetic field of the final photon. This field deforms the target nucleus and it is this deformation that can be described in terms of the generalized polarizabilities.

The theoretical interest for virtual Compton scattering started already in the 1958 [18]. But the experiments were not possible until the arrival of modern electron accelerators facilities that offered high duty-factor beam and high resolution spectrometers. The first dedicated virtual Compton experiment was performed by the A1 collaboration at MAMI during the years 1996 and 1997 [19]. The authors measured a cross section for an unpolarized photon electro-production off proton in the threshold region at a specific four-momentum transfer of $Q^2 = 0.33\,\mathrm{GeV}^2$. The goal was the extraction of two structure functions that are combinations of generalized polarizabilities.

A few similar experiments followed (described in Section 3.2) and now the values of the two structure functions are known at four different values of four-momentum transfer. The problem is that the current theoretical models can not adequately explain the extracted values (see Figure 3.8). For this reason, an additional experiment was performed at MAMI with an aim to determine the two structure functions at three new values of four-momentum transfer of $Q^2 = 0.1$, 0.2 and $0.5\,\mathrm{GeV}^2$ to get a better overview of the momentum-transfer dependence of virtual Compton scattering. This thesis describes the analysis of a part of the data from this experiment and the procedure to extract the structure functions and generalized polarizabilities at one value of four-momentum transfer.

Chapter 2

Theoretical introduction

As it turns out, the electromagnetic interaction is uniquely suitable to explore the proton structure. It is described extremely well within quantum electrodynamics. It is also relatively weak, which enables the perturbative approach to the analysis. The probes usually used are electrons and photons, which are both point-like particles. This means that experiments really give information about the structure of the target without the interference from the probe's own structure.

In this Chapter I first make a short introduction to the elastic electron scattering. The results of such experiments are described in terms of elastic form factors, which carry information of the spatial distribution of charge and magnetization inside the target nucleus.

Then I move on to the description of real Compton scattering where the target is probed by real photons. These experiments give insight into how the target as a whole adapts to an external electromagnetic field. The results can be parametrized by six static polarizabilities: electric, magnetic and six spin-dependent polarizabilities. The electric and magnetic polarizabilities can be accessed in unpolarized Compton scattering, while a polarized experiment is needed for spin polarizabilities.

Finally I introduce virtual Compton scattering with a strong focus on the theory of unpolarized scattering off protons in the threshold region. This reaction is accessed through the photon electro-production reaction, which can be seen as an elastic scattering in a static electromagnetic field. Similarly as elastic scattering expands the notion of total charge and magnetic moment into elastic form factors, virtual Compton scattering generalizes the polarizabilities from real Compton scattering. Generalized polarizabilities here become functions of four-momentum transfer and can be seen as carrying the information about the spatial distribution of these polarizabilities inside the target nucleus.

2.1 Elastic electron scattering

Elastic scattering is one of the standard tools of nuclear physics and was already employed by Rutherford to show that the atoms consist of an electron cloud and a dense nucleus. The more energetic the probe is, the more detailed picture it provides, according to de Broglie:

$$\bar{\lambda} = \frac{\hbar}{\mathrm{p}} = \frac{\hbar c}{\sqrt{2mcT + T^2}} \quad , \tag{2.1}$$

where T is the kinetic energy of the probe. But the result of such experiments can be difficult to interpret if both the probe and the target are extended objects with an internal structure. This is why electrons are usually used as a point-like probe. And the elastic electron scattering off protons is a bit of a special case where the simplest nucleus is studied by an elementary probe.

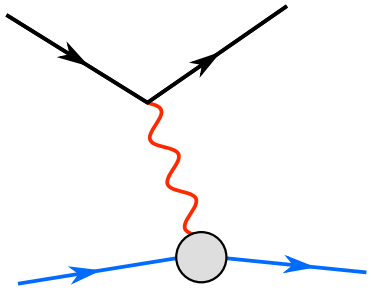

Figure 2.1: Diagram of elastic electron (black lines) scattering off the proton (blue lines). The exchanged virtual photon is marked by the red wavy line. The gray blob indicates the proton's form factors.

2.1.1 Rutherford cross section

The property studied in elastic electron scattering is the shape, or radial distribution of electric charge and magnetic moments in the nucleus. The distributions are parametrized in terms of elastic form factors. An illustration of how the form factors enter the picture is shown in the derivation of Rutherford form factors. This derivation follows [20].

The Rutherford cross section is derived based on two assumptions: the target is heavy enough so that the recoil can be neglected, and Born approximation can be used ($Z\alpha \ll 1$). In the Born approximation, the initial and final states of the electron can be described as plane waves and because of no recoil, three-vectors can be used:

$$\psi_i = \frac{1}{\sqrt{V}} e^{i\vec{k}\cdot\vec{x}/\hbar} \quad , \tag{2.2a}$$

$$\psi_f = \frac{1}{\sqrt{V}} e^{i\vec{k'}\cdot\vec{x}/\hbar} \quad , \tag{2.2b}$$

where $\vec{k}$ and $\vec{k'}$ are the momenta of incoming and scattered electron and V is the volume, which is finite, but large compared to the target nucleus and large enough that discrete states

of the initial and final electron can be approximated by a continuum. From the Fermi's second golden rule the relation between cross section and scattering amplitude follows:

$$\frac{\sigma v_i}{V} = W = \frac{2\pi}{\hbar} \left|M_{fi}\right|^2 \rho(E_f) \quad , \tag{2.3}$$

where v_i is the initial electron velocity and $\rho(E_f)$ is the density of the final states. Since recoil can be neglected, the density of states can be written as:

$$\rho(E_f) = \rho(E') = \frac{4\pi \mathrm{p}'^2 \mathrm{d}\mathrm{p}' V}{(2\pi\hbar)^3 \mathrm{d}E'} = \frac{4\pi V E'^2}{(2\pi\hbar)^3} \quad . \tag{2.4}$$

From first to second line, the assumption of fast electrons was used ($\mathrm{p}' \approx E'/c$, also $v_i \approx c$). The differential cross section for scattering into a small solid angle Ω is:

$$\frac{\mathrm{d}\sigma}{\mathrm{d}\Omega} = \frac{V^2 E'^2}{(2\pi)^2(\hbar c)^4} \left|\langle\psi_f| H_{\text{int}} |\psi_i\rangle\right|^2 \quad . \tag{2.5}$$

The Hamiltonian for an interaction of a charge e with an electric potential ϕ is $H_{\text{int}} = e\,\phi$ and the matrix element is:

$$\langle\psi_f| H_{\text{int}} |\psi_i\rangle = \frac{e}{V} \int \psi(\vec{x}) e^{i\vec{q}\cdot\vec{x}/\hbar} \mathrm{d}^3x \quad , \tag{2.6}$$

where $\vec{q} = \vec{k} - \vec{k'}$ is the momentum transfer. Using the Green's theorem, Poisson's equation and defining the charge distribution function as $\rho(\vec{x}) = Zef(\vec{x})$, the matrix element can be rewritten as:

$$\langle\psi_f| H_{\text{int}} |\psi_i\rangle = \frac{Z 4\pi\alpha\hbar^3 c}{\mathrm{q}^2 V} \int e^{i\vec{q}\cdot\vec{x}/\hbar} f(\vec{x}) \mathrm{d}^3x \quad . \tag{2.7}$$

The integal

$$F(\vec{q}) = \int e^{i\vec{q}\cdot\vec{x}/\hbar} f(\vec{x}) \mathrm{d}^3x \tag{2.8}$$

is called the form factor of the charge distribution. It is a Fourier transform of the charge distribution function, normalized to the total charge. It contains all information about the spatial distribution of charge. To get the Rutherford cross section, the charge distribution is assumed to be a delta function, so $F(\vec{q}) = 1$. The cross section is:

$$\left(\frac{\mathrm{d}\sigma}{\mathrm{d}\Omega}\right)_{\text{Rutherford}} = \frac{Z^2\alpha^2(\hbar c)^2}{4E^2 \sin^4(\theta/2)} \quad , \tag{2.9}$$

where the relation $\mathrm{q} = 2\mathrm{k}\sin(\theta/2)$ that follows from the no recoil assumption has been used.

This is of course only a simplified picture which, with an addition of electron spin effects, works in some applications. But it is also a nice illustration of the origin of form factors.

2.1.2 The elastic form factors of the proton

The Rutherford cross section describes the scattering of a spinless electron off a spinless, point-like and very heavy target. By including the effects of electron spin, target recoil and

target magnetic moment, we get the Mott cross section. By also including the target charge and current distributions, the elastic scattering cross section can be written as [20]:

$$\left(\frac{\mathrm{d}\sigma}{\mathrm{d}\Omega}\right) = \left(\frac{\mathrm{d}\sigma}{\mathrm{d}\Omega}\right)_{\text{Mott}} \cdot \left[\frac{G_{\mathrm{E}}^2(Q^2) + \tau G_{\mathrm{M}}^2(Q^2)}{1+\tau} + 2\tau G_{\mathrm{M}}^2(Q^2)\tan^2(\theta/2)\right] \quad , \tag{2.10a}$$

$$\left(\frac{\mathrm{d}\sigma}{\mathrm{d}\Omega}\right)_{\text{Mott}} = \left(\frac{Z\alpha\hbar c}{2E}\right)^2 \frac{\cos^2(\theta/2)}{\sin^4(\theta/2)} \frac{1}{1+\frac{2E}{mc^2}\sin^2(\theta/2)} \quad , \tag{2.10b}$$

$$\tau = \frac{Q^2}{4m^2c^2} \quad . \tag{2.10c}$$

The $Q^2 = -q^2 > 0$ is a positive Lorentz invariant four-momentum transfer. The G_{E} and G_{M} are the Sachs form factors [21, 22, 23]. The Breit's frame is defined by $p_{\mathrm{B}} + p'_{\mathrm{B}} = (2E_{\mathrm{B}}, \vec{0})$, where $\vec{p}$ and $\vec{p'}$ are four-momenta of the initial and recoiled proton. In this frame, Sachs form factors can again be interpreted as Fourier transforms of the radial distribution of charge and magnetization in the nucleus. In the static limit of $Q^2 \to 0$ they reduce to the total charge in units of e and the total magnetic moment in units of nuclear magneton μ_{N} of the target. For the proton this means:

$$G_{\mathrm{E}}^{\mathrm{p}}(0) = 1 \quad , \tag{2.11a}$$

$$G_{\mathrm{M}}^{\mathrm{p}}(0) = 2.79 \quad . \tag{2.11b}$$

The Q^2 dependence of the form factors is not known a priori, but has to be determined from cross section measurements. The extraction is usually done via Rosenbluth separation [24] based on Equation (2.10a). Recently the extraction has also been possible by a direct multi-parameter fit on measured cross sections [25]. For the proton a very good approximation is a dipole parametrization (see Figure 2.2):

$$G_{\mathrm{E}}^{\mathrm{p}}(Q^2) = \frac{G_{\mathrm{M}}^{\mathrm{p}}(Q^2)}{2.79} = G^{\text{dipole}}(Q^2) \quad , \tag{2.12a}$$

$$G^{\text{dipole}}(Q^2) = \left(1 + \frac{Q^2}{0.71(\,\mathrm{GeV/c})^2}\right)^2 \quad . \tag{2.12b}$$

This means that the proton's charge distribution can be described by an exponential form:

$$\rho(r) = \rho(0)e^{-ar} \quad , \tag{2.13}$$

with $a = 4.27\,\mathrm{fm}^{-1}$.

2.2 Real Compton scattering

The Compton scattering is named after Arthur Holly Compton who won a Nobel prize *"for his discovery of the effect named after him"*. He studied the scattering of X-rays off quasi free electrons (metal surface) where he discovered that after the scattering the photons have longer wavelength than before because part of the photon energy is transferred to the electron.

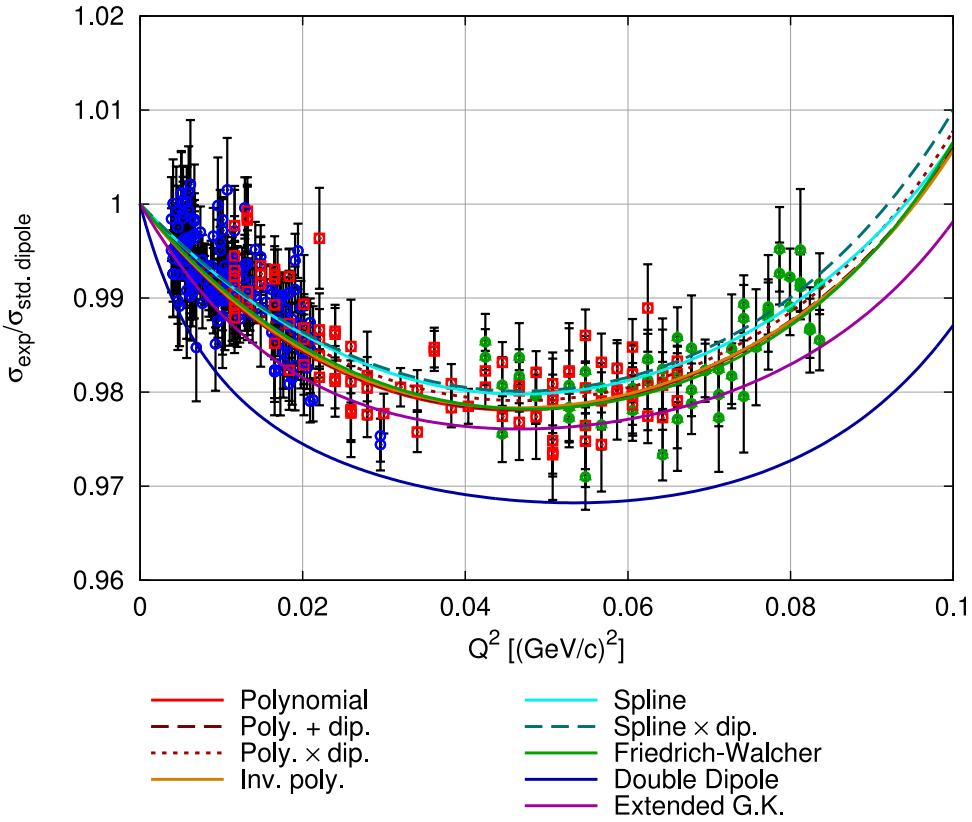

Figure 2.2: Comparison of experimental data on elastic electron scattering off the proton to the calculations based on the standard dipole form factor parametrization (see Equation (2.12)). The lines show alternative parametrizations. This is a part of Bernauer's data [26] at 180 MeV incident beam energy.

Compton described this effect by using a quantum theory of light and relativistic kinematics of the photons [27], thus demonstrating the theory of relativity and particle-wave duality of light. He wrote the famous relation between the incoming and scattered photon wavelengths (λ_0, λ_θ) and the scattering angle θ:

$$\lambda_\theta = \lambda_0 + \frac{2h}{m_e c} \sin^2\left(\frac{\theta}{2}\right) \quad . \tag{2.14}$$

The term Compton scattering can be used as an umbrella term describing a wide variety of scattering of photons, either real or virtual, off small particles. In this section, I will focus on low energy real Compton scattering off a proton, as shown in Figure 2.3.

2.2.1 Low energy expansion

The scattering of photons with large wavelengths (or low energies: $q^0 \to 0$) off a proton can be described as scattering off a point like target by only its static properties, mass and electric charge. This part has already been described by Thomson (see first line of Equation (2.15)).

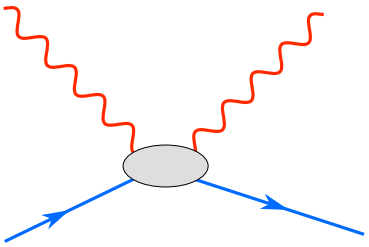

Figure 2.3: Diagram of Compton scattering of the real photon (red lines) off the proton (blue lines). During the scattering the proton deforms (gray blob), which is described by its polarizabilities.

At the next order of low energy expansion, $\mathcal{O}(q_0)$, the magnetic moment of the proton starts to play a role. The scattering amplitude to this order has been calculated e.g. by Low [28].

Calculations to the order of $\mathcal{O}(q_0^2)$ have been made by Petrun'kin [29] and feature proton's polarizabilities $\bar{\alpha}$ and $\bar{\beta}$ [30]:

$$\begin{aligned}
F_{\mathrm{Pet}} = & -\frac{e^2}{m_\mathrm{p}}\vec{\epsilon'}\cdot\vec{\epsilon} \\
& + i(q'^0+q^0)\frac{e^2}{4m_\mathrm{p}^2}(1+2\kappa)\vec{\sigma}\cdot(\vec{\epsilon'}\times\vec{\epsilon}) \\
& - i(q'^0+q^0)\frac{e^2}{4m_\mathrm{p}^2}(1+\kappa)^2\vec{\sigma}\cdot\left[(\hat{q'}\times\vec{\epsilon'})\times(\hat{q}\times\vec{\epsilon})\right] \\
& + i\frac{e^2}{2m_\mathrm{p}^2}(1+\kappa)\left[q'^0(\hat{q'}\cdot\vec{\epsilon})\vec{\sigma}\cdot(\hat{q'}\times\vec{\epsilon'}) - q^0(\hat{q}\cdot\vec{\epsilon'})\vec{\sigma}\cdot(\hat{q}\times\vec{\epsilon})\right] \\
& + q'^0q^0\frac{e^2}{4m_\mathrm{p}^3}(2\kappa+\kappa^2)\vec{\epsilon'}\cdot\vec{\epsilon} \\
& - q'^0q^0\frac{e^2}{4m_\mathrm{p}^3}(1+\kappa)^2(\hat{q'}\times\vec{\epsilon'})\cdot(\hat{q}\times\vec{\epsilon})(\hat{q'}\cdot\hat{q}) \\
& + q'^0q^0\frac{e^2}{4m_\mathrm{p}^3}(\hat{q'}\times\vec{\epsilon'})\cdot(\hat{q}\times\vec{\epsilon}) \\
& + q'^0q^0\left[\bar{\alpha}\,\vec{\epsilon'}\cdot\vec{\epsilon} + \bar{\beta}\,(\hat{q'}\times\vec{\epsilon'})\cdot(\hat{q}\times\vec{\epsilon})\right] \quad . \qquad (2.15)
\end{aligned}$$

Here κ is the proton's anomalous magnetic moment, ϵ and ϵ' are polarization vectors of the incoming and scattered photon with unit momentum vectors of movement $\hat{q}$ and $\hat{q'}$, respectively. The first term is the classical Thomson term. The next six terms arise due to the proton's magnetic moment and the last term is a consequence of the internal structure of the proton, parametrized by two polarizabilities.

The expansion of Equation (2.15) is for energies of the incoming photon up to about $80\,\mathrm{MeV/c}$. After this next order terms must be taken into account. These terms can be described by four spin dependent polarizabilities γ_{E1}, γ_{M1}, γ_{E2} and γ_{M2}. The amplitude at this order is typically written in terms of six invariant amplitudes A_i, which can be calculated in a model like chiral effective theory or χEFT (see e.g. [31]) or DR (see e.g. [32]).

2.2.2 Cross section and polarizabilities

The differential cross sections is calculated by squaring the scattering amplitude. Starting with Equation (2.15), the cross section for unpolarized RCS off the proton is [30]:

$$\left(\frac{\mathrm{d}\sigma}{\mathrm{d}\Omega}\right) = \left(\frac{\mathrm{d}\sigma}{\mathrm{d}\Omega}\right)_{\text{point}} - q^0 q'^0 \left(\frac{q'^0}{q^0}\right)^2 \frac{e^2}{m_\mathrm{p}} \left[\frac{\bar{\alpha}+\bar{\beta}}{2}(1+z)^2 + \frac{\bar{\alpha}-\bar{\beta}}{2}(1-z)^2\right] \quad , \tag{2.16a}$$

$$\left(\frac{\mathrm{d}\sigma}{\mathrm{d}\Omega}\right)_{\text{point}} = \frac{1}{2}\left(\frac{e^2}{m_\mathrm{p}}\right)^2 \left(\frac{q'^0}{q^0}\right)^2 \left[1 + z^2 + \frac{q^0 q'^0}{m_\mathrm{p}^2}\left((1-z)^2 + a_0 + a_1 z + a_2 z^2\right)\right] \quad , \tag{2.16b}$$

with

$$z = \cos\theta \quad , \tag{2.17a}$$

$$a_0 = 2\kappa + \frac{9}{2}\kappa^2 + 3\kappa^3 + \frac{3}{4}\kappa^4 \quad , \tag{2.17b}$$

$$a_1 = -4\kappa - 5\kappa^2 - 2\kappa^3 \quad , \tag{2.17c}$$

$$a_2 = 2\kappa + \frac{1}{2}\kappa^2 - \kappa^3 - \frac{1}{4}\kappa^4 \quad . \tag{2.17d}$$

The polarizabilities enter the cross section at the order of $\mathcal{O}(q_0^2)$ by interference with the Thomson term. Taking only the cross section for the point-like, spin-$1/2$ particles from Equation (2.16b) and taking $\kappa = 0$, Klein-Nishina's formula [33] is retrieved.

By using the optical theorem for the scattering amplitude in correct kinematical limits, three sum rules for RCS [32] can be derived: Baldin sum rule [34], Gerasimov-Drell-Hearn sum rule [35, 36] and the value of forward spin polarizability [37]. The Baldin sum rule is of particular usefulness for extraction of electric and magnetic polarizabilities [30]:

$$\bar{\alpha} + \bar{\beta} = \frac{1}{2\pi^2}\int_{q^0_{\text{thr}}}^{\infty} \mathrm{d}q'^0 \frac{\sigma_{\text{tot}}(q'^0)}{q_0'^2} = (13.8 \pm 0.4)\cdot 10^{-4}\,\mathrm{fm}^3 \quad , \tag{2.18}$$

where the threshold energy $q^0_{\text{thr}} = 150\,\mathrm{MeV/c}$ is at the pion production threshold and σ_{tot} is the total photo-absorption cross section.

The RCS in the low-energy region has been extensively measured by experiments performed by Federspiel et al. [38], MacGibbon et al. [39], Zieger et al. [40] and León et al. (TAPS) [30]. The TAPS data also led to a re-evaluation of the Baldin sum rule. The global averages for the electric and magnetic polarizabilities are [30] (see also Figure 2.4):

$$\bar{\alpha} = (12.1 \pm 0.3 \mp 0.4 \pm 0.3)\cdot 10^{-4}\,\mathrm{fm}^3 \quad , \tag{2.19a}$$

$$\bar{\beta} = (1.6 \pm 0.4 \pm 0.4 \pm 0.4)\cdot 10^{-4}\,\mathrm{fm}^3 \quad , \tag{2.19b}$$

where the first error is statistical, the second is systematic and the third is the model uncertainty.

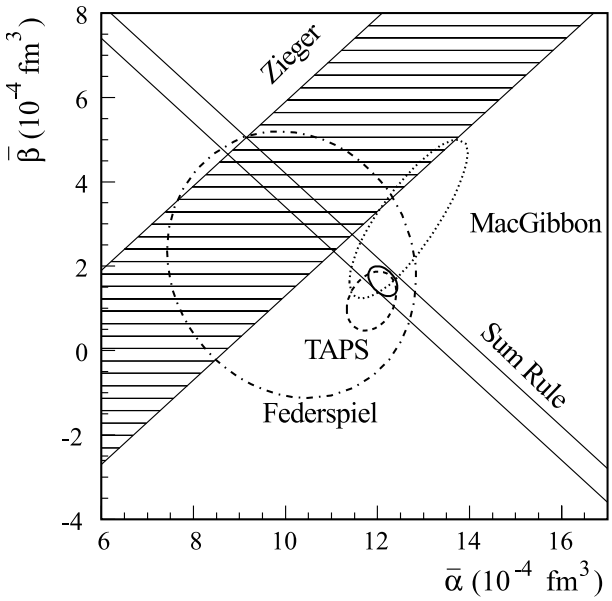

Figure 2.4: The contours at $(\chi^2_{\text{min}} + 1)$ for polarizabilities fit on experimental data. The contour drawn with the thick solid line shows the global fit. The Baldin sum rule and the $(\bar{\alpha} - \bar{\beta})$ constraint from Zieger are also shown. See text for references [30].

2.3 Virtual Compton scattering

Virtual Compton scattering on the proton is the process

$$\gamma^* + p \longrightarrow p' + \gamma \quad , \tag{2.20}$$

where a space-like virtual photon is absorbed by a proton, which then emits a real photon. This is in contrast to RCS, were both photons are real. The reaction (2.20) can be experimentally accessed through photon electro-production reaction off the proton:

$$e + p \longrightarrow e' + \gamma + p \quad . \tag{2.21}$$

In this reaction the final photon can be emitted either by an electron or a proton. The first process is described by the Bethe-Heitler amplitude, which is calculable in quantum electrodynamics (QED). The second process is described by the full virtual Compton scattering amplitude which, in the one photon exchange approximation, is a linear combination of VCS amplitudes.

In this section I will describe the VCS kinematics and derivation of polarizabilities. In this I will mostly follow [41, 42]. An alternative derivation can be found in [43] where generalized polarizabilities are defined in the Breit frame.

2.3.1 Kinematics

The VCS kinematics is shown in Figure 2.5. In the photon-proton center of mass frame, the incident and scattered electron with four-momenta k_{cm} and k'_{cm} define the reaction plane. The angle between the electrons is denoted by $\theta^{\text{e}}_{\text{cm}}$. The scattering plane is defined by the exchanged virtual and final real photon with four-momenta q_{cm} and q'_{cm}. The scattering plane is tilted by an angle ϕ'_{cm} with respect to the reaction plane and the angle between photons is labelled as θ'_{cm}. The target and recoil proton have four-momenta of p_{cm} and p'_{cm}, respectively. In this frame the momenta of the exchanged photon and the target proton are equal but point in opposite directions, $\vec{p}_{\text{cm}} + \vec{q}_{\text{cm}} = \vec{p'}_{\text{cm}} + \vec{q'}_{\text{cm}} = 0$.

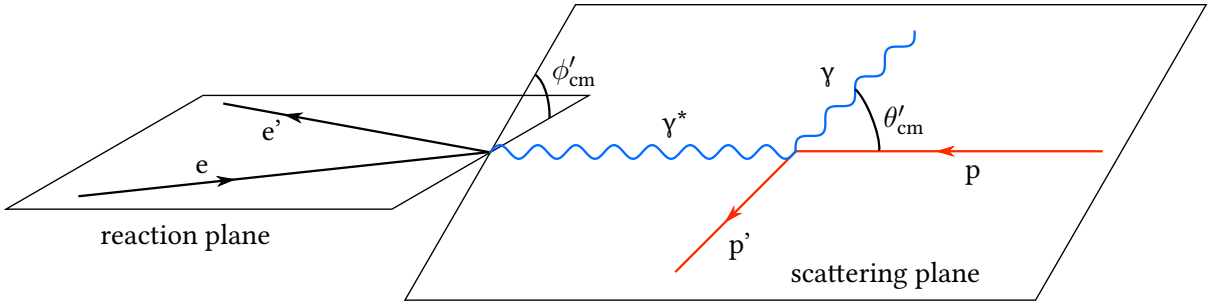

Figure 2.5: VCS kinematics in the center of mass frame where the virtual photon and the proton have equal but opposing momenta. The reaction plane is defined by the momenta of the incident and the scattered electron. The scattering plane is defined by the momenta of the two photons.

The reference angle $\phi'_{\text{cm}} = 0$ is defined when the reaction and the scattering plane are parallel and when the final photon momentum points to the same side of the exchanged photon as does the scattered electron momentum.

Due to the Lorenz boost from the *cm* to *lab* system, the recoil proton momentum is focused in a narrow cone, which greatly enlarges the phase space accessible by high resolution spectrometers.

Table 2.1: Notation used for describing particles involved in the photon electroproduction process off the proton.

	e	e'	γ^*	γ	p	p'
four-momentum	k	k'	$q = k - k'$	q'	p	p'
(rest mass)^2	m_{e}^2	m_{e}^2	$-Q^2 = q^2 < 0$	0	m_{p}^2	m_{p}^2
energy	k^0	k'^0	$q^0 = k^0 - k'^0$	q'^0	p^0	p'^0
momentum	$\vec{k}$	$\vec{k'}$	$\vec{q} = \vec{k} - \vec{k'}$	$\vec{q'}$	$\vec{p}$	$\vec{p'}$
magnitude of momentum	k	k'	$\text{q} = \lvert\text{k} - \text{k}'\rvert$	q'	p	p'

These kind of kinematics are defined by a set of five independent variables (assuming no polarisation is involved). The leptonic side can be described by a *lab* set of three variables

$(\mathrm{k}_{\mathrm{lab}}, \mathrm{k'}_{\mathrm{lab}}, \theta^{\mathrm{e}}_{\mathrm{lab}})$. There are two more sets of variables , a *cm* set with $(\mathrm{q}_{\mathrm{cm}}, \mathrm{q'}_{\mathrm{cm}}, \epsilon)$ and a set of invariants with (Q^2, s, ϵ). Here s is the total energy squared of the *cm* system of the virtual photon and the proton. There is a complete bijection between the three sets given by the following set of equations [44]:

$$Q^2 = 4 \cdot \mathrm{k}_{\mathrm{lab}}\mathrm{k'}_{\mathrm{lab}} \cdot \sin^2\left(\frac{\theta^{\mathrm{e}}_{\mathrm{lab}}}{2}\right) \quad , \tag{2.22a}$$

$$s = -Q^2 + m_{\mathrm{p}}^2 + 2m_{\mathrm{p}}q^0_{\mathrm{lab}} \quad , \tag{2.22b}$$

$$\epsilon = \left[1 + 2 \cdot \frac{\mathrm{q}^2_{\mathrm{lab}}}{Q^2} \cdot \tan^2\left(\frac{\theta^{\mathrm{e}}_{\mathrm{lab}}}{2}\right)\right]^{-1} \quad , \tag{2.22c}$$

$$\mathrm{q}^2_{\mathrm{cm}} = Q^2 + \frac{\left(s - Q^2 - m_{\mathrm{p}}^2\right)^2}{4s} \quad , \tag{2.22d}$$

$$\mathrm{q'}_{\mathrm{cm}} = \frac{s - m_{\mathrm{p}}^2}{2\sqrt{s}} \quad . \tag{2.22e}$$

Two more variables are needed to describe the hadron arm of the reaction. The first one is the angle between the scattering planes, which is the same in both *lab* and *cm* frame, $\phi'_{\mathrm{lab}} = \phi'_{\mathrm{cm}}$. The second one can either be the recoil proton momentum p'_{lab} or the final photon scattering angle θ'_{cm}.

Put together, the sets of five variables look like:

$$\begin{pmatrix} \mathrm{k}_{\mathrm{lab}} \\ \mathrm{k'}_{\mathrm{lab}} \\ \theta^{\mathrm{e}}_{\mathrm{lab}} \\ p'_{\mathrm{lab}} \\ \phi'_{\mathrm{lab}} \end{pmatrix} \leftrightarrow \begin{pmatrix} \mathrm{q}_{\mathrm{cm}} \\ \mathrm{q'}_{\mathrm{cm}} \\ \epsilon \\ \theta'_{\mathrm{cm}} \\ \phi'_{\mathrm{cm}} \end{pmatrix} \leftrightarrow \begin{pmatrix} Q^2 \\ s \\ \epsilon \\ \theta'_{\mathrm{cm}} \\ \phi'_{\mathrm{cm}} \end{pmatrix} \quad . \tag{2.23}$$

From here it can be seen that measuring the scattered electron and recoiled proton is sufficient to determine such kinematics. During the analysis I mainly used the *cm* set of variables (second column in Equation (2.23)).

2.3.2 The threshold regime

The VCS experiment can be performed in different kinematical regimes, but a fruitful interpretation of the result is not always possible. Several different worthwhile regions have been identified until now, like the low energy region, the hard scattering region and the Bjorken region.

In the hard scattering region the $\sqrt{s}$ is large with respect to the typical hadronic scale and angle θ'_{cm} is around $90°$. This regime can be used to test the prediction of PQCD in the hard scattering picture framework [45].

The Bjorken region is often reffered to as deeply virtual Compton scattering (DVCS). It is defined by a large s and Q^2, finite Q^2/s and $\theta'_{\text{cm}} \approx 0$. In this limit the scattering amplitude depends only on four parton distributions.

In the low energy region, the center of mass energy of the final photon and recoil proton is below the pion production threshold:

$$m_{\text{p}} < \sqrt{s} < (m_{\text{p}} + m_{\pi^0}) = \sqrt{s^{\text{thr}}_{\pi^0}} \quad , \tag{2.24}$$

where m_{p} and m_{π^0} are the proton and pion rest masses, respectively. Translated into the final photon momentum, this means:

$$\text{q}'_{\text{cm}} < \frac{s^{\text{thr}}_{\pi^0} - m^2_{\text{p}}}{2s^{\text{thr}}_{\pi^0}} = 126\,\text{MeV} \quad . \tag{2.25}$$

The VCS amplitudes in this region can be parametrised by six generalized polarizabilities, which are real functions of Q^2.

The experiment described in this thesis and the following derivation fall under the low energy regime.

2.3.3 Electron scattering in external field

In the threshold region the energy of the final photon in VCS is small. This means that the electric and magnetic field are almost constant in time and space. If this field is viewed as an external applied field A^{ext}, then VCS can be interpreted as an electron scattering off a target that is placed in a constant electric and magnetic field. The physics is the same as if the target were positioned between two charged plates of a capacitor or in the center of a coil.

Under the influence of the applied field, the charge J^0 and the current density $\vec{J}$ inside the target become modified. If the field is weak, these modifications are linear in the field with so-called polarizabilities as the proportionality coefficients. While only two polarizabilities are needed for a uniform medium, the general case requires a position dependent tensor. The modification of the current density in the linear approximation can be written as:

$$\delta J^\mu(x) = \int \text{d}^4y P^{\mu\nu}(x,y) A^{\text{ext}}_\nu(y) \quad . \tag{2.26}$$

The polarizability tensor can be determined by measuring the modification of the current density by electron scattering. This is analogous to the electron scattering on the free target:

$$J^\mu(q) = \int \text{d}^4x e^{iq\cdot x} J^\mu(x) \quad . \tag{2.27}$$

Here an experiment can be interpreted in terms of a Fourier transform of the current distribution $J^\mu(x)$ or form factors. In the same way VCS gives access to the Fourier transform of $\delta J^\mu(x)$, the modification of this current distribution under the applied field.

In the above it was assumed that the $\delta J^\mu(x)$ term included only a response due to the internal degrees of freedom of the target. If, however, the target has a global static charge and magnetic moment, $\delta J^\mu(x)$ contains also a trivial part due to the global motion under the influence of the external field. At low energies, the proton's response is dominated by this global motion, either movement in the electric field or precession of the magnetic moment. This part of the proton's response can be calculated by knowing the proton's mass, charge and magnetic moment, the internal structure can be ignored. Once this motion is known, one has to calculate the amplitude for electron scattering on this moving proton and the only thing needed for this are the elastic form factors. This domination of the global motion of the proton over the response of the internal degrees of freedom is the classical origin of the low energy theorem [46].

A calculation based on the above considerations is very involved, so usually a quantum derivation is used instead. A sketch of such derivation is showed below.

In the presence of the external field the total current is:

$$\tilde{J}^\mu = ej^\mu + e^2 S^{\mu\nu} A^{\text{ext}}_\nu \quad , \tag{2.28}$$

where j^μ is the hadronic current and $S^{\mu\nu}$ is the contact or seagull term that only has space components because of Hamiltonian formulation. The Schrödinger equation can be written as:

$$i\frac{\partial}{\partial t}\left|t\right\rangle = \left(H_S + V\right)\left|t\right\rangle \quad , \tag{2.29}$$

where the effective Hamiltonian is a sum of the strong interaction Hamiltonian H_S and a perturbation term V given by:

$$V = e\int \mathrm{d}\vec{x}\, j^\mu A^{\text{ext}}_\mu \quad . \tag{2.30}$$

The j^μ does not depend on time because of the Schrödinger representation.

For low energy photons, the target essentially feels a constant electric and magnetic field $\vec{E}$ and $\vec{B}$, and the perturbation is time-independent. Using standard perturbation theory, next result can be written:

$$\begin{aligned}\delta J^\mu_{\text{int}}(\vec{r}) = e^2\ &\left\langle N_{\text{f}}\right| S^{\mu\nu}(\vec{r}) A^{\text{ext}}_\nu(\vec{r})\left|N_{\text{i}}\right\rangle \\ &+ e^2\sum_{n\neq N}\left(\frac{\left\langle N_{\text{f}}\right| V\left|n\right\rangle\left\langle n\right| j^\mu(\vec{r})\left|N_{\text{i}}\right\rangle}{E_{\text{f}} - E_n} + \frac{\left\langle N_{\text{f}}\right| j^\mu(\vec{r})\left|n\right\rangle\left\langle n\right| V\left|N_{\text{i}}\right\rangle}{E_{\text{i}} - E_n}\right) \quad .\end{aligned} \tag{2.31}$$

Here $E_{\text{i(j)}}$ is the energy of the initial (final) state $\left|N_{\text{i(j)}}\right\rangle$. In that expression we have inserted a a complete set of intermediate states between V and j^μ except the nucleon state itself. In the limit of static electric and magnetic field, the nucleon state would produce a singularity, which is the quantum manifestation of the global motion discussed previously and contains no new information. The $\delta J^\mu_{\text{int}}(\vec{r})$ is then the intrinsic induced current. The above equation can be simplified in the case of small Q^2 by setting $E_{\text{i}} = E_{\text{f}} = m$, which is equivalent to neglecting the proton recoil. The m is mass of the nucleon.

The gauge potential for a constant electric field is:

$$A^0_{\text{ext}} = -\vec{r}\cdot\vec{E} \quad , \tag{2.32a}$$

$$\vec{A}_{\text{ext}} = 0 \quad . \tag{2.32b}$$

Using this in Equation (2.31) and remembering that the seagull term has no time component yields:

$$\delta J^{\mu}_{\text{int,E}}(\vec{r}) = e^2 \sum_{n\neq N} \left(\frac{\langle N_{\text{f}}|\, \vec{d}\cdot\vec{E}\,|n\rangle\, \langle n|\, j^{\mu}(\vec{r})\,|N_{\text{i}}\rangle}{E_n - m} + c.c. \right) \quad , \tag{2.33}$$

where the electric dipole moment operator is defined as:

$$\vec{d} = \int \mathrm{d}\vec{r}\,\vec{r} j^0(\vec{r}) \quad . \tag{2.34}$$

The gauge field for a constant magnetic term is:

$$A^0_{\text{ext}} = 0 \quad , \tag{2.35a}$$

$$\vec{A}_{\text{ext}} = -\frac{1}{2}\vec{r}\times\vec{B} \quad . \tag{2.35b}$$

Using this in Equation (2.31) yields:

$$\begin{aligned}\delta J^{\mu}_{\text{int,B}}(\vec{r}) &= e^2 \langle N_{\text{f}}|\, S^{\mu i}(\vec{r})\epsilon_{ijk} r^j\,|N_{\text{i}}\rangle\, B^k \\ &+ e^2 \sum_{n\neq N} \left(\frac{\langle N_{\text{f}}|\, \vec{\mu}\cdot\vec{B}\,|n\rangle\, \langle n|\, j^{\mu}(\vec{r})\,|N_{\text{i}}\rangle}{E_n - m} + c.c \right) \quad ,\end{aligned} \tag{2.36}$$

where the magnetic dipole operator is defined as:

$$\vec{\mu} = \frac{1}{2}\int \mathrm{d}\vec{r}\,\vec{r}\times\vec{j}(\vec{r}) \quad . \tag{2.37}$$

If the trivial part of the response can be eliminated, a low energy VCS experiment allows a measurement of the Fourier transform of the induced currents of Equations (2.33) and (2.36). The induced dipole moments can be calculated from Equations (2.33) and (2.36) as:

$$\delta\vec{d} = \int \mathrm{d}\vec{r}\,\vec{r}\delta J^0_{\text{int,E}} = \bar{\alpha}_{\text{E}}\vec{E} \quad , \tag{2.38a}$$

$$\delta\vec{\mu} = \frac{1}{2}\int \mathrm{d}\vec{r}\,\vec{r}\times\vec{J} = \bar{\beta}_{\text{M}}\vec{B} \quad , \tag{2.38b}$$

after averaging over the nucleon spin projection σ. The magnetic polarizability has a paramagnetic, $\bar{\beta}_{\text{para}}$, and diamagnetic contribution, $\bar{\beta}_{\text{dia}}$. The polarizabilities are given by:

$$\bar{\alpha}_{\text{E}} = \frac{e^3}{2}\sum_{n\neq N,\sigma,\sigma'} \frac{\left|\langle N,\sigma|\,\vec{d}\,|n,\sigma'\rangle\right|^2}{E_n - m} > 0 \quad , \tag{2.39a}$$

$$\bar{\beta}_{\text{para}} = \frac{e^2}{3}\sum_{n\neq N,\sigma,\sigma'} \frac{\left|\langle N,\sigma|\,\vec{\mu}\,|n,\sigma'\rangle\right|^2}{E_n - m} > 0 \quad , \tag{2.39b}$$

$$\bar{\beta}_{\text{dia}} = -\frac{e^2}{6}\sum_{\sigma}\langle N,\sigma|\int \mathrm{d}\vec{r}\, r^2 j^0(\vec{r})\,|N,\sigma\rangle < 0 \quad . \tag{2.39c}$$

These equations show that the polarizabilities are sensitive to the whole excitation spectrum of the nucleon, but since we are below threshold, they contribute only virtually.

2.3.4 Photon electro-production cross section

The S-matrix for the photon electro-production reaction $(\mathrm{e}, \mathrm{e}'\gamma)$ is:

$$S_{\mathrm{fi}} = i(2\pi)^4 \delta^4(p + k - p' - k' - q') T^{\mathrm{ee}'\gamma} \quad . \tag{2.40}$$

In the photo electro-production the final photon can be emitted by either the electron or the proton (see Figure 2.6). These two processes are experimentally indistinguishable. The first process is the so-called Bethe-Heitler (BH) and the second is called full virtual Compton scattering (FVCS) process. The T-matrix can now be written as:

$$T^{\mathrm{ee}'\gamma} = T^{\mathrm{BH}} + T^{\mathrm{FVCS}} \quad . \tag{2.41}$$

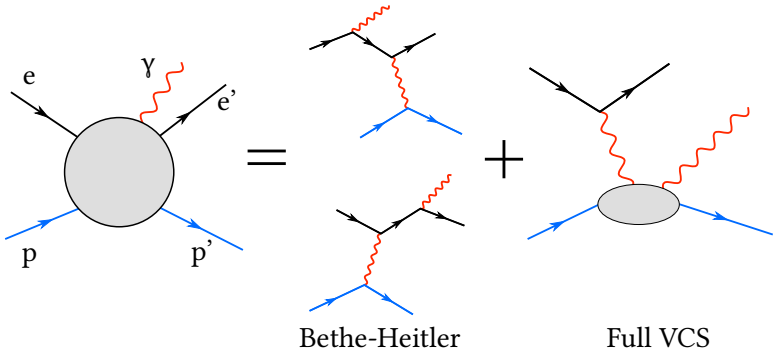

Figure 2.6: The photon electro-production covers two processes; the Bethe-Heitler process where final photon is emitted by one of the electrons; and the full VCS process, where the final photon is emitted by the hadronic vertex.

The experiments are usually performed by detecting the scattered electron and recoiled proton in coincidence. The photo electro-production events are tagged by a zero missing mass squared $(p + k - p' - k')^2 = 0$. The unpolarized cross section in this case in the laboratory frame is:

$$\frac{\mathrm{d}^5\sigma_{\mathrm{lab}}}{\mathrm{dk'_{lab}} \mathrm{d}\hat{k}'_{\mathrm{lab}} \mathrm{d}\hat{p}'_{\mathrm{cm}}} = \frac{(2\pi)^{-5}}{64 m_{\mathrm{p}}} \frac{\mathrm{k'_{lab}}}{\mathrm{k_{lab}}} \frac{s - m_{\mathrm{p}}^2}{s} \mathcal{M} = \frac{(2\pi)^{-5}}{64 m_{\mathrm{p}}} \frac{\mathrm{k'_{lab}}}{\mathrm{k_{lab}}} \frac{2\mathrm{q'_{cm}}}{\sqrt{s}} \mathcal{M} \quad , \tag{2.42}$$

where $\mathrm{d}\hat{p}'_{\mathrm{cm}}$ is $\mathrm{d}\Omega_{\mathrm{cm}}$ and $\mathcal{M}$ is the Lorentz invariant probability for the interaction:

$$\mathcal{M} = \frac{1}{4} \sum_{\sigma,\sigma',h',\lambda'} \left| T^{\mathrm{ee}'\gamma} \right| \quad . \tag{2.43}$$

The sum goes over all possible spin states of the particles.

In the one-photon exchange approximation, the BH amplitude can be written as:

$$T^{\mathrm{BH}} = \frac{-e^3}{t}\varepsilon'^{*}_{\mu} L^{\mu\nu}\, \bar{u}(p')\Gamma_{\nu}(p',p)u(p) \quad , \tag{2.44}$$

where ε'^{*}_{μ} is the polarization vector of the final photon, Γ^{ν} represents the hadronic vertex and $L^{\mu\nu}$ is the leptonic tensor. In QED $L^{\mu\nu}$ gets the form:

$$L^{\mu\nu} = \bar{u}(k')\left(\gamma^{\mu}\frac{(\not{k}' + \not{q}' + m_{\mathrm{e}})}{(k'+q')^2 - m_{\mathrm{e}}^2}\gamma^{\nu} + \gamma^{\nu}\frac{(\not{k}' - \not{q}' + m_{\mathrm{e}})}{(k'-q')^2 - m_{\mathrm{e}}^2}\gamma^{\mu}\right)u(k) \quad , \tag{2.45}$$

where the first denominator can be rewritten as:

$$\frac{1}{(k'+q')^2 - m_{\mathrm{e}}^2} = \frac{1}{2\,k'q'} \quad . \tag{2.46}$$

This means that the BH amplitude has a singularity when it is expanded in powers of $\mathrm{q'}_{\mathrm{cm}}$:

$$T^{\mathrm{BH}} = \frac{a^{\mathrm{BH}}_{-1}}{\mathrm{q'}_{\mathrm{cm}}} + a^{\mathrm{BH}}_{0} + a^{\mathrm{BH}}_{1}\mathrm{q'}_{\mathrm{cm}} + \mathcal{O}(\mathrm{q'}^{2}_{\mathrm{cm}}) \quad . \tag{2.47}$$

The FVCS amplitude has the form:

$$T^{\mathrm{FVCS}} = \frac{e^3}{q^2}\varepsilon'^{*}_{\mu} H^{\mu\nu}\, \bar{u}(k')\gamma_{\nu}u(k) \quad . \tag{2.48}$$

If the lepton current is expanded in terms of the basis polarization vectors, the amplitude can be written as:

$$T^{\mathrm{FVCS}}(\lambda') = \frac{e^3}{-Q^2}\sum_{\lambda}\Omega(h,\lambda)T^{\mathrm{VCS}}(\lambda',\lambda) \quad , \tag{2.49a}$$

$$T^{\mathrm{VCS}}(\lambda',\lambda) = \varepsilon'^{*}_{\mu}(\lambda)H^{\mu\nu}\varepsilon_{\nu}(\lambda) \quad , \tag{2.49b}$$

with $\Omega(h,\lambda)$ being the lepton current. The T^{VCS} is the VCS amplitude that is decoupled from the lepton current and is the main object of our study. Evaluating its transverse part ($\lambda = \pm 1$) along the $\mathrm{q'} = \mathrm{q}$ (or $Q^2 \to 0$) path yields the real Compton amplitude. Hence it is possible to define the observables describing the T^{VCS} in such a way that in this limit they correspond to the polarizabilities from RCS.

Another decomposition of T^{FVCS} is into the so-called Born and non-Born parts. The Born part contains the emission of the final photon from a local coupling to the nucleon, while the non-Born part describes the emission from a nonlocal two-photon interaction with a nucleon. The FVCS amplitude can be written as:

$$T^{\mathrm{FVCS}} = T^{\mathrm{FVCS}}_{\mathrm{B}} + T^{\mathrm{FVCS}}_{\mathrm{NB}} \quad , \tag{2.50a}$$

$$H = H_{\mathrm{B}} + H_{\mathrm{NB}} \quad . \tag{2.50b}$$

The Born term is defined by:

$$H_{\mathrm{B}}^{\mu\nu} = \bar{u}(p')\Gamma^{\mu}(p', p'+q')\frac{(\not{p}'+\not{q}')+m_{\mathrm{p}}}{(p'+q')^2-m_{\mathrm{p}}^2}\Gamma^{\nu}(p'+q', p)u(p) + \bar{u}(p')\Gamma^{\nu}(p', p-q')\frac{(\not{p}-\not{q}')+m_{\mathrm{p}}}{(p-q')^2-m_{\mathrm{p}}^2}\Gamma^{\mu}(p-q', p)u(p) \quad , \tag{2.51}$$

where the first denominator can be rewritten as:

$$\frac{1}{(p'+q')^2-m_{\mathrm{p}}^2} = \frac{1}{2\,p'q'} \quad . \tag{2.52}$$

This means that the Born amplitude also has a singularity when expanded in powers of $\mathrm{q'}_{\mathrm{cm}}$:

$$T_{\mathrm{B}}^{\mathrm{FVCS}} = \frac{a_{-1}^{\mathrm{B}}}{\mathrm{q'}_{\mathrm{cm}}} + a_0^{\mathrm{B}} + a_1^{\mathrm{B}}\mathrm{q'}_{\mathrm{cm}} + \mathcal{O}(\mathrm{q'}_{\mathrm{cm}}^2) \quad . \tag{2.53}$$

The decomposition in Equation (2.50) is such that the H_{NB} is a regular function of q'. This, along with the first part of the gauge invariance requirement,

$$q'_{\mu}H_{\mathrm{NB}}^{\mu\nu} = H_{\mathrm{NB}}^{\mu\nu}q_{\nu} = 0 \quad , \tag{2.54}$$

leads to the low-energy theorem (LET) for VCS. It tells us that the expansion of H_{NB}, which is the unknown part of the VCS amplitude, starts at the order $\mathrm{q'}_{\mathrm{cm}}$:

$$T_{\mathrm{NB}}^{\mathrm{FVCS}} = a_1^{\mathrm{NB}}\mathrm{q'}_{\mathrm{cm}} + \mathcal{O}(\mathrm{q'}_{\mathrm{cm}}^2) \quad . \tag{2.55}$$

This low energy theorem was first shown in [46]. There is also an analogous theorem for the case of RCS [28].

By using Equations (2.47), (2.53) and (2.55) the photon electro-production amplitude can be written as:

$$\begin{aligned} T^{\mathrm{ee'}\gamma} &= T^{\mathrm{BH}} + T_{\mathrm{B}}^{\mathrm{FVCS}} + T_{\mathrm{NB}}^{\mathrm{FVCS}} \\ &= \frac{a_{-1}^{\mathrm{BH}} + a_{-1}^{\mathrm{B}}}{\mathrm{q'}_{\mathrm{cm}}} + (a_0^{\mathrm{BH}} + a_0^{\mathrm{B}}) + \left((a_0^{\mathrm{BH}} + a_0^{\mathrm{B}}) + a_0^{\mathrm{NB}}\right)\mathrm{q'}_{\mathrm{cm}} + \mathcal{O}(\mathrm{q'}_{\mathrm{cm}}^2) \\ &= \frac{a_{-1}^{\mathrm{BH+B}}}{\mathrm{q'}_{\mathrm{cm}}} + a_0^{\mathrm{BH+B}} + (a_1^{\mathrm{BH+B}} + a_1^{\mathrm{NB}})\mathrm{q'}_{\mathrm{cm}} + \mathcal{O}(\mathrm{q'}_{\mathrm{cm}}^2) \quad , \end{aligned} \tag{2.56}$$

where a_i are functions of the remaining four kinematic variables of VCS $(\mathrm{q}_{\mathrm{cm}}, \epsilon, \theta'_{\mathrm{cm}}, \phi'_{\mathrm{cm}})$. The Bethe-Heitler and Born parts depend only on global properties of the proton, i.e. charge, mass and anomalous magnetic moment, and on elastic form factors. They are completely calculable in QED. The new information on proton structure is contained in the factor a_1^{NB}, that appears only in the third order of the expansion. This is the factor that is parametrized by six generalized polarizabilities.

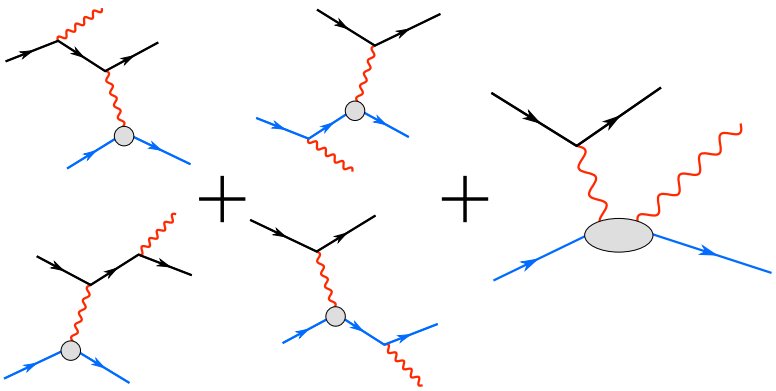

Figure 2.7: The decomposition of the photon electro-production process into Bethe-Heitler, VCS Born and VCS non-Born processes. The red lines mark the photons, the blue protons and black electrons. The gray circles stand for elastic nucleon form factors, except for gray blob in the VCS non-Born case where the internal structure is deformed. This is an expansion of Figure 2.6.

2.3.5 Multipole expansion and generalized polarizabilities

Since H_{BH} and H_{B} are exactly calculable, only H_{NB} remains. The parametrization of this term can be done by a electro-magnetic multipole expansion in the center of mass frame: $H_{\mathrm{NB}}^{(\rho' L', \rho L) S}(\mathrm{q}', \mathrm{q})$. The L and L' represent the angular momentum of the initial and final electromagnetic transition. The S marks the spin-flip ($S = 1$) or non spin-flip ($S = 0$) transitions on the nucleon side. The ρ and ρ' can take four values: one for charge or 'C' transition, one for magnetic or 'M', two for electric or 'E' and three for longitudional transition. This can further be restricted to $\rho \in [0, 1, 2]$ and $\rho' \in [1, 2]$ in the case of VCS.

Due to parity and angular momentum conservation the selection rules are:

$$S \in [0, 1] \quad , \tag{2.57a}$$
$$|L' - S| \leq L \leq L' + S \quad , \tag{2.57b}$$
$$(-1)^{\rho' + L'} = (-1)^{\rho + L} \quad , \tag{2.57c}$$

with additional knowledge that the electric and magnetic multipoles vanish for $L = L' = 0$. By restricting the multipole search to the ones proportional to $\mathrm{q}'_{\mathrm{cm}}$, and by using the above selection rules, only ten multipoles remain:

$$\begin{aligned} &H_{\mathrm{NB}}^{(11,00)1}, H_{\mathrm{NB}}^{(11,02)1}, H_{\mathrm{NB}}^{(11,22)1}, H_{\mathrm{NB}}^{(21,12)1}, \\ &H_{\mathrm{NB}}^{(11,11)S}, H_{\mathrm{NB}}^{(21,01)S}, H_{\mathrm{NB}}^{(21,21)S} \quad . \end{aligned} \tag{2.58}$$

At low energies but arbitrary q, the behaviour of the non-Born amplitude can be described by ten functions of q:

$$\lim_{\mathrm{q}' \to 0} \frac{1}{\mathrm{q}'} \frac{1}{\mathrm{q}} H^{(\rho' 1, \rho L) S}(\mathrm{q}'_{\mathrm{cm}}, \mathrm{q}_{\mathrm{cm}}) \quad . \tag{2.59}$$

In RCS, the polarizabilities are defined in the limit $q'_{cm} = q_{cm} \to 0$. In VCS, on the other hand, the polarizabilities are defined by the limit $q'_{cm} \to 0$ at fixed q_{cm}. One would like to see that the polarizabilities match the RCS case when $q_{cm} \to 0$ (see Figure 2.8). Unfortunately, this is not true for all polarizabilities as defined by Equations (2.58) and (2.59).

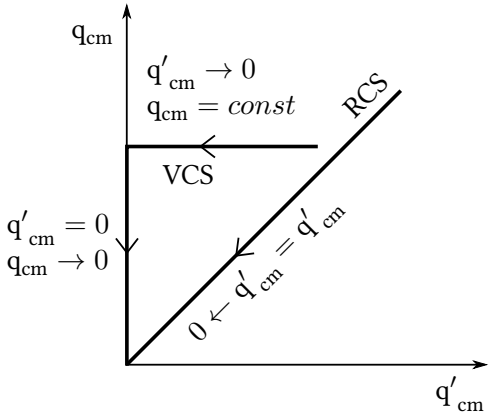

Figure 2.8: In the RCS the limit is taken along the $q'_{cm} \to 0$ line, while in the VCS the limit is $q'_{cm} \to 0$ with a constant non-zero q_{cm}. To get to the RCS case an additional $q_{cm} \to 0$ limit has to be be taken.

To solve the problem of different limits in RCS and VCS case, one can first write the generalized polarizabilities for multipoles where the two limits are equal:

$$P^{(11,00)1}(q_{cm}) = \left[\frac{1}{q'_{cm}} H_{NB}^{(11,00)1}(q'_{cm}, q_{cm})\right]_{q'_{cm}=0} , \tag{2.60a}$$

$$P^{(11,02)1}(q_{cm}) = \left[\frac{1}{q'_{cm} q_{cm}^2} H_{NB}^{(11,02)1}(q'_{cm}, q_{cm})\right]_{q'_{cm}=0} , \tag{2.60b}$$

$$P^{(11,11)S}(q_{cm}) = \left[\frac{1}{q'_{cm} q_{cm}} H_{NB}^{(11,11)S}(q'_{cm}, q_{cm})\right]_{q'_{cm}=0} . \tag{2.60c}$$

Next, the Siegert relation [47] can be used to specify the low energy behaviour of $H_{NB}^{(21,01)S}$ and $H_{NB}^{(21,12)1}$ by defining:

$$P^{(01,01)S}(q_{cm}) = \left[\frac{1}{q'_{cm} q_{cm}} H_{NB}^{(01,01)S}(q'_{cm}, q_{cm})\right]_{q'_{cm}=0} , \tag{2.61a}$$

$$P^{(01,12)1}(q_{cm}) = \left[\frac{1}{q'_{cm} q_{cm}^2} H_{NB}^{(01,12)1}(q'_{cm}, q_{cm})\right]_{q'_{cm}=0} . \tag{2.61b}$$

Drechsel et al. showed in [48, 49] that the low energy limits of all ten multipoles can be expressed by six generalized polarizabilities already defined by the above equations (see Appendix A). These polarizabilities are:

$$P^{(01,01)S}(q), P^{(11,11)S}(q), \\ P^{(11,02)1}(q), P^{(01,12)1}(q) \quad . \tag{2.62}$$

It can be further shown that the following relations hold in the RCS limit:

$$P^{(01,01)1}(0) = P^{(11,11)1}(0) = 0 \quad , \tag{2.63a}$$

$$P^{(01,01)0}(0) = -\sqrt{\frac{2}{3}}\,\frac{\alpha_{\mathrm{E}}}{\alpha_{\mathrm{QED}}} \quad , \tag{2.63b}$$

$$P^{(11,11)0}(0) = -\sqrt{\frac{8}{3}}\,\frac{\beta_{\mathrm{M}}}{\alpha_{\mathrm{QED}}} \quad . \tag{2.63c}$$

2.3.6 Observables

The photon electro-production cross section from Equation (2.42) can be rewritten as:

$$\frac{\mathrm{d}^5\sigma^{\mathrm{pep}}}{\mathrm{d}\Omega^5} = (\phi \mathrm{q'}_{\mathrm{cm}})\,\mathcal{M}^{\mathrm{pep}} \quad , \tag{2.64}$$

where $(\phi \mathrm{q'}_{\mathrm{cm}})$ is the kinematical factor and $\mathcal{M}^{\mathrm{pep}}$ is the Lorentz invariant interaction probability for photon electro-production. From Equations (2.43) and (2.56) it can be seen that also $\mathcal{M}$ can be expanded in powers of $\mathrm{q'}_{\mathrm{cm}}$:

$$\mathcal{M}^{\mathrm{pep}} = \frac{\mathcal{M}^{\mathrm{pep}}_{-2}}{\mathrm{q'}^2_{\mathrm{cm}}} + \frac{\mathcal{M}^{\mathrm{pep}}_{-1}}{\mathrm{q'}_{\mathrm{cm}}} + \mathcal{M}^{\mathrm{pep}}_{0} + \mathcal{O}(\mathrm{q'}_{\mathrm{cm}}) \quad , \tag{2.65a}$$

$$\mathcal{M}^{\mathrm{the}} = \frac{\mathcal{M}^{\mathrm{BH+B}}_{-1}}{\mathrm{q'}^2_{\mathrm{cm}}} + \frac{\mathcal{M}^{\mathrm{BH+B}}_{-1}}{\mathrm{q'}_{\mathrm{cm}}} + \mathcal{M}^{\mathrm{BH+B}}_{0} + \mathcal{M}^{\mathrm{NB}}_{0} + \mathcal{O}(\mathrm{q'}_{\mathrm{cm}}) \quad . \tag{2.65b}$$

This is also known as a low energy expansion or LEX. The terms $\mathcal{M}^{\mathrm{pep}}_{-2}$ and $\mathcal{M}^{\mathrm{pep}}_{-1}$ are equal to $\mathcal{M}^{\mathrm{BH+B}}_{-2}$ and $\mathcal{M}^{\mathrm{BH+B}}_{-1}$, respectively, and can be calculated exactly for given $(\mathrm{q}_{\mathrm{cm}}, \epsilon, \theta'_{\mathrm{cm}}, \phi'_{\mathrm{cm}})$ when the elastic form factors are known. The information on generalized polarizabilities is contained in the $\mathcal{M}^{\mathrm{pep}}_{0}$ part and it comes from the interference terms between $a^{\mathrm{BH+B}}_{-1}$ and a^{NB}_{1} of Equation (2.56). The unknown part of the amplitude can be extracted from the experiment via:

$$\mathcal{M}^{\mathrm{NB}}_{0} = \mathcal{M}^{\mathrm{pep}}_{0} - \mathcal{M}^{\mathrm{BH+B}}_{0} = \left[\mathcal{M}^{\mathrm{pep}} - \mathcal{M}^{\mathrm{BH+B}}\right]_{\mathrm{q'}_{\mathrm{cm}} \to 0} \quad . \tag{2.66}$$

By using the above equations, the cross section becomes:

$$\begin{aligned}\frac{\mathrm{d}^5\sigma^{\mathrm{pep}}}{\mathrm{d}\Omega^5} &= (\phi \mathrm{q'}_{\mathrm{cm}}) \left(\frac{\mathcal{M}^{\mathrm{BH+B}}_{-1}}{\mathrm{q'}^2_{\mathrm{cm}}} + \frac{\mathcal{M}^{\mathrm{BH+B}}_{-1}}{\mathrm{q'}_{\mathrm{cm}}} + \mathcal{M}^{\mathrm{BH+B}}_{0} \right) + (\phi \mathrm{q'}_{\mathrm{cm}}) \left(\mathcal{M}^{\mathrm{NB}}_{0}\right) + \mathcal{O}(\mathrm{q'}^2_{\mathrm{cm}}) \\ &= \frac{\mathrm{d}^5\sigma^{\mathrm{BH+B}}}{\mathrm{d}\Omega^5} + (\phi \mathrm{q'}_{\mathrm{cm}}) \left(\mathcal{M}^{\mathrm{pep}}_{0} - \mathcal{M}^{\mathrm{BH+B}}_{0}\right) + \quad \mathcal{O}(\mathrm{q'}^2_{\mathrm{cm}}),\end{aligned} \tag{2.67}$$

where the cross section in the first term is completely calculable. The second term is in general parametrized by six generalized polarizabilities. In the case of the unpolarized cross section the parametrization requires only five generalized polarizabilities and the above equation is usually written as:

$$\frac{\mathrm{d}^5\sigma^{\mathrm{pep}}}{\mathrm{d}\Omega^5} = \frac{\mathrm{d}^5\sigma^{\mathrm{BH+B}}}{\mathrm{d}\Omega^5} + (\phi \mathrm{q'}_{\mathrm{cm}}) \left[v_{\mathrm{LL}} \left(P_{\mathrm{LL}}(\mathrm{q}_{\mathrm{cm}}) - \frac{P_{\mathrm{TT}}(\mathrm{q}_{\mathrm{cm}})}{\epsilon} \right) + v_{\mathrm{LT}} P_{\mathrm{LT}}(\mathrm{q}_{\mathrm{cm}}) \right] \quad , \tag{2.68}$$

where v_{LL} and v_{LT} are only functions of $(\phi'_{\mathrm{cm}}, \theta'_{\mathrm{cm}})$ and of $(q_{\mathrm{cm}}, \epsilon)$, but the latter two are kept constant. The structure functions are given by:

$$P_{\mathrm{LL}}(\mathrm{q_{cm}}) = -2\sqrt{6} m_{\mathrm{p}} G_{\mathrm{E}}(\mathrm{q_{cm}}) P^{(01,01)0}(\mathrm{q_{cm}}) \quad , \tag{2.69a}$$

$$P_{\mathrm{TT}}(\mathrm{q_{cm}}) = -3 G_{\mathrm{M}}(\mathrm{q_{cm}}) \frac{\mathrm{q_{cm}^2}}{\tilde{q_0}} \left(P^{(11,11)1}(\mathrm{q_{cm}}) - \sqrt{2}\tilde{q_0} P^{(01,12)1}(\mathrm{q_{cm}}) \right) \quad , \tag{2.69b}$$

$$P_{\mathrm{LT}}(\mathrm{q_{cm}}) = \sqrt{\frac{3}{2}} m_{\mathrm{p}} \frac{\mathrm{q_{cm}}}{\tilde{Q}} G_{\mathrm{E}}(\mathrm{q_{cm}}) P^{(11,11)0}(\mathrm{q_{cm}}) + \frac{3}{2} \frac{\mathrm{q_{cm}}}{\tilde{q_0}} \tilde{Q} G_{\mathrm{M}}(\mathrm{q_{cm}}) P^{(01,01)1}(\mathrm{q_{cm}}) \quad . \tag{2.69c}$$

Here $\tilde{}$ denotes the limit $\mathrm{q'_{cm}} \to 0$, and $\tilde{q_0} = -\tilde{Q}^2/2m_{\mathrm{p}}$. The functional dependence of v_{LL} and v_{LT} is given in Appendix A.

The experimental determination of the two structure functions $(P_{\mathrm{LL}}(\mathrm{q_{cm}}) - P_{\mathrm{TT}}(\mathrm{q_{cm}})/\epsilon)$ and $P_{\mathrm{LT}}(\mathrm{q_{cm}})$ is possible by measuring the photon electro-production cross section at different values of v_{LL} and v_{LT}, i.e. different $(\phi'_{\mathrm{cm}}, \theta'_{\mathrm{cm}})$, and at fixed values for $(\mathrm{q_{cm}}, \epsilon)$. This is called a LEX extraction and is detailed in Section 6.4.3. Extracting the values of these two structure functions for a case of $Q^2 = 0.1\,\mathrm{GeV}^2$ is the goal of this thesis. Further separation of $(P_{\mathrm{LL}}(\mathrm{q_{cm}})$ and $P_{\mathrm{TT}}(\mathrm{q_{cm}})$ could be achieved by measuring at different values of ϵ. To extract the values of all six generalized polarizabilities, a double polarization experiment would be needed.

Chapter 3

Theoretical and experimental studies of VCS

The first part of this chapter gives an overview of some theoretical models for virtual Compton scattering and their predictions for the polarizabilities. In the second part, previous virtual Compton experiments and their results are presented.

3.1 Theoretical models

Generalized polarizabilities of the nucleons have been calculated in various models, spanning over the non-relativistic quark model (nRQM), the effective Lagrangian model (ELM), the linear σ model (LSM), heavy baryon chiral perturbation theory (HBχPT) and the dispersion relation model (DR). Below a short description of these models is given.

3.1.1 Dispersion relation model

The DR model for VCS off the proton was developed by Pasquini et al. [50] who also made calculations for generalized polarizabilities in this model. The model is valid beyond the pion production threshold into the $\Delta(1232)$ resonance region.

The VCS process is described within the DR model by independent variables Q^2, t and ν that change sign under crossing:

$$\nu = \frac{s-u}{4M_{\mathrm{p}}} \quad . \tag{3.1}$$

The s, t and u are Mandelstam variables:

$$s = (q+p)^2 \quad , \tag{3.2a}$$
$$t = (q-q')^2 \quad , \tag{3.2b}$$
$$u = (q-p')^2 \quad , \tag{3.2c}$$
$$s+t+u = 2M_{\mathrm{p}}^2 - Q^2 \quad . \tag{3.2d}$$

The VCS tensor $\mathcal{M}^{\kappa\sigma}$ is parametrized in terms of twelve independent amplitudes:

$$\mathcal{M}^{\kappa\sigma} = \sum_{i=1}^{12} F_i(Q^2,\nu,t)\nu^l \rho_i^{\kappa\sigma} \quad , \tag{3.3}$$

where $l = 1$ for $i \in 3,4,8,10$ and $l = 0$ otherwise. The $\rho_i^{\mu\nu}$ are independent tensors in such a basis, that the resulting non-Born invariant amplitudes are free of kinematical singularities and constraints. The amplitudes F_i are even in ν.

The generalized polarizabilities are defined in the limit $\mathrm{q}'_{\mathrm{cm}} \to 0$ at a finite value of q_{cm}. This limit corresponds to the limit of $\nu \to 0$ and $t \to -Q^2$. The polarizabilities can then be expressed in terms of:

$$\bar{F}_i(Q^2) \equiv F_i^{\mathrm{NB}}(Q^2, \nu = 0, t = -Q^2) \quad . \tag{3.4}$$

If the amplitudes have appropriate high-energy behaviour and analyticity, they can be evaluated in the framework of unsubtracted dispersion relations:

$$\bar{F}_i(Q^2) = \frac{2}{\pi} \int_{\nu_{\mathrm{thr}}}^{+\infty} \mathrm{d}\nu' \frac{\Im_s F_i(Q^2, \nu', t = -Q^2)}{\nu'} \quad . \tag{3.5}$$

The integral is calculated by taking into the account the dominant contribution of the πN states. The calculation uses the phenomenological MAID analysis [51] for the evaluation of the pion photo- and electro-production multipoles.

As it turns out, the amplitudes $\bar{F}_1$ and $\bar{F}_5$ do not have appropriate high-energy behaviour, so only four of six generalized polarizabilities can be evaluated directly. These two amplitudes are then split into integral and asymptotic parts. The integral part is limited to the $-\nu_{\mathrm{max}} < \nu < \nu_{\mathrm{max}}$ and is finite for an appropriately chosen boundary. For $\bar{F}_5$, the asymptotic part contribution comes mainly from the t-channel π^0-exchange and can be estimated.

The $\bar{F}_1(Q^2)$ can be expressed in terms of generalized magnetic polarizability $P^{(11,11)0}(Q^2)$. A convenient parametrization exists in the form of:

$$\beta_{\mathrm{M}}(Q^2) - \beta_{\mathrm{M}}^{\pi\mathrm{N}}(Q^2) = \frac{\beta_{\mathrm{M}} - \beta_{\mathrm{M}}^{\pi\mathrm{N}}}{\left(1 + Q^2/\Lambda_\beta^2\right)^2} \quad , \tag{3.6}$$

that fixes the value at $Q^2 = 0$ to the RCS point. Similar procedure is also done with $\bar{F}_2$ to extend the energy range to the $\Delta(1232)$ resonance region. The parametrization in this case is analogous:

$$\alpha_{\mathrm{E}}(Q^2) - \alpha_{\mathrm{E}}^{\pi\mathrm{N}}(Q^2) = \frac{\alpha_{\mathrm{E}} - \alpha_{\mathrm{E}}^{\pi\mathrm{N}}}{\left(1 + Q^2/\Lambda_\alpha^2\right)^2} \quad . \tag{3.7}$$

The parameters $\Lambda_{\alpha,\beta}$ are the only free parameters of the model and have to be fitted to the experimental data.

3.1.2 Effective Lagrangian model

The scalar electric and magnetic generalized polarizabilities α_{E} and β_{M} have been calculated by Vanderhaeghen [52] in the effective Lagrangian model formalism. The study was later expanded by Korchin and Scholten [53] by a more general treatment of the Δ degrees of freedom and by also including the calculation of the spin-dependent polarizabilities.

In this model the contribution of nucleon resonances is given by summing appropriate Feynman diagrams. The diagrams for π^0 exchange and scalar meson σ (correlated $\pi\pi$) exchange are also included. The resonances considered are $\mathrm{P}_{33}(\Delta 1232)$, $\mathrm{P}_{11}(\mathrm{N}1440)$, $\mathrm{D}_{13}(\mathrm{N}1520)$, $\mathrm{S}_{11}(\mathrm{N}1535)$, $\mathrm{P}_{33}(\Delta 1600)$, $\mathrm{S}_{11}(\mathrm{N}1620)$, $\mathrm{S}_{31}(\Delta 1620)$, $\mathrm{D}_{13}(\mathrm{N}1700)$, $\mathrm{D}_{33}(\Delta 1700)$ and $\mathrm{P}_{11}(\mathrm{N}1710)$. The parameters of the model, such as couplings of resonances, are adjusted to the experimental data.

In this model, the electric and magnetic polarizabilities in the real Compton limit are [53]:

$$\alpha_{\mathrm{E}} = 5.6 \cdot 10^{-4}\,\mathrm{fm}^3 \quad , \tag{3.8a}$$

$$\beta_{\mathrm{M}} = 2.6 \cdot 10^{-4}\,\mathrm{fm}^3 \quad . \tag{3.8b}$$

3.1.3 Heavy baryon chiral perturbation theory

The generalized polarizabilities of the proton within the HBχPT framework were first calculated by Hemmert et al. [54, 55, 56]. The calculations were performed to order $\mathcal{O}(p^3)$ and to $\mathcal{O}(\epsilon^3)$ for small scale expansion. The calculations were later pushed to $\mathcal{O}(p^4)$ by Kao et al. [57, 58] for the generalized spin polarizabilities of the nucleon.

The HBχPT is an effective field theory. Here one only works at the low energies, according to some set scale. The theory is then expanded in powers of this characteristic scale. The expansion is renormalized order-by-order, by specifying the theory with a finite number of coupling constants. All observables are then parametrized by these few constants. The order of expansion is denoted by $\mathcal{O}(p^n)$ where p is the characteristic scale, which is either a mass or a momentum.

Chiral perturbation theory (ChPT) starts with chiral symmetry, which states that for massless fermions the chirality is a constant of motion. The underlying symmetry of such fermions is $\mathrm{SU}(n)_{\mathrm{L}} \times \mathrm{SU}(n)_{\mathrm{R}}$, where n is the number of fermions. If the symmetry gets spontaneously broken, the fermions acquire mass (same for all). The remaining symmetry is $\mathrm{SU}(n)_{\mathrm{V}}$ and $n^2 - 1$ massless Goldstone bosons are generated. By explicitly breaking the symmetry by giving fermions different masses, the bosons also gain mass. The typical case in ChPT are the quarks $(\mathrm{u}, \mathrm{d}, \mathrm{s})$, with $n = 3$. Breaking the chiral symmetry gives rise to eight bosons: three pions $(\pi^{\pm}, \pi^0)$, four kaons $(\mathrm{K}^{\pm}, \bar{\mathrm{K}}^0, \mathrm{K}^0)$ and the η. More information on ChPT can be found in [11].

In the HBχPT approach to VCS, the starting point are the nucleons, proton and neutron with

underlying SU(2) symmetry. After chiral symmetry breaking the remaining bosons are pions, which give rise to pion-nucleon interaction. The πN loop diagrams are important in the calculation, since they model the interaction between photons and the proton's pion cloud. The model is also highly constrained, since all parameters used in the effective Lagrangian are known.

An alternative approach to pion-nucleon ChPT is the small-scale expansion [56], where the nucleon resonance $\Delta(1232)$ is contributing as a dynamical degree of freedom. This allows one to move away from near-threshold processes. The power counting has to be modified to bring the $\Delta(1232)$ related effects into lower orders of the calculation. The power scale ϵ now also includes the $\Delta(1232) - \mathrm{N}(940)$ mass splitting, $\Delta = M_\Delta - M_\mathrm{N}$, in addition to the chiral expansion parameters of small momenta q and pion mass m_π.

The model shows slow convergence for the generalized polarizabilities, since large corrections for spin-dependent polarizabilities were observed when going from $\mathcal{O}(p^3)$ to $\mathcal{O}(p^4)$. In this approach, the real Compton limits for electric and magnetic polarizabilities for $\mathcal{O}(p^3)$ are [56]:

$$\alpha_\mathrm{E} = 12.5 \cdot 10^{-4}\,\mathrm{fm}^3 \quad , \tag{3.9a}$$

$$\beta_\mathrm{M} = 1.3 \cdot 10^{-4}\,\mathrm{fm}^3 \quad . \tag{3.9b}$$

3.1.4 Linear σ model

The three scalar generalized polarizabilities were calculated in the pion-nucleon LSM by Metz and Drechsel [59] who later calculated in this framework also seven vector polarizabilities [60]. This calculation also offered the first model prediction of scalar polarizabilities for the neutron. See also [61, 62, 63] for calculations of static electromagnetic polarizabilities of nucleons.

The LSM is not a very realistic model, but it fulfills the Lorentz, gauge and chiral symmetries. It also satisfies the partially conserved axial current (PCAC) relation:

$$\partial^\mu A^a_\mu = f_\pi m_\pi^2 \pi^a \quad , \tag{3.10}$$

where f_π is the pion decay constant and π^a represents the three charge states of pion. The meson-pion coupling is governed by a pseudoscalar coupling constant $g_{\mathrm{N}\pi} = 13.4$. The mass of the σ is a free parameter of the model.

The calculations were done in the limit of infinite σ mass in the one loop approximation. Because the model does not include the $\Delta(1232)$ resonance and its paramagnetic contribution, β_M is expected to be too low. The values of electric and magnetic polarizabilities in the real photon limit for the proton are [59]:

$$\alpha_\mathrm{E} = 7.5 \cdot 10^{-4}\,\mathrm{fm}^3 \quad , \tag{3.11a}$$

$$\beta_\mathrm{M} = -2.0 \cdot 10^{-4}\,\mathrm{fm}^3 \quad . \tag{3.11b}$$

3.1.5 Non-relativistic quark model

The first calculation of the generalized polarizabilities was done by Guichon et al. [41] in the nRQM. The method was later improved by Liu et al. [64] by including the proton recoil effect. The model was also revisited by Pasquini et al. [65].

The model is defined by a nRQM Hamiltonian:

$$H_{\text{nRQM}} = \sum_{\alpha=1}^{N} -\frac{(\vec{\nabla}_\alpha)^2}{2m_\alpha} + \sum_{\alpha<\beta} V_{\alpha\beta}(\vec{r}_{\alpha\beta}) \quad , \tag{3.12}$$

that satisfies the Schrödinger equation:

$$i\frac{\partial}{\partial t}\Psi(\vec{r}_1,\vec{r}_2,\vec{r}_3,t) = H_{\text{nRQM}}\Psi(\vec{r}_1,\vec{r}_2,\vec{r}_3,t) \quad . \tag{3.13}$$

Here m_α is the constituent quark mass and $\vec{r}_\alpha$ and $\vec{\nabla}_\alpha$ are quark position and momentum operators, respectively. The photon interaction is introduced via minimal substitution, such that the Schrödinger equation is invariant under the gauge transformation.

The model is non-relativistic, violates gauge invariance, and does not obey chiral symmetry. The results should therefore be treated with caution but they still provide order-of-magnitude estimates for nuclear resonance contributions. In the nRQM, the electric and magnetic polarizabilities in the real photon limit are [65]:

$$\alpha_{\text{E}} = 5.5 \cdot 10^{-4}\,\text{fm}^3 \quad , \tag{3.14a}$$

$$\beta_{\text{M}} = 4.7 \cdot 10^{-4}\,\text{fm}^3 \quad . \tag{3.14b}$$

3.2 Experiments

The first dedicated VCS experiment was performed at MAMI during the years 1996-1997 with the goal of extracting two structure functions $(P_{\text{LL}} - P_{\text{TT}}/\epsilon)$ and P_{LT} at $Q^2 = 0.33\,\text{GeV}^2$. Two experiments followed at MIT-Bates and JLab with the same goal, but at different values of Q^2: $0.06\,\text{GeV}^2$ at Bates and 0.92 and $1.76\,\text{GeV}^2$ at JLab.

Besides the unpolarized measurements, there was also polarized-beam experiment and a double-polarized VCS experiment, both performed at MAMI. In the first experiment [66, 67] the authors measured the single-spin asymmetry above the pion production threshold with the aim of testing the DR predictions. In the second experiment [68, 69, 70] the authors measured the $P_{\text{LT}}^{\perp}$ structure function for the first time. As part of this data-taking, the unpolarized MAMI point was also remeasured.

The new efforts on the VCS front were also done at MAMI. The most recent experiment focused on measuring the structure functions $(P_{\text{LL}} - P_{\text{TT}}/\epsilon)$ and P_{LT} at three values of Q^2 of

$0.1\,\mathrm{GeV}^2$ (described in this thesis), $0.2\,\mathrm{GeV}^2$ and $0.5\,\mathrm{GeV}^2$ to get a better overview of the Q^2 dependence [71]. The second experiment was a measurement of VCS in the delta resonance region [72]. The analysis for these experiments is still under way.

3.2.1 MAMI 96-97

The first dedicated VCS experiment [19] was performed by the A1 collaboration at MAMI. The authors measured the absolute photon electro-production cross sections $\mathrm{d}^5\sigma$ at fixed four-momentum transfer $Q^2 = 0.33\,\mathrm{GeV}^2$ or $\mathrm{q}_{\mathrm{cm}} = 600\,\mathrm{MeV}$ and at fixed virtual photon polarization $\epsilon = 0.62$. The final photon momentum $\mathrm{q'}_{\mathrm{cm}}$ covered five values of 33.6, 45.0, 67.5, 90.0 and $111.5\,\mathrm{MeV}$. The out-of-plane angle ϕ'_{cm} range was determined by spectrometer acceptance around $0°$ and $180°$, with the angle θ'_{cm} ranging from $-141°$ to $6°$.

The scattered electron and the recoiled proton were detected in coincidence with two high-resolution magnetic spectrometrs. The photon electro-production process was selected by a cut on missing mass around zero. The target used was a $49.5\,\mathrm{mm}$ long target cell with havar walls that was filled with liquid hydrogen.

The proton form factor parametrization used in analysis was from Höhler et al. [73]. The values of the structure functions were extracted by using the LEX extraction:

$$P_{\mathrm{LL}} - P_{\mathrm{TT}}/\epsilon = (23.7 \pm 2.2 \pm 0.6 \pm 4.3)\,\mathrm{GeV}^{-2} \quad , \tag{3.15a}$$

$$P_{\mathrm{LT}} = (-5.0 \pm 0.8 \pm 1.1 \pm 1.4)\,\mathrm{GeV}^{-2} \quad . \tag{3.15b}$$

The first quoted error is statistical only, the second is systematic due to normalization of the angular distribution, and the third stems from the distortion of the distribution.

More can be found in the paper by Roche et al. [19] and in the theses of D. Lhuillier [74], J. Roche [75] and by J. M. Friedrich [76].

3.2.2 JLab experiment

Another VCS experiment was done at the Thomas Jefferson National Accelerator Facility in the Hall A collaboration [77, 78]. A beam with the energy of $4.030\,\mathrm{GeV}$ was directed on the $15\,\mathrm{cm}$ long liquid hydrogen target. The scattered electron and the recoiled proton were detected in coincidence. The photon electro-production events were identified by the missing mass technique.

The cross sections were measured as a function of $\mathrm{q'}_{\mathrm{cm}}$, θ'_{cm} and ϕ'_{cm} in two kinematical settings I and II with fixed values of q_{cm} (1.080 and $1.625\,\mathrm{GeV/c}$, respectively) and ϵ (0.95 and 0.88, respectively). The setting I was broken into two parts, I-a with energy mostly below the pion production threshold, and I-b with energy mostly in the $\Delta(1232)$ resonance region. The energy of the setting II was also mostly below the pion threshold.

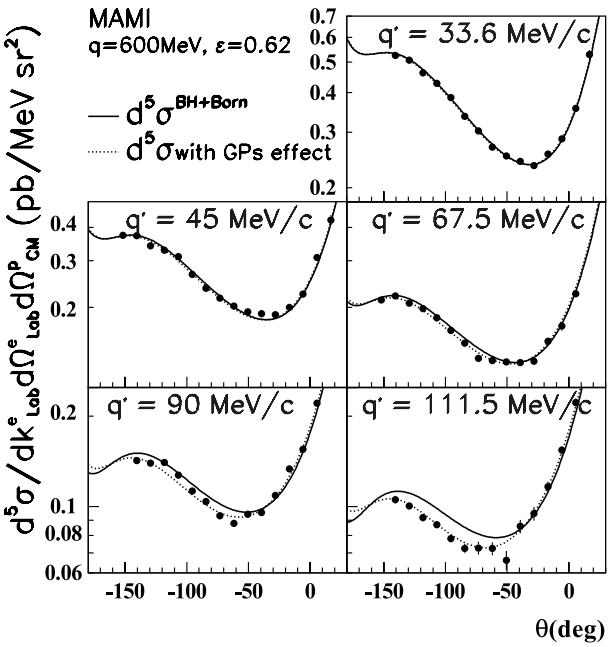

Figure 3.1: The match of measured cross sections with theoretical calculations for experiment MAMI 96-97 [19].

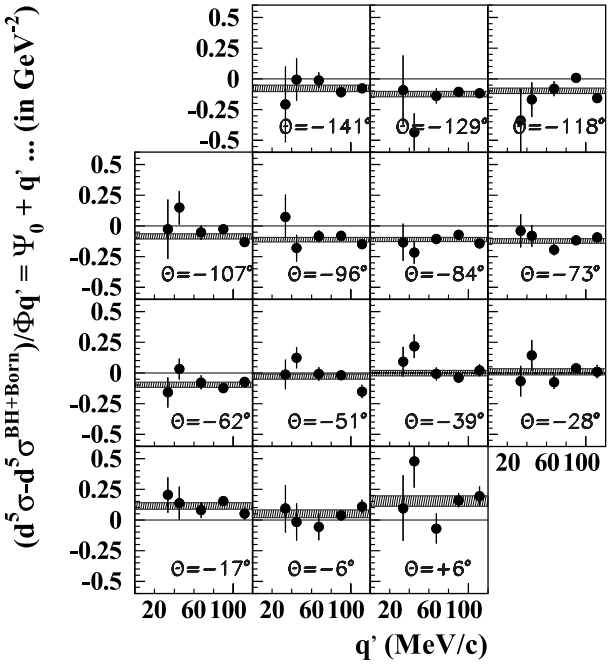

Figure 3.2: The extrapolation $q'_{cm} \rightarrow 0$ for the MAMI 96-97 experiment. This is used as a test of LEX [19].

The LEX analysis was done for settings I-a and II and not for I-b because of limitations of LEX analysis. These limitations do not hold for the DR analysis which was applied to all three settings. The results are shown in Table 3.1. The form factor parametrization used was from Brash et al. [79].

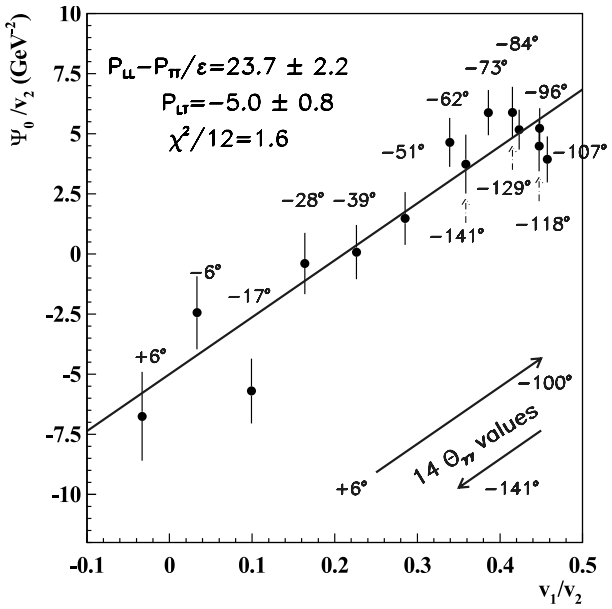

Figure 3.3: The LEX fit of polarizabilities $(P_{\mathrm{LL}} - P_{\mathrm{TT}}/\epsilon)$ and P_{LT} for the experiment MAMI 96-97. [19]

Table 3.1: Results of LEX and DR analysis of the polarizabilities $(P_{\mathrm{LL}} - P_{\mathrm{TT}}/\epsilon)$ and P_{LT} for the experiment JLab. [77]

setting	Q^2 [GeV^2]	q_{cm} [GeV]	ϵ	$P_{\mathrm{LL}} - P_{\mathrm{TT}}/\epsilon$ [GeV^{-2}]	P_{LT} [GeV^{-2}]
I-a LEX	0.92	1.080	0.95	$1.77 \pm 0.24 \pm 0.70$	$-0.56 \pm 0.12 \pm 0.17$
II LEX	1.76	1.625	0.88	$0.54 \pm 0.09 \pm 0.20$	$-0.04 \pm 0.05 \pm 0.06$
I-a DR	0.92	1.080	0.95	$1.70 \pm 0.21 \pm 0.89$	$-0.36 \pm 0.10 \pm 0.27$
I-b DR	0.92	1.080	0.95	$1.50 \pm 0.18 \pm 0.19$	$-0.71 \pm 0.07 \pm 0.05$
II DR	1.76	1.625	0.88	$0.40 \pm 0.05 \pm 0.16$	$-0.09 \pm 0.02 \pm 0.03$

More can be found in the paper of G. Laveissière et al. [77] or in theses of S. Jaminion [80], L. Todor [81], N. Degrande [44], C. Jutier [82] and G. Laveissière [83].

3.2.3 MIT-Bates experiment

The out-of-plane scattering facility at the MIT-Bates was used to perform a VCS experiment [84] with a goal to extract the structure functions $(P_{\mathrm{LL}} - P_{\mathrm{TT}}/\epsilon)$ and P_{LT} at very low values of Q^2 and to extract the mean square polarizability radius of the proton.

The beam was extracted from the MIT-Bates South Hall Ring with energies ranging from 570 to 670 MeV. The target used was 1.6 cm liquid hydrogen. This experiment also marked the first use of the full Out-of-Plane Spectrometer system with gantry for proton detection and the

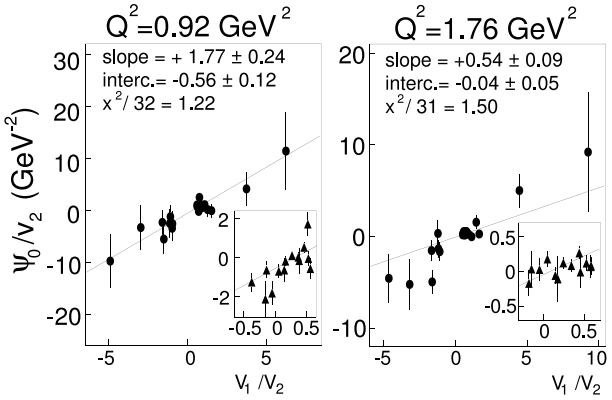

Figure 3.4: LEX fit of the polarizabilities $(P_{\mathrm{LL}} - P_{\mathrm{TT}}/\epsilon)$ and P_{LT} for the JLab experiment [77].

One-Hundred-Inch-Proton Spectrometer for electrons. The data was taken at $\mathrm{q}_{\mathrm{cm}} = 240\,\mathrm{MeV}$ ($Q^2 \approx 0.06\,\mathrm{GeV}^2$), $\epsilon = 0.9$ and at ϕ'_{cm} angles of $90°$, $180°$ and $270°$ simultaneously. The final state photon identification was done by missing mass and time-of-flight techniques.

Both LEX and DR analysis were made for the structure functions:

$$(P_{\mathrm{LL}} - P_{\mathrm{TT}}/\epsilon)^{\mathrm{LEX}} = (54.5 \pm 4.8 \pm 2.0)\,\mathrm{GeV}^{-2} \quad , \tag{3.16a}$$

$$P_{\mathrm{LT}}^{\mathrm{LEX}} = (-20.4 \pm 2.9 \pm 0.8)\,\mathrm{GeV}^{-2} \quad ; \tag{3.16b}$$

$$(P_{\mathrm{LL}} - P_{\mathrm{TT}}/\epsilon)^{\mathrm{DR}} = (46.7 \pm 4.9 \pm 2.0)\,\mathrm{GeV}^{-2} \quad , \tag{3.16c}$$

$$P_{\mathrm{LT}}^{\mathrm{DR}} = (-8.9 \pm 4.2 \pm 0.8)\,\mathrm{GeV}^{-2} \quad . \tag{3.16d}$$

The proton form factor parametrizations used were from Höhler et al [73] and Friedrich-Walcher [85]. The disagreement between LEX and DR for P_{LT} originates in the near cancelation of the electric and magnetic polarizability responses at the order of $\mathcal{O}(\mathrm{q'}_{\mathrm{cm}})$. So the dominant polarizability effect comes from the next order, which renders the LEX invalid.

The authors also managed to extract the mean square electric polarizability radius $\langle r_\alpha^2 \rangle$ by a HBχPT fit to the RCS and Bates $\alpha_{\mathrm{E}}(Q^2)$ data. The extracted value is significantly larger than the proton mean square charge radius, which signals the dominance of mesonic effects in the electric polarizability.

$$\langle r_\alpha^2 \rangle = (2.16 \pm 0.31)\,\mathrm{fm}^2 \quad . \tag{3.17}$$

3.2.4 MAMI 05-06

During the years 2005 and 2006, the A1 collaboration at MAMI performed another VCS experiment [86]. The setting used was very similar to the one of MAMI 96-97 (Section 3.2.1). The central values of kinematical variables were $\mathrm{q}_{\mathrm{cm}} = 600\,\mathrm{MeV/c}$ (or $Q^2 = 0.33\,\mathrm{GeV}^2$), $\mathrm{q'}_{\mathrm{cm}} = 90\,\mathrm{Mev/c}$, $\epsilon = 0.645$ and $\phi'_{\mathrm{cm}} = 180°$. The covered range for angle θ'_{cm} was $[70°, 180°]$.

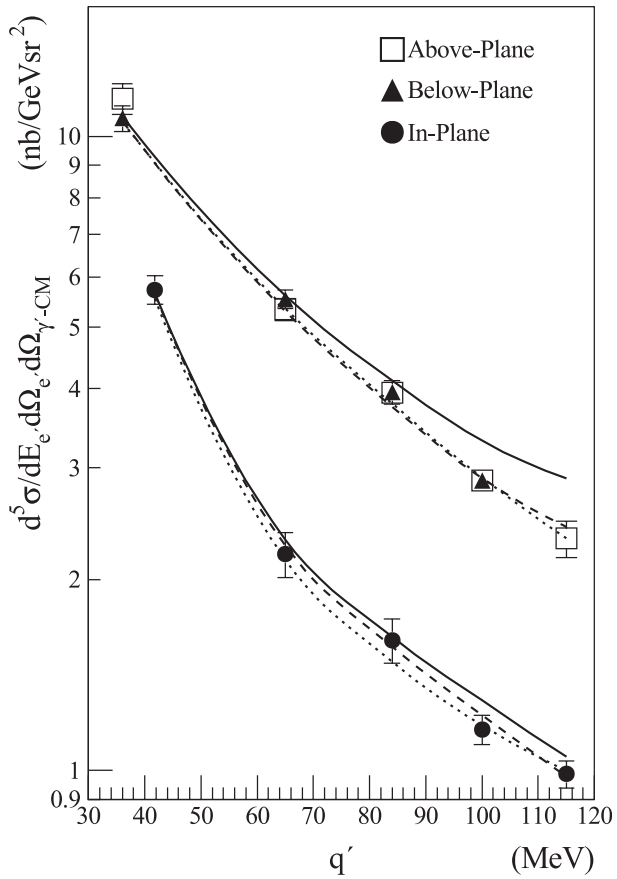

Figure 3.5: The match of measured cross sections with theoretical calculations for the MIT-Bates experiment. The solid line shows the BH+B cross section and the dashed and dotted curves are fits with LEX and DR analyses, respectively [84].

The photon electro-production events were separated from pion production events by a missing-mass reconstruction. The analysis was done with several different proton form factor parametrizations [85, 87, 88, 89, 73, 90].

The iterative approach was used to determine the final values of the structure functions from the data. The experimental cross section is extracted from a comparison with a simulation. The first step is to select a value for the structure functions used in the simulation. Then the structure functions are extracted from the data by using the LEX procedure. These values for structure functions are then plugged back into the simulations and the whole process is iterated until it converges. See Figure 3.6 for a graphical description of the process.

The extracted values of the cross sections for the Friedrich-Walcher form factor parametrization after the iteration procedure are:

$$P_{\mathrm{LL}} - P_{\mathrm{TT}}/\epsilon = (27.1 \pm 1.9 \pm 3.0)\,\mathrm{GeV}^{-2} \quad , \tag{3.18a}$$

$$P_{\mathrm{LT}} = (-8.0 \pm 0.7 \pm 2.2)\,\mathrm{GeV}^{-2} \quad . \tag{3.18b}$$

The comparison with extracted values from MAMI 96-97 is much better when no iteration is applied.

More can be found in the paper of P. Janssens [86] or in theses of L. Doria [69] and P. Janssens [70].

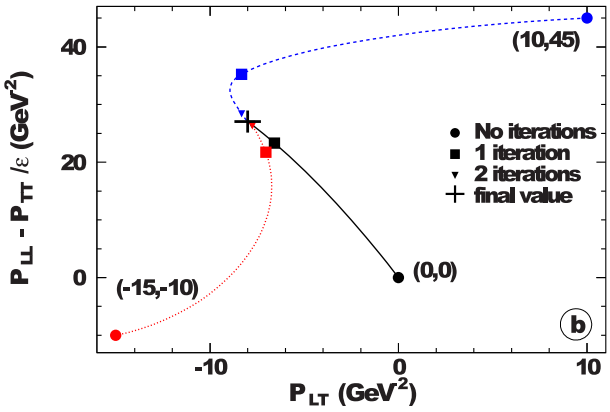

Figure 3.6: The iteration procedure used to extract the structure functions in the MAMI 05-06 experiment with the Friedrich-Walcher form factor parametrization [85]. See text for description [86].

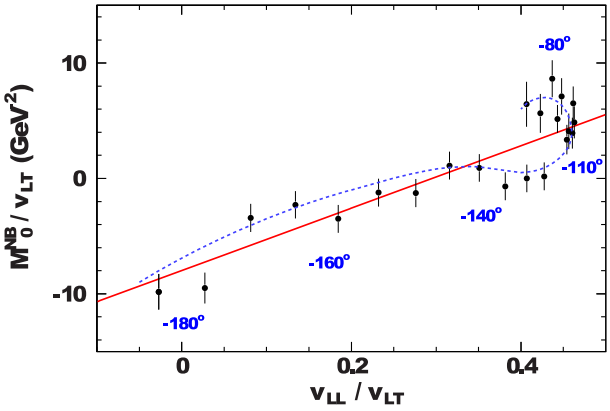

Figure 3.7: The final polarizability fit for the MAMI 05-06 experiment with the Friedrich-Walcher form factor parametrization [85, 86].

3.2.5 World data up to now

Figure 3.8 shows the current world data for VCS structure functions $(P_{\mathrm{LL}} - P_{\mathrm{TT}}/\epsilon)$ and P_{LT}. The values for the points are taken from [30, 84, 19, 86, 77]. The dashed curve is a DR fit on RCS and JLab points with parameters $\Lambda_\alpha = 0.7$ and $\Lambda_\beta = 0.63$, with $\epsilon = 0.645$ and Friedrich-Walcher form factor parametrization [85]. The curve agrees well with current points, except with the two MAMI measurements. For this reason, an experiment has been made to measure the structure functions at three additional values of Q^2 at 0.1 (described in this thesis), 0.2 and $0.5\,\mathrm{GeV}^2$.

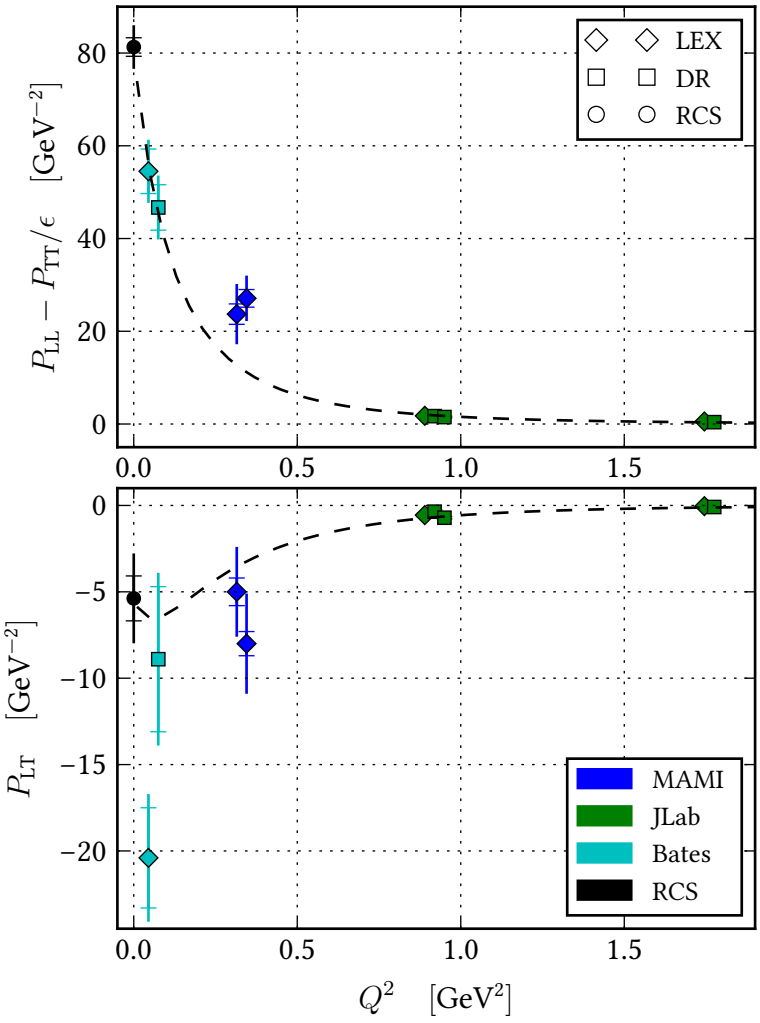

Figure 3.8: Current world data for VCS structure functions $(P_{LL} - P_{TT}/\epsilon)$ and P_{LT}. The points at the same value of Q^2 are offset a bit for clarity. The black line shows the DR model fitted on RCS and JLab points with parameters $\Lambda_\alpha = 0.7$ and $\Lambda_\beta = 0.63$, with $\epsilon = 0.645$ and Friedrich-Walcher form factor parametrization [85]. See Section 3.2 for description of individual experiments.

Chapter 4

Experimental setup

The experiment described in this thesis was performed at the Institut für Kernphysik (KPH) which is a part of the Johannes Gutenberg Universität in Mainz, Germany. The KPH features a continuous-wave (CW) electron accelerator facility MAMI, which is an acronym for Mainz Microtron. MAMI provides an electron beam for several experimental halls; A1 for electron scattering experiments; A2 the photon tagging facility for real photon experiments; A4 for parity violation experiments; and X1 for X-ray radiation sources research.

4.1 Accelerator

MAMI [91, 92] is a CW electron accelerator, that provides a polarized or unpolarized electron beam with energies up to 1.6 GeV and beam current up to $100\,\mu$A from an unpolarized source and up to $20\,\mu$A from a polarized source. The accelerator has two electron sources. The first is a thermionic gun for high quality and very reliable unpolarized beam. The second is GaAs based photo source, which is used for producing polarized beam or special conditions like single bunch operation. The beam is then accelerated to 3.5 MeV and injected to the first race-track mictrotron (RTM1) by a linac injector. RTM1 recirculates the beam eighteen times, increasing its energy to 14 MeV. The beam then enters the second race-track microtron (RTM2), where it makes fifty-one turns and is accelerated to 180 MeV. The accelerator up to this stage is called MAMI-A. At this point, the beam can be extracted and delivered to experimental halls or be passed to the third race-track microtron (RTM3). In the RTM3, the beam can be recirculated up to ninety times to the energy of 855 MeV. The beam extraction is possible at every even pass. This stage is called MAMI-B. The last acceleration stage is called MAMI-C and consists of a harmonic double-sided microtron (HDSM). Here the beam can reach the maximal energy of 1604 MeV after being recirculated forty-three times, or be extracted with lower energy at each turn. The energy spread after MAMI-B is 13 keV and after MAMI-C it is 110 keV. The schematic of the whole complex is shown in Figure 4.1.

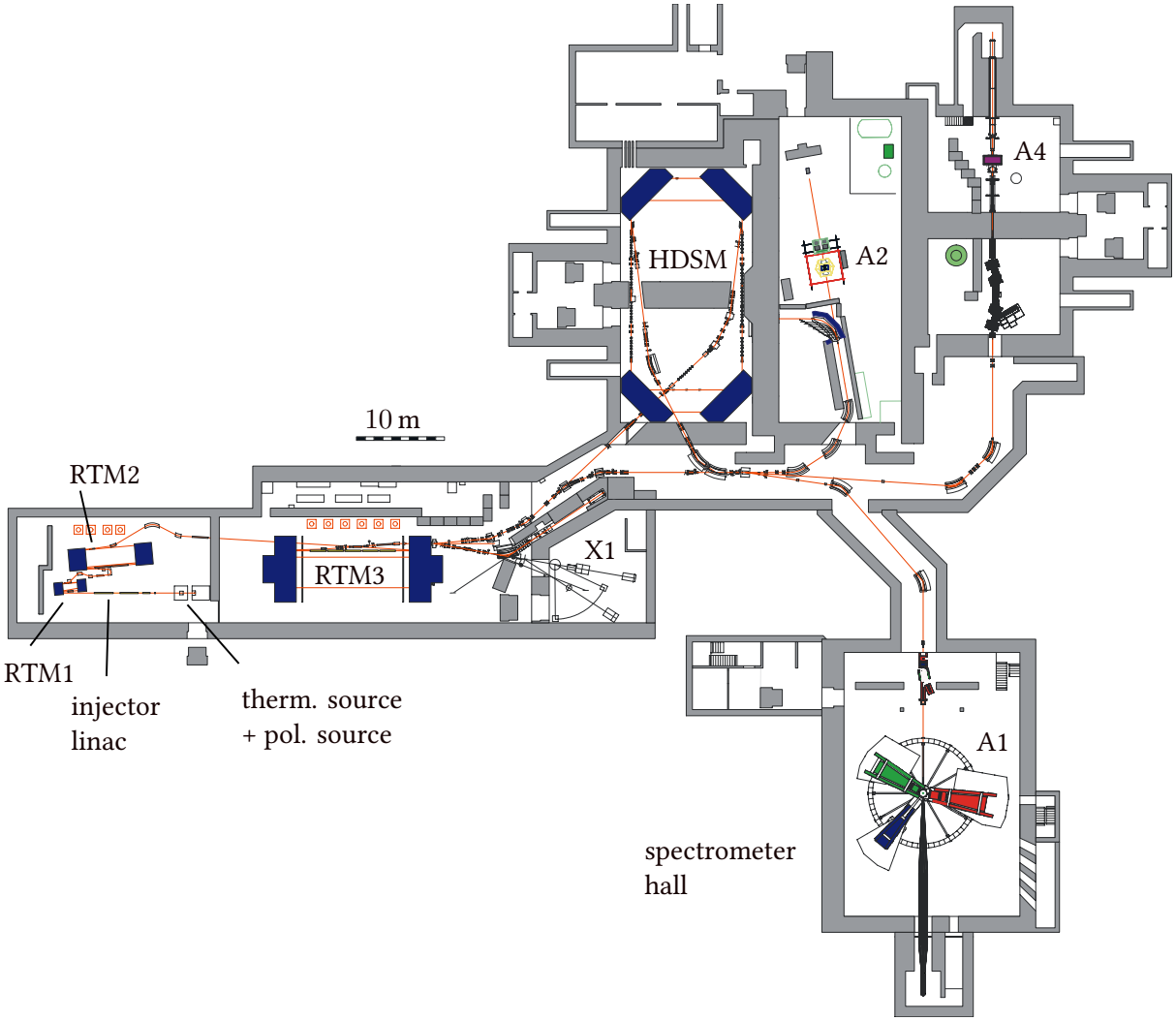

Figure 4.1: MAMI floor plan schematic. Shown are all accelerator stages and experimental halls. The beam starts with a polarized or unpolarized electron source, goes through the injector to the RTM cascade, optionally also HDSM and then enters one of the experimental halls; A1 for electron scattering experiments; A2 the photon tagging facility for real photon experiments; A4 for parity violation experiments; and X1 for X-ray radiation sources research [91].

4.1.1 Microtron

Racetrack microtron (RTM) is a particle accelerator device (Figure 4.2). It consists of two $180°$ bending dipole magnets and one linac as an accelerating stage (detailed design description in [93]). The trajectory of particles is such that they pass through the acceleration stage multiple times before the beam is extracted. After each turn the recirculation path is a little longer, which resembles a to racetrack if seen from above, hence the name. The linac uses RF cavities operated at the frequency of 2.45 GHz. This means that the time structure of the beam is of the order of 0.4 ns which is too small to be detected by the experiments, so the beam appears to be continuous. Both the cavities and magnets used in MAMI are normal conducting.

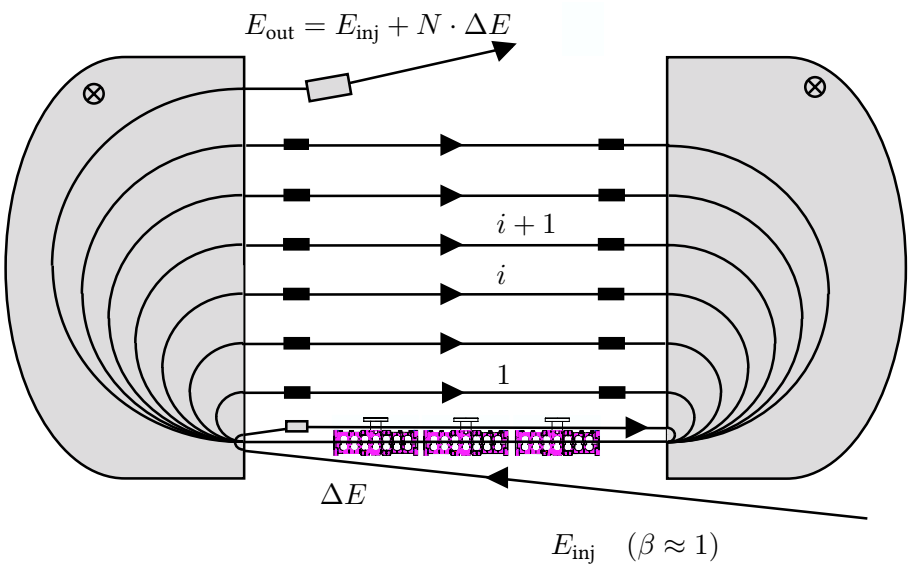

Figure 4.2: Schematic of a racetrack microtron (RTM). It has two dipole magnets that guide the electrons through a linac multiple times before extracting the beam [91].

The only two ways to get to higher energies with RTMs is to increase the magnet field strength or to increase the size of the magnets. Since the field strength of the iron core magnets is limited at about 1.5 T and the cost of magnets increases quickly with size, this meant that MAMI-C could not be designed as a fourth RTM, leaving RTM3 as the largest RTM in the world. Instead a proposal was made for a higher-order microtron [94]. It uses four 90° bending magnets with two anti-parallel linacs as accelerator stages (Figure 4.3). To suppress some instabilities, one of the linacs is operated at the doubled frequency of 4.90 GHz, giving this device the name harmonic double-sided microtron or HDSM.

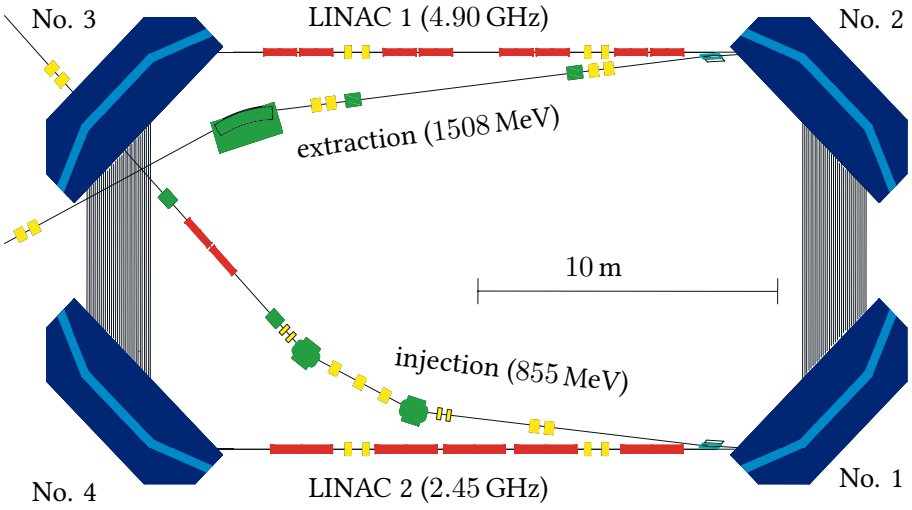

Figure 4.3: Schematic of a harmonic double-sided microtron (HDSM). It has four dipole magnets that guide the electrons through two anti-parallel linacs, one at each side. The radio-frequency of one of the linacs is doubled compared to the RTMs [91].

4.2 The A1 experimental hall

The experimental hall of the A1 collaboration houses, among other detectors, the so-called three-spectrometer set-up. This set-up [95] features three high-resolution spectrometers, that are named simply A, B and C. They can be independently rotated around the central axis, where the target chamber is located. Spectrometer B can also be tilted to enable an out-of-plane configuration. The spectrometers can be operated in a single, double or triple coincidence mode to suit different experimental requirements. The detector packages used in each of the spectrometers can also be adjusted for each of the experiments.

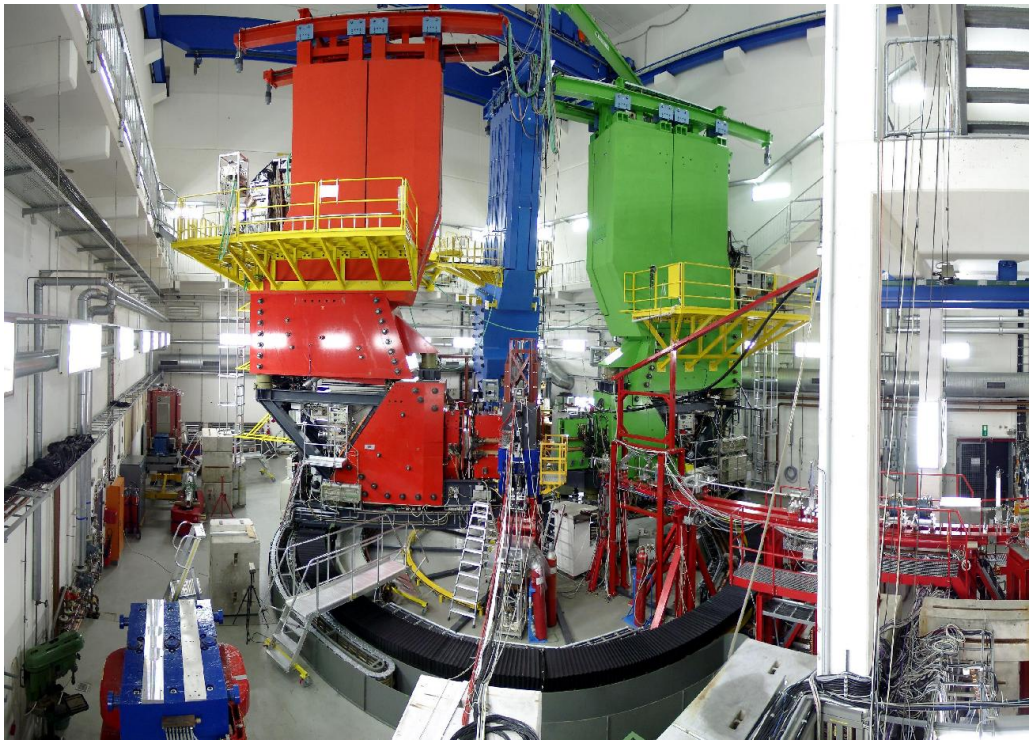

Figure 4.4: A photograph of the experimental hall A1. In the center is the three-spectrometer set-up with spectrometer A in red, B in blue and C in green. The beam line comes from the right side and goes to the target chamber, which is located in the center of the spectrometer ring. Spectrometer B is tilted into out-of-plane position on this photo [96].

4.2.1 Scattering chamber

The vacuum scattering chamber is located at the pivot point of the three-spectrometer set-up. It houses a target ladder which holds several solid targets, depending on the need of the experiment. Commonly used targets are graphite target, tantalum target, HAVAR stack and aluminium oxide screen which is used for beam position monitoring. The target ladder can be remotely moved vertically to select a particular target. There is also a possibility to exchange

the scattering chamber lid, as they hold different targets. Here one can select between a waterfall target, polarized ^{3}He target, a high pressure gas target or cryo-target.

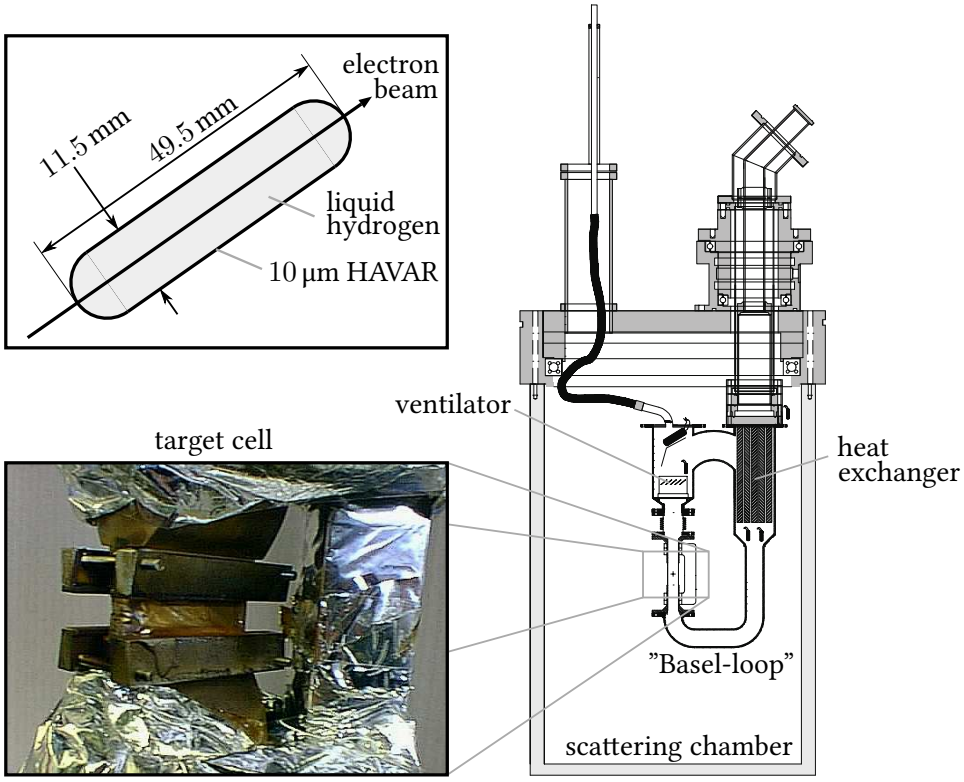

Figure 4.5: The cryo-target of the A1 collaboration. On the left are cross section schematic (top) and a photo of the target cell. On the right is a schematic of the cryo-target inside the scattering chamber [97].

In our experiment we used a cryo-target filed with liquid hydrogen at around 22 K and 2 bar that acted as a proton target. The schematic of this target is shown in Figure 4.5. The cryo-target system has two loops, outer and inner. The outer loop is connected to a Philips machine, which liquefies hydrogen flowing toward the target chamber where it cools the heat exchanger. The hydrogen is warmed there and it evaporates and rises back to the Philips machine. The connection between the Philips machine and the target chamber is made of a counterflow pipe, with liquid hydrogen in the inner pipe and evaporated hydrogen in outer pipe. The inner or "Basel" loop is also filled with liquid hydrogen. It has an exchangeable target cell. We used a cigar-like one as shown on figure 4.5. To prevent local overheating this loop also has a ventilator that constantly circulates the hydrogen and we used beam raster to enlarge the beam surface on the target. There is also a heater present in the inner loop. It is used to keep the hydrogen at a constant temperature when the beam is shut off or the beam current is changed.

4.2.2 Magnetic spectrometers

The spectrometer set-up was designed to cover a broad spectrum of electron scattering experiments, without compromising too much on the performance (detailed description in [95]). It consists of three high-resolution magnetic spectrometers, A, B and C. The optics of the spectrometers A and C is composed of an entrance quadrupole, sextupole and two dipoles. They have a point-to-point optics in the dispersive plane for a high momentum resolution and parallel-to-point optics in the non-dispersive plane for precise first-order determination of the scattering angle. On the other hand, the spectrometer B has only one clamshell dipole, named so because of its characteristic shape. This is a consequence of a demand that one spectrometer should reach very small scattering angles. Because of this it covers a smaller solid angle and momentum resolution than spectrometers A and C, but it reaches the highest momentum. It has point-to-point optics in both the dispersive and non-dispersive planes. The polarity of all of the magnets can be reversed, so each spectrometer can be used for detecting positively or negatively charged particles, depending on the experiment. The central momentum of each spectrometer is measured by a Hall and/or NMR probe. The schematics is shown in Figure 4.6.

Table 4.1: Design parameters of the three spectrometers.

		A	B	C
magnet configuration		QSDD	clamshell D	QSDD
maximum momentum	[MeV/c]	735	870	551
momentum acceptance	[%]	20	15	25
horizontal angular acceptance	[mrad]	± 100	± 20	± 100
vertical angular acceptance	[mrad]	± 70	± 70	± 70
solid angle	[msr]	28	5.6	28
scattering angle range	[°]	$18 - 160$	$7 - 62$	$18 - 160$
momentum resolution		$\leq 10^{-4}$	$\leq 10^{-4}$	$\leq 10^{-4}$
angular resolution at target	[mrad]	≤ 3	≤ 3	≤ 3
position resolution at target	[mm]	$3 - 5$	≤ 1	$3 - 5$

Each spectrometer rests in a cradle attached to a central pivot on one side and to a massive concentric steel railing on the other side. The cradles allow for a precise alignment of each magnet and precise rotation of spectrometers about the central axis. Spectrometers A and C cover angular ranges of $18° - 160°$ on left and right side, respectively, relative to the incoming beam. Spectrometer B normally covers a range of $7° - 62°$ on the right side, but it can be moved to the left side, if the exit beam-line is removed. There it covers the range of $7° - 90°$. An important thing for scattering experiments is the ability to tilt the spectrometer B toward the central axis, thus enabling the out-of-plane measurements. The tilt is in the range of $0° - 10°$.

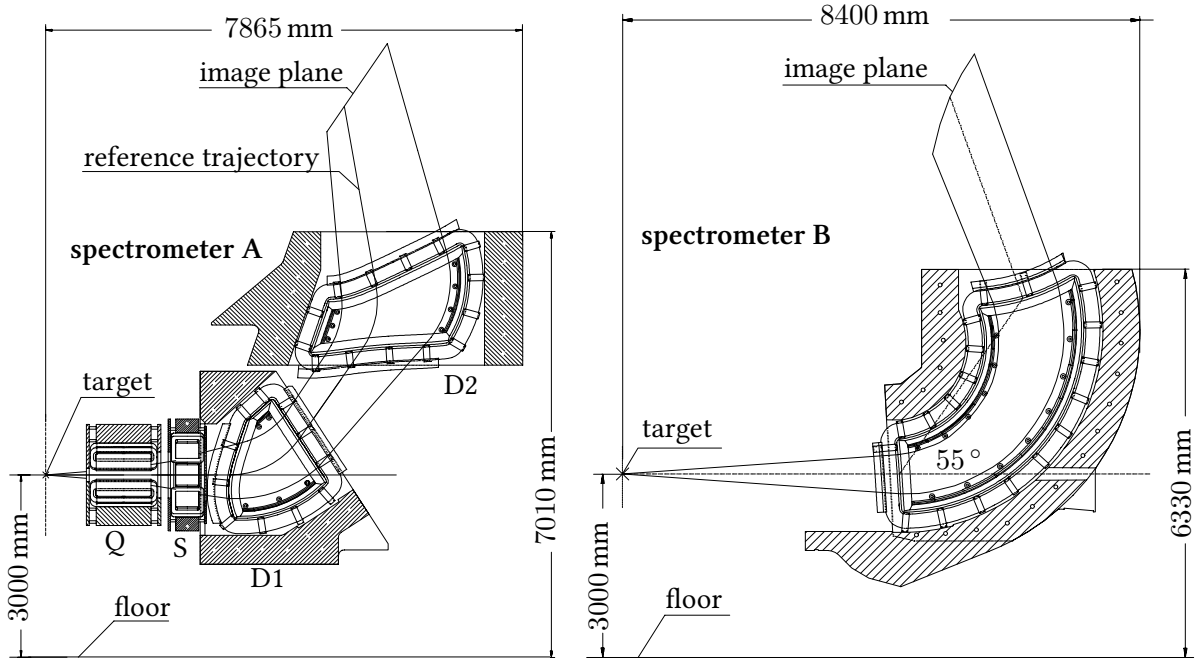

Figure 4.6: The schematic of spectrometers A (left) and B (right) The spectrometer C is just a scaled-down version of spectrometer A (scaling factor of $11/14$). Spectrometers A have a quadrupole, sextupole and two dipole magnets, while spectrometer B has single large clamshell dipole [95].

4.2.3 Detector packages

The standard detector package is similar in all three spectrometers. It has two pairs of vertical drift chambers (VDCs), two scintillator planes and a Čerenkov detector. If there is a need, the configuration can also be changed, like swapping a Čerenkov detector for a focal plane polarimeter. The detector packages are mounted on top of spectrometers inside heavy shielding. The shielding can be opened to allow an easy access to the detectors. A schematics of a detector package is shown in Figure 4.7 and a detailed description can be found in [95].

Vertical drift chambers

The first part of the detector system is the focal plane track detector, whose purpose is to determine the track of the passing particles, namely the position and angle in the dispersive and non-dispersive direction. It features two pairs of VDCs, with each pair in x-s configuration. The x-plane measures the position along the dispersive direction. The wires in the s-plane are rotated by an angle of $\Gamma = 40^\circ$ with respect to the wires in x-plane and are used to measure the position along the non-dispersive direction. While VDCs can be used to determine a two-dimensional projection of the particle track, two pairs are used to achieve a sufficient angular resolution. The chambers are filled with a mixture of equal parts of argon and isobutane with a $1.5\,\%$ admixture of pure ethanol to minimize ageing. At a typical incident angle of $\theta = 45^\circ$ a track traverses five to six individual cells which gives high detection efficiency. The

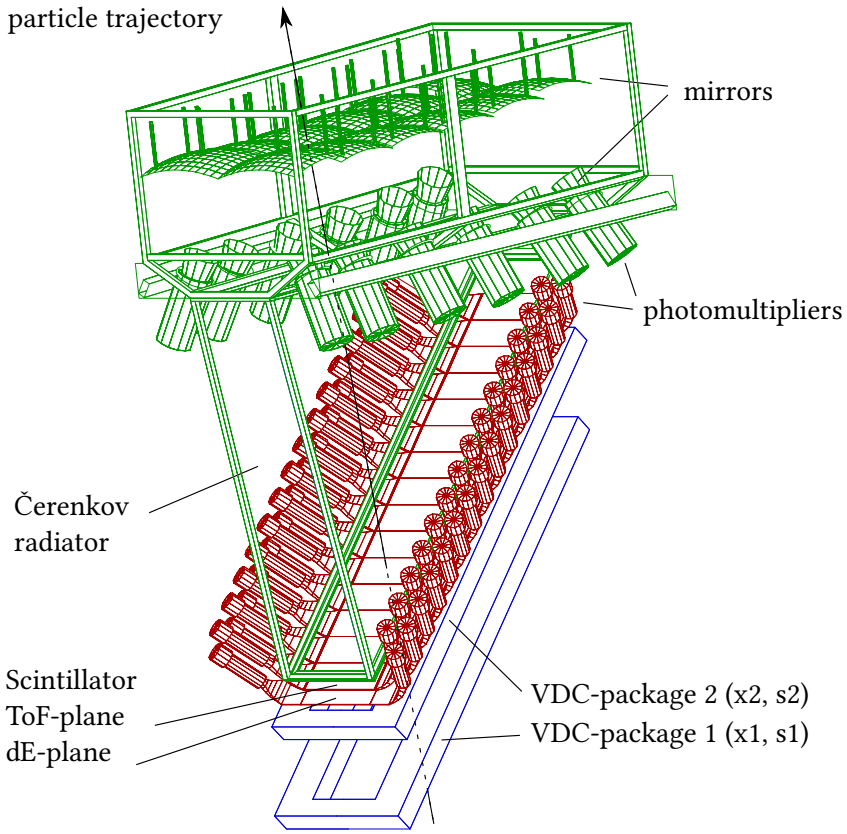

Figure 4.7: The schematic of a typical detector package in spectrometer A (similar for B and C). In green is drawn a Čerenkov detector, in red are two scintillator planes and in blue are two sets of vertical drift chambers [26].

measured focal plane coordinates $(x_{\rm fp}, \theta_{\rm fp}, y_{\rm fp}, \phi_{\rm fp})$ are transformed to the target coordinates $(\delta_0, \theta_0, y_0, \phi_0)$ where $\delta_0 = (p - p_{\rm c})/p_{\rm c}$ and $p_{\rm c}$ is the central momentum, and y_0 is the distance along the beam direction as seen by the spectrometer. The transformation is done by using the transfer coefficients:

$$G = \sum_{i,j,k,l} \left\langle G \,|\, x_{\rm fp}^i \, \theta_{\rm fp}^j \, y_{\rm fp}^k \, \phi_{\rm fp}^l \right\rangle x_{\rm fp}^i \, \theta_{\rm fp}^j \, y_{\rm fp}^k \, \phi_{\rm fp}^l \quad , \tag{4.1}$$

where G stands for any of the four target coordinates and $i, j, k, l = 0, 1, 2, \ldots$. The coefficients of the expansion are measured by using dedicated runs with a sieve-slit collimator placed at the spectrometer entrance window. The shorthand notation for expansion coefficients is:

$$\left\langle G \,|\, x_{\rm fp}^i \, \theta_{\rm fp}^j \, y_{\rm fp}^k \, \phi_{\rm fp}^l \right\rangle = G_{ijkl} \quad . \tag{4.2}$$

Scintillators

The second part of the detector package is a scintillator detector. Its function is threefold; to provide a trigger for a data acquisition system; to provide timing information for the particle track; and to measure the energy loss of passing particles. The detector consists of of

two scintillator planes. Each plane consists of fifteen (spectrometers A and C) or fourteen (spectrometer B) individual detectors. The detectors have a plastic scintillator with an area of $45\,\text{cm} \times 16\,\text{cm}$ (A) and $14\,\text{cm} \times 16\,\text{cm}$ (B) that is coupled via light-guides to a photomultiplier (PMT) on each side. In spectrometer B, the detector is short enough to be read from just one side. The scintillators are covered with crumpled aluminized Mylar foil to minimize photon loss and then wrapped in lightproof black plastic foil to minimize the background signal. The bottom plane is $3\,\text{mm}$ thick and is called "delta-E" or dE plane. It is used as a first energy loss detector and usually provides timing information for low-energy protons or deuterons. The second plane is $1\,\text{cm}$ thick and is called "Time-of-Flight" or ToF plane. It is used as a second energy loss detector and usually provides the fast timing signal. Energy loss information from both planes can be used for particle identification as protons and deuterons can be distinguished from minimum ionizing particles like electrons or pions.

Čerenkov detector

The last standard detector is a threshold gas Čerenkov detector. Its primary goal is to provide a discrimination between electrons (or positrons) and pions. It is filled with a decafluorobutane (C_4F_{10}) at atmospheric pressure as a radiator gas, which has a Čerenkov threshold for electrons and pions at $10\,\text{MeV}$ and $2.7\,\text{GeV}$, respectively. The flight path through the radiator is $90\,\text{cm}$ at the high and $245\,\text{cm}$ on the low momentum side. The emitted light is reflected by twelve mirrors to light funnels that lead it to the photomultipliers. Since spectrometer B is much narrower, five mirrors are sufficient.

Laser monitoring system

To calibrate the trigger detector systems before beam-times and monitoring of the performance during runtime, a nitrogen laser system was installed. This system fires a $40\,\text{kW}$, $3\,\text{ns}$ long, UV laser pulses at maximum frequency of $20\,\text{Hz}$. Optical fibres are used to connect the laser system to detectors in the spectrometers or to other detector systems used. The light is directly coupled to each scintillator of the spectrometers. In the Čerenkov detector, the fibres are pointed to each of the mirrors.

4.2.4 Trigger and data acquisition system

To maximize the possible event rate each spectrometer acts independently and has its own trigger electronics. The minimal trigger condition is a single hit in one scintillator PMT. To lower the PMT noise, a coincidence between the left and right PMTs of the scintillator paddle is required. Different trigger conditions can be set in each spectrometer, depending on the experiment. One can also include a Čerenkov detector in the trigger to tag or veto the electrons. These trigger conditions are analysed by the programmable logic unit which sends

a trigger signal downstream to a fast programmable gate array (FPGA) when conditions are met. The FPGA collects the signals from all three spectrometers and analyzes them based on coincidence conditions set for the experiment. Depending on experimental kinematics, each signal can be delayed or widened. There is also a possibility to scale down the signals if needed (e.g.: take every coincidence event between A and B, but only each 1000^{th} single-arm event from A and B). When FPGA accepts an event, an interrupt signal is sent to front-end electronics of spectrometers to digitize the detector signals and to start the read-out process. The data are then sent to the workstation where the event builder combines them. The event builder also registers the dead times of various coincidence combinations. More details are available in [95, 98].

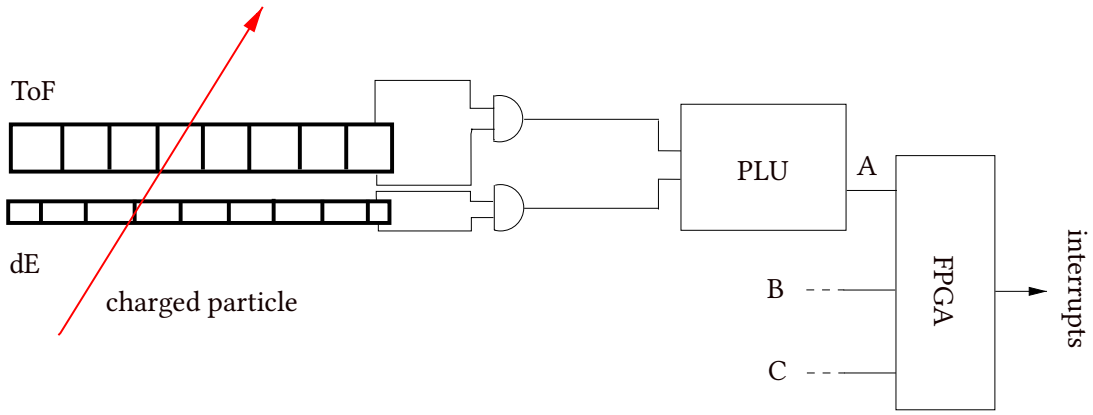

Figure 4.8: Schematic of the trigger system logic. The PLU stands for programmable logic unit which creates a trigger for each spectrometer. These triggers are then sent to the FPGA (fast programmable gate array), which decides when to send an interrupt signal to the readout electronics [69].

4.3 Kinematical settings

The goal of this experiment was to determine the polarizability effect at three values of Q^2: 0.1, 0.2 and $0.5\,\text{GeV}^2$. The data of $Q^2 = 0.2$ and $0.2\,\text{GeV}^2$ is analysed by a French team consisting of dr. Helene Fonvieille, Loup Correa and Meriem Ben Ali from IN2P3, Clermont-Ferrand, while I analysed the data at $Q^2 = 0.1\,\text{GeV}^2$.

For each Q^2 value three different settings were planned: an "in-plane" setting, an "out-of-plane" setting and so-called "low" setting. The low settings were designed to allow measurements at low values of q'_{cm} around $37.5\,\text{MeV}$. Here the polarizability effect is suppressed and this data can be used for normalization since the expected values of measured cross sections are precisely known. The other two setting cover higher values of q'_{cm} and are designed to maximize the lever arm in v_{LL} and v_{LT} to get better sensitivity to the structure functions (see Figure 4.9). In the out-of-plane setting spectrometer B is moved into the out-of-plane position, hence the name. In my kinematics of $Q^2 = 0.1\,\text{GeV}^2$ the out-of-plane setting covers the region around $\phi'_{\text{cm}} \approx 90^\circ$ and $\cos(\theta'_{\text{cm}}) \approx 0$ where the sensitivity to P_{LT} is suppressed. The

in-plane setting, on the other hand, covers a wide range in ϕ'_{cm} and in the backward region of $\cos(\theta'_{\mathrm{cm}}) \approx -1$. This is a region with smaller sensitivity to structure function $P_{\mathrm{LL}} - P_{\mathrm{TT}}/\epsilon$.

For an overview of all measured settings see Table 4.2.

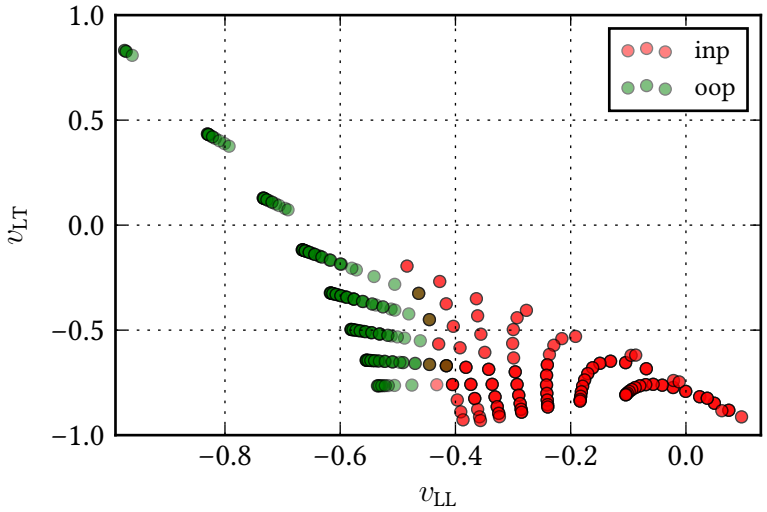

Figure 4.9: The range in kinematical factors v_{LL} and v_{LT} covered by settings *q2_01_inp* and *q2_01_oop* in the LEX analysis. These two kinematical factors represent the sensitivity to the structure functions (see Equation (2.68)).

Table 4.2: List of all kinematical settings that were measured during our experiment. The first number in setting name stands for the Q^2 value of the kinematics in tenths of GeV^2, e.g. q2_01_inp: $Q^2 = 0.1\,\mathrm{GeV}^2$. The 'year' column marks the year of datataking. The 'polarity' stands for polarity of the magnets in spectrometers and this determines which particles are accepted by each spectrometer. The E_{beam} is the beam energy for the setting. The p, θ and ϕ^{oop} are central momentum, angle and out-of-plane angle of spectrometers. I analysed the setting written in bold script.

setting	year	polarity	E_{beam} [MeV]	$\mathrm{p_A}$ [MeV]	θ_{A} [°]	$\mathrm{p_B}$ [MeV]	θ_{B} [°]	$\phi_{\mathrm{B}}^{\mathrm{oop}}$ [°]
q2_01_inp	2011	e' in B	871.1	425	53.1	702	23.1	0.0
q2_01_oop	2012	e' in B	871.1	343	52.6	693	21.9	9.0
q2_01_low	2011	e' in B	871.1	365	58.0	745	22.3	0.0
q2_01_low_2	2012	e' in B	871.1	365	58.0	745	22.4	0.0
q2_01_low_3	2012	e' in B	871.1	340	56.5	735	22.4	0.0
q2_02_inp	2011	e' in B	1002.4	580	51.5	766	30.4	0.0
q2-02-inp	2015	e' in B	1002.0	580	51.5	771	30.4	0.0
q2_02_oop	2011	e' in B	1002.4	486	51.0	767	29.2	8.5
q2-02-oop	2015	e' in B	1002.0	486	51.0	771	29.2	8.5
q2-02-oop-forward	2015	e' in B	1002.0	411	42.5	769	29.2	8.5
q2_02_low	2011	e' in B	904.4	462	52.2	723	32.5	0.0
q2_02_low-bis	2011	e' in B	904.4	442	52.2	715	32.5	0.0
q2_05_inp	2012	e' in A	1034.1	649	51.2	634	32.7	0.0
q2_05_inp_new	2013	e' in A	1034.1	648	51.2	636	32.7	0.0
q2_05_inp_new_again	2013	e' in A	1034.1	649	51.2	636	32.7	0.0
q2_05_oop	2013	e' in A	1034.1	646	51.0	751	39.2	8.0
q2_05_low	2013	e' in A	937.7	644	52.3	717	40.5	0.0

Chapter 5

Pre-analysis calibration

Before any meaningful physics results can be extracted from data a calibration needs to be made. This calibration ensures that the analysis software is aware of conditions as they were during the data taking, or are at least close to them. The first calibration is already done online, just before the data taking. A more detailed calibration is then done offline and this chapter describes the procedure I took for calibration.

5.1 Software stack

The A1 collaboration uses an in-house built software stack for data acquisition and analysis. It has several components including `Aqua++`, `Cola++`, `Simul++` and `Luminosity++`.

`Aqua++` is a data acquisition software. It receives data from all spectrometers and merges it into events. The events are collected during the duration of single data-taking, so-called runs, and are then saved to disk. Each run is signed with a time-stamp, marking the beginning of the run.

`Cola++` is a data analysis software. Its main purpose is to histogram events from run files. Besides run files, `Cola++` needs several additional files to function properly, rundb files, col files and tma files. A rundb or run database files contain a time ordered list of parameters that describe in detail the experimental conditions and the state of detectors at the time of data-taking. As an example, the rundb file contains a type of reaction studied, the beam energy, the angles of spectrometers and drift velocity of electrons in VDCs. In this chapter I detail the procedure I took to calibrate these parameters. Col files describe all the histograms to be produced by `Cola++` and the relations of histogrammed variables to the raw variables written in run files. Among other things, `Cola++` also features full support for four-vector manipulation, elaborate data cuts and custom event weighting, and all this can be defined in col files. The tma or transfer matrix files define the transformation of the measured focal plane coordinates to the target coordinates (see also Section 4.2.3).

`Simul++` is a simulation program. Similarly as `Cola++`, it reads a rundb file and produces histograms based on col files. But instead of analysing experimental data, `Simul++` code uses a Monte Carlo event generator and accurate physical models to realistically simulate different reactions. It includes models for different reactions including elastic scattering, deuteron breakup, VCS and isotropic model. The isotropic model can be used to simulate only the experimental acceptance function. The VCS model also includes the HBχPT calculations for the effects of the generalized polarizabilities, which unfortunately did not work well so I had to exclude them from simulation and use only the Bethe-Heitler and Born cross section. `Simul++` code also includes a detailed description of radiative losses.

`Luminosity++` is used to calculate the experimental luminosity and dead time fraction for each run.

Besides the A1 software stack, for calibration and data analysis I also used Python [99] and its scientific packages Numpy [100], SciPy [101], Matplotlib [102] and Pandas [103].

The theoretical cross sections were calculated using two codes, `VCS-BHB` code [104] for LEX calculations, and `VCS-DR` [105] for DR calculations.

5.2 Primary data filtering

Before starting with the calibration of the detector systems, the data need to be filtered. It is not necessary to make exact cuts as in the data analysis, basic PID (Particle IDentification) cuts should suffice. This is because it is necessary to select the particles for which we are calibrating each detector, in my case protons for spectrometer A and electrons for spectrometer B. This selection can be coarse since the events will not be counted yet, so it does not matter if some of the good events are filtered out or some others are left. The cuts I used here were:

- require coincidence between spectrometers,
- events lie in the coincidence time peak,
- cut on energy deposited in ToF scintillator of spectrometer A to select protons,
- cut on center of the target to eliminate events scattered from target cell wall.

5.3 Calibration of vertical drift chambers

5.3.1 Disabling wires

I started my calibration with VDCs. The first thing to do here is to disable dead or inefficient wires. These wires can be identified in the wire number spectrum (look at Figure 5.1) because they have none or very little counts compared to neighbouring wires. Another thing to look

at here are so-called hot or noisy wires. These are wires with too much counts as they trigger even when no particle passes them. Here an efficiency spectrum should be checked. If efficiency around the wire is normal, there is no need to disable it. This is because the timing of the signal from a hot wire is usually wrong in comparison to the neighbouring wires and this is corrected for later in the calibration. If, however, there is a local decrease in the efficiency, that wire should be disabled.

If this is not done, it can lead to locally lowered efficiency around inefficient or noisy wires. It can also have an effect on track of the particle as it can cause wrong reconstruction.

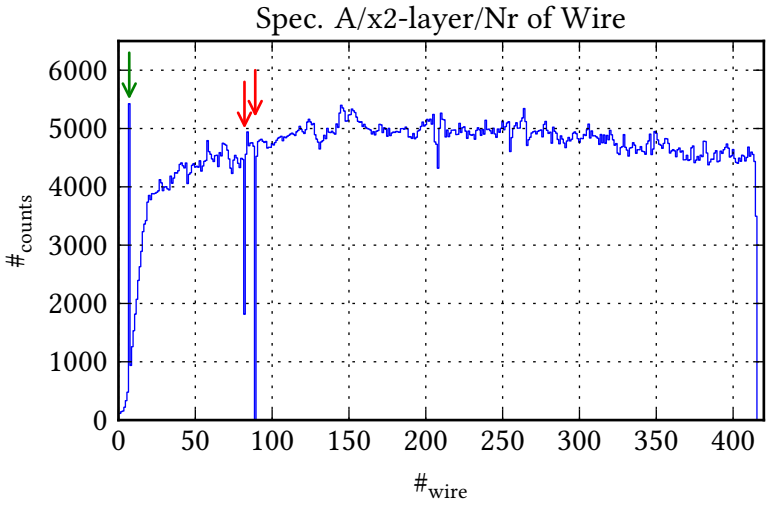

Figure 5.1: A sample number-of-wire spectrum for the x2 layer of the spectrometer A VDC. The green arrow marks the position of noisy a wire and red arrows mark the positions of two inefficient wires. These wires need to be disabled or they can cause local inefficiency or wrong track reconstruction.

5.3.2 TDC offsets and drift velocity

To optimize the track reconstruction the TDC (Time-to-Digital Converter) offsets and drift velocity in the VDC gas need to be precisely set. A quick way to set the TDC offsets is to extrapolate the right falling edge of the drift time spectrum to zero and use that channel number (see Figure 5.2).

A more precise way to calibrate both the TDC offsets and the drift velocity is to minimize the track reconstruction error. For each of the four focal plane coordinates a reconstruction error is calculated for each track and is then histogrammed (see Figure 5.3). The goal is to then find such a combination of TDC offsets and drift velocity to minimize the average value of these errors. I did this by using a script that finds a minimum for each parameter separately and then I iterated until it converged.

After setting these parameters it is necessary to check if they change with time and if they do, to try and find the reason behind it. An example is an isobutane bottle change, which

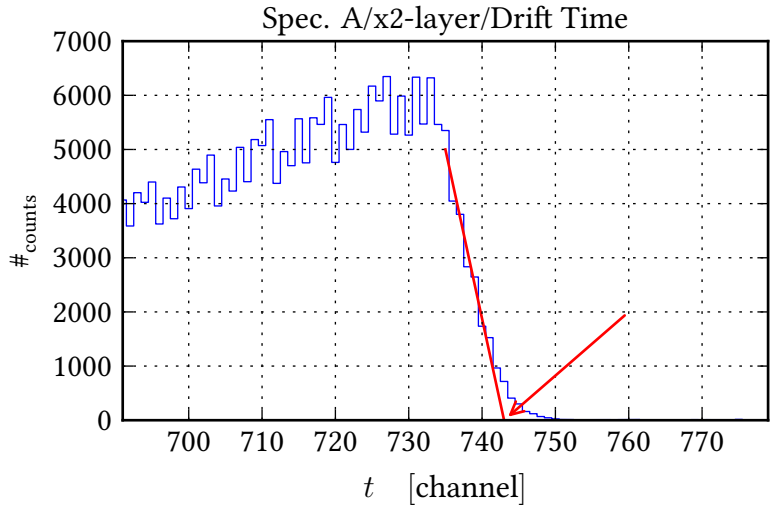

Figure 5.2: A part of the drift time spectrum for the x2 layer of spectrometer A VDC. The drift time offset can be quickly calibrated by extrapolating the falling edge to zero and using that channel number (shown in red).

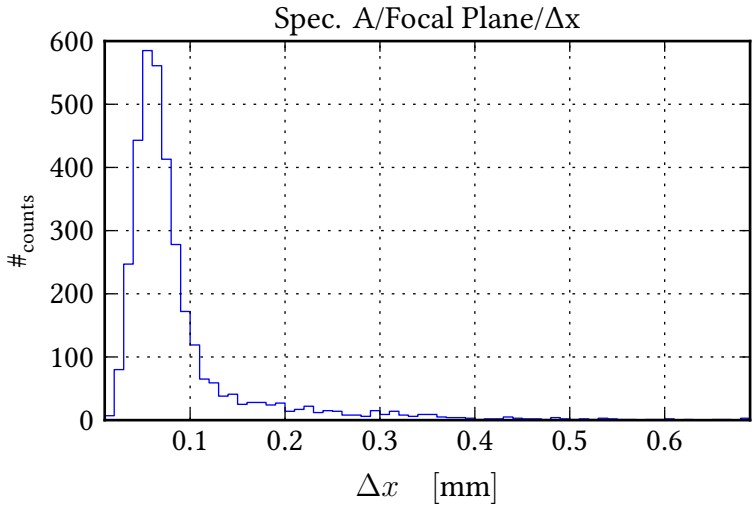

Figure 5.3: The reconstruction error for the x_{fp}-coordinate for spectrometer A. The smaller the average error is, the better is the calibration of the TDC offsets and the drift velocity.

can alter the drift velocity for a few runs. To do this, I extracted the values of reconstruction errors for each run and checked if they remained stable.

5.3.3 Drift time difference criterion

The next thing I did was to look at the timing differences between signals in neighbouring wires. This information can be used to differentiate between good events, δ-electrons and signal coming from noisy wires. This is schematically shown in Figure 5.4. Following the

good event, the time it took for the signal to arise is shortening from left to right and then it starts to get bigger again. But the δ-electron produces a signal with decreasing time again, so we can filter it out. As for the hot wire, the neighbouring wires usually produce no signal and it can be filtered out again.

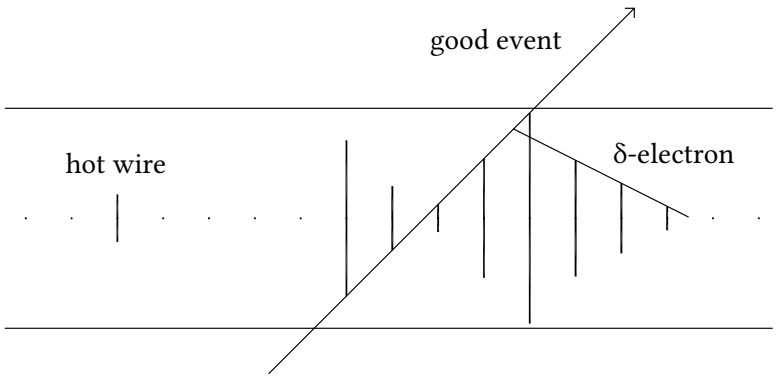

Figure 5.4: By looking at the timing difference of signals at neighbouring wires, it can be differentiated between good events, δ-electrons and signals coming from noisy wires. The vertical lines represent the time it took the signal to arise after the passage of a particle through VDC. They are drawn on both sides because only the timing information is provided and not whether the particle passed through the bottom or top half of the chamber.

This configuration is achieved by setting three parameters that define two parallel cuts (look at Figure 5.5) for allowed time difference between two wires. Cuts must be set such that the bulk of events are encompassed as closely as possible without cutting into it. There is an additional parameter that can be set. This parameter defines how triggers with only a single wire firing are handled. For the x-plane such events are usually discarded. But in the s-plane, wires are rotated toward the particle path, so there is an increased probability that just one wire will produce the signal. This is the reason why for the s-plane these events are usually kept.

5.4 Calibration of Čerenkov detector

The Čerenkov detector can be used for separation of electrons from heavier particles, specially pions. Since other cuts provide sufficient suppression of pions I did not make any Čerenkov related cuts. This is why I only made a very basic calibration of this detector in spectrometer B; I only shifted the pedestal values to zero. This needs to be done for each of the five photomultipliers.

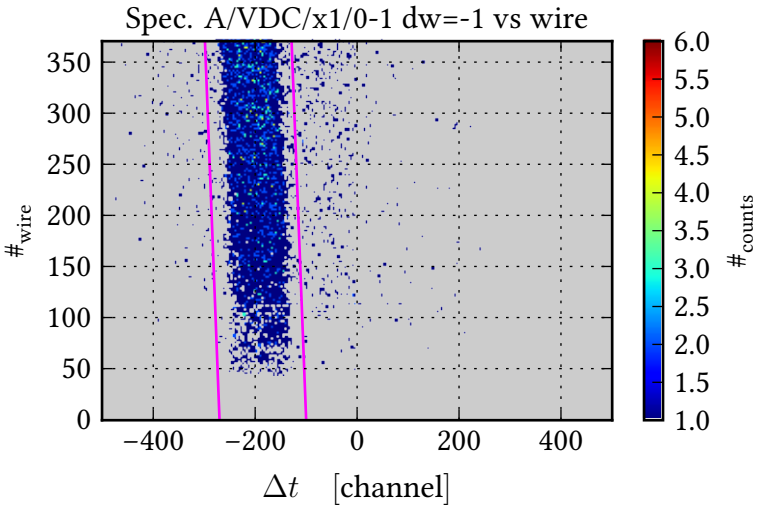

Figure 5.5: The difference in the timing of a signal for two neighbouring wires in the x-plane of spectrometer A VDCs. Two purple lines show the position of two parallel cuts used as a drift time difference criterion. They must encompass the bulk as closely as possible, without cutting into it.

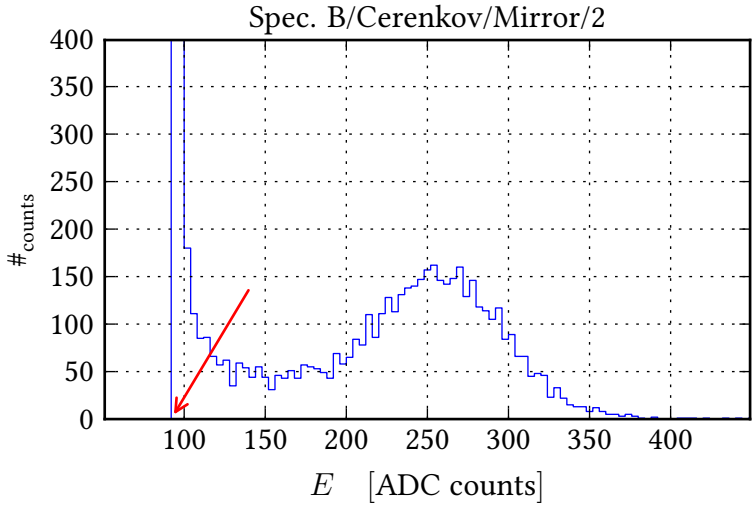

Figure 5.6: The ADC spectrum of a photomultiplier of the Čerenkov detector. The red arrow marks the pedestal value which needs to be set during calibration.

5.5 Calibration of scintillator detectors

5.5.1 Scintillator timing

I wanted to have as good timing calibration as possible. The narrower the coincidence timing peak is, the narrower timing cut is necessary and the smaller is the effect of random coincidences. The timing calibration is due to three effects; global timing difference between spectrometers A and B; local timing differences between paddles in a spectrometer; and time walk effect.

Global timing offset

Global timing offset is a global timing difference between spectrometers A and B. The difference in timing comes from different path lengths and velocities of the particles in both spectrometers and from different length of cables the signals must traverse. To precisely set this offset, I looked at plots like the one shown in Figure 5.7 and measured how far the center of the coincidence time peak is from zero. I then used this value to correct the global timing offset.

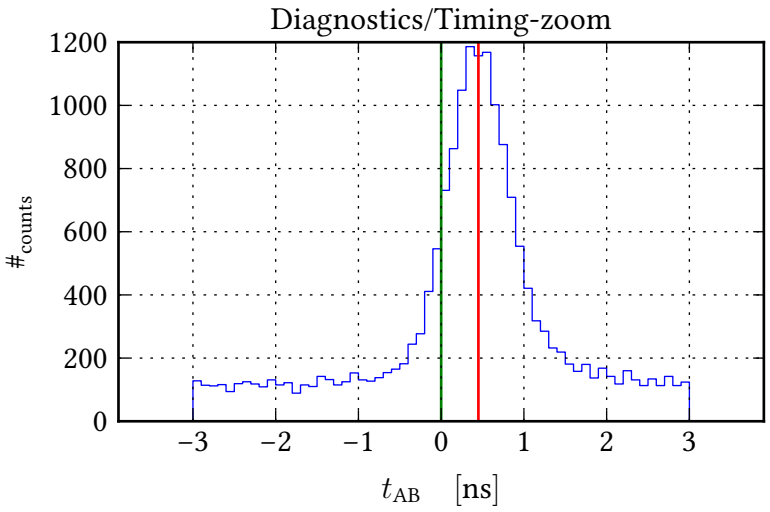

Figure 5.7: Coincidence time spectrum between spectrometers A and B. The global timing offset needs to be corrected such that the timing peak lies at zero. So the red and green line coincide.

Per-paddle offsets

There is a slight timing difference for signals coming from different paddles in a scintillator detector. This means that on average the signals from one paddle arrive a bit sooner than signals from another paddle and this widens the cumulative coincidence time peak. For this reason an offset needs to be set for each paddle, such that the timing signal for each lies at zero. The procedure is very similar to the one for setting the global timing offset. But since the narrowest, not the highest coincidence time peak is desired, I centered the middle of the peak at half-maximum, not highest point of the peak. This is the same if the peak for a paddle is symmetrical, but there is a small difference for asymmetrical peaks. This timing correction needs to be done only for the triggering scintillator plane, or the plane that defines timing, in case both are required in the trigger.

Walk correction

The signal from the scintillators is lead to the single threshold discriminator. Here two pulses that arrive at the same time, but are of different heights, trigger the discriminator at different times (look at Figure 5.8), with smaller pulses triggering a bit later than the bigger ones. This effect is called time walk and must be accounted for.

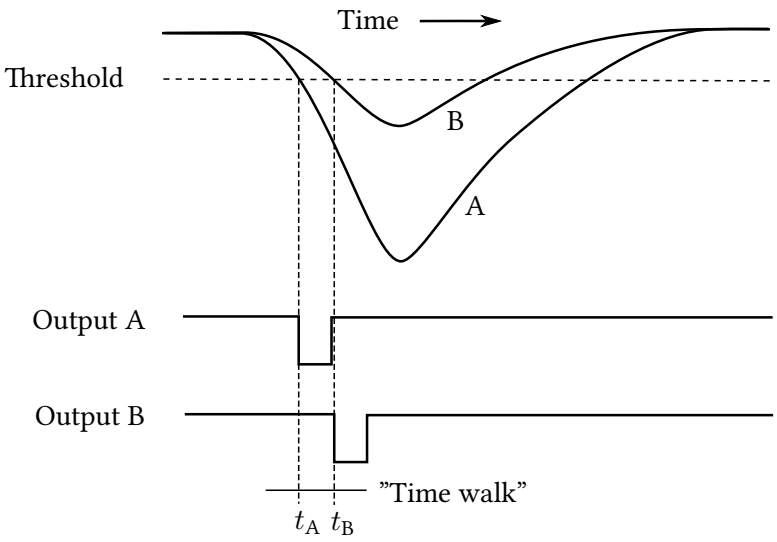

Figure 5.8: Time walk is an effect where two signals of different heights that arrive at the discriminator at the same time produce the output signal at slightly different times [106].

In `Cola++` a quadratic approximation for the beginning of a pulse shape is used:

$$U_{\text{threshold}} = U(t) = a \cdot Q \cdot (t - t_0)^2 \quad , \tag{5.1}$$

where Q is the total charge collected, t_0 is the pulse start time and a is a parameter. The pulse start time can be calculated as:

$$t_0 = t - \sqrt{\frac{U_{\text{threshold}}}{a \cdot Q}} = t - b \cdot \frac{1}{\sqrt{Q}} \quad , \tag{5.2}$$

where $b = U_{\text{threshold}}/a$. This parameter is essentially what one tries to set with the walk correction.

To make this correction I looked at plots like the one shown in Figure 5.9 that shows the relation between the coincidence time and the scintillator pulse size as described by Equation (5.2). Then I changed the walk parameter until the blob on the plot was horizontal. Again, this needs to be done only for the triggering scintillator plane.

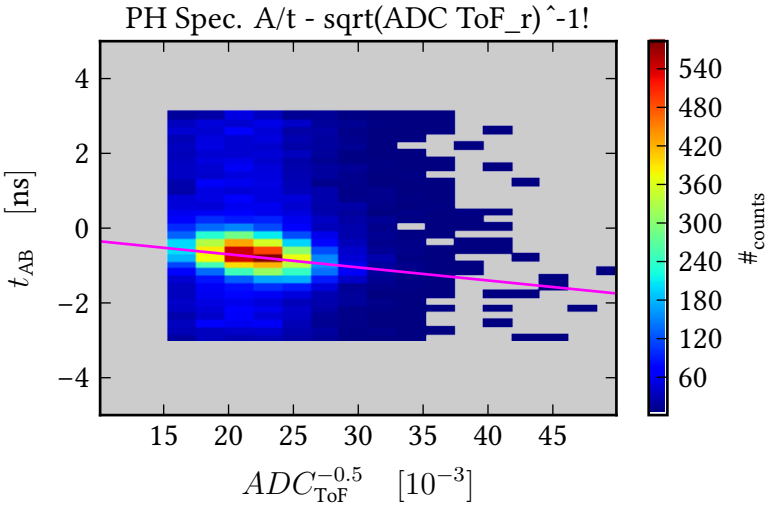

Figure 5.9: The correlation between the coincidence time and the scintillator ADC pulse size. By correcting for time walk effect the blob on the plot becomes horizontal.

Iteration

This whole procedure of global timing offset correction, per-paddle offset correction and walk correction needs to be iterated. This is because the walk correction affects the global timing offset and per-paddle offset a bit, and vice-versa. But after each iteration necessary corrections become smaller and smaller, and after three to five iterations the process converges.

5.5.2 ADC calibration

Besides providing timing information for a track, scintillators also help measure the energy loss of passing particles. This information can be used for particle identification, namely for discriminating protons from pions (and possible positrons and kaons). It can not be used for separating electrons from pions or muons, because in this kinematical region they are all minimum ionizing particles and they deposit approximately the same amount of energy. This can be seen in the ADC spectrum. On the proton side (spectrometer A in my case) two bumps are seen, one for protons and one for pions. But on the electron side (spectrometer B in my case) only one bump is present.

The goal of ADC calibration is to make a proton/pion separation easier, or cleaner. For this I decided to scale and offset the ADC spectra for each paddle in such a way that all the proton peaks become aligned and all pion peaks become aligned. This differs from gain matching for PMTs. At gain matching the goal is to scale the output of each PMT ADC in such a way, that is it proportional to the energy deposited by a particle in the scintillator (slower protons have higher energy loss).

Because I want to see the whole ADC spectra, I had to remove the cut on the energy deposited in the ToF scintillator plane from the filter described in Section 5.2. And since I wanted to do the proton/pion separation, I only needed to do this calibration for spectrometer A. The calibration needs to be done for dE and ToF scintillator layers and for each layer for the left and right set of PMTs.

The first step in this calibration is to decide where the proton and pion peaks should lie. I decided to select the same position for the left and right set of PMTs within the scintillator layer, but different value for dE and ToF layer, since particles deposit more energy in ToF than in dE. The actual values were selected based on ADC vs paddle number plots, like the one shown in Figure 5.10. I selected values close to the position of the peaks before any calibration.

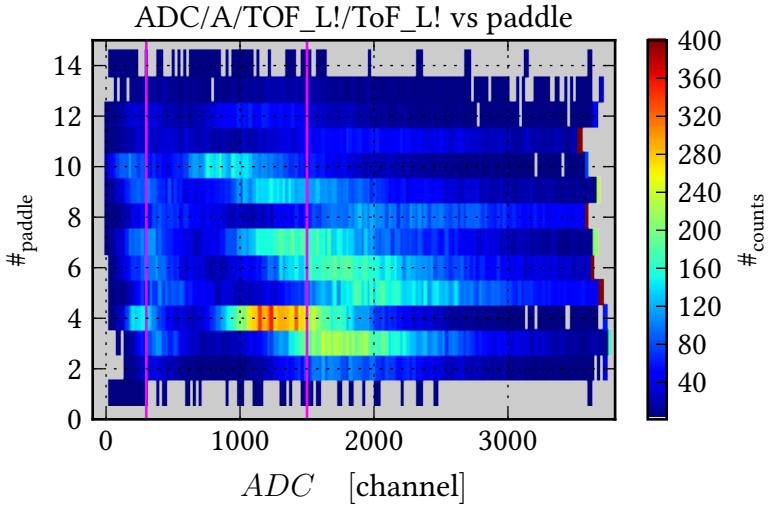

Figure 5.10: The ADC spectra of the left set of PMTs for the ToF scintillator layer of spectrometer A. Protons on average deposit more energy than pions, so the bumps on the right side are protons and the ones on the left are pions. For easier separation I calibrated the spectrometers such that all proton peaks align with the right purple line and the pion peaks with the left purple line.

Next I looked at the ADC spectra for each paddle separately (look at Figure 5.11). From there I determined the position of the proton and pion peaks and calculated the scale and offset necessary to align the peaks at desired positions. Scale and offset represent a linear transformations and can be calculated from set of equations:

$$r_1 \cdot \text{scale} + \text{offset} = p_1 \quad , \tag{5.3a}$$
$$r_2 \cdot \text{scale} + \text{offset} = p_2 \quad , \tag{5.3b}$$

where $r_{1,2}$ and $p_{1,2}$ are references to the red and purple lines from Figure 5.11. The scale and offset can now be calculated as:

$$\text{scale} = \frac{p_2 - p_1}{r_2 - r_1} \quad , \tag{5.4a}$$
$$\text{offset} = p_1 - r_1 \cdot \text{scale} \quad . \tag{5.4b}$$

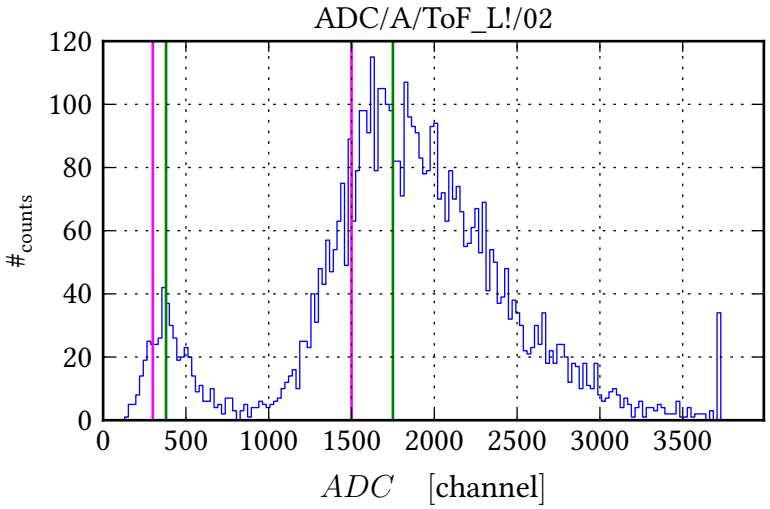

Figure 5.11: The ADC spectrum of the second left PMT for the ToF scintillator layer of spectrometer A. The green lines mark the position of the pion (left) and the proton (right) peak, and purple lines mark the desired positions of the peaks (see Figure 5.10). The scale and offset parameters for each PMT can be used to align the spectrum such that the red and the purple lines coincide.

I should mention that this rescaling of ADC values does not affect the time walk corrections from Section 5.5.1 because raw ADC values are used there.

5.5.3 Scintillator efficiencies

Since the scintillation detectors are used in the trigger, it is important to know their detection efficiency, most importantly the efficiency of the triggering plane. If that plane does not provide a signal, then the event is not recorded and is lost. The efficiency of the non triggering plane is also needed, if any two dimensional cut is made on the deposited energy, like described in Section 5.7. The special case is our 2011 beam time when the trigger was set to demand the signal from both scintillator planes, and so both efficiencies are needed regardless on the presence of the cut.

To measure the efficiency of the scintillators we have taken dedicated efficiency runs either on carbon target or on cryo target. One can only measure the efficiency of the non-triggering plane, so we always took two sets of efficiency runs, one where the ToF layer is set as the trigger and another with the dE layer.

I used following method [107] to determine the efficiency as a function of coordinates on the scintillator plane $(x_{\text{scint}}, y_{\text{scint}})$. Two two-dimensional histograms are needed and both measure the distribution of number of events in the scintillator plane. The first histogram is for the triggering plane. The condition on making this histogram is that a good track exists. This cuts away badly reconstructed track or events where no track information exists either because the particle did not pass the VDCs or because of some other reason. The second

histogram is for the non-triggering plane. The same requirement for a good track is made here along with two other cuts. One cut is made on raw timing difference between the scintillator planes and it discards events where the TDC had an overflow, which signals that the non-triggering layer did not produce a signal. This is basically a demand that both planes saw the event. The third cut on the non-triggering plane is a requirement that there exists a paddle with two valid ADC values (left and right). This is needed because there are rare cases when an event produces a signal that is above the discriminator threshold, but at least one ADC value is below the pedestal value. The efficiency is now calculated as the ratio of the second to the first histogram.

When determining the scintillator efficiency on the proton side, another PID cut is needed. This is because along protons also pions and positrons fly into the spectrometer. And since these are minimum ionizing particles they leave a different signal and the efficiency for their detection can be lower than the one for protons. But one needs to be careful when making this cut to avoid conditions on the scintillator plane whose efficiency is being measured or the results can be distorted.

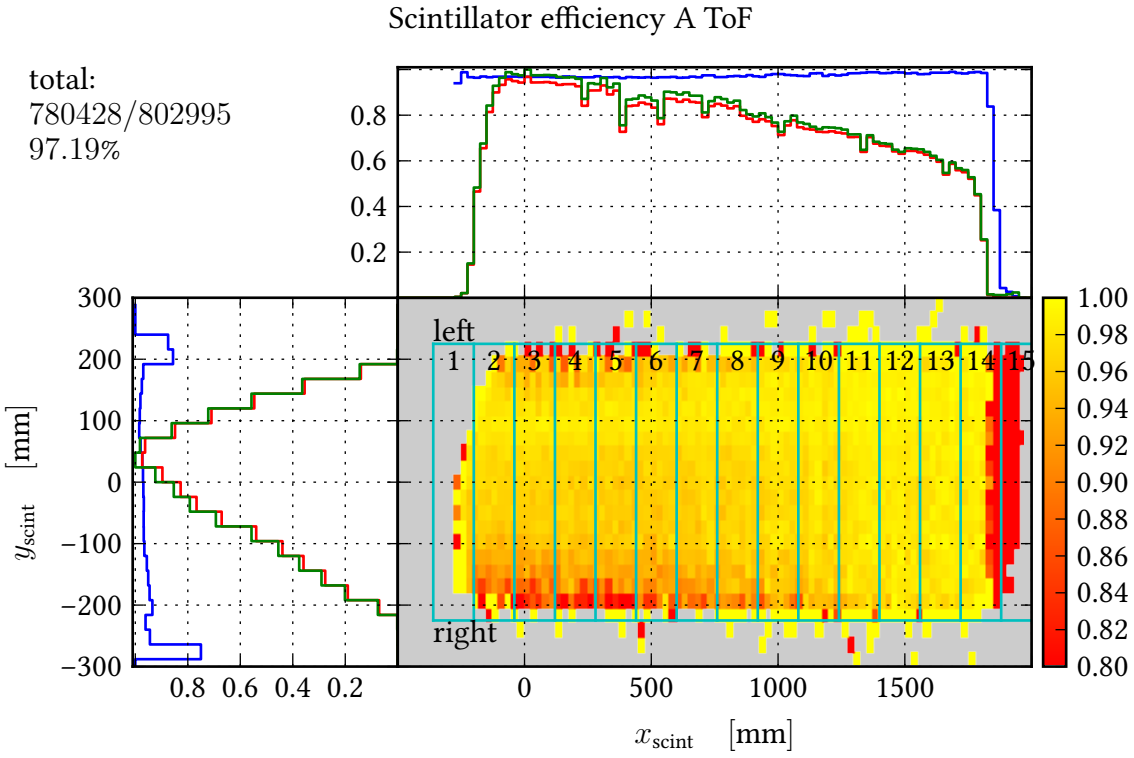

Figure 5.12: The efficiency for the ToF scintillator layer of spectrometer A for protons with central momentum of 361 MeV. The blue lines on the side plots mark aggregate efficiency along the axis. The green lines show the relative number of counts summed along the axis for the triggering plane. The red lines are the same as green just for non-triggering plane.

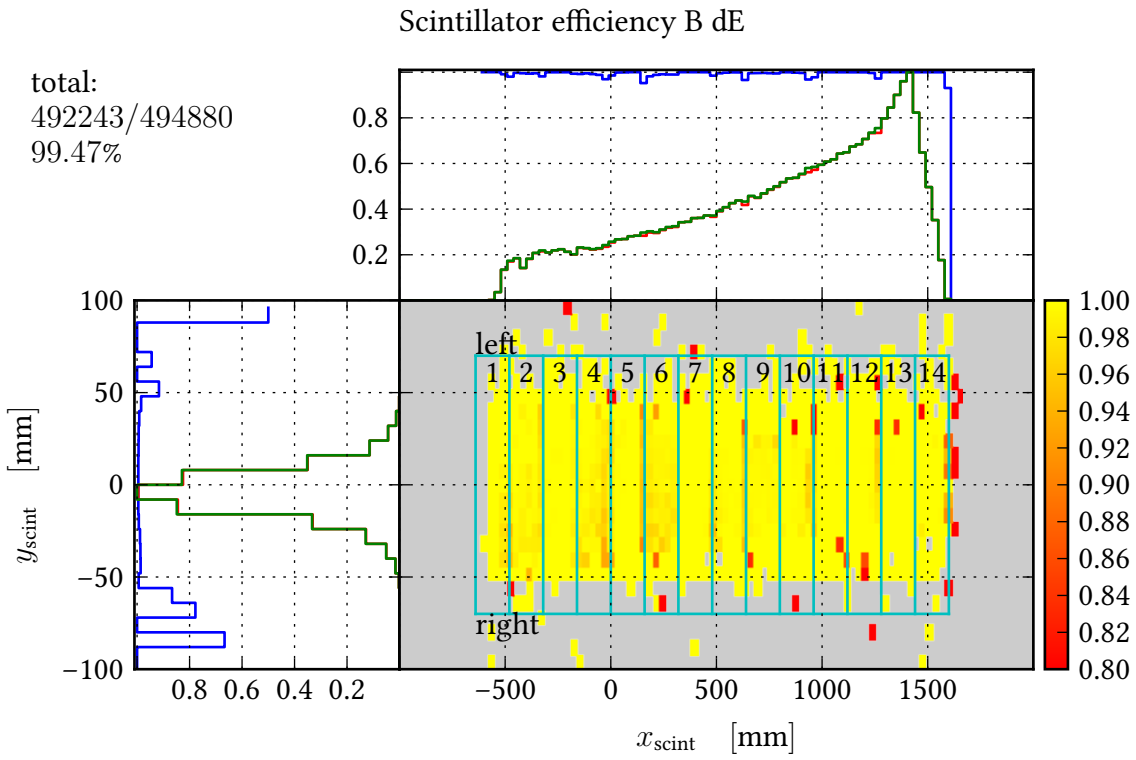

Figure 5.13: Same as Figure 5.12, only for dE scintillator layer of spectrometer B for electrons with central momentum of 729 MeV.

5.6 Beam and target position calibration

For the data analysis, I wanted to have as low background as possible, this means only events that come from scattering of electrons on liquid hydrogen. So I need to filter the events that come from scattering on target walls and from the deposit that accumulates on the target over time. To do this efficiently, I needed good resolution of target coordinates.

5.6.1 Transfer matrix selection

Target coordinates are reconstructed from the focal plane coordinates by using the transfer coefficients, which are described in Section 4.2.3. The so-called transfer matrix (or TMA) is a file with these transfer coefficients that `Cola++` uses. Each spectrometer uses a different TMA, because of their construction differences. But there is not just one TMA file for each spectrometer that would cover all possible setups, but many that are tuned a bit differently.

To get a good starting point for my calibration, I decided to try several different matrices and see which gives the best result. Some of the TMAs I tried were already optimized for kinematics similar to mine. To do this comparison I had to remove the cut on the center of the target from the filter described in Section 5.2. The results for setting *q2_01_inp* are shown in Figure 5.14.

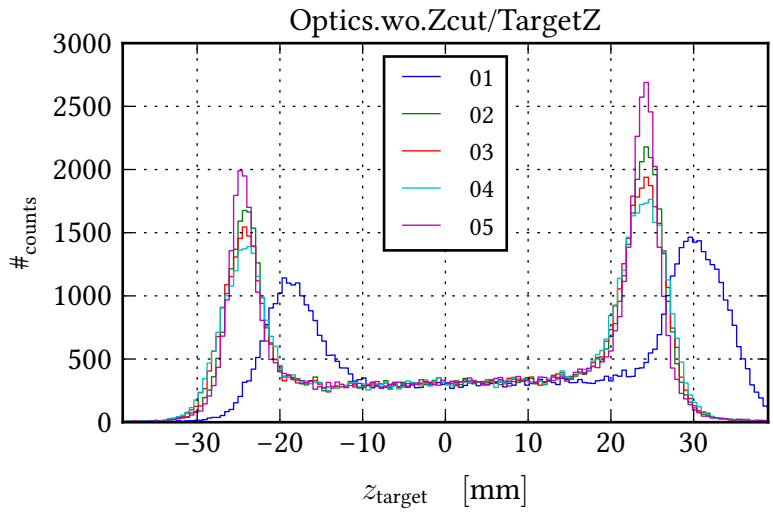

Figure 5.14: The comparison of reconstructed z coordinate on target for different transfer matrices for setting *q2_01_inp*. As a basis for fine tuning I selected the one with sharpest peaks (labeled *05*). The peaks come from target walls and from the deposit that accumulates on them. The central part corresponds to electron scattering on liquid hydrogen.

It should be noted that, because of the superior optics of spectrometer B, the target coordinates are reconstructed by that spectrometer, if possible. This is why the TMA selection for B is more important than A in terms of resolution on target. The comparison of reconstructed target for both spectrometers is shown in Figure 5.15.

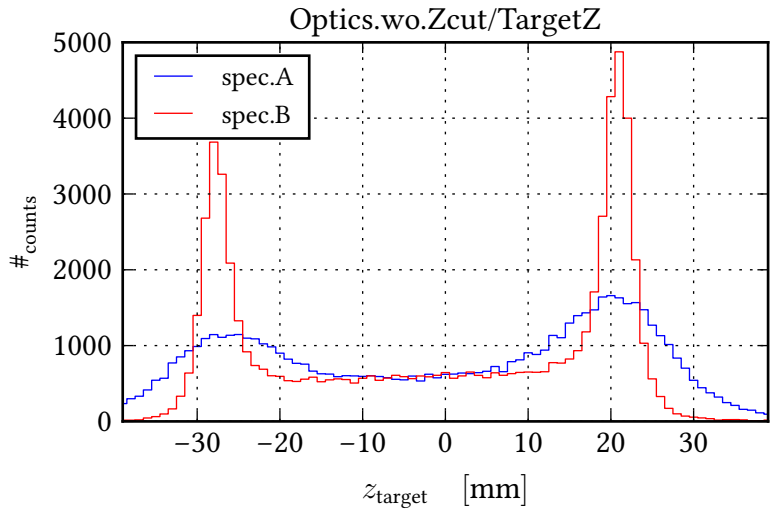

Figure 5.15: The comparison of the target resolution for spectrometers A and B. As expected, spectrometer B has much better position resolution.

5.6.2 Target center and Y_{0000} transfer coefficient

The Y_{0000} is the zeroth order matrix element for z_{target}. Changing this element directly correlates with moving the target. To set it precisely one would ideally have a run with carbon target whose position is known from theodolite measurement and a centered beam. For various reasons I did not have any such runs. So I had to do the next best thing for this calibration.

From calibration of other settings it is known that the cryogenic target was centered at $z_{\text{target}} = -2.7\,\text{mm}$, which allowed me the calibration of Y_{0000} on the cryogenic target. To get a good measure of where the reconstructed center of the target is, I fitted the z_{target} spectrum with a nine parameter model (see Appendix B.1) and then calculated the center from fitted parameters (see Figure 5.16).

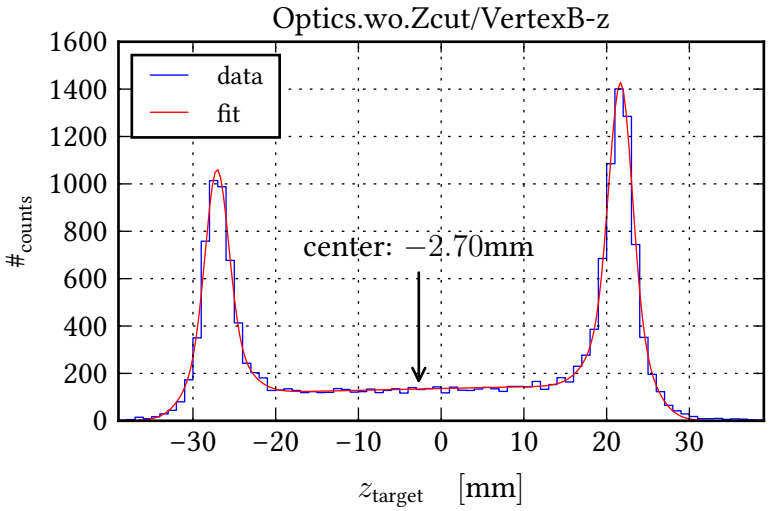

Figure 5.16: A sample result of a fit of the target model to an experimental spectrum.

The Y_{0000} matrix element moves the target as seen by the spectrometer in the so-called spectrometer coordinate system (more on coordinate systems in Appendix C). Since the spectrometer is located at an angle θ_0 measured from the beamline, the change in Y_{0000} is magnified by a factor of $\sin(\theta_0)^{-1}$ in the z_{target}. This relation can be used to determine the value of Y_{0000} to center the target on $-2.7\,\text{mm}$ (see Figure 5.17).

It is important for this calibration that the beam is centered on the target (more on this in Section 5.6.4). But because of problems with the target ladder in year 2012, we then did not know the exact position of the beam, so for those settings I needed to rely on setting *q2_01_inp*.

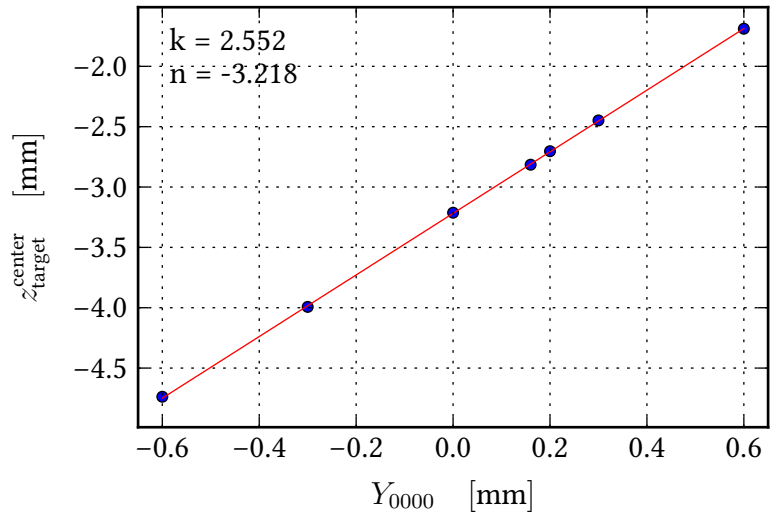

Figure 5.17: The calibration of the Y_{0000} matrix element for the spectrometer B for the setting *q2_01_inp*. The optimal value centers the target at -2.7 mm. The slope of the fit is very close to $\sin(23.06°)^{-1}$ as expected from the actual angular position of the spectrometer.

5.6.3 Wobbler calibration

To avoid local overheating of the target we used the raster or beam wobbler. This wobbler displaces the beam in the horizontal and vertical direction. The actual beam position on target for an event is then calculated from the current on the raster.

There are four parameters that need to be checked here. Two parameters set the central position in the vertical and horizontal direction and two parameters that set the scale. They can be set by comparing the target snapshot and plot reconstructed from the data.

There is another way to check the calibration of the scale parameter for the x direction. The reconstruction of z_{target} depends on the reconstruction of x_{target} (more on this in Section 5.6.4). So I made a two dimensional plot of these two variables (see Figure 5.18). If the scale parameter is set correctly, then the reconstructed target walls should be independent of the x_{target}.

5.6.4 Beam position calibration

During the experiment the beam position on the target has been periodically checked. This has been done by inserting the screen target by moving the target ladder and visually measuring the beam position (see Figure 5.19). From these checks it is seen that the beam is not stationary but moves around a bit with time. This needs to be corrected for, because the beam offset also affects the the reconstruction of z_{target}.

When the beam wobbler is used to rasterize the beam, the event coordinates on target x_{target}

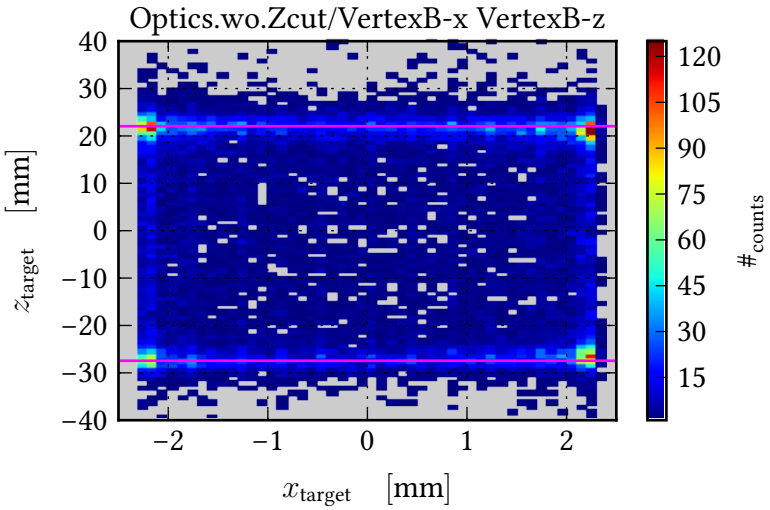

Figure 5.18: This plot can be used to check the calibration of the wobbler scale parameter for the x direction. If it is set correctly, the reconstructed z_{target} of the target walls should not depend on reconstructed x_{target}. The two purple lines show the expected position of the target walls and serve as guidelines to aid the visual check.

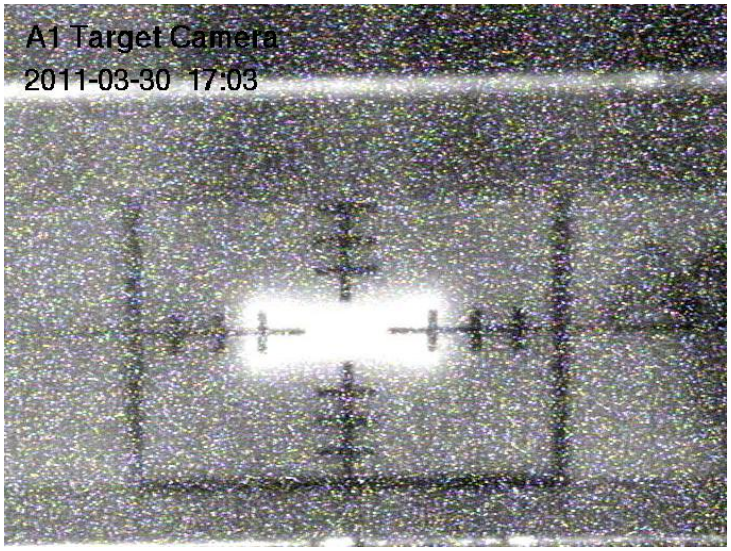

Figure 5.19: A snapshot of a beam on a screen target. The screen target is made of aluminium oxide and glows where the electrons strike it because of fluorescence. The ticks on the crosshair are 1 mm apart. The wobbler was used at the time the picture was taken.

and y_{target} (transversal coordinates) are calculated from wobbler information and offset of the center of the beam. The z_{target}, on the other hand, is calculated as an intersection point of x_{target} and $y_{\text{spectrometer}}$, which is where the spectrometer sees an event. For example, let us assume that the beam is off-center but no there is no offset set and that the spectrometer is at angle θ_0 (see Figure 5.20). To reconstruct the z_{target} one follows the particle back towards the target until the path crosses the x_{target} as given by the wobbler. But if the true x_{target} is

different than assumed, an error in z_{target} is made:

$$\Delta z_{\text{target}} \doteq \frac{\Delta x_{\text{target}}}{\tan(\theta_0)} \quad . \tag{5.5}$$

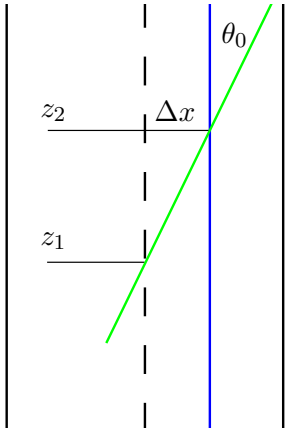

Figure 5.20: The top view of the target cell. The black dashed line is the central line towards the beam dump (up). The blue line is the path of the incoming electron. The green line is the reconstruction of the scattered electron path. The z_{target} is reconstructed at the intersection of the green and blue lines. The error in x_{target} reconstruction is then translated into an error of z_{target}.

To test this I determined the center of the target for several different offsets of the beam position in the x direction and made a linear fit (see Figure 5.21 for example). I found that the slope of the fit closely matches the expectations.

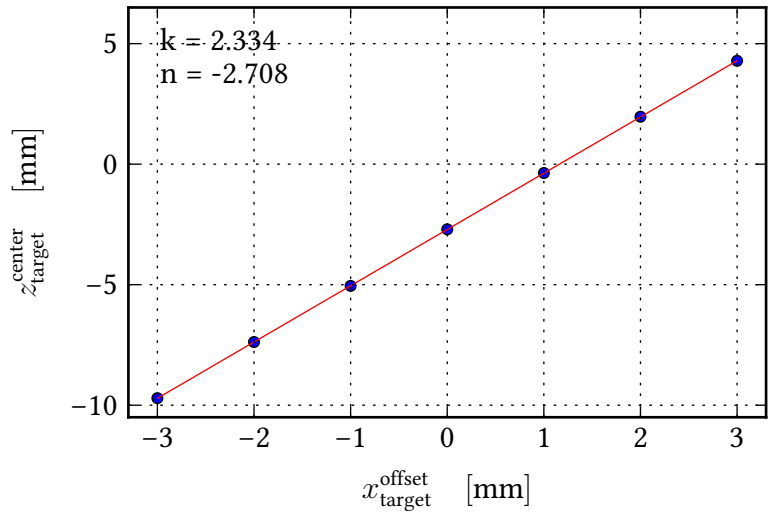

Figure 5.21: The relation between the beam offset in the x direction and the reconstructed position of the target center in the z direction for the setting *q2_01_inp*. The slope of the fit is very close to $\tan(23.06°)^{-1}$ as expected from Equation (5.5).

With this I was able to determine the correct offset for each run. First I measured the center of the target without any offset applied. Then I calculated the offset necessary to center the

target on $-2.7\,\mathrm{mm}$. After I made the corrections for all runs I remeasured the center of the target to see if the corrections were good. Then I cross referenced the offsets with the target snapshots where it is possible to see if they make sense.

Unfortunately, for a beam offset in the y direction, no such method exists. So I had to rely only on target snapshots to make this correction. During 2012 data taking, these are not reliable because of the problems with the target ladder. On the other hand, the whole analysis is mostly insensitive to this offset, with only a handful of observables showing a weak dependence on it.

5.7 Secondary data filtering

Up to this point I mainly described the calibration of raw detector variables. Before I moved to the next part of the calibration, I defined a finer filter for data. In contrast to the filter described in Section 5.2, these cuts are more precise. These are also the cuts I usually used in the final data analysis.

I should note that because some of the further calibration may move some events across the defined cuts, I did not prefilter all the data, but applied these cuts every time separately while analysing data.

Cut on trigger

During data taking we did store only coincidence events, but also a small part of single arm events. To select only coincidences, I demand that events were triggered both by spectrometer A and B. This cut is probably not needed, since the cut on coincidence time implicitly incorporates this cut, but I decided to keep it nonetheless.

Cut on coincidence time

After an event is detected in a spectrometer a time window is opened in the trigger electronics. If an event is detected in the other spectrometer during this time window, these two events are recognized as a single event or a coincidence. But not all coincidence events are true coincidences. There are also random coincidences that originate from two separate events and just happen to trigger both spectrometers during that time window. The difference is that true coincidences form a peak in spectrum while the random coincidences provide a flat background (see Figure 5.22).

This is why I make two cuts in coincidence time. The first one selects only events in the coincidence time peak and the second one only events in the flat part of the spectrum. The

second cut can then be used to make a background subtraction.

Care needs to be taken when making a cut on the coincidence time peak. The preference is to make this cut as narrow as possible. But there is a glitch in calculating the coincidence time when a particle traverses two neighbouring paddles, as can be seen in Figure 5.23.

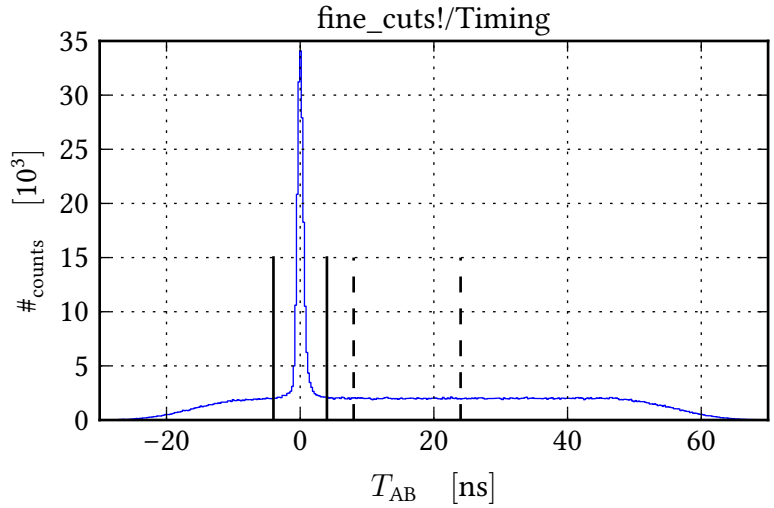

Figure 5.22: The spectrum of coincidence time between spectrometers A and B. The solid lines mark the events kept by the coincidence time peak cut and the dashed lines mark the cut on random coincidences. The reason why I did not extend the latter cut is that in the second half of this setting, the time window was moved and this cut is applicable to both cases.

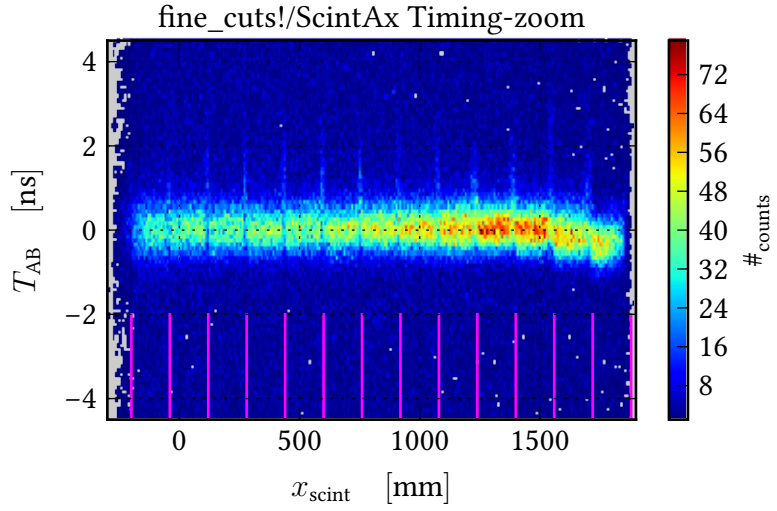

Figure 5.23: Coincidence time versus the position in the dispersive direction in the scintillator plane. The purple colour marks the border between the scintillator paddles. It can be seen that when a particle crosses two neighbouring paddles, there is a glitch in the coincidence time calculation. This limits how narrow the cut on the coincidence time peak can be.

Cut on target

as already explained in Section 5.6.2, many of the coincidence events do not originate from scattering on hydrogen, but rather on target walls and deposits on walls. To remove these events, I made a cut on z_{target}. The goal at doing this cut is to make it as wide as possible without taking events from the target walls. This is because here one is basically cutting away also good events, and the tighter the cut is, the less statistics remains for the analysis.

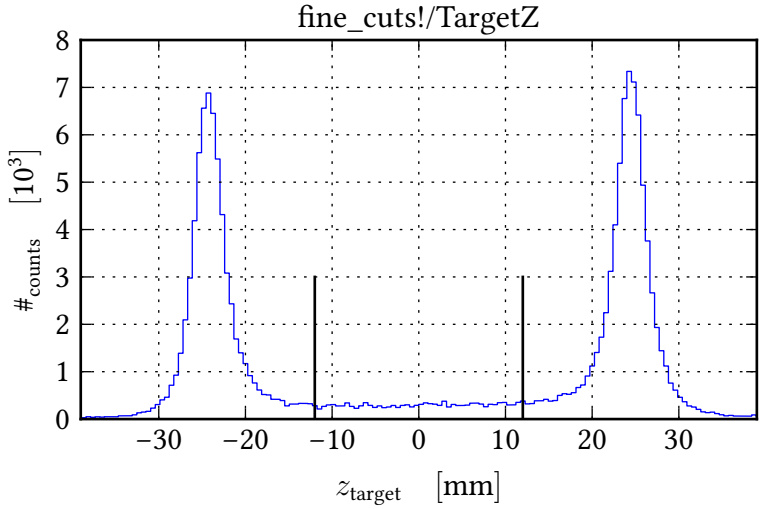

Figure 5.24: The background-subtracted target z spectrum. The events originating from the target walls represent a large fraction of all coincident events. Two black lines mark the region kept by the cut.

Cut on scintillator ADC

In our kinematical settings, there was enough energy to not only produce photons but also pions via pion electro-production process and these events are also registered as coincidences. Since protons and pions deposit different amount of energy in scintillators, two clear peaks can be seen in the ADC dE versus ToF spectrum (see Figure 5.25). To remove pions (and other possible minimum ionizing particles) from spectrometer A, I made a two dimensional cut in the scintillator ADC histogram.

Cut on missing mass squared

The missing mass squared is a very useful variable. The photon electro-production events form a peak around zero in this variable. This is why I made a cut to only select this peak, as seen in Figure 5.26.

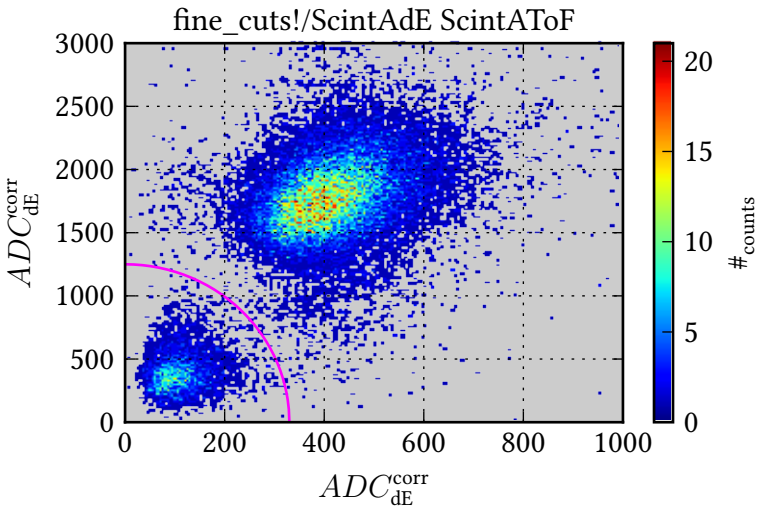

Figure 5.25: The energy deposit of particles in two scintillator planes of spectrometer A. Two clear peaks can be seen. The one at smaller energies are mostly pions, and the one at higher energies are protons. The purple line indicates the cut I made to remove the pions from further analysis.

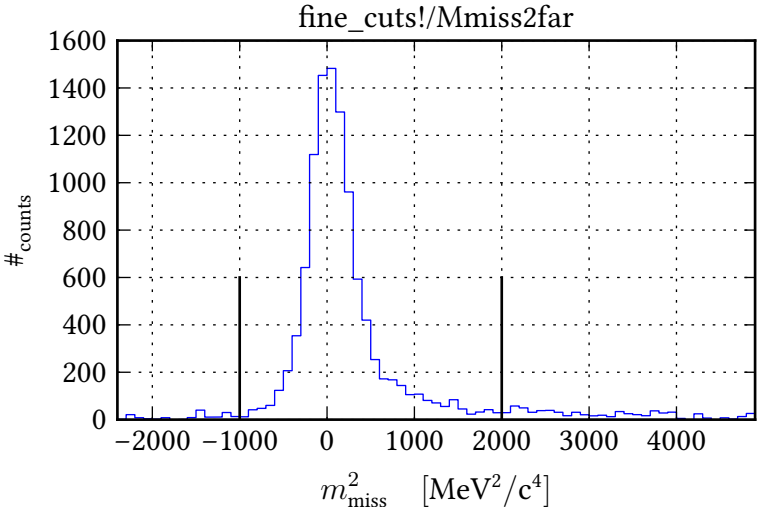

Figure 5.26: Background-subtracted missing mass squared spectrum. For photon electro-production process the peak should be centered around zero. Two black lines show the cut made in this variable.

Cut on momentum acceptance

The actual momentum acceptance of spectrometers is, at least in my case, a bit larger than the nominal acceptances. But the simulation uses a hard cut on the momentum acceptance at the nominal values. Since in the analysis I compare the simulation and measurements, I need to make the same cut (shown in Figure 5.27).

In order to compare the simulation and experimental data, I used the same values for applicable cuts also in `Simul++` code.

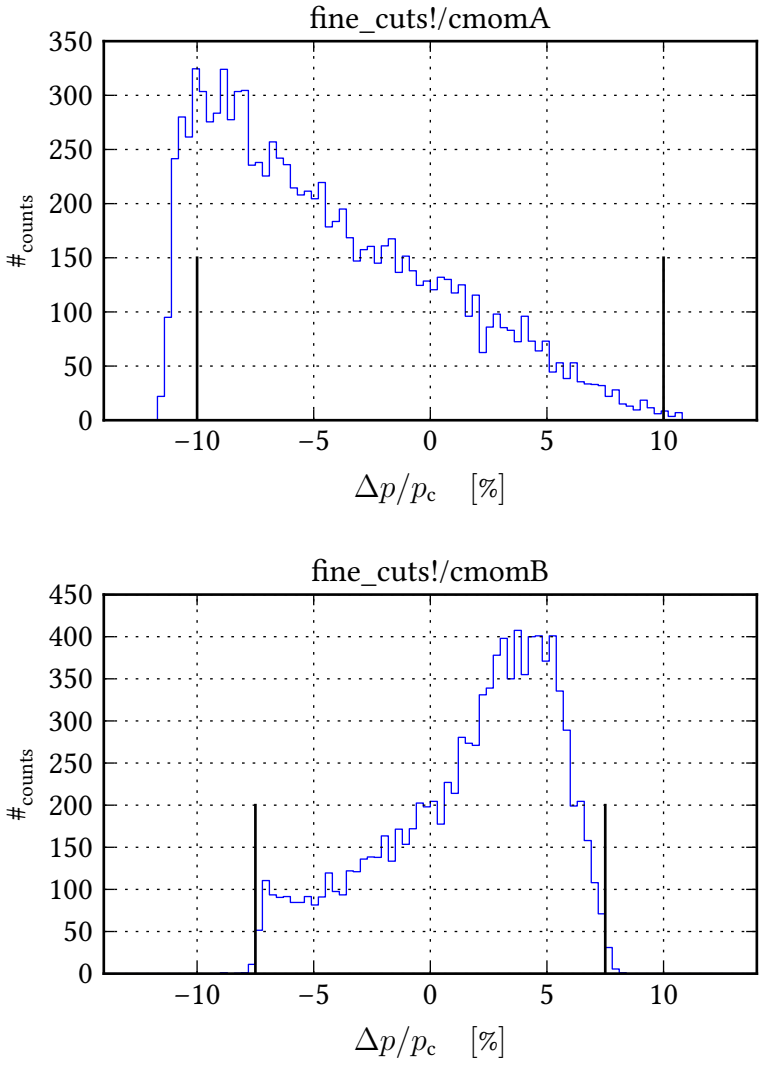

Figure 5.27: Background-subtracted momentum acceptance plots for spectrometers A and B. The black lines show the cuts made on the nominal acceptance.

5.8 Luminosity calculation

To compare the simulation and measurements a precise calculation of experimental luminosity is needed. For this a program called `Luminosity++` exists, which is used to calculate the average target density, runtime, dead time, beam current, integrated beam current and integrated luminosity for each run. This calculation uses a fixed value for target density, which is usually a bit different than the average density for each run. So a density correction needs to be made along with the dead time correction. The corrected luminosity is calculated as:

$$\mathcal{L}^{\text{int}}_{\text{corr}} = \mathcal{L}^{\text{int}} \cdot \frac{\rho_{\text{average}}}{\rho_0} \cdot (1 - \eta_{\text{dead}}) \quad , \tag{5.6}$$

where ρ_{average} is the average target density, ρ_0 is the density used in `Luminosity++` and η_{dead} is the dead time fraction.

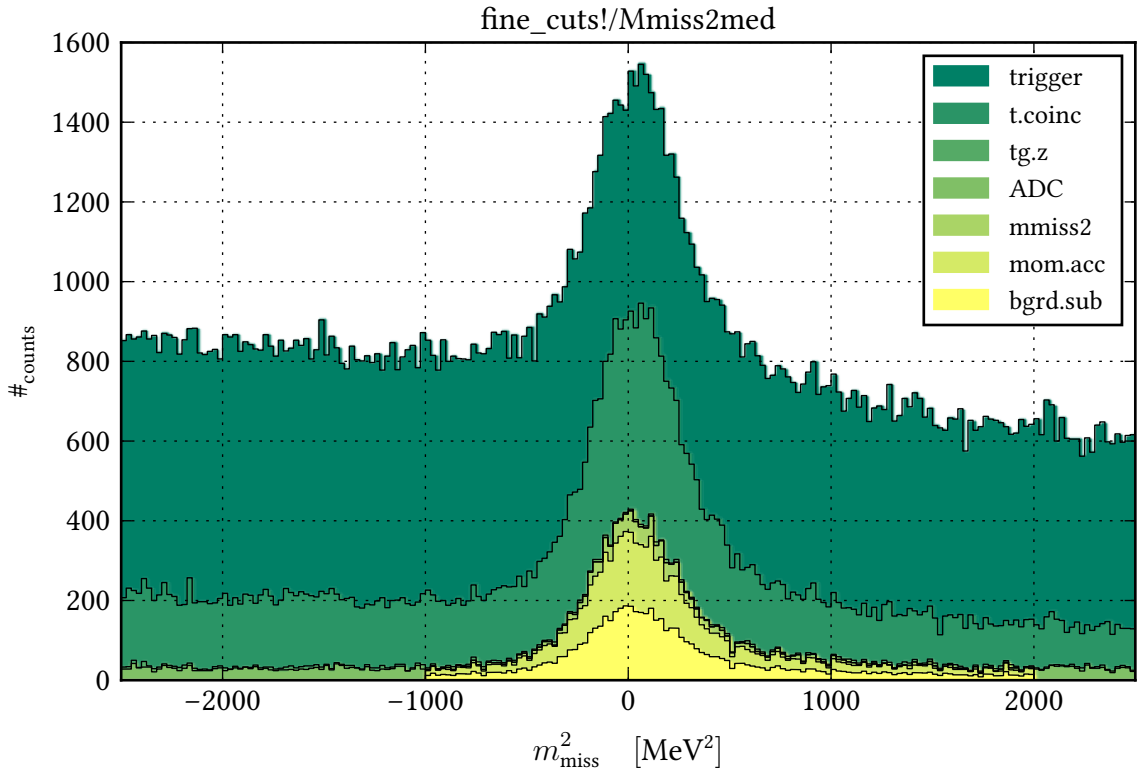

Figure 5.28: This plot shows how the missing mass squared spectrum changed with each applied cut.

A typical value for the average density is $0.0682\,\mathrm{g/cm^3}$ with $\rho_0 = 0.0688\,\mathrm{g/cm^3}$ and a typical dead time fraction is $8.5\,\%$.

Corrected luminosity, or similarly corrected beam charge, can be used as a weight for `Simul++` code which then produces histograms that can be directly compared to the experimental ones.

5.8.1 Event rate stability

The calculated luminosity together with the number of photon electro production events in a run can be used to test the event rate stability. The event rate can naively be written as:

$$\dot{N} = \mathcal{L} \cdot \frac{\mathrm{d}\sigma}{\mathrm{d}\Omega} \cdot \Delta\Omega \quad . \tag{5.7}$$

Integrating this over a time and dividing by luminosity we get:

$$\frac{N}{\mathcal{L}^{\text{int}}} = \frac{\mathrm{d}\sigma}{\mathrm{d}\Omega} \cdot \Delta\Omega \quad , \tag{5.8}$$

where both the cross section and the detector solid angle should remain constant over a kinematical setting. On the left hand side N can be replaced by the number of photon electro production events in a run and $\mathcal{L}^{\text{int}}$ by the corrected luminosity from Equation (5.6). This ratio should remain stable over a setting despite fluctuations in runtime, beam current and target density fluctuations (see Figure 5.29).

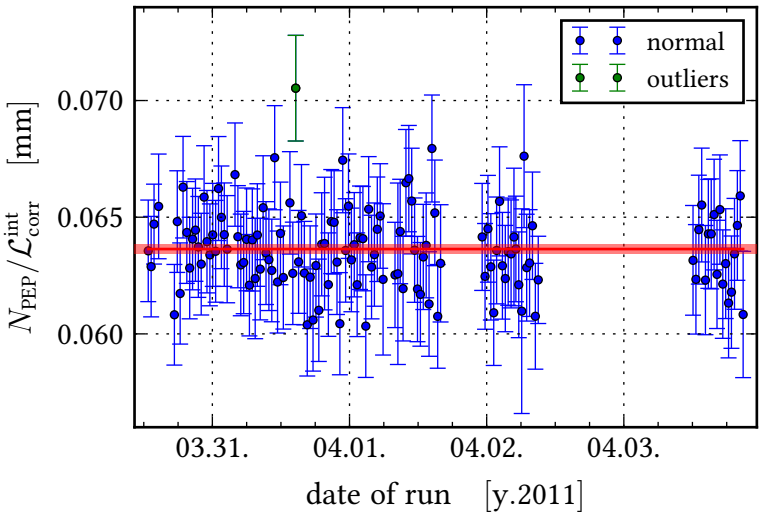

Figure 5.29: The event rate from Equation (5.8) for each run in the *q2_01_inp* setting. The red line and band show a regression of a constant to the dataset. The point in green is an outlier which needs to be checked and possibly excluded from further analysis.

5.9 Calibration of simulation specific parameters

`Simul++` code reads the same calibration file as `Cola++` and determines most of the parameters from entries that describe the experimental calibration. But there are few simulation specific entries that need to be set.

A set of such parameters describes the target position. Since the target was off-centered in the experiment, I had to input the same offsets here (for z-direction).

Another set of entries describes the beam wobbler. In `Cola++` the beam position for each event is calculated from the wobbler driver readout. This means that `Simul++` code does not have enough information to determine the wobbler amplitudes and they have to be input separately. I did this by measuring the amplitude from the experimental spectra for beam position (see Figure 5.30).

The third set of parameters describes the ranges for the event generator. The simulation generates events with random parameters and then checks whether the event can be detected by the spectrometers at all, i.e. whether it falls within their acceptance. Because the spectrometers cover only a small part of the whole phase space, this process can generate a lot of events that are discarded by these cuts. This is why I used this set of entries to limit the phase space of the event generator and by doing so quicken the simulation. To do this I looked at the experimental spectra and determined the ranges from there. I should note that it is better to take a bit wider range than smaller since it is better to wait a bit more time to get the statistics than to have the simulation produce truncated spectra. I set the following:

- range of the size of the virtual photon four-momentum q^2,

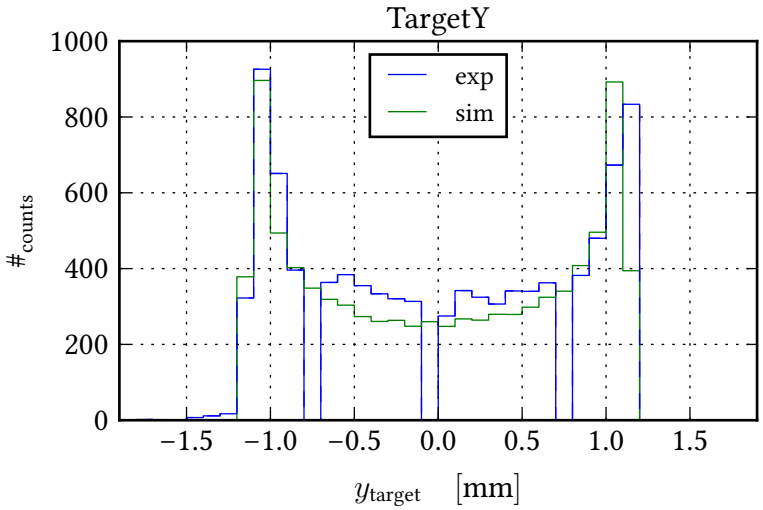

Figure 5.30: A comparison of experiment and simulation for the target coordinate y.

- range of the scattering angle θ'_{cm},
- range of the scattering angle ϕ'_{cm} and
- range of the final photon momentum q′ (see Figure 5.31).

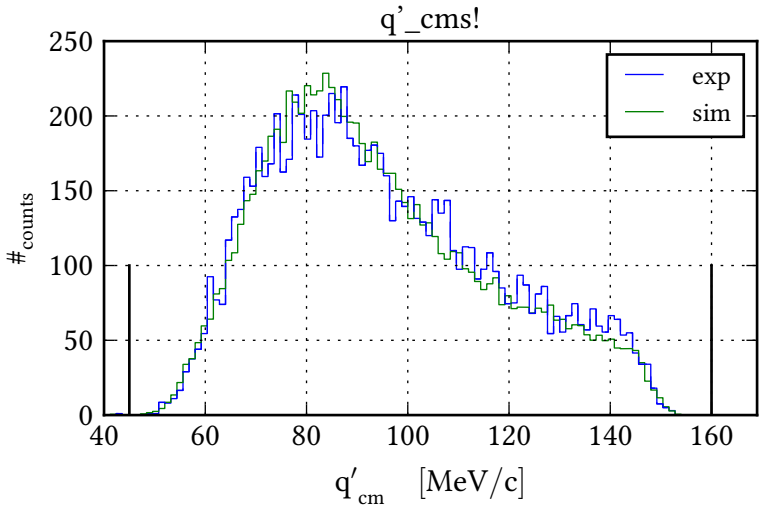

Figure 5.31: A comparison between experiment and simulation for the momentum of the final photon. The black lines mark the limits for `Simul++` code.

5.10 Calibration of transfer coefficients

Since I used transfer matrices that were already calibrated for my kinematics, I had to change only a few coefficients. I only checked and fine-tuned the zeroth order elements. The calibration of the Y^{B}_{0000} element is already described in Section 5.6.2.

Both spectrometers have the entrance collimator centered with respect to the spectrometer optical axis. For centered beam and in-plane kinematics this means that the θ_0 spectrum for both spectrometers should also be centered and symmetric about zero. I used this property to fix the value of the θ_{0000} transfer elements, which directly influence these plots. To do this I made a histogram plot of θ_0 and $-\theta_0$ to measure the offset (see Figure 5.32). I used this offset to change the transfer element, until the histogram was well centered.

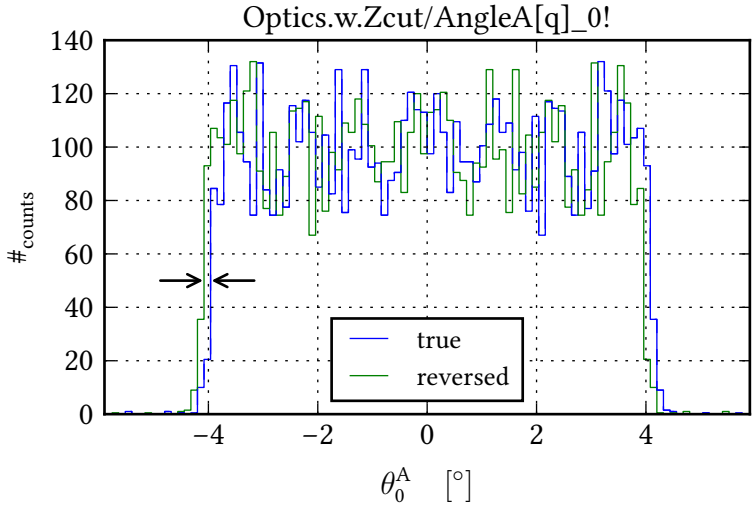

Figure 5.32: The histogram of θ_0 for spectrometer A and the same histogram flipped over the origin for the *q2_01_inp* setting. The offset between histograms (marked with black arrows) can be used to calibrate the θ^A_{0000} matrix element. Analogous for spectrometer B.

Unfortunately the above procedure does not work for the out-of-plane setting and for the ϕ_{0000} transfer element. This is because the corresponding histograms are not symmetric and such comparison is thus more difficult or impossible. In this case I made a comparison of experimental plots with the simulation. The simulation does not use the transfer matrices since there is no need to reconstruct the particle trajectory from the focal plane coordinates back to target and so it is not sensitive to changes in transfer coefficients. I chose such values that the offset between the simulation and the data was minimal (see Figure 5.33).

As an additional check, I plotted the missing mass squared around the VCS peak against focal plane variables of both spectrometers. The missing mass squared should be independent of these variables, so a slope in these plots could indicate that some offset needs adjustment. As an example, a correlation between m^2_{miss} and θ^B_{fp} is sensitive to changes in the dispersive transfer elements θ^B_{0000} and x^B_{0000}. But one needs to be careful, since fixing this slope might create a slope in the same plot for spectrometer A. This is why I always checked the whole set of plots when fixing one parameter.

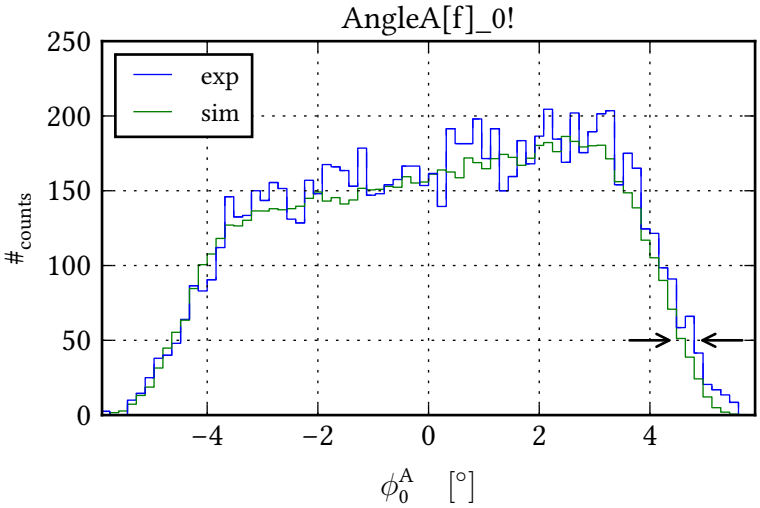

Figure 5.33: The histogram of ϕ_0 for spectrometer A for experiment and simulation for setting *q2_01_inp*. The offset between the histograms (marked with black arrows) can be used to calibrate the ϕ^A_{0000} matrix element. Analogous for spectrometer B.

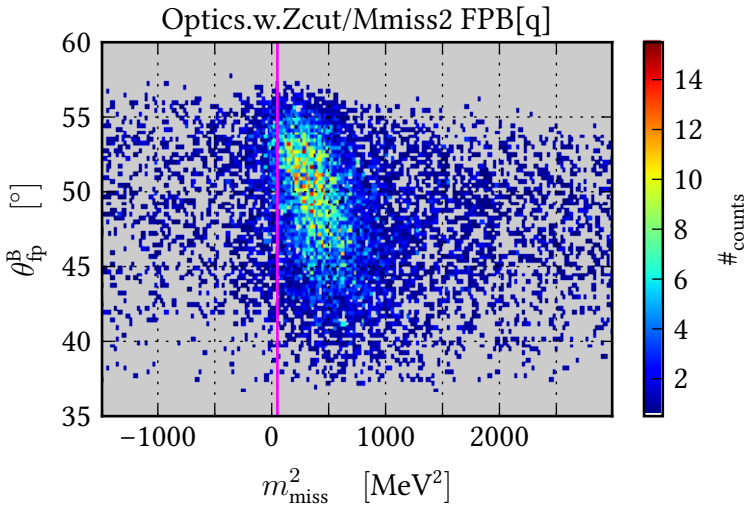

Figure 5.34: The dependence of the VCS missing mass squared peak on the focal plane coordinate θ for spectrometer B. The tilt of the peak is sensitive to the θ^B_{0000} and x^B_{0000} elements of the transfer matrix. The purple line acts as a guide of where the peak should be positioned.

5.11 Asymmetry of ϕ'_{cm} and out-of-plane angle

The angle ϕ'_{cm} is the angle between the scattering and the reaction plane. The Bethe-Heitler and Born cross sections are both symmetric under this angle, i.e. changing the sign of the angle does not change the cross section. The same holds true for the virtual Compton scattering cross section and so for the whole photon electro-production process. This means that in the in-plane kinematics approximately the same number of events should be scattered below

and above the scattering plane, thus the ϕ'_{cm} spectrum is expected to be symmetrical.

The simulated histogram was indeed symmetrical, but the experimental histogram was not (see Figure 5.35) and this signalled a problem. The asymmetry by itself is not a problem, because it could be caused by some kinematical properties or acceptance cuts. The problem was the mismatch between the simulation and the data.

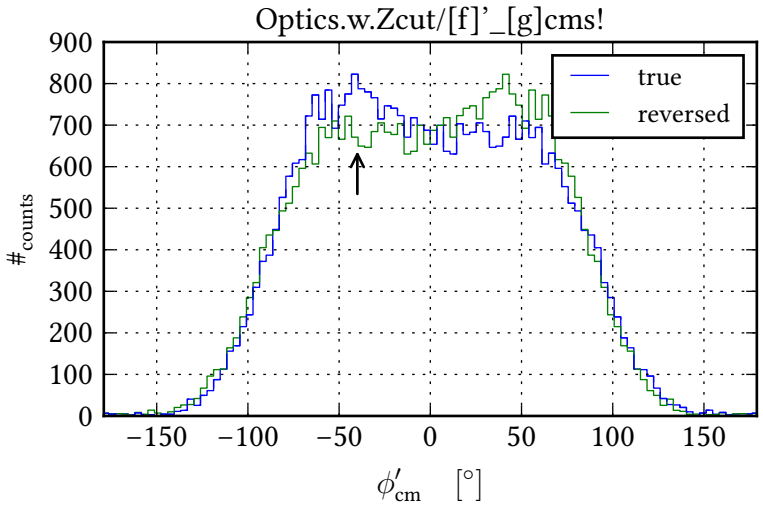

Figure 5.35: The histogram of ϕ'_{cm} for setting *q2_01_low_3* and same histogram reversed. The black arrow point to the asymmetry in the plot.

To reconcile the difference between the simulation and the data there were two possible paths:

- try to make the experimental histogram symmetric,
- or allow the histogram to be asymmetric and make the simulation asymmetric also.

I could not find any solution, that would symmetrize the measured histogram, while also not worsen the previous calibration. Then I tried the second option. I found two parameters that affect both simulation and experimental data in such a way that the ϕ'_{cm} histograms matched better. The two parameters are a beam offset in y-direction and an out-of-plane angle of spectrometer B. While the changing the beam offset worked, the required value was of the order of few millimeters which would mean we missed the target and such offsets are not supported by target snapshots. This is why I chose to fine tune the out-of-plane angle of spectrometer B.

Adjusting the out-of-plane angle of spectrometer B also works in in-plane kinematics, where the angle should be zero. While it is known that the hall floors are not perfectly even, the required offset of about 2 to 3 mrad (see Figure 5.36) is too big to be explained this way. But there could be also other effect that could be essentially described by this angle. One such possibility is that the collimator of spectrometer A, which is close to the target, is a bit off-centered. This would effectively create an out-of-plane angle between the two spectrometers.

5.11.1 Correction of the mismatch

The value of out-of-plane angle required for correction of this asymmetry problem could be derived by a comparison of simulated and experimental histogram. But it is very hard to judge if two histograms are similar enough, especially with lower statistics. Because of this I decided to try another approach.

As it turns out, changing the value also changes the width of the VCS missing mass squared peak. So I selected a few values of out-of-plane angle and determined the full width at half maximum (FWHM) of the peak for each of them. The points form a parabolic shape (see Figure 5.36) with a clear minimum. I chose the value at the minimum as the optimal value for the out-of-plane angle. With this I also got a good match between the simulation and the data for ϕ'_{cm} plot (see Figure 5.37).

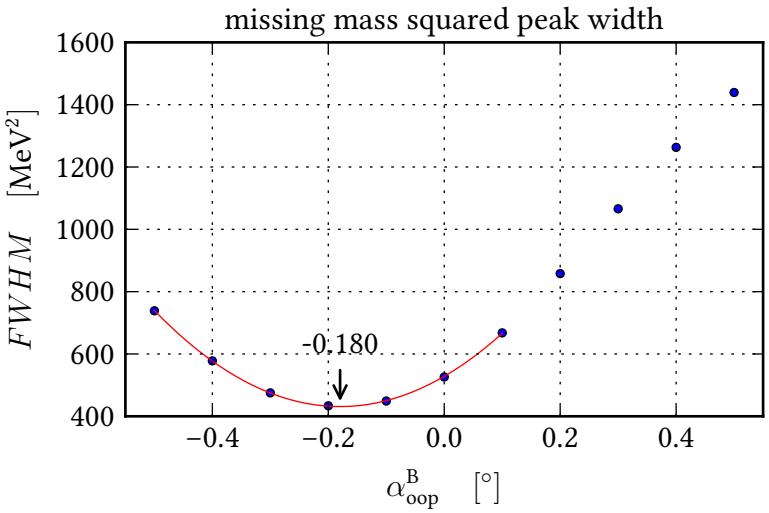

Figure 5.36: The relationship between out-of-plane angle for spectrometer B and the width of the VCS missing mass squared peak for the *q2_01_low_3* setting. The red line is a quadratic fit to the data points and the black arrow points to the minimum of the fit. This is also the optimal value for the out-of-plane angle.

5.12 Snow thickness and spectrometer B momentum - constrained minimization

This section describes the calibration of two parameters that at first sight are not really connected, and one observable. The two parameters are the snow thickness and the momentum of spectrometer B, and the observable is the VCS missing mass squared peak.

The cryogenic target cell is cooled to around 21 K and any particle that comes into contact with it adsorbs on the surface. Even with good vacuum there are still enough particles left to form a layer of deposit, i.e. snow. The scattered particles must now traverse this layer and

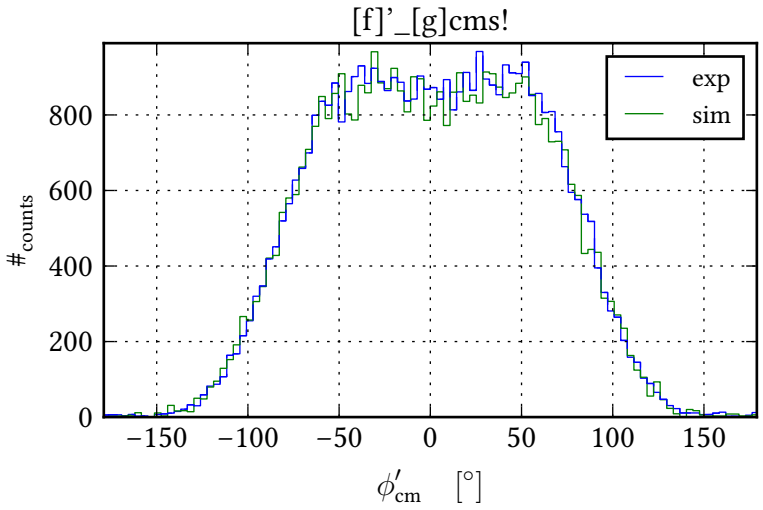

Figure 5.37: The comparison of data and simulation for setting *q2_01_low_3* after the calibration of the out-of-plane angle for spectrometer B. Both curves are a bit asymmetric, but it is hard to see this because of the low statistics.

incur additional energy loss that needs to be taken into account. Both `Cola++` and `Simul++` code have built in a snow model (see Figure 5.38) with two parameters, snow thickness and density. But the important thing is their product, thickness times density or surface density.

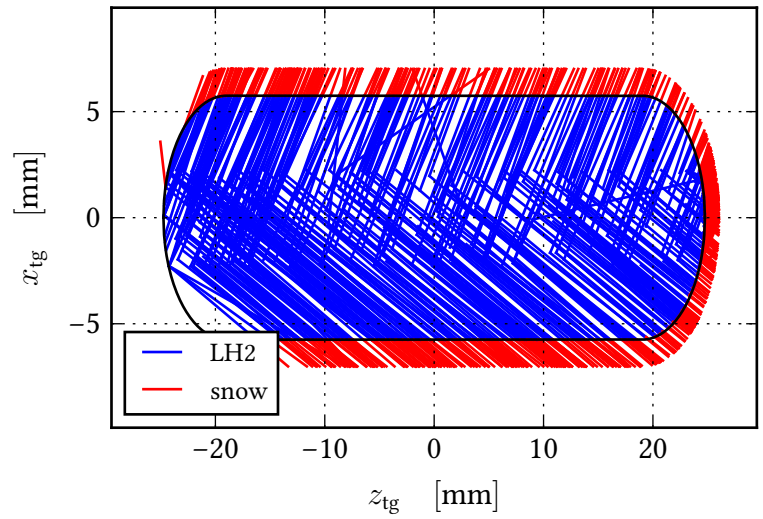

Figure 5.38: Top view of the target cell and reconstructed particle tracks. The blue part shows the track through the liquid hydrogen and red part through snow. The current model for snow assumes a constant thickness around the cell, as can be seen from the red band.

To determine the central momentum of the spectrometers, they are equipped with NMR and Hall probes that measure the magnetic field of the magnets. Usually the NMR output is used to calculate the momentum. But during our beam time the NMR in the spectrometer B did not work and we had to use the Hall probe readings for calculation. And since the Hall probe is not as accurate as NMR, the central momentum can be slightly optimized.

Both of these two parameters affect the VCS missing mass squared peak width and position. To obtain the peak width and position, I fitted the missing mass squared histogram with the Crystal Ball function (described in Appendix B.2). I took the FWHM of the fit as the peak width and the fit parameter μ as the peak position.

At first I tried to calibrate each parameter separately. I started by plotting the width of the missing mass squared versus the snow thickness, determined the minimum and proclaimed that value as optimal (similarly as shown in Figure 5.36). Then I performed the same procedure with the central momentum of spectrometer B. As it turns out, these two calibrations affect each other, so I needed a few iterations to determine the minimum of the missing mass squared peak and with that both parameters.

To complicate things, there is a constraint to this procedure. The position of the VCS missing mass squared peak for data needs to match the one from the simulation. This position in the simulation is slightly sensitive to the choice of the above parameters, but the sensitivity of the experimental peak is much bigger. While I did obtain the minimum of the peak width, the position was not the same as in the simulation.

To get a better overview, I decided on the next procedure. I made a two dimensional grid in the central momentum and snow thickness. On each grid point I determined the width and the position of the VCS missing mass squared peak and made a plot (see Figure 5.39). On this plot I selected a point for which a position of the peak is around the desired value and is close to the minimum of the peak width.

Since the spectrometer momentum should not change during a single setting, this part of the calibration was done. But snow thickness can change with time, especially if data taking for a setting spans a few days. To avoid the trial and error procedure for calibrating the snow thickness for each run, I made a calibration curve (see Figure 5.40) for the dependence of the peak position on snow thickness. Then I determined the VCS missing mass squared peak position for each run. Since the spectrometer momentum is fixed, the change in position should correspond to the change in snow thickness. So I used the calibration curve to quickly calculate the necessary snow to keep the peak at the desired position.

I should note that this procedure is decoupled from the out-of-plane angle calibration, even though both rely on the VCS missing mass squared peak. I ran the out-of-plane calibration again after finishing with snow thickness and spectrometer B momentum calibration, and found basically the same value for the out-of-plane angle of the spectrometer B.

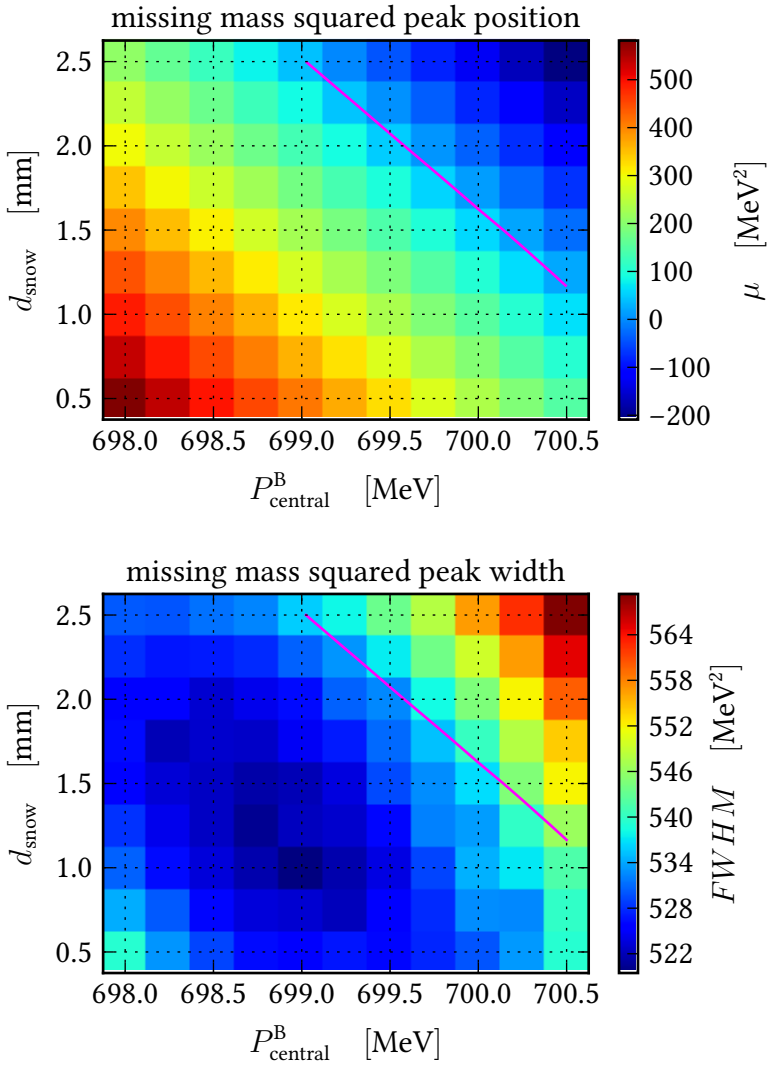

Figure 5.39: The position (top) and width (bottom) of the VCS missing mass squared peak change with snow thickness and central momentum of spectrometer B. The purple lines show the parameters for which the peak position matches the simulated one. The chosen values should lie on this line and near the minimum of the peak width.

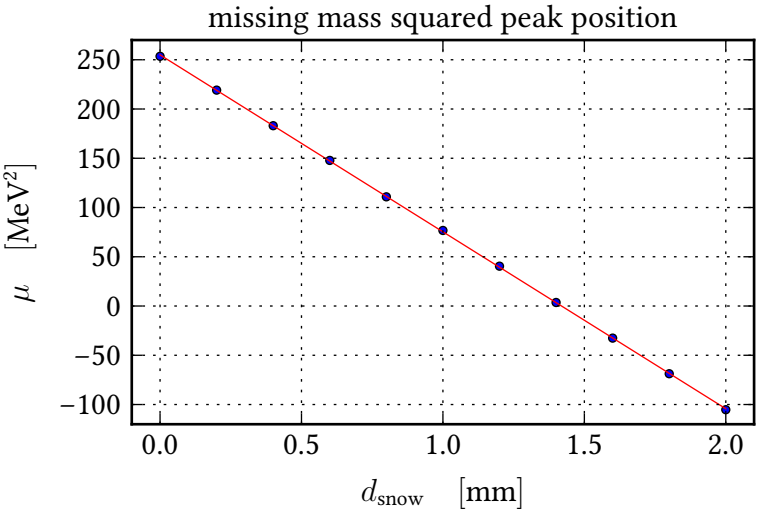

Figure 5.40: The dependence of VCS missing mass squared peak position on snow thickness. The red line is linear fit to the points and is used as a calibration curve determination of snow thickness.

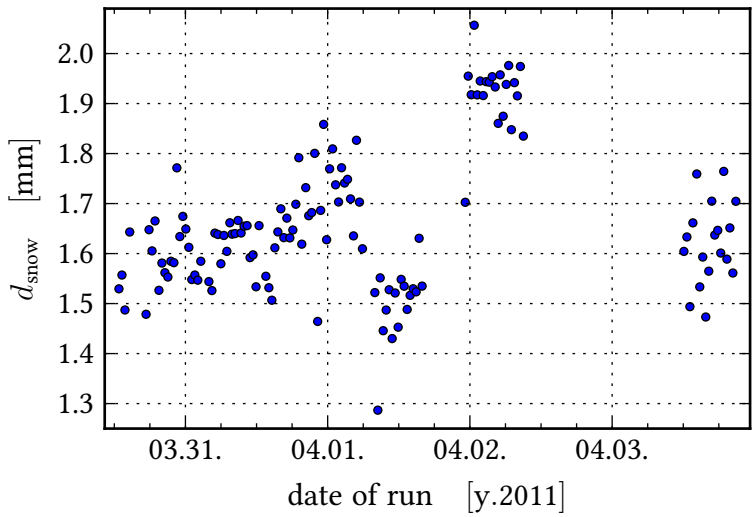

Figure 5.41: The time evolution of snow thickness for setting *q2_01_inp*. To get each point I determined the peak position without any snow set and then used the slope of the fit shown in Figure 5.40 to calculate the required snow thickness to position the peak at the simulated location.

Chapter 6

From counts to results

This chapter describes the procedure I used to extract physics results from data counts.

6.1 Binning of the data

The photon electro-production reaction $\mathrm{e} + \mathrm{p} \longrightarrow \mathrm{e}' + \mathrm{p}' + \gamma'$ can be defined by five independent variables (see Section 2.3.1), which implies a five-fold differential cross section. With the choice of variables we made for our analysis (see Equation(2.23)), the cross section can be written as:

$$\frac{\mathrm{d}^5\sigma}{\mathrm{d}\Omega^5} = \frac{\mathrm{d}^5\sigma}{\mathrm{d}q'_{\mathrm{cm}}\,\mathrm{d}\cos(\theta'_{\mathrm{cm}})\,\mathrm{d}\phi'_{\mathrm{cm}}\,\mathrm{d}q_{\mathrm{cm}}\,\mathrm{d}\epsilon} \quad . \tag{6.1}$$

Generally, a five-dimensional binning would be needed for the cross section extraction. But in our case two variables, q_{cm} and ϵ, were kinematically constrained to a narrow range. So only a three-dimensional binning in the remaining variables was needed. We decided on the following selection of bins:

- q'_{cm}: five bins over the range of 25 to $150\,\mathrm{MeV}$,
- $\cos(\theta'_{\mathrm{cm}})$: forty bins over the range of -1 to 1 and
- ϕ'_{cm}: thirty-six bins over the range of $-180°$ to $180°$.

This gives a total of 7200 bins, most of which are empty due to the experimental phase space restrictions. I achieved the binning by defining five two-dimensional histograms of ϕ'_{cm} versus $\cos(\theta'_{\mathrm{cm}})$ and placing a different cut in q'_{cm} on each of it.

6.2 From counts to cross section

The cross section extraction procedure I used is based on the technique described in [108].

The number of events in a bin is connected to the cross section via:

$$N_{\text{exp}} = \mathcal{L}_{\text{exp}} \cdot \iiiint \left(\frac{\mathrm{d}^5\sigma}{\mathrm{d}\Omega^5}\right)_{\text{exp}} \cdot A(\Omega) \cdot \mathrm{d}\Omega^5 \quad , \tag{6.2}$$

where the $\mathcal{L}_{\text{exp}}$ is the experimental luminosity and $A(\Omega)$ is the acceptance function. The acceptance function is a measure of probability that an event in the bin will be accepted. The above expression can be rewritten as:

$$\begin{aligned}\frac{N_{\text{exp}}}{\mathcal{L}_{\text{exp}}} &= \frac{\iiiint \left(\frac{\mathrm{d}^5\sigma}{\mathrm{d}\Omega^5}\right)_{\text{exp}} \cdot A(\Omega) \cdot \mathrm{d}\Omega^5}{\iiiint A(\Omega) \cdot \mathrm{d}\Omega^5} \cdot \iiiint A(\Omega) \cdot \mathrm{d}\Omega^5 \\ &= \left\langle \left(\frac{\mathrm{d}^5\sigma}{\mathrm{d}\Omega^5}\right)_{\text{exp}} \right\rangle \cdot \Delta\Omega_1 \quad . \end{aligned} \tag{6.3}$$

This equation connects the number of counts in a bin with the average value of the cross section in the same bin. Since the cross section is not constant over the bin, the average cross section does not generally correspond to the value in the center of the bin. Equating the two values would introduce a bias. This can be solved in two ways. The first is to attribute the value to an appropriate different point, but since we are dealing with a five-fold differential cross section, this seems unpractical. The second way is to select a reference point in a bin and include a correction factor to the solid angle:

$$\begin{aligned}\frac{N_{\text{exp}}}{\mathcal{L}_{\text{exp}}} &= \left(\frac{\mathrm{d}^5\sigma}{\mathrm{d}\Omega^5}\right)^0_{\text{exp}} \cdot \iiiint \left(1 + \frac{\left(\frac{\mathrm{d}^5\sigma}{\mathrm{d}\Omega^5}\right)_{\text{exp}} - \left(\frac{\mathrm{d}^5\sigma}{\mathrm{d}\Omega^5}\right)^0_{\text{exp}}}{\left(\frac{\mathrm{d}^5\sigma}{\mathrm{d}\Omega^5}\right)^0_{\text{exp}}}\right) \cdot A(\Omega) \cdot \mathrm{d}\Omega^5 \\ &= \left(\frac{\mathrm{d}^5\sigma}{\mathrm{d}\Omega^5}\right)^0_{\text{exp}} \cdot (\Delta\Omega_1 + \omega) \\ &= \left(\frac{\mathrm{d}^5\sigma}{\mathrm{d}\Omega^5}\right)^0_{\text{exp}} \cdot \Delta\Omega_2 \quad , \end{aligned} \tag{6.4}$$

where $(\mathrm{d}^5\sigma/\mathrm{d}\Omega^5)^0$ denotes the cross section at the chosen point and ω measures the deviation of the solid angle $\Delta\Omega_2$ from $\Delta\Omega_1$. This deviation depends on the selected point in the bin and on the variation of the cross section.

The same procedure can be made for the number of counts in the simulation.

$$\begin{aligned}\frac{N_{\text{sim}}}{\mathcal{L}_{\text{sim}}} &= \left(\frac{\mathrm{d}^5\sigma}{\mathrm{d}\Omega^5}\right)^0_{\text{sim}} \cdot \iiiint \left(1 + \frac{\left(\frac{\mathrm{d}^5\sigma}{\mathrm{d}\Omega^5}\right)_{\text{sim}} - \left(\frac{\mathrm{d}^5\sigma}{\mathrm{d}\Omega^5}\right)^0_{\text{sim}}}{\left(\frac{\mathrm{d}^5\sigma}{\mathrm{d}\Omega^5}\right)^0_{\text{sim}}}\right) \cdot A(\Omega) \cdot \mathrm{d}\Omega^5 \\ &= \left(\frac{\mathrm{d}^5\sigma}{\mathrm{d}\Omega^5}\right)^0_{\text{sim}} \cdot \Delta\Omega_3 \quad . \end{aligned} \tag{6.5}$$

The cross section that is used by the simulation should ideally equal the unknown cross section that is being measured. In the case of VCS, the BH+B cross section can be used instead, since it is very close to the expected cross section and because its curvature is a very good approximation. The simulation must also reproduce very accurately the acceptance function of the spectrometers, which must not only include the geometrical acceptance, but also resolution effects and possibly also local inefficiencies of the detectors. This is why solid angles $\Delta\Omega$'s are called 'effective' and why they can only be calculated by a Monte Carlo simulation.

If the simulation describes the effective solid angles well enough (and in our case it does), the experimental cross section can be calculated as:

$$\begin{aligned}\left(\frac{\mathrm{d}^5\sigma}{\mathrm{d}\Omega^5}\right)^0_{\text{exp}} &= \left(\frac{\mathrm{d}^5\sigma}{\mathrm{d}\Omega^5}\right)^0_{\text{sim}} \cdot \frac{N_{\text{exp}}}{N_{\text{sim}}} \cdot \frac{\mathcal{L}_{\text{sim}}}{\mathcal{L}_{\text{exp}}} \cdot \frac{\Delta\Omega_3}{\Delta\Omega_2} \\ &\doteq \left(\frac{\mathrm{d}^5\sigma}{\mathrm{d}\Omega^5}\right)^0_{\text{sim}} \cdot \frac{N_{\text{exp}}}{N_{\text{sim}}} \cdot \frac{\mathcal{L}_{\text{sim}}}{\mathcal{L}_{\text{exp}}} \quad . \end{aligned} \tag{6.6}$$

This means that the number of counts in the experiment and simulation are needed in order to calculate the cross section. To get the correct value for N_{exp}, the random coincidences must be subtracted. The coincidence time spectrum (shown in Figure 6.1) has a sharp peak corresponding to true coincidences between spectrometers A and B, and a flat background that comes from random coincidences. To make the subtraction, I count the number of events in a part of the flat region, scale them and subtract from the number of events in the peak. The scaling factor equals to the ratio of the widths of sampling intervals for coincidence peak and for the flat part. The N_{exp} now becomes:

$$N_{\text{exp}} = N_{\text{TT}} - \eta N_{\text{TB}} \quad , \tag{6.7}$$

where N_{TT} is the number of events under coincidence time peak, N_{TB} the number of events in the sampled flat region and $\eta = \Delta T_{\text{TT}}/\Delta T_{\text{TB}}$ is the ratio of widths of the two intervals.

To get the N_{sim} I used the `Simul++` code with the same kinematical cuts as used on experimental data (the ones that are applicable) and with the same binning as described in 6.1. The simulation also allows for the normalization to the experimental luminosity, such that $\mathcal{L}_{\text{sim}} = \mathcal{L}_{\text{exp}}$. With this the number of experimental and simulated counts can be directly compared on an absolute scale.

The expression for the experimental cross section from Equation (6.6) now becomes:

$$\left(\frac{\mathrm{d}^5\sigma}{\mathrm{d}\Omega^5}\right)_{\text{exp}} = \left(\frac{\mathrm{d}^5\sigma}{\mathrm{d}\Omega^5}\right)_{\text{sim}} \cdot \frac{N_{\text{TT}} - \eta N_{\text{TB}}}{N_{\text{sim}}} \quad , \tag{6.8}$$

where I chose the center of the bin as reference point and dropped the superscript ^{0}.

The statistical uncertainty of the cross section comes from the uncertainties of the counts of events in the bin, N_{TT}, N_{TB} and N_{sim}. The first two are governed by Poisson statistics, so the variance equals to the number of counts. But this is not true for the uncertainty in the case of the simulation. The number of counts in a histogram bin is the result of a Monte

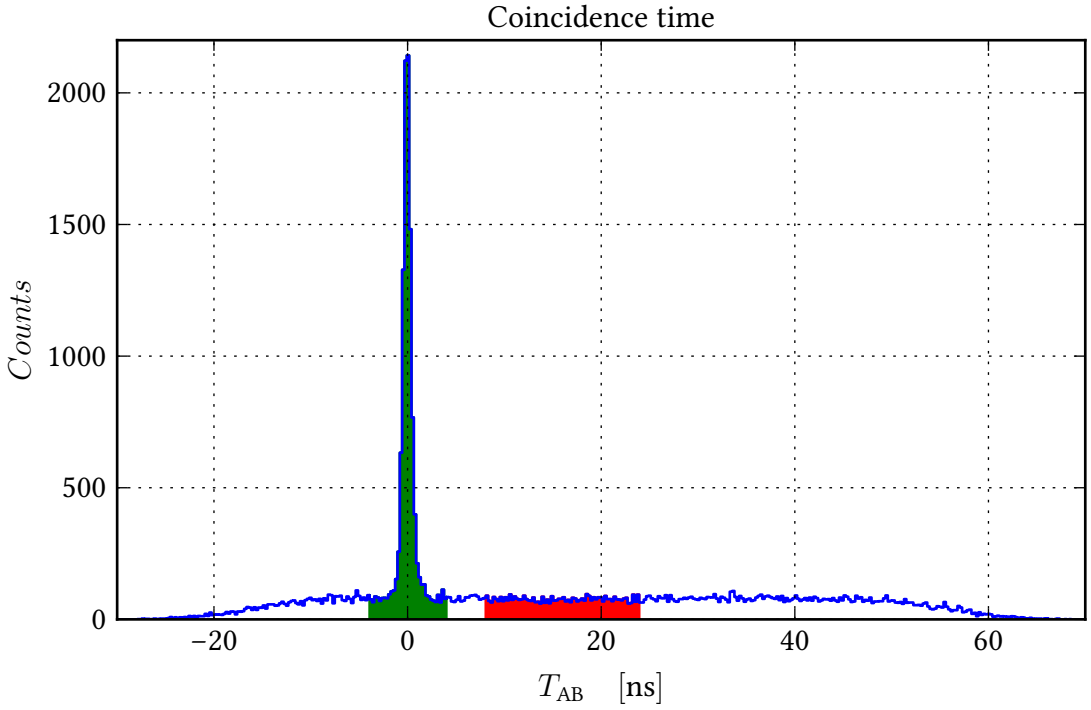

Figure 6.1: A typical coincidence time spectrum between spectrometers A and B. The sharp peak corresponds to the true coincidences (signal) and the flat region to the random coincidences (background). To get a proper number of coincidence events, random coincidences need to be subtracted. This is done by taking the number of events in the green interval and subtract from them the scaled number of events in the red. The scaling factor is the ratio of the green and red interval widths.

Carlo integration of the cross section and the phase space with an overall normalization which combine to the weight of the event. So the uncertainty is not directly connected to the number of events in the histogram bin, but to the weight and number of simulated events, which generally differs from the former. For this reason the `Simul++` code also stores the minimal statistics for variance calculation: sum of weights, sum of squared weights and number of Monte Carlo events - $(\text{data}, \text{datasq}, n)$. With this information the uncertainties can be written as:

$$N_{\text{TT}} \longrightarrow N_{\text{TT}} \pm \delta N_{\text{TT}} = N_{\text{TT}} \pm \sqrt{N_{\text{TT}}} \quad , \tag{6.9a}$$

$$N_{\text{TB}} \longrightarrow N_{\text{TB}} \pm \delta N_{\text{TB}} = N_{\text{TB}} \pm \sqrt{N_{\text{TB}}} \quad , \tag{6.9b}$$

$$N_{\text{sim}} \longrightarrow N_{\text{sim}} \pm \delta N_{\text{sim}} = N_{\text{sim}} \pm \sqrt{\frac{\text{datasq} - \text{data}^2}{n}} \quad . \tag{6.9c}$$

The uncertainty of the cross section can be obtained by summing all contributions quadrati-

cally:

$$\delta\left(\frac{\mathrm{d}^5\sigma}{\mathrm{d}\Omega^5}\right)_{\text{exp}} = \left(\frac{\mathrm{d}^5\sigma}{\mathrm{d}\Omega^5}\right)_{\text{sim}} \cdot \left[\left(\frac{\delta N_{\text{TT}}}{N_{\text{sim}}}\right)^2 + \left(\frac{\delta N_{\text{TB}}}{N_{\text{sim}}}\right)^2 + \left(\frac{N_{\text{TT}} + \eta N_{\text{TB}}}{N_{\text{sim}}}\delta N_{\text{sim}}\right)^2\right]^{1/2} \quad . \tag{6.10}$$

The uncertainty of the simulation can be reduced by simulating more events. In practice it can be made negligible compared to the experimental uncertainty, so only the first two contributions remain in the Equation (6.10).

6.3 From cross section to corrected cross sections

The cross sections extracted according to the previous section need to be corrected by a normalization factor. This is basically a consequence of three effects:

The correction for the effect of detector inefficiencies is straightforward. Since the detectors are not registering all of the passing particles, some events are not detected or some events do not have complete information. If an event is not detected we simply lose it. We also lose an event if it is missing information about a variable on which we are applying a cut. For example, if the scintillators do not measure the deposited energy of a passing particle and there is a PID cut on that energy, the event is removed from further analysis, even though in reality that event would have passed the cut. In both cases the number of measured events in a bin needs to be corrected for this inefficiency. A problem could arise if some detectors have localized inefficiencies. Then it is better to include this correction in the simulation as an additional position-dependent weight.

The `Simul++` code takes into account radiative corrections, but these effects are not exactly known. This can cause a bias in the extracted cross section.

Different form factor parametrizations yield different values for a given Q^2 as can be seen from Figure 6.2. Note that the extracted the cross section does not depend on this parametrization choice. This can be seen from Equation (6.6) where the simulation cross section is the same as used in the simulation to acquire N_{sim}. The form factor parametrization only affects the calculation of structure functions and generalized polarizabilities where a comparison is made between measured cross sections and theoretical calculations. This can be seen in Equation (2.68)), where the Bethe-Hetiler and Born cross section depends on the choice of form factor parametrization. Because of this I used a different renormalization for each form factor parametrization used.

The corrected cross section can now be written as:

$$\left(\frac{\mathrm{d}^5\sigma}{\mathrm{d}\Omega^5}\right)^{\text{i}}_{\text{exp}} = \left(\frac{\mathrm{d}^5\sigma}{\mathrm{d}\Omega^5}\right)_{\text{exp}} \cdot F_{\text{eff}} \cdot F^{\text{i}}_{\text{norm}} \quad , \tag{6.11}$$

where superscript $^{\text{i}}$ stands for the chosen form factor parametrization, F_{eff} is a correction due to the inefficiency of the detectors and $F^{\text{i}}_{\text{norm}}$ is a correction due to the other two effects,

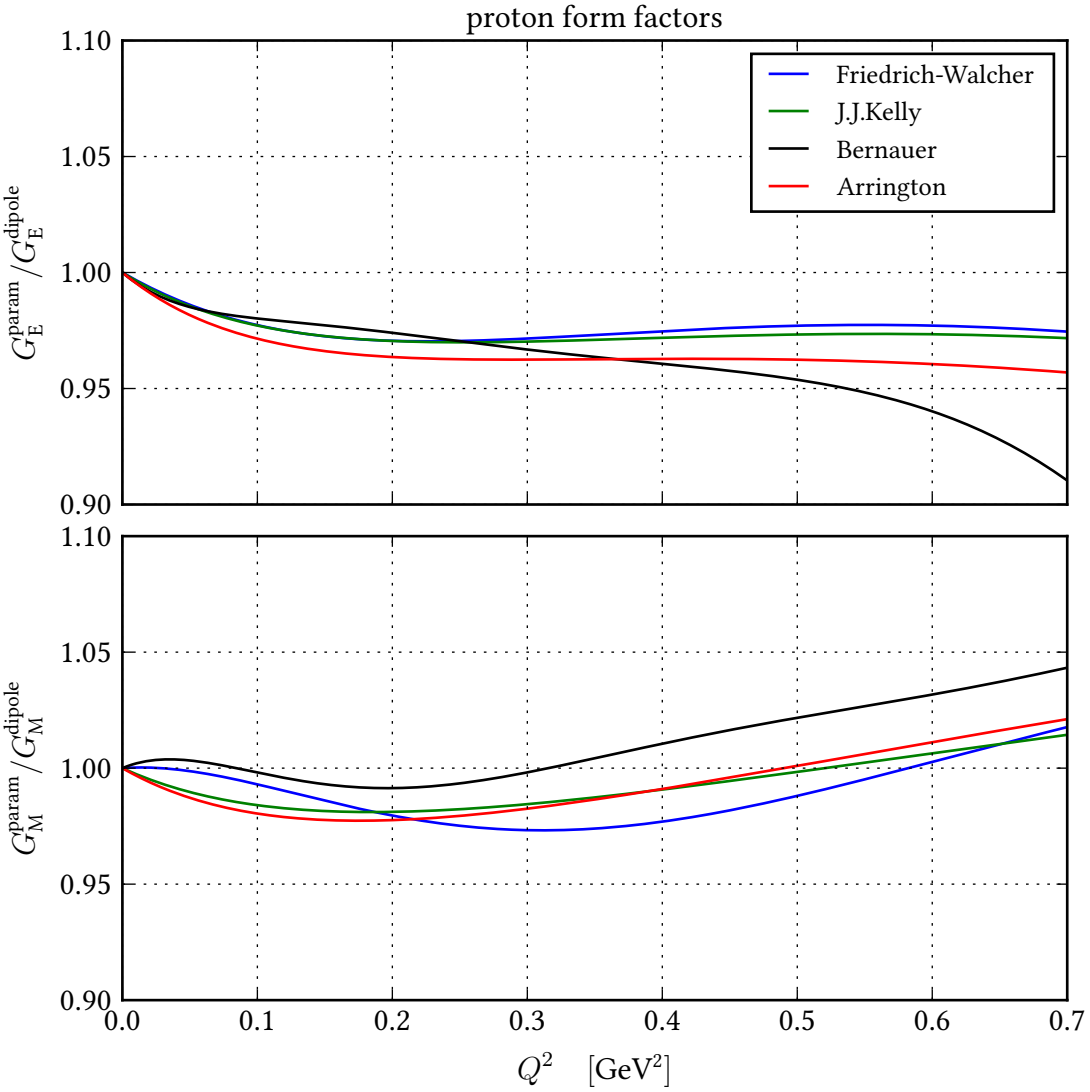

Figure 6.2: Values of proton form factors as given by different parametrizations. Since the BH+B cross section depends on these form factors, and since the extracted polarizabilities depend on the BH+B cross section, one can get different values for polarizabilities with different form factor parametrizations. One can correct for this effect, as described in Section 6.3 [85, 90, 25, 109].

the so-called normalization factor. The same correction factors should also be applied to the uncertainty of the extracted cross section. The F_{eff} is more thoroughly described in Section 5.5.3. To get the normalization factor I used the lowest q'_{cm} bins of the *low* kinematics. At that value of q'_{cm} the polarizability effect is minimal and the cross section can be described by the BH+B part and a small polarizability effect. This means that the extracted cross section with efficiency corrections should match the theoretical BH+B cross section with first order LEX

correction (see Figure 6.3). A χ^2 can be constructed as:

$$\chi^2 = \sum_j \left[\frac{\left(\frac{\mathrm{d}^5\sigma}{\mathrm{d}\Omega^5}\right)^{\mathrm{j}}_{\mathrm{exp}} \cdot F_{\mathrm{eff}} \cdot F^{\mathrm{i}}_{\mathrm{norm}} - \left(\frac{\mathrm{d}^5\sigma}{\mathrm{d}\Omega^5}\right)^{\mathrm{j}}_{\mathrm{LEX}}}{\delta\left(\frac{\mathrm{d}^5\sigma}{\mathrm{d}\Omega^5}\right)_{\mathrm{exp}} \cdot F_{\mathrm{eff}} \cdot F^{\mathrm{i}}_{\mathrm{norm}}} \right]^2 . \tag{6.12}$$

The optimal value $F^{\mathrm{i0}}_{\mathrm{norm}}$ can be found by minimizing the above χ^2 value. I did this by scanning $F^{\mathrm{i}}_{\mathrm{norm}}$ step-by-step and computing the χ^2 at each step. At the end I fitted the values with a parabola to get the minimum (see Figure 6.4).

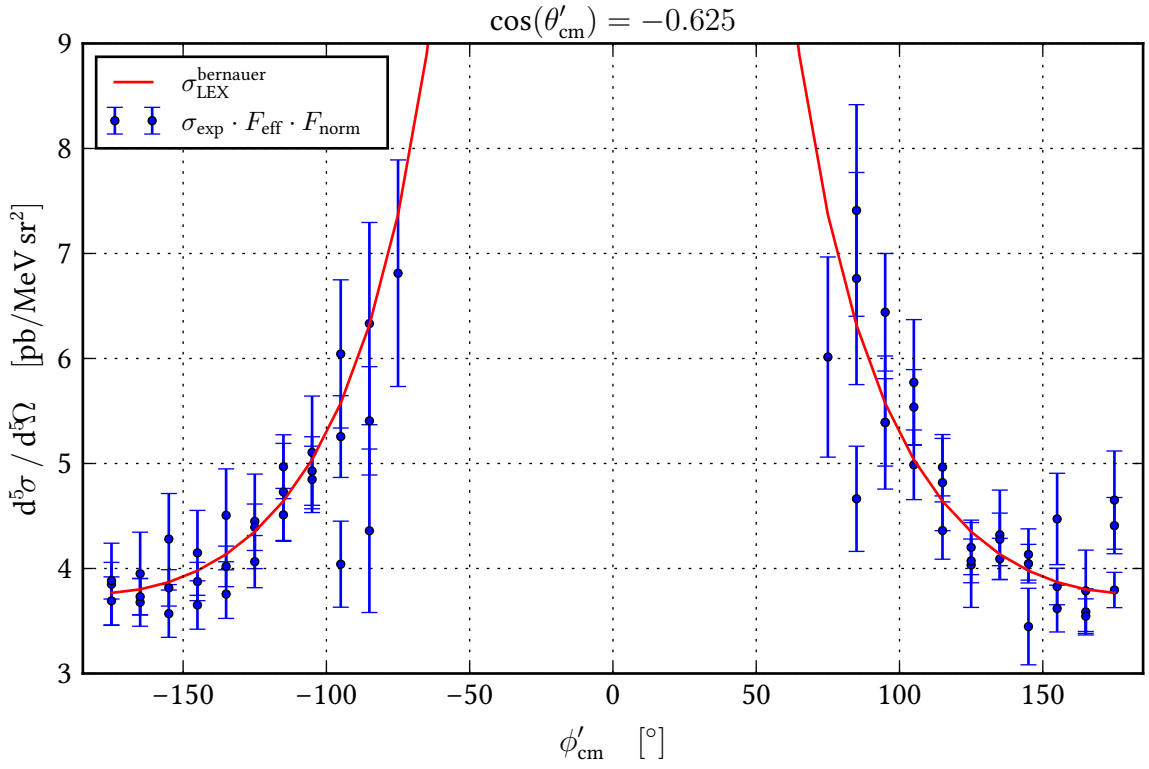

Figure 6.3: Comparison of normalized cross sections extracted from lowest q'_{cm} bin of *low* kinematics and the theoretical BH+B cross section with first order LEX corrections. The Bernauer form factor parametrization [25] was used in the calculations. This plot is made for a single value $\cos(\theta'_{\mathrm{cm}}) = -0.625$ and for $F_{\mathrm{norm}} = 0.896$.

6.4 From corrected cross sections to structure functions or LEX analysis

The low energy expansion or LEX tells us that the photon electro-production cross section can be written as a sum of Bethe-Heitler and Born cross section, and a VCS term, plus higher order terms (see Equation (2.68)). The VCS term can be parametrized by two structure functions $(P_{\mathrm{LL}} - P_{\mathrm{TT}}/\epsilon)$ and P_{LT}. Since the Bethe-Heitler and Born cross section can be accurately

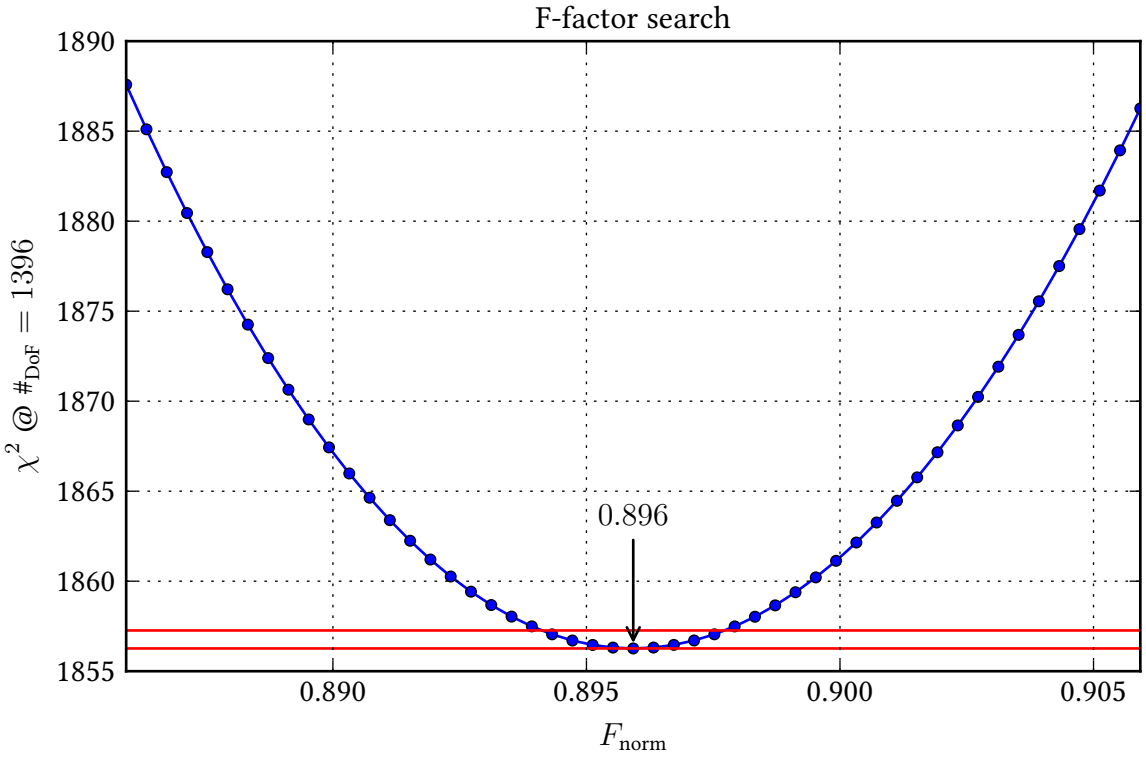

Figure 6.4: The minimum of χ^2 as defined in Equation (6.12) gives the optimal value of the normalization factor $F^{\mathrm{i0}}_{\mathrm{norm}}$. The red lines denote the χ^2_{min} and $\chi^2_{\mathrm{min}} + 1$, where the second one gives a measure of uncertainty on $F^{\mathrm{i0}}_{\mathrm{norm}}$.

calculated, this expansion can be used to extract the two structure functions from measured cross sections.

6.4.1 Bin selection

While the reaction cross section can be calculated for each bin covered by the experiment and the simulation, not all of them can be used for the extraction of structure functions. I used several veto criteria to eliminate bins from further analysis.

Number of counts in bin

There are many bins of the three-dimensional binning that are empty because of kinematical restrictions. These bins clearly can not be used in the analysis, because it is impossible to even determine the experimental cross section. There are also bins that contain only few events. These bins usually lie on the edge of the acceptance. The cross section calculation is possible here, but it is not precise. This is why I decided to not use the bins with too low statistics.

The applied accept criterion was:

$$\delta\left(\frac{\mathrm{d}^5\sigma}{\mathrm{d}\Omega^5}\right)^{i}_{\mathrm{exp}} \Bigg/ \left(\frac{\mathrm{d}^5\sigma}{\mathrm{d}\Omega^5}\right)^{i}_{\mathrm{exp}} < 0.20 \quad .$$

Pion production threshold

The low energy expansion only works below the pion production threshold. The value of this threshold in our experiment is $\mathrm{q}'_{\mathrm{cm}} = 126.5\,\mathrm{MeV}$. This limit coincides with the lower bound of the highest $\mathrm{q}'_{\mathrm{cm}}$ bin of $125\,\mathrm{MeV}$. This means that this whole bin cannot be used in further analysis. I accepted the bins with

$$\mathrm{q}'^{i}_{\mathrm{cm}} < 125\,\mathrm{MeV} \quad .$$

BH+B cross section gradient

The Bethe-Heitler cross section exhibits two distinct peaks where the cross section diverges. Around those peaks the BH+B changes dramatically over a small range in phase space. If some offset in the detector calibration is slightly over- or under-estimated, this could mean big changes in the calculated cross section in this region. This is why I eliminate from further analysis bins in areas with high cross section gradient. The applied accept criterion was:

$$\left(\frac{\mathrm{d}^5\sigma}{\mathrm{d}\Omega^5}\right)^{\mathrm{i}}_{\mathrm{BH+B}} \Bigg/ \left(\frac{\mathrm{d}^5\sigma}{\mathrm{d}\Omega^5}\right)^{\mathrm{j}}_{\mathrm{BH+B}} < 2 \quad ;$$

where i and j represent neighbouring bins.

LEX - DR agreement

The truncation of the low energy expansion to the first order in $\mathrm{q}'_{\mathrm{cm}}$ does not hold everywhere. One way to check where it does not hold is to compare the cross section calculated from LEX to the one calculated from the DR model. The DR model includes all orders in $\mathrm{q}'_{\mathrm{cm}}$, so where the two cross sections disagree, the truncation is not expected to hold. Because of this I only include in the further analysis the bins, where these two calculations agree. The comparison is done by using the GP effects as predicted in the experiment proposal. The applied accept criterion was:

$$\left| \left(\frac{\mathrm{d}^5\sigma}{\mathrm{d}\Omega^5}\right)^{\mathrm{i}}_{\mathrm{LEX}} \Bigg/ \left(\frac{\mathrm{d}^5\sigma}{\mathrm{d}\Omega^5}\right)^{\mathrm{i}}_{\mathrm{DR}} - 1 \right| < 0.02 \quad .$$

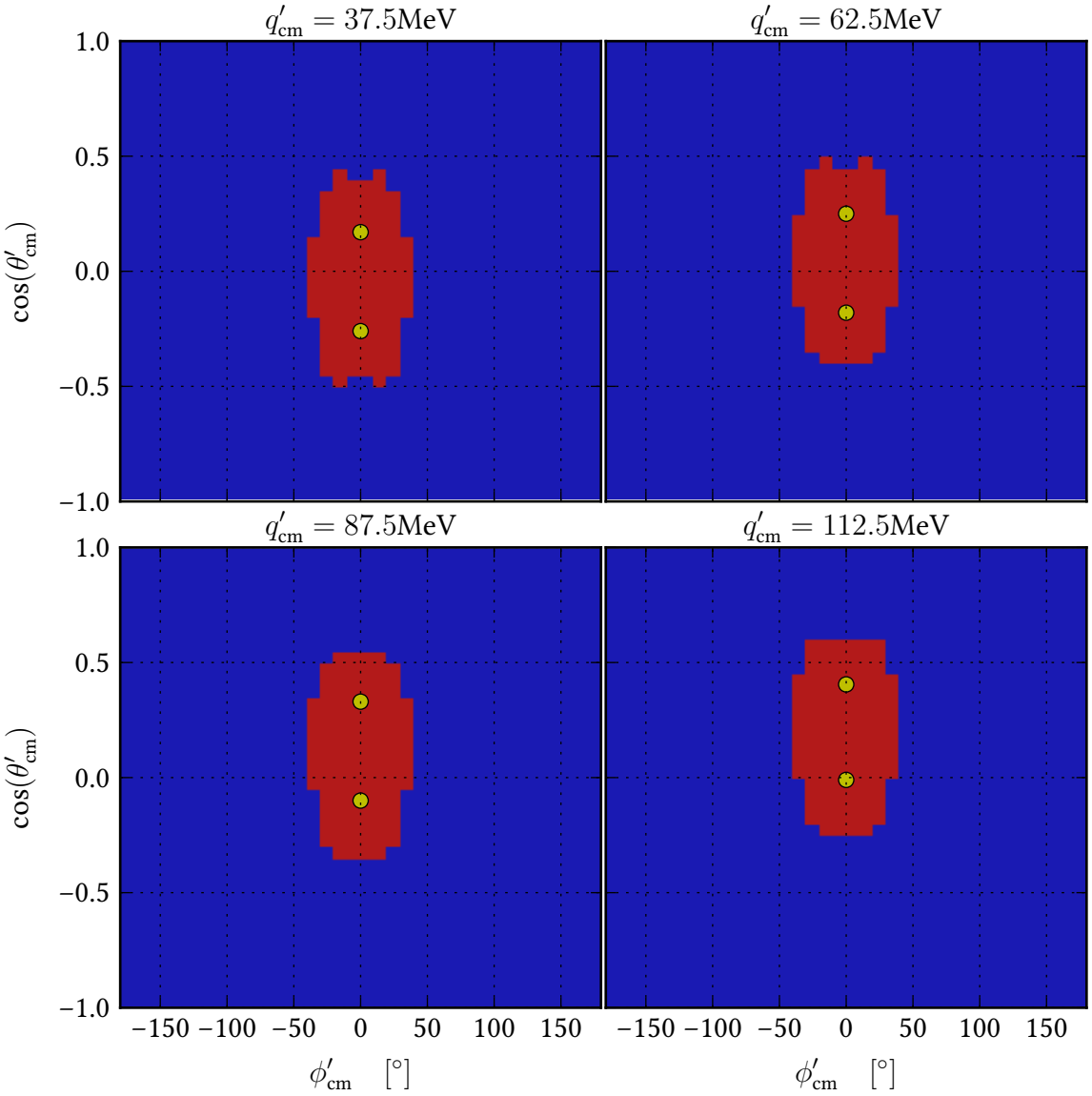

Figure 6.5: The selection mask produced by accept criterion for the BH+B cross section gradient. The bins in blue color pass the selection and the ones in red are removed from further analysis. Each plot shows the mask for different $\mathrm{q}'^{i}_{\mathrm{cm}}$ value. The yellow points show the positions of the Bethe-Heitler peaks.

6.4.2 Ψ_0 fit

The low energy expansion of the photon electro-production cross section from Equation (2.68) can be rewritten as:

$$\Delta M(\mathrm{q}'_{\mathrm{cm}}) = \frac{\left(\frac{\mathrm{d}^5\sigma}{\mathrm{d}\Omega^5}\right)_{ep\gamma} - \left(\frac{\mathrm{d}^5\sigma}{\mathrm{d}\Omega^5}\right)_{\mathrm{BH+B}}}{\Phi\, \mathrm{q}'_{\mathrm{cm}}} = v_{\mathrm{LL}} \cdot (P_{\mathrm{LL}} - P_{\mathrm{TT}}/\epsilon) + v_{\mathrm{LT}} \cdot P_{\mathrm{LT}} + \mathcal{O}(\mathrm{q}'^2_{\mathrm{cm}}) \quad , \quad (6.13)$$

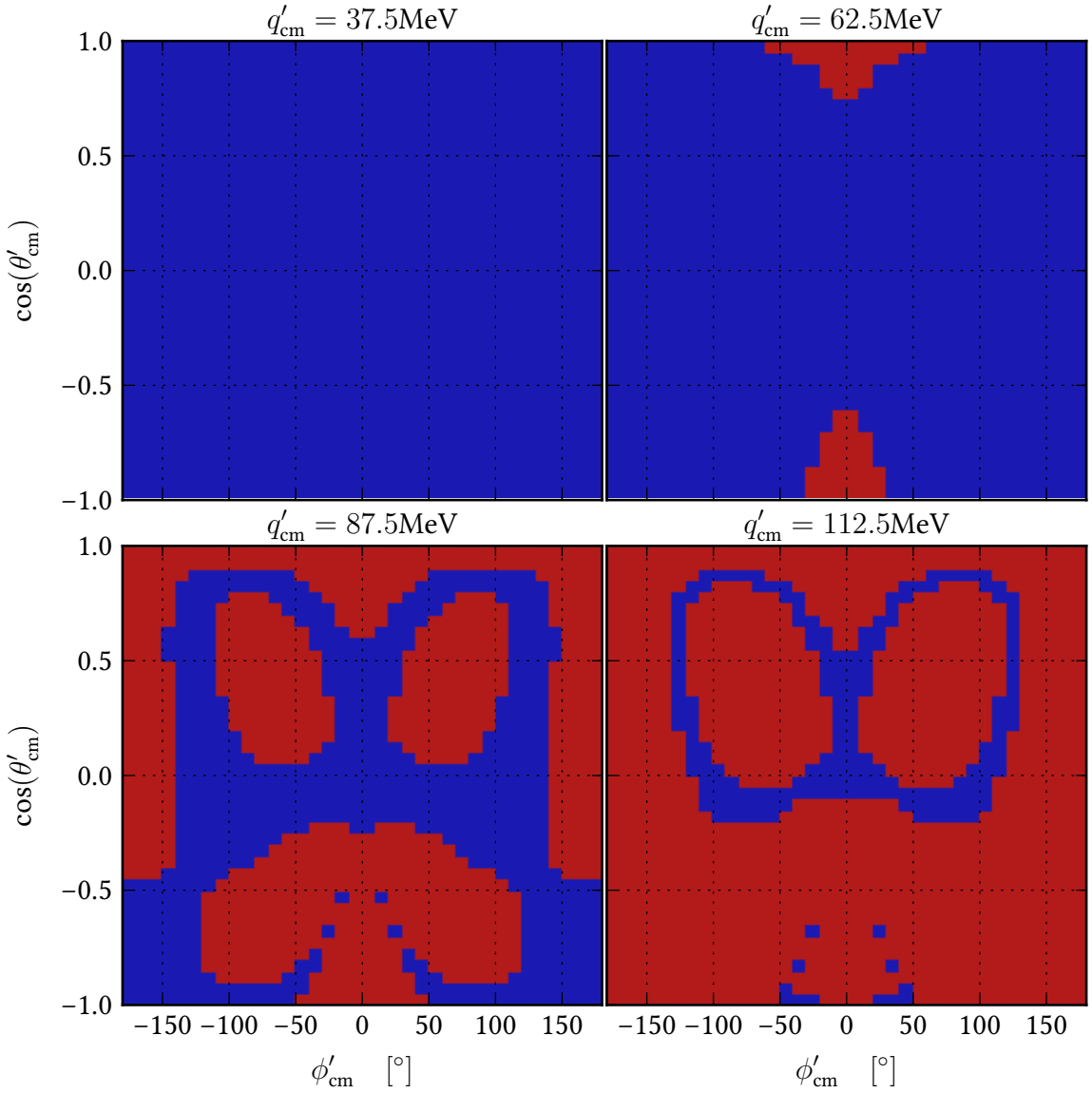

Figure 6.6: The selection mask produced by the accept criterion for LEX-DR agreement. The bins in blue color pass the selection and the ones in red are removed from further analysis. Each plot shows the mask for a different $\mathrm{q}'^{i}_{\mathrm{cm}}$ value.

where the newly defined ΔM depends on the difference of the photon electro-production cross section and the BH+B cross section. From here another quantity can be defined as:

$$\Psi_0 = \Delta M(\mathrm{q}'_{\mathrm{cm}} \to 0) = v_{\mathrm{LL}} \cdot (P_{\mathrm{LL}} - P_{\mathrm{TT}}/\epsilon) + v_{\mathrm{LT}} \cdot P_{\mathrm{LT}} \quad . \tag{6.14}$$

These two quantities can be used to study the $\mathrm{q}'_{\mathrm{cm}}$ dependence of the measured cross section. To do this, I calculated the ΔM in each of the remaining bins of the three-dimensional grid by replacing the theoretical photon electro-production cross section in Equation (6.13) by the measured one. Then I made a $\Delta M(\mathrm{q}'_{\mathrm{cm}})$ plot and a Ψ_0 extrapolation for each bin in $(\cos(\theta'_{\mathrm{cm}}), \phi'_{\mathrm{cm}})$ (see Figure 6.7). Since I removed the bins where the LEX truncation to first order in $\mathrm{q}'_{\mathrm{cm}}$ is not expected to hold, the value of ΔM should be constant in each bin. This

means that I could do the Ψ_0 extrapolation by fitting a constant function. By examining the plots, I determined that this was a good approximation.

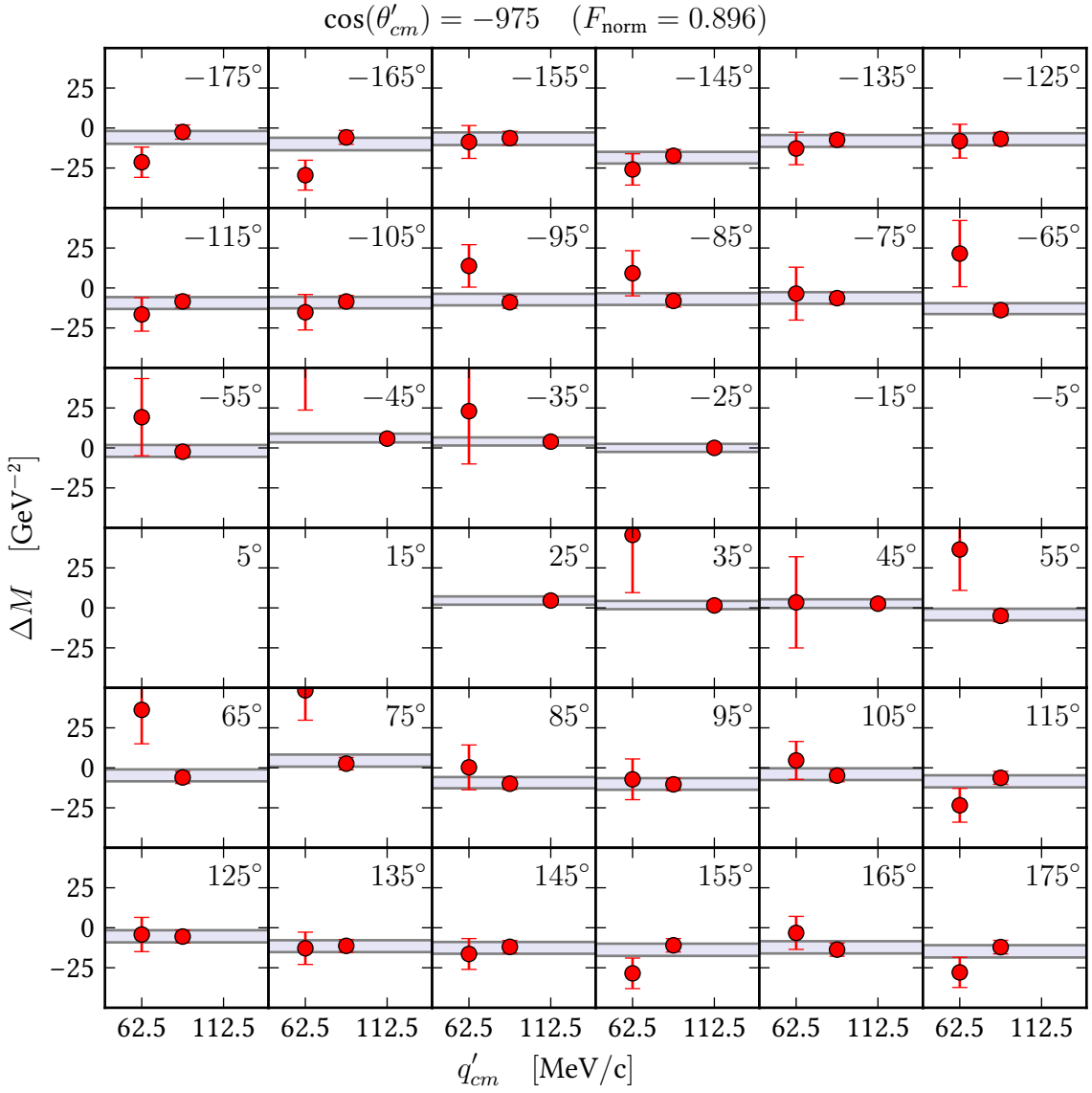

Figure 6.7: An example of the Ψ_0 fit for a bin in $\cos(\theta'_{\text{cm}})$ and all corresponding ϕ'_{cm} bins. The points show the value of ΔM and the shaded band represents the uncertainty of extrapolation to $q'_{\text{cm}} = 0$ by a constant function.

6.4.3 Extraction of structure functions

The definition of Ψ_0 in Equation (6.14) presents a nice way for the extraction of structure functions as a two-parameter linear fit. After the Ψ_0 is calculated in each two-dimensional $(\cos(\theta'_{\text{cm}}), \phi'_{\text{cm}})$ bin, the structure functions can easily be obtained by either a direct two parameter fit, or by a on-grid-minimization procedure. But, since in fitting the Ψ_0 term I assumed that ΔM has no q'_{cm} dependence, the fit can also be done directly, without Ψ_0 fit. Here

a value of ΔM for each three-dimensional $(q'_{cm}, \cos(\theta'_{cm}), \phi'_{cm})$ bin can be used in a structure function fit.

These two ways are equivalent, because they both rely on the same assumption of ΔM behaviour. Both methods produce the same result, but the reduced χ^2 value may not be the same, because of intermediate fitting and reduction in number of degrees of freedom involved in the first method.

To plot the fit results, Equation (6.14) can be rewritten as:

$$\frac{\Psi_0}{v_{LT}} = (P_{LL} - P_{TT}/\epsilon) \cdot \frac{v_{LL}}{v_{LT}} + P_{LT} \quad . \tag{6.15}$$

This can be plotted as a linear function with the first structure function being the slope and the second being the intercept (see Figure 6.8). One could also choose to divide by v_{LL} and reverse the meaning of structure functions. These kinds of plots are useful as they can serve as a good diagnostics tool to check whether there are any problems in some parts of the fit.

6.5 From corrected cross sections to generalized polarizabilities or DR analysis

6.5.1 Bin selection

Similar to the LEX analysis, not all bins covered by the experiment and simulation can be used for DR analysis. But since the DR model is expected to be valid over a larger phase space than LEX, there are fewer constraints on bin selection. In the end I used only two accept criteria: the number of counts in bin

$$\delta\left(\frac{d^5\sigma}{d\Omega^5}\right)^i_{exp} \Big/ \left(\frac{d^5\sigma}{d\Omega^5}\right)^i_{exp} < 0.20$$

and the BH+B cross section gradient

$$\left(\frac{d^5\sigma}{d\Omega^5}\right)^i_{BH+B} \Big/ \left(\frac{d^5\sigma}{d\Omega^5}\right)^j_{BH+B} < 5$$

where i and j represent neighbouring bins. The rationale behind these two criteria is the same as described in Section 6.4.1.

6.5.2 On-grid-minimization

The DR extraction of polarizabilities is based on the on-grid-minimization technique, similarly as shown already for the LEX analysis in Figure 6.9. There are two choices for the grid

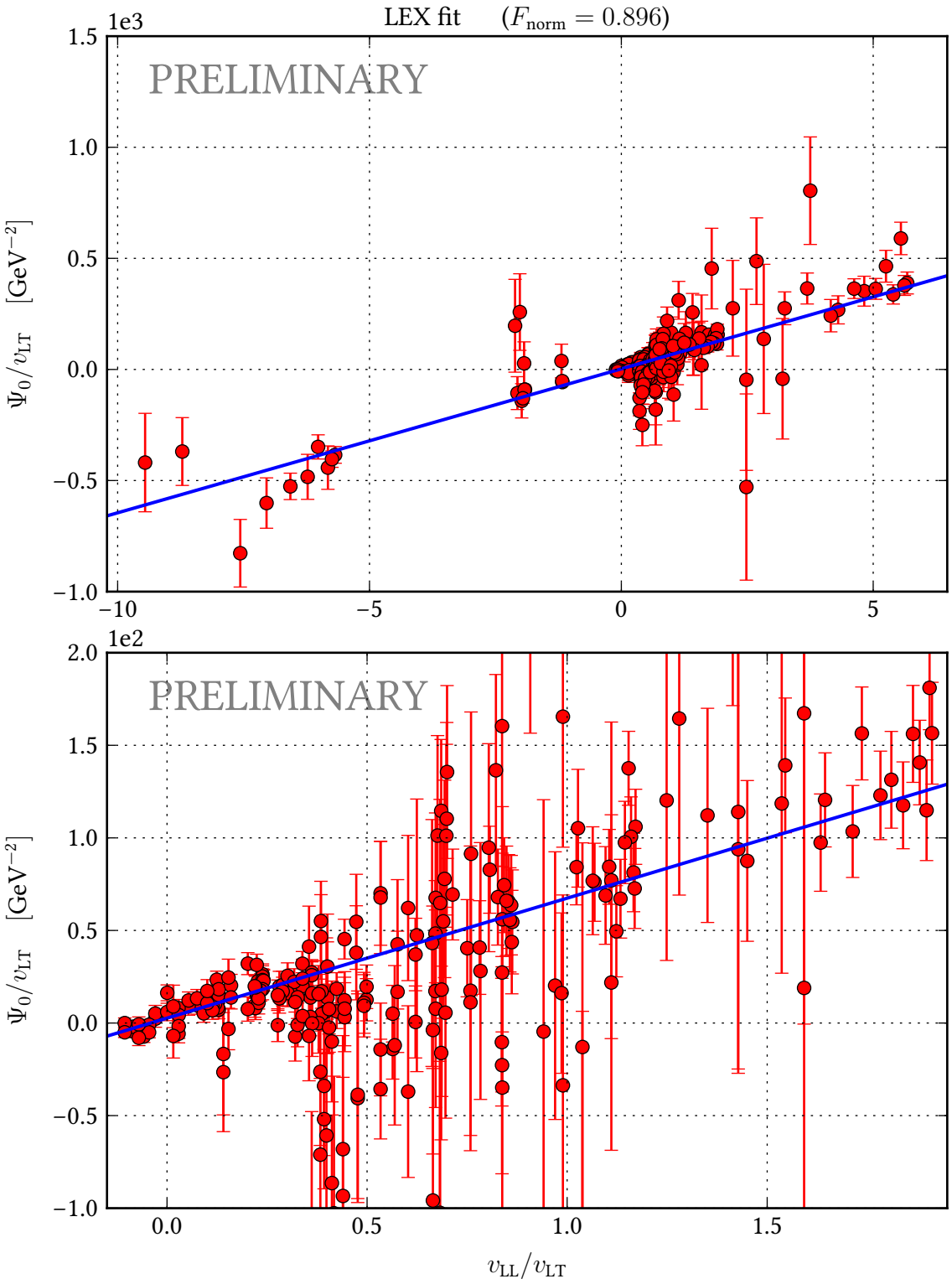

Figure 6.8: The structure function fit to the ΔM as defined in Equation (6.15). The top panel shows the full range in $v_{\text{LL}}/v_{\text{LT}}$ and the bottom panel is zoomed in to the dense part of the fit. The $P_{\text{LL}} - P_{\text{TT}}/\epsilon$ is represented as a slope of the fit and the P_{LT} is the intercept at $v_{\text{LL}}/v_{\text{LT}} = 0$.

variables; two GPs α_{E} and β_{M} or their DR parameters Λ_α and Λ_β. I chose to make the grid in GPs since it has two advantages. The values of GPs are bounded so the grid can cover the whole phase space, whereas the DR parameters are unbounded. The second advantage is that the minimization of χ^2 in the GPs' grid produces a paraboloidal shape, while it does not for grid in the DR parameters.

The goal is to calculate the cross section on each grid point with that pair of α_{E} and β_{M} for each bin in the kinematical binning $(\mathrm{q}'_{\mathrm{cm}}, \cos(\theta'_{\mathrm{cm}}), \phi'_{\mathrm{cm}})$ and then compare this with the experimental cross section by forming a χ^2. But the DR corrections to BH+B cross section can not be calculated on the fly by kinematical factors as in the LEX analysis, I had to pre-calculate all the cross sections. For this I used the `VCS-DR` code [105]. As it turns out, the DR calculations are quite slow and this limited the size of the grid I could pre-calculate. I decided on a 21×21 grid in α_{E} and β_{M} ($\times 969$ for kinematical bins!) and the calculations took nearly two days on my PC with six threads running in parallel. This turned out to be the most CPU intensive part of my analysis.

The grid size limits the precision of the extracted polarizabilities and the 21×21 grid is too coarse. Taking a single kinematical bin, the cross section changes smoothly by varying the α_{E} and β_{M}. This allowed me to refine the grid by making a bivariate spline interpolation of the calculated cross sections on the $(\alpha_{\mathrm{E}}, \beta_{\mathrm{M}})$ grid for each kinematical bin. The final grid size I used was 81×81 which offers sufficient extraction precision.

I compared these interpolated cross sections to the experimental values by calculating a χ^2 on each grid point:

$$\chi^2(\alpha_i, \beta_j) = \sum_k \left[\frac{\left(\frac{\mathrm{d}^5\sigma}{\mathrm{d}\Omega^5}\right)^k_{\mathrm{exp}} - \left(\frac{\mathrm{d}^5\sigma}{\mathrm{d}\Omega^5}\right)^k_{\mathrm{DR}}(\alpha_i, \beta_j)}{\delta\left(\frac{\mathrm{d}^5\sigma}{\mathrm{d}\Omega^5}\right)^k_{\mathrm{exp}}} \right]^2 , \tag{6.16}$$

where indices i and j denote the grid point in α_{E} and β_{M}, and k runs over all kinematical bins. The optimal values of α_{E} and β_{M} are given by α_i and β_j for which the χ^2 value is minimal. The uncertainty of the extraction is estimated from the contour at $\chi^2_{\mathrm{min}} + 1$. The distance from the minimum to the extreme value of the contour at $\chi^2_{\mathrm{min}} + 1$ along the α_{E} and β_{M} give the 1σ uncertainty for the extracted values of α_{E} and β_{M}, respectively.

The precision of the extraction is limited by the interpolated grid size. To make it better, one could increase the density of the interpolation points and make a minimization on finer grid. I decided on another approach. I took the grid points around the minimum and fitted them with a paraboloid (see Appendix B.3 for details). This allowed me to get a precise position of the χ^2 minimum and of the contour at $\chi^2_{\mathrm{min}} + 1$.

See Figure 6.10 for the result of this procedure.

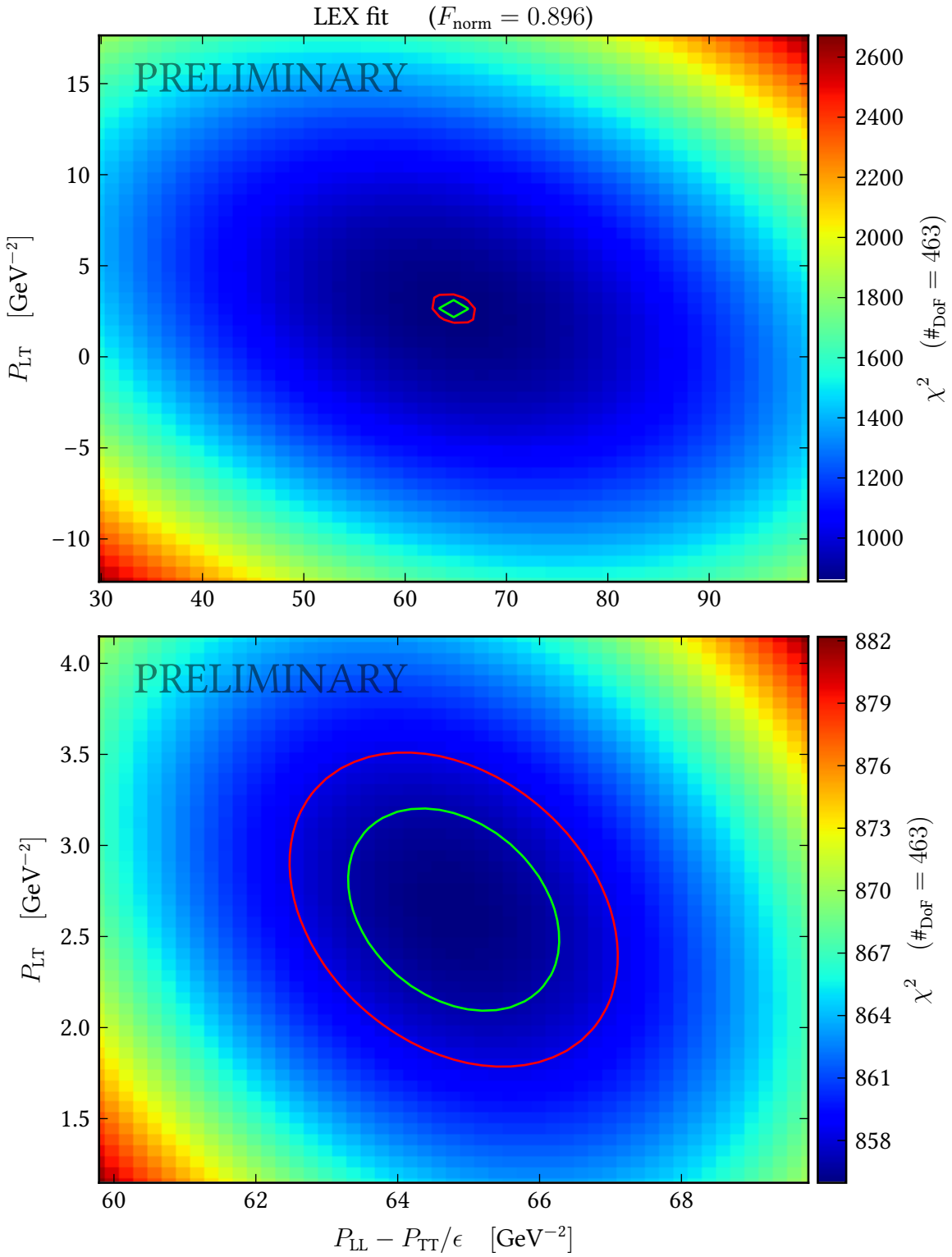

Figure 6.9: The structure function extraction by utilizing the on-grid-minimization technique. Here a grid is made which covers a range in both structure functions. Then on each grid point a ΔM is calculated for each bin in the three-dimensional $(q'_{\text{cm}}, \cos(\theta'_{\text{cm}}), \phi'_{\text{cm}})$ binning and a χ^2 is calculated by comparing calculated ΔMs to measured ones. The most probable values for structure functions lie at the minimum of χ^2 and the contours at $\chi^2_{\text{min}} + 1$ (in green) and $\chi^2_{\text{min}} + 2.41$ (in red) represent the uncertainty of the fit.

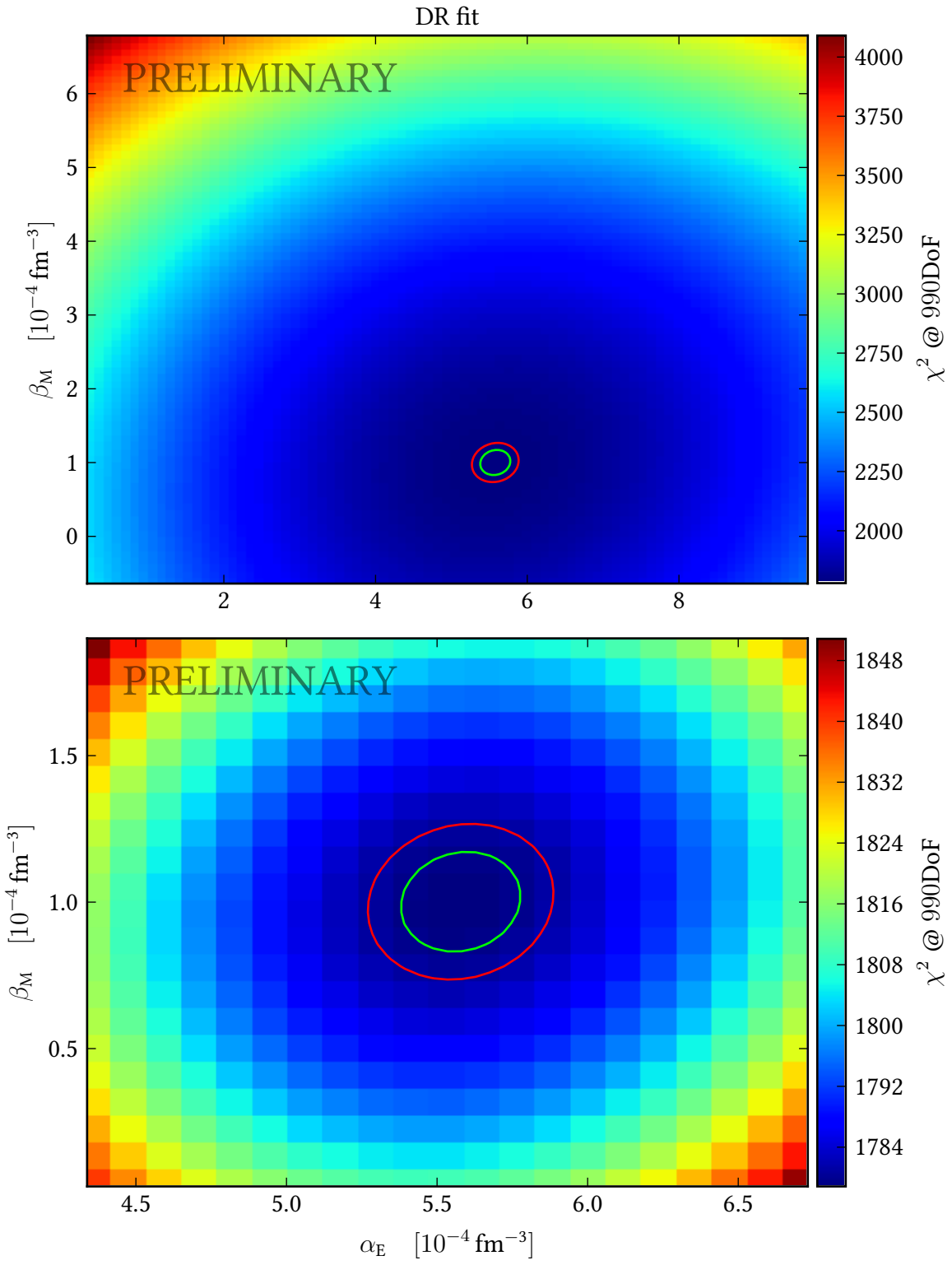

Figure 6.10: The extraction of generalized polarizabilities α_E and β_M by the on-grid-minimization technique as described in Section 6.5.2. The best estimate for GPs are the values at minimal χ^2. The green and red contours represent the contours at $\chi^2_{\mathrm{min}} + 1$ and $\chi^2_{\mathrm{min}} + 2.41$, respectively. This minimization was done for $F_{\mathrm{norm}} = 1$, Bernauer parametrization of form factors and combined settings *q2_01_inp* and *q2_01_oop*.

Chapter 7

Results and discussion

7.1 Normalization factor

The extracted values of structure functions and generalized polarizabilities strongly depend on overall normalization of the measured cross sections. This was the reason for the introduction of the normalization factor F_{norm} in Section 6.3. The expected relative magnitude of this correction is of the order of 4%, but the current extracted value (as shown in Table 7.1) is 0.896 (for Bernauer's FF parametrization), a more than 10% correction. I am still trying to understand the origin of the discrepancy.

Table 7.1: Normalization factors for different proton's form factors parametrizations.

FF parametrization	F_{norm}
Bernauer [25]	0.896 ± 0.002
Kelly [90]	0.885 ± 0.002
Friedrich-Walcher [85]	0.889 ± 0.002

The effect of the normalization factor on the extracted structure functions is shown in Figure 7.1. The extracted values of the structure functions move significantly by including the normalization factor. Current DR predictions favor the values obtained without the normalization factor. This is best seen in the case of P_{LT}, which changes sign by introducing the F_{norm}, where as all current world data predicts a negative value. Translating this into generalized polarizability β_{M} would yield a negative value. This would mean the diamagnetic contribution to the polarizability is bigger than the paramagnetic contribution.

The second effect of the normalization factor can be seen by comparing the extracted values for different form factor parametrizations. Since the normalization factor is determined separately for each parametrization it should compensate for the effect that the differences

in form factors induce in the cross section calculations. Figure 7.1 (top) indeed shows that the extracted values of the polarizabilities for three different form factor parametrizations are within the statistical uncertainties, while they are further apart in Figure 7.1 (bottom), where the same value of normalization factor is considered for all parametrizations.

7.2 LEX results

Table 7.2: Structure functions as obtained from LEX fit for different proton's form factors parametrizations. The quoted uncertainties are statistical and systematical, respectively.

FF parametrization	F_{norm}	$P_{\text{LL}} - P_{\text{TT}}/\epsilon$ $[\text{GeV}^{-2}]$	P_{LT} $[\text{GeV}^{-2}]$	χ^2 (276 NDoF)
Bernauer	0.896	$64.8 \pm 1.5 \pm 8.5$	$2.65 \pm 0.56 \pm 3.21$	452
Kelly	0.885	$63.6 \pm 1.5 \pm 8.5$	$2.37 \pm 0.55 \pm 3.21$	452
Friedrich-Walcher	0.889	$64.2 \pm 1.5 \pm 8.5$	$2.38 \pm 0.55 \pm 3.21$	452
Bernauer	1	$35.2 \pm 1.7 \pm 8.5$	$-8.47 \pm 0.62 \pm 3.21$	467
Kelly	1	$31.0 \pm 1.7 \pm 8.5$	$-9.89 \pm 0.62 \pm 3.21$	473
Friedrich-Walcher	1	$32.6 \pm 1.7 \pm 8.5$	$-9.47 \pm 0.62 \pm 3.21$	472

The results for structure functions as obtained from LEX fit to the joined data for settings *q2_01_inp* and *q2_01_oop* are shown in Table 7.2. The quoted uncertainties are statistical and systematic, respectively. The systematic uncertainties are estimated by changing the normalization factor for $\pm 3\%$ and comparing the result obtained for central value of F_{norm}. This is the major contribution to the full statistical uncertainty. I compared different contributions in the case of Bernauer form factor parametrization and $F_{\text{norm}} = 1$. The relative change of the $(P_{\text{LL}} - P_{\text{TT}}/\epsilon)$ (and P_{LT}) because of changing the normalization was 24% (38%). A small contribution comes from changing the binning in the $(\theta'_{\text{cm}}, \phi'_{\text{cm}})$. I reanalyzed the data once with a finer grid and once with a coarser grid and estimated the relative change to 3% (1%). A bigger contribution comes from changing the allowed deviation of LEX from the DR cross section (see Section 6.4.1) to 1% and 3%. The relative change observed was 10% (17%). Summing these contributions in squares gave a total systematic uncertainty of 26% (42%). This justifies the estimation of systematic uncertainties by just uncertainty due to the normalization, as given in the Table 7.2.

The two settings cover a different area of the phase space and have a different sensitivity to structure functions. The sensitivity is related to the kinematical factors v_{LL} and v_{LT} in front of the structure functions (see Equation (6.14)). The coverage of each setting is shown in Figure 4.9. The out-of-plane setting is more sensitive to the structure function $(P_{\text{LL}} - P_{\text{TT}}/\epsilon)$ while the in-plane setting is more sensitive to the P_{LT}. This can also be seen in Figure 7.2 that shows the structure functions for settings *q2_01_inp* and *q2_01_oop* separately and combined. Naively we would expect to find the combined value somewhere between the

values of settings analyzed separately, which is not the case here. But what we do see is that the combined point lies within the area bounded by the main axes of the uncertainty ellipses of the in-plane and out-of-plane points. The fact that the three ellipses are so far apart also signifies an additional problem in the extraction.

7.3 DR results

I used the dispersion relations model to directly fit the two generalized polarizabilities α_{E} and β_{M}, as described in Section 6.5.2. Unlike LEX, the DR model can not describe an arbitrarily large polarizability effect. This is why I was unable to extract the polarizabilities in the case of the optimal value for F_{norm} (see Figure 7.3). The minimal value of χ^2 was found to be in the lower right corner, which represents the intrinsic limits of the DR model, while it appears that the true minimum lies beyond this point. However, the plot is consistent with the appropriate LEX values that translate to $\alpha_{\mathrm{E}} = 12.3 \cdot 10^{-4}\,\mathrm{fm}^{-3}$ and $\beta_{\mathrm{M}} = -1.9 \cdot 10^{-4}\,\mathrm{fm}^{-3}$ using the DR model. This finite range of generalized polarizabilities is not an artifact of the `VCS-DR` code I used to calculate the cross sections, but is an inherent property of the model, where the dipole parametrization is used to model the two polarizabilities (see Section 3.1.1).

In the case of $F_{\mathrm{norm}} = 1$, the DR extraction was successful and it yielded the following results:

$$\begin{aligned} \alpha_{\mathrm{E}} &= (5.58 \pm 0.20 \pm 1.75) \cdot 10^{-4}\,\mathrm{fm}^3 \quad , \\ \beta_{\mathrm{M}} &= (1.00 \pm 0.17 \pm 1.31) \cdot 10^{-4}\,\mathrm{fm}^3 \quad , \end{aligned} \tag{7.1}$$

with $\chi^2 = 1779$ at 990 degrees of freedom. The first uncertainty is statistical and the second is systematical, which was obtained by changing the normalization factor for $\pm 3\%$ (see Section 7.2). The comparison with LEX results is shown in Figure 7.4. Both results are consistent, however there is a rather big discrepancy for the P_{LT} structure functions.

7.4 Conclusion and outlook

Current world data hints at an enhancement of the electric polarizability effect around the two MAMI data points [19, 86] at $Q^2 = 0.33\,\mathrm{GeV}^2$. To get a better overview in this region, a new experiment was conducted at MAMI with an aim of measuring the VCS structure functions $(P_{\mathrm{LL}} - P_{\mathrm{TT}}/\epsilon)$ and P_{LT}, or generalized polarizabilities α_{E} and β_{M}, at three new values of Q^2: 0.1, 0.2 and $0.5\,\mathrm{GeV}^2$.

This thesis describes the calibration and analysis procedure I used to extract the VCS structure functions and generalized polarizabilities from the data at $Q^2 = 0.1\,\mathrm{GeV}^2$. Since the polarizabilities are obtained from a cross section measurement, I had to implement a careful calibration procedure and do a precise luminosity calculation to avoid a bias in the results. This is crucial for high-precision cross-section measurements of this type (see, e.g. [110]). In

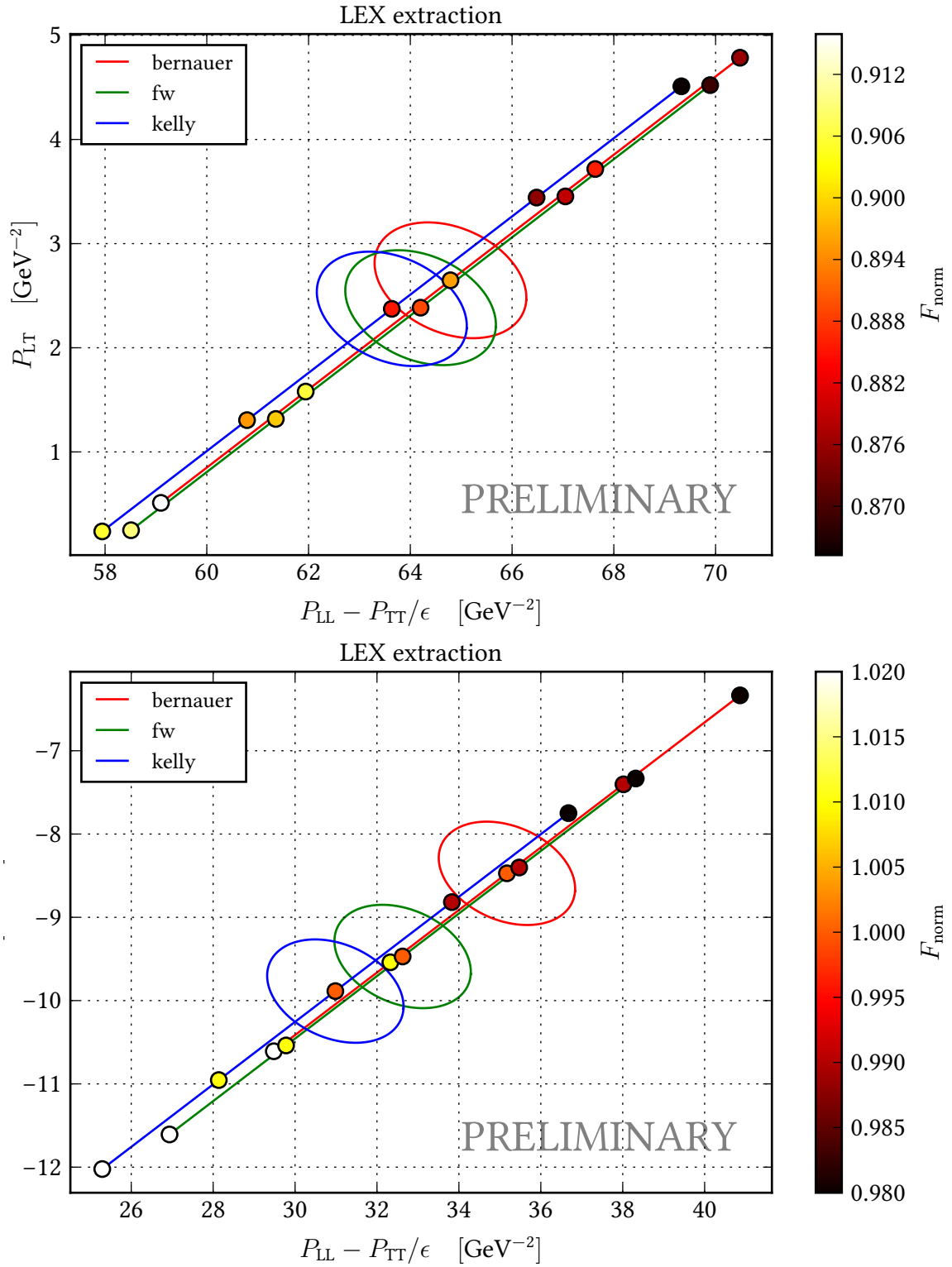

Figure 7.1: The evolution of extracted values of structure functions with F_{norm} for three different parametrizations of proton's form factors. The ellipses show the statistical extraction uncertainty at optimal value of F_{norm} (top) and $F_{\text{norm}} = 1$ (bottom).

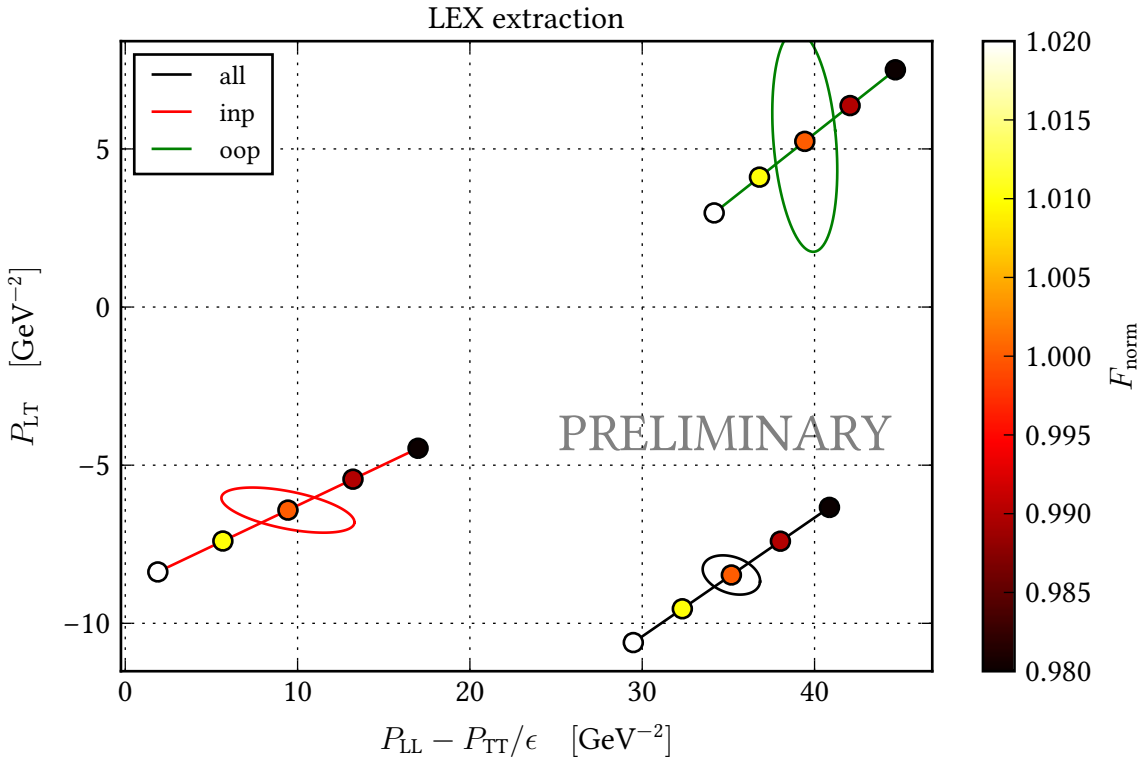

Figure 7.2: Comparison of extracted structure functions for two settings and for Bernauer parametrization of proton's form factors. The *all* data set shows the in-plane and the out-of-plane settings combined.

the calibration phase of this work, we have developed by far the most sophisticated procedure to date to deal with the background processes on the cryogenic target. Due to the high precision requirements, extreme care was needed to properly account for seemingly unimportant offsets in the simulation, which led to a long optimization of the target parameters and reconstruction algorithms. The extraction procedure had to be done in a systematic way to ensure a consistency between LEX and DR analysis.

The comparison of preliminary results, along with preliminary results of separate analysis from Clermont-Ferrand team for the data at $Q^2 = 0.2$ and $0.5\,\mathrm{GeV}^2$, with the current world data is shown in Figure 7.6 for structure functions and in Figure 7.7 for generalized polarizabilities. The statistical precision we achieved in this experiment is much better than in the MIT-Bates [84] and previous two MAMI experiments [19, 86]. This is also the first VCS experiment where a strict consistency of LEX and DR was required during the analysis. Currently the results agree well with previous DR fit and disagree somewhat with the two MAMI points at $Q^2 = 0.33\,\mathrm{GeV}^2$ as they do not support any structure in this region.

Another hint at a change of the proton's structure in this region comes from recent measurements of the proton's form factors [25]. Compared to the standard dipole form, the authors found a strong change of the slope in G_E around $Q^2 = 0.1\,\mathrm{GeV}^2$ and a dip in G_M around $Q^2 = 0.2\,\mathrm{GeV}^2$. This change in the electric and magnetic distributions could also affect the distribution of polarizabilities in the proton. The precise results of this thesis therefore pro-

vide another strict test on the models of nucleon structure in this most relevant region of Q^2.

Further work will be focused on solving the problem of the normalization factor F_{norm} and on bringing closer the results from settings *q2_01_inp*, *q2_01_oop*. An avenue for exploration opened up recently when I compared the histograms from `Simul++` code with histograms from another sophisticated simulation. The comparison showed a very good match for most of the histograms except for ϕ_0 angle of spectrometer A (and few related histograms). Here the `Simul++` code showed less events for larger angles compared to the other simulation. To test the effect of this disagreement I reanalyzed the data but keeping only the range where the two simulations match. The results are promising, since I saw a small increase in F_{norm}, the results from settings *q2_01_inp*, *q2_01_oop* agree better (see Figure 7.5) and the overall reduced χ^2 of the fit is smaller.

Besides the results from our experiment, we are also waiting on the analysis of the VCS experiment in the delta resonance region [72] (also performed at MAMI). Recently there was also a publication of the results of the double polarization VCS experiment [68] (also performed at MAMI). In this double polarization experiment the authors measured the structure function $P_{\text{LT}}^{\perp}$ for the first time, providing a test for the DR model. Further VCS experiments are currently planed at JLab [111].

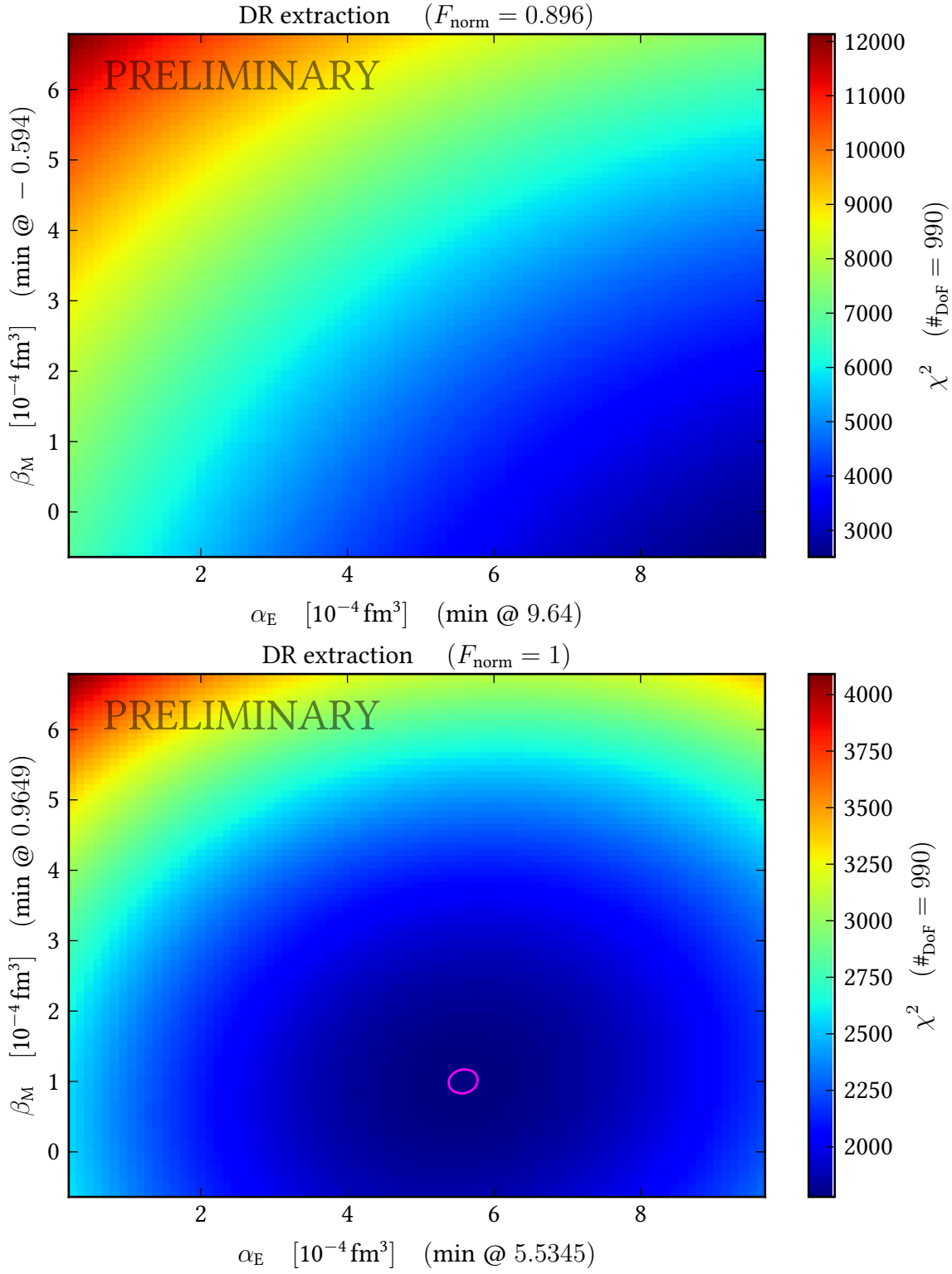

Figure 7.3: DR extraction of generalized polarizabilities for Bernauer parametrization of proton's form factors and different values of normalization factor. The minimum of χ^2 for optimal value of F_{norm} (top) is in the bottom right corner. This means that the DR model has an insufficient range to describe this polarizability effect at this value of F_{norm}.

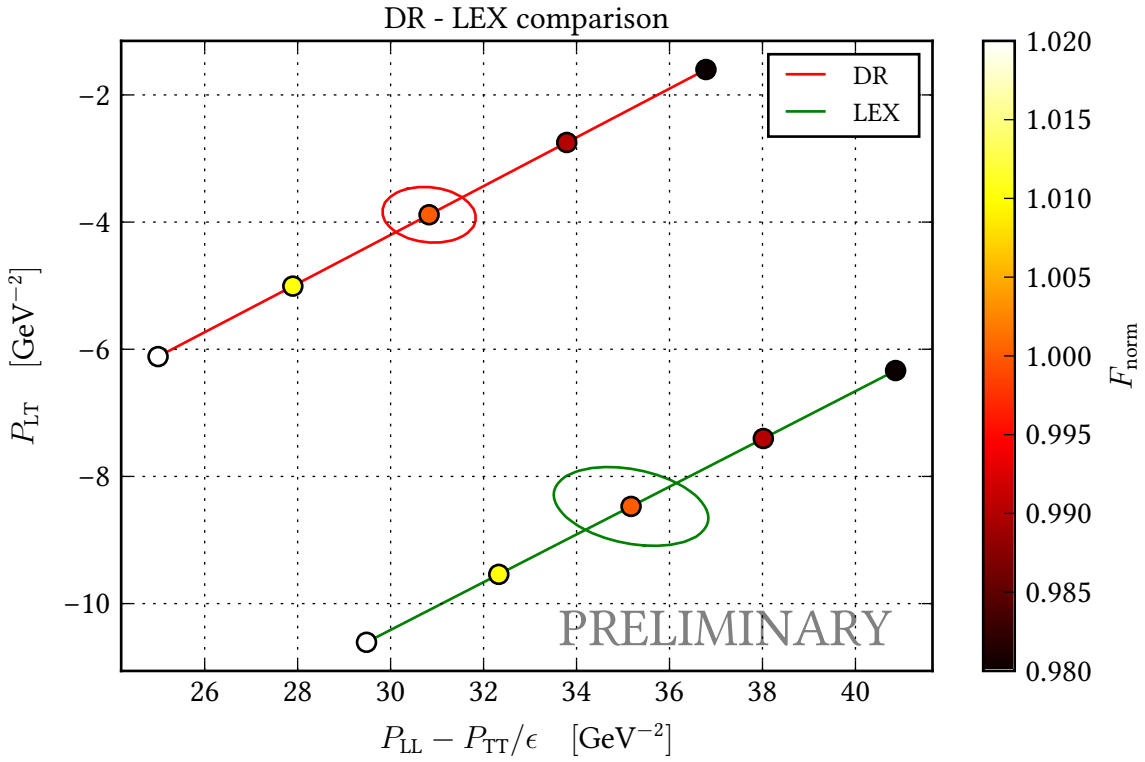

Figure 7.4: Comparison of DR and LEX results for $F_{\text{norm}} = 1$ and Bernauer parametrization of proton's form factors.

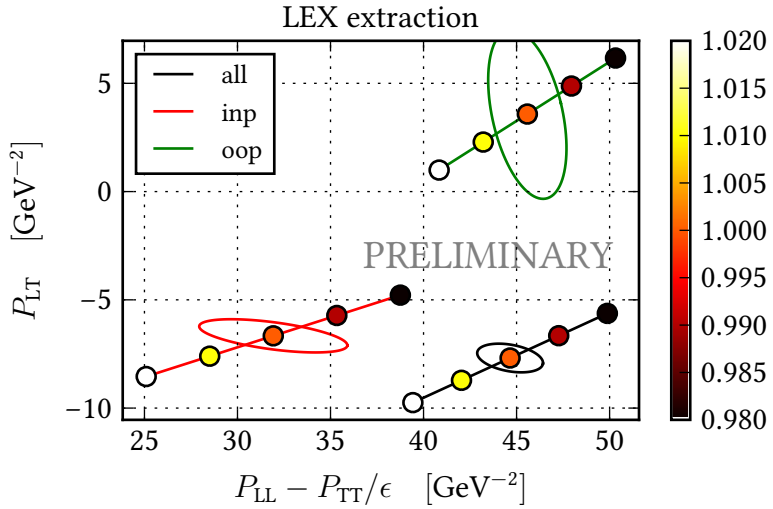

Figure 7.5: Comparison of extracted structure functions for two settings and for Bernauer parametrization of proton's form factors. The *all* data set shows the in-plane and the out-of-plane settings combined. Here an additional cut has been made on θ angle of spectrometer A (see Section 7.4).

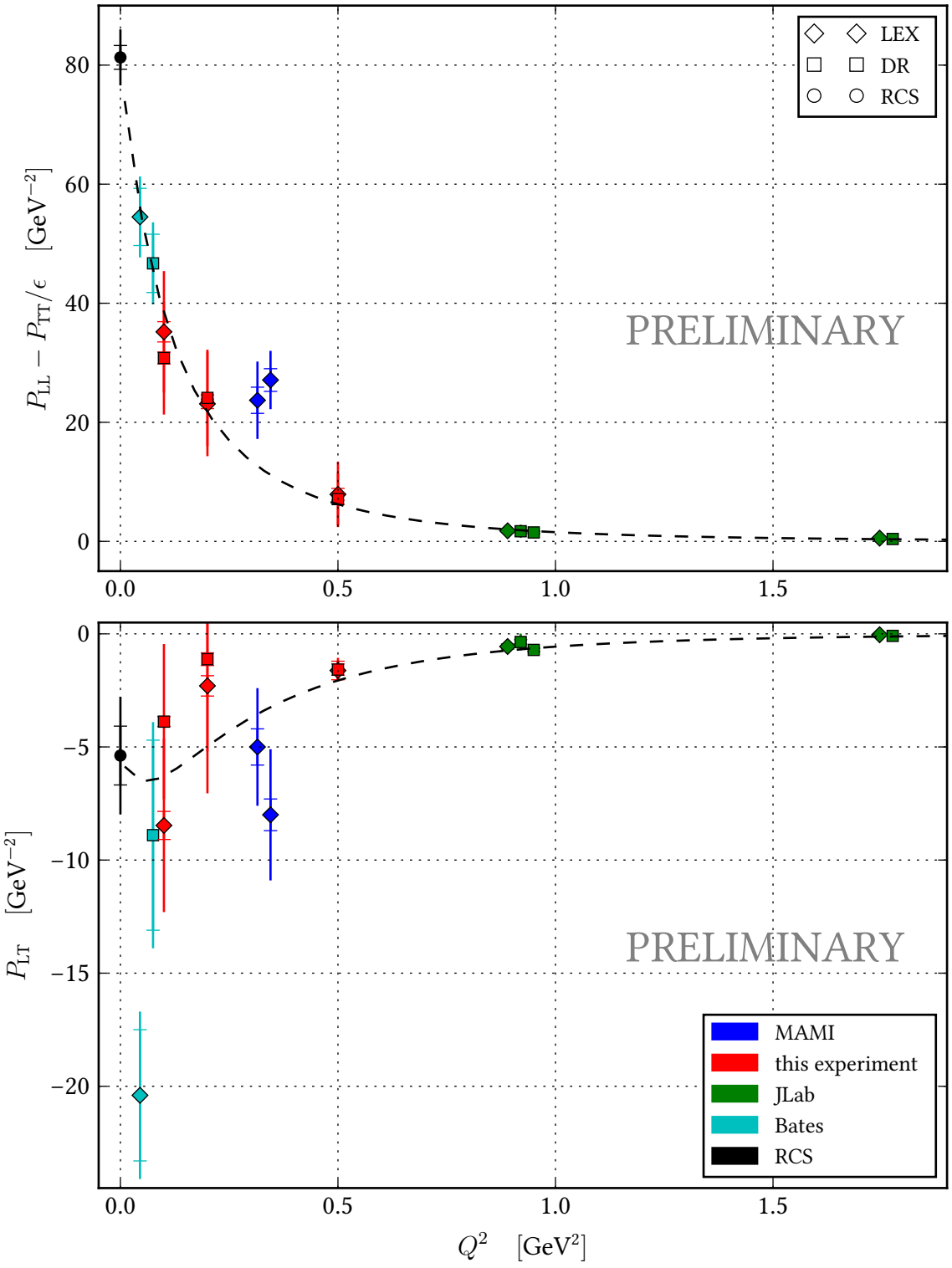

Figure 7.6: World data on VCS structure functions $(P_{LL} - P_{TT}/\epsilon)$ and P_{LT} together with the results from this thesis. The values for other points are taken from [30, 84, 19, 86, 77]. The dashed curve is a DR fit on RCS and JLab points with parameters $\Lambda_\alpha = 0.7$ and $\Lambda_\beta = 0.63$, with $\epsilon = 0.645$ and Friedrich-Walcher form factor parametrization [85]. The points at the same value of Q^2 are offset a bit for clarity.

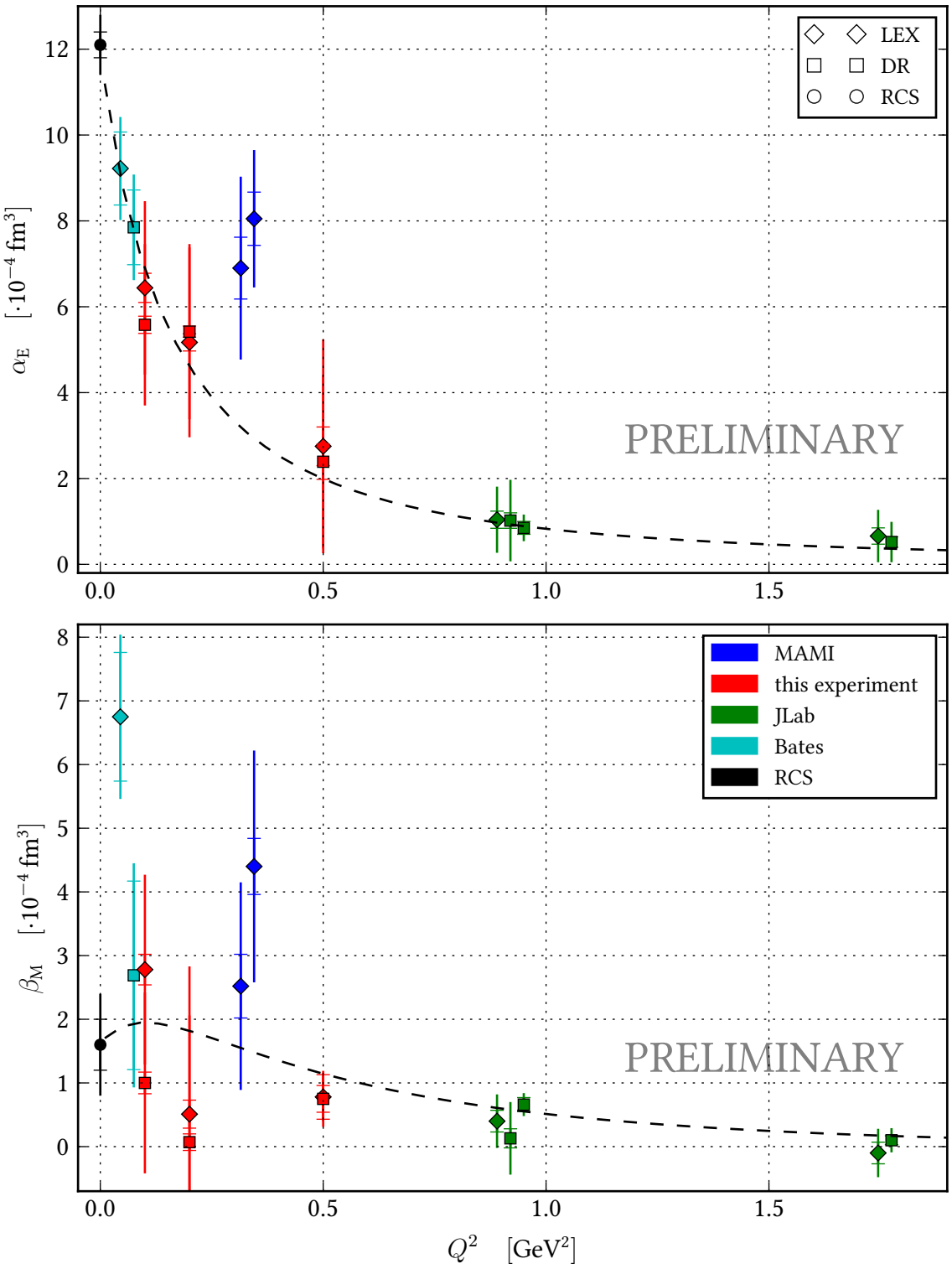

Figure 7.7: World data on VCS generalized polarizabilities α_E and β_M together with the results from this thesis. The values for other points are taken from [30, 84, 19, 86, 77]. Where the values for LEX were not given in terms of polarizabilities, I used a DR model to make a conversion from structure functions. The dashed curve is a DR fit on RCS and JLab points with parameters $\Lambda_\alpha = 0.7$ and $\Lambda_\beta = 0.63$, and with $\epsilon = 0.645$. The points at the same value of Q^2 are offset a bit for clarity.

Bibliography

[1] J. J. Thomson M.A. F.R.S. "XL. Cathode Rays". In: *Philosophical Magazine Series 5* 44.269 (1897), pp. 293–316. DOI: 10.1080/14786449708621070. eprint: http://dx.doi.org/10.1080/14786449708621070. URL: http://dx.doi.org/10.1080/14786449708621070.

[2] E. Rutherford F.R.S. "LXXIX. The scattering of α and β particles by matter and the structure of the atom". In: *Philosophical Magazine Series 6* 21.125 (1911), pp. 669–688. DOI: 10.1080/14786440508637080. eprint: http://dx.doi.org/10.1080/14786440508637080. URL: http://dx.doi.org/10.1080/14786440508637080.

[3] J. Chadwick. "Possible Existence of a Neutron". In: *Nature* 129 (1932), p. 312. DOI: 10.1038/129312a0.

[4] W. Pauli. In: *Structures et propriétés des noyaux atomiques.* (Brussels, 1933). Paris: Gauthier-Villars, 1934.

[5] C. L. Cowan et al. "Detection of the Free Neutrino: a Confirmation". In: *Science* 124.3212 (1956), pp. 103–104. DOI: 10.1126/science.124.3212.103. eprint: http://www.sciencemag.org/content/124/3212/103.full.pdf. URL: http://www.sciencemag.org/content/124/3212/103.short.

[6] M. Gell-Mann. "Symmetries of baryons and mesons". In: *Phys.Rev.* 125 (1962), pp. 1067–1084. DOI: 10.1103/PhysRev.125.1067.

[7] M. Gell-Mann. "A schematic model of baryons and mesons". In: *Physics Letters* 8.3 (1964), pp. 214–215. ISSN: 0031-9163. DOI: http://dx.doi.org/10.1016/S0031-9163(64)92001-3. URL: http://www.sciencedirect.com/science/article/pii/S0031916364920013.

[8] G. Aad et al. "Observation of a new particle in the search for the Standard Model Higgs boson with the {ATLAS} detector at the {LHC}". In: *Physics Letters B* 716.1 (2012), pp. 1–29. ISSN: 0370-2693. DOI: http://dx.doi.org/10.1016/j.physletb.2012.08.020. URL: http://www.sciencedirect.com/science/article/pii/S037026931200857X.

[9] J. Schwinger. "On Quantum-Electrodynamics and the Magnetic Moment of the Electron". In: *Phys. Rev.* 73 (4 Feb. 1948), pp. 416–417. DOI: 10.1103/PhysRev.73.416. URL: http://link.aps.org/doi/10.1103/PhysRev.73.416.

[10] P. Colangelo and A. Khodjamirian. "QCD sum rules, a modern perspective". In: (2000). arXiv: hep-ph/0010175 [hep-ph].

[11] V. Bernard, N. Kaiser, and U. G. Misßner. "Chiral Dynamics In Nucleons And Nuclei". In: *International Journal of Modern Physics E* 04.02 (1995), pp. 193–344. DOI: 10.1142/S0218301395000092. eprint: http://www.worldscientific.com/doi/pdf/10.1142/S0218301395000092. URL: http://www.worldscientific.com/doi/abs/10.1142/S0218301395000092.

[12] H. B. Meyer. "Lattice QCD: A Brief Introduction". In: *Lect.Notes Phys.* 889 (2015), pp. 1–34. DOI: 10.1007/978-3-319-08022-2_1.

[13] C. Hoelbling. "Lattice QCD: concepts, techniques and some results". In: *Acta Phys.Polon.* B45 (2014), pp. 2143–2204. DOI: 10.5506/APhysPolB.45.2143. arXiv: 1410.3403 [hep-lat].

[14] R. Pohl et al. "The size of the proton". In: *Nature* 466 (2010), pp. 213–216. DOI: 10.1038/nature09250.

[15] A. Antognini et al. "Proton Structure from the Measurement of 2S-2P Transition Frequencies of Muonic Hydrogen". In: *Science* 339.6118 (2013), pp. 417–420. DOI: 10.1126/science.1230016. eprint: http://www.sciencemag.org/content/339/6118/417.full.pdf. URL: http://www.sciencemag.org/content/339/6118/417.abstract.

[16] A. W. Thomas, X. G. Wang, and R. D. Young. "Electromagnetic contribution to the proton-neutron mass splitting". In: *Phys. Rev. C* 91 (1 Jan. 2015), p. 015209. DOI: 10.1103/PhysRevC.91.015209. URL: http://link.aps.org/doi/10.1103/PhysRevC.91.015209.

[17] W. N. Cottingham. "The neutron proton mass difference and electron scattering experiments". In: *Annals of Physics* 25.3 (1963), pp. 424–432. ISSN: 0003-4916. DOI: http://dx.doi.org/10.1016/0003-4916(63)90023-X. URL: http://www.sciencedirect.com/science/article/pii/000349166390023X.

[18] J. D. Bjorken, S. D. Drell, and S. C. Frautschi. "Wide-Angle Pair Production and Quantum Electrodynamics at Small Distances". In: *Phys. Rev.* 112 (4 Nov. 1958), pp. 1409–1417. DOI: 10.1103/PhysRev.112.1409. URL: http://link.aps.org/doi/10.1103/PhysRev.112.1409.

[19] J. Roche et al. "First Determination of Generalized Polarizabilities of the Proton by a Virtual Compton Scattering Experiment". In: *Phys. Rev. Lett.* 85 (4 July 2000), pp. 708–711. DOI: 10.1103/PhysRevLett.85.708. URL: http://link.aps.org/doi/10.1103/PhysRevLett.85.708.

[20] B. Povh et al. *Particles and nuclei. An introduction to the physical concepts, 4th edition.* Berlin: Springer-Verlag, 2004. ISBN: 3-540-20168-8.

[21] D. R. Yennie, M. M. Lévy, and D. G. Ravenhall. "Electromagnetic Structure of Nucleons". In: *Rev. Mod. Phys.* 29 (1 Jan. 1957), pp. 144–157. DOI: 10.1103/RevModPhys.29.144. URL: http://link.aps.org/doi/10.1103/RevModPhys.29.144.

[22] F. J. Ernst, R. G. Sachs, and K. C. Wali. "Electromagnetic Form Factors of the Nucleon". In: *Phys. Rev.* 119 (3 Aug. 1960), pp. 1105–1114. DOI: 10.1103/PhysRev.119.1105. URL: http://link.aps.org/doi/10.1103/PhysRev.119.1105.

[23] R. G. Sachs. "High-Energy Behavior of Nucleon Electromagnetic Form Factors". In: *Phys. Rev.* 126 (6 June 1962), pp. 2256–2260. DOI: 10.1103/PhysRev.126.2256. URL: http://link.aps.org/doi/10.1103/PhysRev.126.2256.

[24] M. N. Rosenbluth. "High Energy Elastic Scattering of Electrons on Protons". In: *Phys. Rev.* 79 (4 Aug. 1950), pp. 615–619. DOI: 10.1103/PhysRev.79.615. URL: http://link.aps.org/doi/10.1103/PhysRev.79.615.

[25] J. C. Bernauer et al. "High-Precision Determination of the Electric and Magnetic Form Factors of the Proton". In: *Phys. Rev. Lett.* 105 (24 Dec. 2010), p. 242001. DOI: 10.1103/PhysRevLett.105.242001. URL: http://link.aps.org/doi/10.1103/PhysRevLett.105.242001.

[26] J. C. Bernauer. "Measurement of the elastic electron-proton cross section and separation of the electric and magnetic form factor in the Q^2 range from 0.004 to 1 $(\mathrm{GeV/c})^2$". PhD. Johannes Gutenberg-Universität Mainz, 2010.

[27] A. H. Compton. "A Quantum Theory of the Scattering of X-rays by Light Elements". In: *Phys. Rev.* 21 (5 May 1923), pp. 483–502. DOI: 10.1103/PhysRev.21.483. URL: http://link.aps.org/doi/10.1103/PhysRev.21.483.

[28] F. E. Low. "Scattering of Light of Very Low Frequency by Systems of Spin ½". In: *Phys. Rev.* 96 (5 Dec. 1954), pp. 1428–1432. DOI: 10.1103/PhysRev.96.1428. URL: http://link.aps.org/doi/10.1103/PhysRev.96.1428.

[29] V. A. Petrun'kin. "Scattering of low-energy photons on a system with spin ½". In: *Sov. Phys. JETP* 13 (4 Apr. 1961), pp. 808–812. URL: http://jetp.ac.ru/cgi-bin/dn/e_013_04_0808.pdf.

[30] V. Olmos de León et al. "Low-energy Compton scattering and the polarizabilities of the proton". English. In: *The European Physical Journal A - Hadrons and Nuclei* 10.2 (2001), pp. 207–215. ISSN: 1434-6001. DOI: 10.1007/s100500170132. URL: http://dx.doi.org/10.1007/s100500170132.

[31] H. W. Grießhammer et al. "Using Effective Field Theory to analyse low-energy Compton scattering data from protons and light nuclei". In: *Progress in Particle and Nuclear Physics* 67.4 (2012), pp. 841–897. ISSN: 0146-6410. DOI: http://dx.doi.org/10.1016/j.ppnp.2012.04.003. URL: http://www.sciencedirect.com/science/article/pii/S0146641012000750.

[32] D. Drechsel, B. Pasquini, and M. Vanderhaeghen. "Dispersion relations in real and virtual Compton scattering". In: *Physics Reports* 378.2–3 (2003), pp. 99–205. ISSN: 0370-1573. DOI: http://dx.doi.org/10.1016/S0370-1573(02)00636-1. URL: http://www.sciencedirect.com/science/article/pii/S0370157302006361.

[33] O. Klein and Y. Nishina. "Über die Streuung von Strahlung durch freie Elektronen nach der neuen relativistischen Quantendynamik von Dirac". German. In: *Zeitschrift für Physik* 52.11-12 (1929), pp. 853–868. ISSN: 0044-3328. DOI: 10.1007/BF01366453. URL: http://dx.doi.org/10.1007/BF01366453.

[34] A. M. Baldin. "Polarizability of nucleons". In: *Nuclear Physics* 18 (1960), pp. 310–317. ISSN: 0029-5582. DOI: http://dx.doi.org/10.1016/0029-5582(60)90408-9. URL: http://www.sciencedirect.com/science/article/pii/0029558260904089.

[35] S. B. Gerasimov. "A Sum rule for magnetic moments and the damping of the nucleon magnetic moment in nuclei". In: *Sov.J.Nucl.Phys.* 2 (1966), pp. 430–433.

[36] S. D. Drell and A. C. Hearn. "Exact Sum Rule for Nucleon Magnetic Moments". In: *Phys. Rev. Lett.* 16 (20 May 1966), pp. 908–911. DOI: 10.1103/PhysRevLett.16.908. URL: http://link.aps.org/doi/10.1103/PhysRevLett.16.908.

[37] M. Gell-Mann and M. L. Goldberger. "Scattering of Low-Energy Photons by Particles of Spin ½". In: *Phys. Rev.* 96 (5 Dec. 1954), pp. 1433–1438. DOI: 10.1103/PhysRev.96.1433. URL: http://link.aps.org/doi/10.1103/PhysRev.96.1433.

[38] F. J. Federspiel et al. "Proton Compton effect: A measurement of the electric and magnetic polarizabilities of the proton". In: *Phys. Rev. Lett.* 67 (12 Sept. 1991), pp. 1511–1514. DOI: 10.1103/PhysRevLett.67.1511. URL: http://link.aps.org/doi/10.1103/PhysRevLett.67.1511.

[39] B. E. MacGibbon et al. “Measurement of the electric and magnetic polarizabilities of the proton”. In: *Phys. Rev. C* 52 (4 Oct. 1995), pp. 2097–2109. DOI: 10.1103/PhysRevC.52.2097. URL: http://link.aps.org/doi/10.1103/PhysRevC.52.2097.

[40] A. Zieger et al. “180° Compton scattering by the proton below the pion threshold”. In: *Physics Letters B* 278.1–2 (1992), pp. 34–38. ISSN: 0370-2693. DOI: http://dx.doi.org/10.1016/0370-2693(92)90707-B. URL: http://www.sciencedirect.com/science/article/pii/037026939290707B.

[41] P. A. M. Guichon, G. Q. Liu, and A. W. Thomas. “Virtual compton scattering and generalized polarizabilities of the proton”. In: *Nuclear Physics A* 591.4 (1995), pp. 606–638. ISSN: 0375-9474. DOI: http://dx.doi.org/10.1016/0375-9474(95)00217-O. URL: http://www.sciencedirect.com/science/article/pii/037594749500217O.

[42] P. A. M. Guichon and M. Vanderhaeghen. “Virtual Compton scattering off the nucleon”. In: *Progress in Particle and Nuclear Physics* 41 (1998), pp. 125–190. ISSN: 0146-6410. DOI: http://dx.doi.org/10.1016/S0146-6410(98)00056-8. URL: http://www.sciencedirect.com/science/article/pii/S0146641098000568.

[43] M. Gorchtein. “New approach to low energy virtual Compton scattering and generalized polarizabilities of the nucleon”. In: *Phys. Rev. C* 81 (1 Jan. 2010), p. 015206. DOI: 10.1103/PhysRevC.81.015206. URL: http://link.aps.org/doi/10.1103/PhysRevC.81.015206.

[44] N. Degrande. “Experimental study of the virtual compton scattering process at $Q^2 = 1.0(\,\mathrm{GeV/c})^2$”. PhD thesis. Ghent University, 2001. URL: http://dx.doi.org/1854/370.

[45] G. P. Lepage and S. J. Brodsky. “Exclusive processes in perturbative quantum chromodynamics”. In: *Phys. Rev. D* 22 (9 Nov. 1980), pp. 2157–2198. DOI: 10.1103/PhysRevD.22.2157. URL: http://link.aps.org/doi/10.1103/PhysRevD.22.2157.

[46] F. E. Low. “Bremsstrahlung of Very Low-Energy Quanta in Elementary Particle Collisions”. In: *Phys. Rev.* 110 (4 May 1958), pp. 974–977. DOI: 10.1103/PhysRev.110.974. URL: http://link.aps.org/doi/10.1103/PhysRev.110.974.

[47] A. J. F. Siegert. “Note on the Interaction Between Nuclei and Electromagnetic Radiation”. In: *Phys. Rev.* 52 (8 Oct. 1937), pp. 787–789. DOI: 10.1103/PhysRev.52.787. URL: http://link.aps.org/doi/10.1103/PhysRev.52.787.

[48] D. Drechsel et al. “Generalized polarizabilities and the spin-averaged amplitude in virtual Compton scattering off the nucleon”. In: *Phys. Rev. C* 55 (1 Jan. 1997), pp. 424–430. DOI: 10.1103/PhysRevC.55.424. URL: http://link.aps.org/doi/10.1103/PhysRevC.55.424.

[49] D. Drechsel et al. “Structure analysis of the virtual Compton scattering amplitude at low energies”. In: *Phys. Rev. C* 57 (2 Feb. 1998), pp. 941–952. DOI: 10.1103/PhysRevC.57.941. URL: http://link.aps.org/doi/10.1103/PhysRevC.57.941.

[50] B. Pasquini et al. “Dispersion relation formalism for virtual Compton scattering off the proton”. In: *Eur. Phys. J. A* 11.2 (2001), pp. 185–208. DOI: 10.1007/s100500170084. URL: http://dx.doi.org/10.1007/s100500170084.

[51] D. Drechsel et al. “A unitary isobar model for pion photo- and electroproduction on the proton up to 1 GeV”. In: *Nuclear Physics A* 645.1 (1999). http://kph.uni-mainz.de/MAID/, pp. 145–174. ISSN: 0375-9474. DOI: http://dx.doi.org/10.1016/S0375-9474(98)00572-7. URL: http://www.sciencedirect.com/science/article/pii/S0375947498005727.

[52] M. Vanderhaeghen. “Virtual Compton scattering study below pion production threshold”. In: *Physics Letters B* 368.1–2 (1996), pp. 13–19. ISSN: 0370-2693. DOI: http://dx.

doi.org/10.1016/0370-2693(95)01495-0. URL: http://www.sciencedirect.com/science/article/pii/0370269395014950.

[53] A. Yu. Korchin and O. Scholten. "Nucleon polarizabilities in virtual Compton scattering". In: *Phys. Rev. C* 58 (2 Aug. 1998), pp. 1098–1100. DOI: 10.1103/PhysRevC.58.1098. URL: http://link.aps.org/doi/10.1103/PhysRevC.58.1098.

[54] T. R. Hemmert et al. "Virtual Compton scattering off the nucleon in chiral perturbation theory". In: *Phys. Rev. D* 55 (5 Mar. 1997), pp. 2630–2643. DOI: 10.1103/PhysRevD.55.2630. URL: http://link.aps.org/doi/10.1103/PhysRevD.55.2630.

[55] T. R. Hemmert et al. "Generalized Polarizabilities and the Chiral Structure of the Nucleon". In: *Phys. Rev. Lett.* 79 (1 July 1997), pp. 22–25. DOI: 10.1103/PhysRevLett.79.22. URL: http://link.aps.org/doi/10.1103/PhysRevLett.79.22.

[56] T. R. Hemmert et al. "Generalized polarizabilities of the nucleon in chiral effective theories". In: *Phys. Rev. D* 62 (1 May 2000), p. 014013. DOI: 10.1103/PhysRevD.62.014013. URL: http://link.aps.org/doi/10.1103/PhysRevD.62.014013.

[57] C. W. Kao and M. Vanderhaeghen. "Generalized Spin Polarizabilities of the Nucleon in Heavy-Baryon Chiral Perturbation Theory at Order $\mathcal{O}(p^4)$". In: *Phys. Rev. Lett.* 89 (27 Dec. 2002), p. 272002. DOI: 10.1103/PhysRevLett.89.272002. URL: http://link.aps.org/doi/10.1103/PhysRevLett.89.272002.

[58] C. W. Kao, B. Pasquini, and M. Vanderhaeghen. "New predictions for generalized spin polarizabilities from heavy baryon chiral perturbation theory". In: *Phys. Rev. D* 70 (11 Dec. 2004), p. 114004. DOI: 10.1103/PhysRevD.70.114004. URL: http://link.aps.org/doi/10.1103/PhysRevD.70.114004.

[59] A. Metz and D. Drechsel. "Generalized polarizabilities of the nucleon studied in the linear sigma model". English. In: *Zeitschrift für Physik A Hadrons and Nuclei* 356.3 (1987), pp. 351–357. ISSN: 0939-7922. DOI: 10.1007/s002180050188. URL: http://dx.doi.org/10.1007/s002180050188.

[60] A. Metz and D. Drechsel. "Generalized polarizabilities of the nucleon studied in the linear sigma model (II)". English. In: *Zeitschrift für Physik A Hadrons and Nuclei* 359.2 (1997), pp. 165–172. ISSN: 0939-7922. DOI: 10.1007/s002180050384. URL: http://dx.doi.org/10.1007/s002180050384.

[61] W. Broniowski, M. K. Banerjee, and T. D. Cohen. "Splitting of the neutron and proton electric polarizabilities in a hedgehog model". In: *Physics Letters B* 283.1–2 (1992), pp. 22–26. ISSN: 0370-2693. DOI: http://dx.doi.org/10.1016/0370-2693(92)91419-A. URL: http://www.sciencedirect.com/science/article/pii/037026939291419A.

[62] W. Broniowski and T. D. Cohen. "Response of nucleons to external probes in hedgehog models. I. Electromagnetic polarizabilities". In: *Phys. Rev. D* 47 (1 Jan. 1993), pp. 299–312. DOI: 10.1103/PhysRevD.47.299. URL: http://link.aps.org/doi/10.1103/PhysRevD.47.299.

[63] B. Golli and R. Sraka. "Electromagnetic polarizabilities of the nucleon in a linear sigma model". In: *Physics Letters B* 312.1–2 (1993), pp. 24–29. ISSN: 0370-2693. DOI: http://dx.doi.org/10.1016/0370-2693(93)90480-6. URL: http://www.sciencedirect.com/science/article/pii/0370269393904806.

[64] G. Q. Liu, A. W. Thomas, and P. A. M. Guichon. "Virtual Compton Scattering from the Proton and the Properties of Nucleon Excited States". In: *Austral. J. Phys.* 49 (5 1996), pp. 905–918. DOI: http://dx.doi.org/10.1071/PH960905. URL: http://www.publish.csiro.au/paper/PH960905.

[65] B. Pasquini, S. Scherer, and D. Drechsel. "Generalized polarizabilities of the proton in a constituent quark model revisited". In: *Phys. Rev. C* 63 (2 Jan. 2001), p. 025205. DOI: 10.1103/PhysRevC.63.025205. URL: http://link.aps.org/doi/10.1103/PhysRevC.63.025205.

[66] I. K. Bensafa et al. "Beam-helicity asymmetry in photon and pion electroproduction in the Δ(1232)-resonance region at Q2 = 0.35(GeV/c)2". In: *Eur. Phys. J. A* 32.1 (2007), pp. 69–75. DOI: 10.1140/epja/i2006-10277-3. URL: http://dx.doi.org/10.1140/epja/i2006-10277-3.

[67] I. K. Bensafa. "Mesure de l'asymétrie de spin de faisceau en diffusion Compton virtuelle polarisée sur le proton". PhD thesis. Université Blaise Pascal, 2006.

[68] L. Doria, [...], and J. Beričič et al. (A1 collaboration). "Measurement of the Beam-Recoil Polarization in Low-Energy Virtual Compton Scattering from the Proton". In: (2015). arXiv: 1505.06106 [nucl-ex].

[69] L. Doria. "Polarization Observables in Virtual Compton Scattering". PhD. Johannes Gutenberg-Universität Mainz, 2007.

[70] P. Janssens. "Double-polarized virtual Compton scattering as a probe of the proton structure". PhD. Universiteit Gent, 2007.

[71] H. Merkel (spokesperson). *A study of the Q^2-dependence of the structure functions $P_{\mathrm{LL}} - P_{\mathrm{TT}}/\epsilon$ and P_{LT} and the generalized polarizabilities α_{E} and β_{B} in Virtual Compton Scattering at MAMI*. 9. URL: http://wwwa1.kph.uni-mainz.de/A1/publications/proposals/MAMI-A1-1-09.pdf.

[72] A. Blomberg. PhD. Temple University, in preparation.

[73] G. Höhler et al. "Analysis of electromagnetic nucleon form factors". In: *Nuclear Physics B* 114.3 (1976), pp. 505–534. ISSN: 0550-3213. DOI: http://dx.doi.org/10.1016/0550-3213(76)90449-1. URL: http://www.sciencedirect.com/science/article/pii/0550321376904491.

[74] D. Lhuillier. "Diffusion compton virtuelle a basse energie". PhD. l'université de Caen, 1997. URL: http://inspirehep.net/record/1243019.

[75] J. Roche. "Diffusion Compton virtuelle à MAMI et mesures des polarisabilités du proton". PhD thesis. Université Blaise Pascal, 1998.

[76] J. M. Friedrich. "Messung der Virtuellen Comptonstreuuung an MAMI zur Bestimmung Generalisierter Polarisierbarkeiten des Protons". PhD. Johannes Gutenberg-Universität Mainz, 2000. URL: http://wwwa1.kph.uni-mainz.de/A1/publications/doctor/friedrich.pdf.

[77] G. Laveissière et al. "Measurement of the Generalized Polarizabilities of the Proton in Virtual Compton Scattering at $Q^2 = 0.92$ and 1.76 GeV^2". In: *Phys. Rev. Lett.* 93 (12 Sept. 2004), p. 122001. DOI: 10.1103/PhysRevLett.93.122001. URL: http://link.aps.org/doi/10.1103/PhysRevLett.93.122001.

[78] H. Fonvieille et al. "Virtual Compton scattering and the generalized polarizabilities of the proton at $Q^2 = 0.92$ and 1.76 GeV^2". In: *Phys. Rev. C* 86 (1 July 2012), p. 015210. DOI: 10.1103/PhysRevC.86.015210. URL: http://link.aps.org/doi/10.1103/PhysRevC.86.015210.

[79] E. J. Brash et al. "New empirical fits to the proton electromagnetic form factors". In: *Phys. Rev. C* 65 (5 Apr. 2002), p. 051001. DOI: 10.1103/PhysRevC.65.051001. URL: http://link.aps.org/doi/10.1103/PhysRevC.65.051001.

[80] S. Jaminion. "Diffusion Compton Virtuelle a Jefferson Lab (experience E93050) : resultat preliminaire des sections efficaces (ep $\rightarrow$ epγ) en vue d'extraire des polarisabilites generalisees du proton a Q^2 = 1.9 GeV^2". PhD. Université Blaise Pascal, 2000.

[81] L. Todor. "Virtual Compton scattering in the nucleon resonance region". PhD. Old Dominion University, 2000.

[82] C. Jutier. "Measurement of virtual Compton scattering below pion threshold at invariant four-momentum transfer squared $Q^2 = 1.(GeV/c)^2$". PhD. Old Dominion University and Université Blaise Pascal, 2001. URL: https://tel.archives-ouvertes.fr/tel-00001066/document.

[83] G. Laveissière. "Electroproduction De Photons Et De Pions Sur Le Proton Au Quadrimoment De Transfert Q^2 = 1.0 Gev^2. Mesure Des Sections Efficaces Et Extraction Des Polarisabilites Generalisees". PhD. Université Blaise Pascal, 2001.

[84] P. Bourgeois et al. "Measurements of the Generalized Electric and Magnetic Polarizabilities of the Proton at Low Q^2 Using the Virtual-Compton-Scattering Reaction". In: *Phys. Rev. Lett.* 97 (21 Nov. 2006), p. 212001. DOI: 10.1103/PhysRevLett.97.212001. URL: http://link.aps.org/doi/10.1103/PhysRevLett.97.212001.

[85] J. Friedrich and Th. Walcher. "A coherent interpretation of the form factors of the nucleon in terms of a pion cloud and constituent quarks". In: *Eur. Phys. J. A* 17.4 (2003), pp. 607–623. DOI: 10.1140/epja/i2003-10025-3. URL: http://dx.doi.org/10.1140/epja/i2003-10025-3.

[86] P. Janssens et al. "A new measurement of the structure functions PLL - PTT/ε and PLT in virtual Compton scattering at Q2 = 0.33 (GeV/c)2". In: *Eur. Phys. J. A* 37.1 (2008), pp. 1–8. DOI: 10.1140/epja/i2008-10609-3. URL: http://dx.doi.org/10.1140/epja/i2008-10609-3.

[87] P. Mergell, Ulf-G. Meißner, and D. Drechsel. "Dispersion-theoretical analysis of the nucleon electromagnetic form factors". In: *Nuclear Physics A* 596.3–4 (1996), pp. 367–396. ISSN: 0375-9474. DOI: http://dx.doi.org/10.1016/0375-9474(95)00339-8. URL: http://www.sciencedirect.com/science/article/pii/0375947495003398.

[88] H. W. Hammer and Ulf-G. Meißner. "Updated dispersion-theoretical analysis of the nucleon electromagnetic form factors". In: *Eur. Phys. J. A* 20.3 (2004), pp. 469–473. DOI: 10.1140/epja/i2003-10223-y. URL: http://dx.doi.org/10.1140/epja/i2003-10223-y.

[89] M. A. Belushkin, H. W. Hammer, and Ulf-G. Meißner. "Dispersion analysis of the nucleon form factors including meson continua". In: *Phys. Rev. C* 75 (3 Mar. 2007), p. 035202. DOI: 10.1103/PhysRevC.75.035202. URL: http://link.aps.org/doi/10.1103/PhysRevC.75.035202.

[90] J. J. Kelly. "Simple parametrization of nucleon form factors". In: *Phys. Rev. C* 70 (6 Dec. 2004), p. 068202. DOI: 10.1103/PhysRevC.70.068202. URL: http://link.aps.org/doi/10.1103/PhysRevC.70.068202.

[91] A. Jankowiak. "The Mainz Microtron MAMI – Past and future". In: *The European Physical Journal A - Hadrons and Nuclei* 28.1 (2006), pp. 149–160. ISSN: 1434-6001. DOI: 10.1140/epja/i2006-09-016-3. URL: http://dx.doi.org/10.1140/epja/i2006-09-016-3.

[92] H. J. Kreidel et al. "Sustaining the Reliability of the MAMI-C Accelerator". In: *Proceedings of IPAC2012*. 2012, pp. 4023–4025.

[93] H. Herminghaus et al. "The design of a cascaded 800 MeV normal conducting C.W. race track microtron". In: *Nuclear Instruments and Methods* 138.1 (1976), pp. 1–12. ISSN:

0029-554X. DOI: http://dx.doi.org/10.1016/0029-554X(76)90145-2. URL: http://www.sciencedirect.com/science/article/pii/0029554X76901452.

[94] K. H. Kaiser et al. "The 1.5 GeV harmonic double-sided microtron at Mainz University". In: *Nuclear Instruments and Methods in Physics Research Section A: Accelerators, Spectrometers, Detectors and Associated Equipment* 593.3 (2008), pp. 159–170. ISSN: 0168-9002. DOI: http://dx.doi.org/10.1016/j.nima.2008.05.018. URL: http://www.sciencedirect.com/science/article/pii/S0168900208007341.

[95] K. I. Blomqvist et al. "The three-spectrometer facility at the Mainz microtron MAMI". In: *Nuclear Instruments and Methods in Physics Research Section A: Accelerators, Spectrometers, Detectors and Associated Equipment* 403.2–3 (1998), pp. 263–301. ISSN: 0168-9002. DOI: http://dx.doi.org/10.1016/S0168-9002(97)01133-9. URL: http://www.sciencedirect.com/science/article/pii/S0168900297011339.

[96] Nov. 10, 2014. URL: http://wwwa1.kph.uni-mainz.de/A1/gallery/.

[97] T. Pospischil. "Aufbau und Inbetriebnahme eines Protonen-Polarimeters an MAMI und Messung der Proton-Polarisation in der Reaktion $p(\vec{e}, e'\vec{p})\pi^0$ in paralleler Kinematik im Bereich der $\Delta(1232)$-Resonanz". PhD. Johannes Gutenberg-Universität Mainz, 2000.

[98] P. Merle. "Entwicklung des programmierbaren Koinzidenztriggersystems und Messung von A_Y^0 in der Reaktion ${}^3\vec{H}e(e, e', n)$". PhD. Johannes Gutenberg-Universität Mainz, 2002.

[99] Apr. 24, 2015. URL: https://www.python.org/.

[100] S. van der Walt, S. C. Colbert, and G. Varoquaux. "The NumPy Array: A Structure for Efficient Numerical Computation". In: *Computing in Science Engineering* 13.2 (Mar. 2011), pp. 22–30. ISSN: 1521-9615. DOI: 10.1109/MCSE.2011.37.

[101] E. Jones, T. Oliphant, P. Peterson, et al. *SciPy: Open source scientific tools for Python*. Apr. 24, 2015. URL: http://www.scipy.org/.

[102] J. D. Hunter. "Matplotlib: A 2D Graphics Environment". In: *Computing in Science Engineering* 9.3 (May 2007), pp. 90–95. ISSN: 1521-9615. DOI: 10.1109/MCSE.2007.55.

[103] W. McKinney. "Data Structures for Statistical Computing in Python". In: *Proceedings of the 9th Python in Science Conference*. Ed. by Stéfan van der Walt and Jarrod Millman. 2010, pp. 51–56.

[104] M. Vanderhaeghen (Mainz U.) and L. Van Hoorebeke (Gent U). *VCS-BHB*. Computer code.

[105] B. Pasquini (Pavia U). *VCS-DR*. Computer code.

[106] W. R. Leo. *Techniques for Nuclear and Particle Physics Experiments. A How-to Approach*. New York: Springer-Verlag, 1994. ISBN: 3540572805.

[107] B. S. Schlimme. Private communication. 2015.

[108] P. Janssens et al. "Monte Carlo simulation of virtual Compton scattering below pion threshold". In: *Nuclear Instruments and Methods in Physics Research Section A: Accelerators, Spectrometers, Detectors and Associated Equipment* 566.2 (2006), pp. 675–686. ISSN: 0168-9002. DOI: http://dx.doi.org/10.1016/j.nima.2006.07.039. URL: http://www.sciencedirect.com/science/article/pii/S0168900206013027.

[109] J. Arrington, W. Melnitchouk, and J. A. Tjon. "Global analysis of proton elastic form factor data with two-photon exchange corrections". In: *Phys. Rev. C* 76 (3 Sept. 2007), p. 035205. DOI: 10.1103/PhysRevC.76.035205. URL: http://link.aps.org/doi/10.1103/PhysRevC.76.035205.

[110] H. Merkel, [...], and J Beričič et al (A1 collaboration). "Search at the Mainz Microtron for Light Massive Gauge Bosons Relevant for the Muon g-2 Anomaly". In: *Phys.Rev.Lett.* 112.22 (2014), p. 221802. DOI: 10.1103/PhysRevLett.112.221802. arXiv: 1404.5502 [hep-ex].

[111] M. Paolone and N. Sparveris and A. Camsonne and M. Jones (co-spokepersons). *Measurement of the generalized polarizabilities of the proton in virtual Compton scattering*. Jefferson Lab Proposal to PAC 43. May 2015.

[112] J. E. Gaiser. "Charmonium Spectroscopy From Radiative Decays of the J/ψ and ψ'". PhD. Stanford University, 1982. URL: http://www.slac.stanford.edu/cgi-wrap/getdoc/slac-r-255.pdf.

[113] Feb. 20, 2015. URL: https://en.wikipedia.org/wiki/Crystal_Ball_function.

[114] Feb. 20, 2015. URL: https://root.cern.ch/root/html/tutorials/fit/langaus.C.html.

[115] Feb. 20, 2015. URL: https://github.com/ndawe/landau.

[116] P. Sauer. "Entwicklung, Aufbau und Inbetriebnahme der vertikalen Driftkammern der Drei-Spektrometer-Anlage am Mainzer Mikrotron MAMI und Studium der Reaktion ^{12}C(e,e'p)^{11}B für mittlere und hohe Nukleonenimpulse im Kern". PhD. Johannes Gutenberg-Universität Mainz, 1995.

Appendix A

Additional equations

This appendix holds additional formulas for the Chapter 2.

A.1 Multipoles

Following Section 2.3.5, the non-Born part of the hadronic tensor can be written as a multipole expansion, involving ten multipoles. The low energy behaviour of these multipoles can be described by six generalized polarizabilities, as written below [42]:

$$H_{\mathrm{NB}}^{(11,00)1}(\mathrm{q'}_{\mathrm{cm}},\mathrm{q}_{\mathrm{cm}}) = \mathrm{q'}_{\mathrm{cm}}\left(\sqrt{3}\frac{\mathrm{q}_{\mathrm{cm}}^2}{\tilde{q}_0}P^{(01,01)1}(\mathrm{q}_{\mathrm{cm}}) - \frac{1}{\sqrt{2}}\mathrm{q}_{\mathrm{cm}}^2 P^{(11,02)1}(\mathrm{q}_{\mathrm{cm}})\right) + \mathcal{O}(\mathrm{q'}_{\mathrm{cm}}^2) \quad , \tag{A.1a}$$

$$H_{\mathrm{NB}}^{(11,02)1}(\mathrm{q'}_{\mathrm{cm}},\mathrm{q}_{\mathrm{cm}}) = \mathrm{q'}_{\mathrm{cm}}\mathrm{q}_{\mathrm{cm}}^2 P^{(11,02)1}(\mathrm{q}_{\mathrm{cm}}) + \mathcal{O}(\mathrm{q'}_{\mathrm{cm}}^2) \quad , \tag{A.1b}$$

$$H_{\mathrm{NB}}^{(11,11)S}(\mathrm{q'}_{\mathrm{cm}},\mathrm{q}_{\mathrm{cm}}) = \mathrm{q'}_{\mathrm{cm}}\mathrm{q}_{\mathrm{cm}} P^{(11,11)S}(\mathrm{q}_{\mathrm{cm}}) + \mathcal{O}(\mathrm{q'}_{\mathrm{cm}}^2) \quad , \tag{A.1c}$$

$$H_{\mathrm{NB}}^{(21,01)S}(\mathrm{q'}_{\mathrm{cm}},\mathrm{q}_{\mathrm{cm}}) = -\mathrm{q'}_{\mathrm{cm}}\mathrm{q}_{\mathrm{cm}}\sqrt{2}P^{(01,01)S}(\mathrm{q}_{\mathrm{cm}}) + \mathcal{O}(\mathrm{q'}_{\mathrm{cm}}^2) \quad , \tag{A.1d}$$

$$H_{\mathrm{NB}}^{(21,12)1}(\mathrm{q'}_{\mathrm{cm}},\mathrm{q}_{\mathrm{cm}}) = -\mathrm{q'}_{\mathrm{cm}}\mathrm{q}_{\mathrm{cm}}^2\sqrt{2}P^{(01,12)1}(\mathrm{q}_{\mathrm{cm}}) + \mathcal{O}(\mathrm{q'}_{\mathrm{cm}}^2) \quad , \tag{A.1e}$$

$$H_{\mathrm{NB}}^{(11,22)1}(\mathrm{q'}_{\mathrm{cm}},\mathrm{q}_{\mathrm{cm}}) = \mathrm{q'}_{\mathrm{cm}}\mathrm{q}_{\mathrm{cm}} P^{(11,11)1}(\mathrm{q}_{\mathrm{cm}}) + \mathcal{O}(\mathrm{q'}_{\mathrm{cm}}^2) \quad , \tag{A.1f}$$

$$H_{\mathrm{NB}}^{(21,21)0}(\mathrm{q'}_{\mathrm{cm}},\mathrm{q}_{\mathrm{cm}}) = -\mathrm{q'}_{\mathrm{cm}}\tilde{q}_0 P^{(11,11)0}(\mathrm{q}_{\mathrm{cm}}) + \mathcal{O}(\mathrm{q'}_{\mathrm{cm}}^2) \quad , \tag{A.1g}$$

$$H_{\mathrm{NB}}^{(21,21)1}(\mathrm{q'}_{\mathrm{cm}},\mathrm{q}_{\mathrm{cm}}) = -\mathrm{q'}_{\mathrm{cm}}\left(2\frac{\mathrm{q}_{\mathrm{cm}}^2}{\tilde{q}_0}P^{(11,11)1}(\mathrm{q}_{\mathrm{cm}}) - \sqrt{2}\mathrm{q}_{\mathrm{cm}}^2 P^{(01,12)1}(\mathrm{q}_{\mathrm{cm}})\right) + \mathcal{O}(\mathrm{q'}_{\mathrm{cm}}^2) \quad . \tag{A.1h}$$

A.2 Kinematical factors

Coming from Equation 2.67 to Equation 2.68 I used this relation:

$$\mathcal{M}_0^{\text{pep}} - \mathcal{M}_0^{\text{BH+B}} = v_{\text{LL}} \left(P_{\text{LL}}(\mathrm{q}_{\text{cm}}) - \frac{P_{\text{TT}}}{\epsilon} \right) + v_{\text{LT}} P_{\text{LT}}(\mathrm{q}_{\text{cm}}) \quad . \tag{A.2}$$

The angular dependant functions v_{LL} and v_{LT} are [42]:

$$v_{\text{LL}}(\phi'_{\text{cm}}, \theta'_{\text{cm}}; q_{\text{cm}}, \epsilon) = 2K_2 \epsilon v_1 \quad , \tag{A.3a}$$

$$v_{\text{LT}}(\phi'_{\text{cm}}, \theta'_{\text{cm}}; q_{\text{cm}}, \epsilon) = 2K_2 \left(v_2 - \frac{\tilde{q}_0}{\mathrm{q}_{\text{cm}}} \right) \sqrt{2\epsilon(1+\epsilon)} \quad , \tag{A.3b}$$

with

$$K_2 = e^6 \frac{\mathrm{q}_{\text{cm}}}{\tilde{Q}^2} \frac{2m_{\text{p}}}{1-\epsilon} \sqrt{\frac{2E_q}{E_q + m_{\text{p}}}} \quad , \tag{A.4a}$$

$$E_q = \sqrt{m_{\text{p}}^2 + \mathrm{q}_{\text{cm}}} \quad , \tag{A.4b}$$

$$v_1 = \sin(\theta'_{\text{cm}}) \left(\omega'' \sin(\theta'_{\text{cm}}) - k_{\text{T}} \omega' \cos(\theta'_{\text{cm}}) \cos(\phi'_{\text{cm}}) \right) \quad , \tag{A.4c}$$

$$v_2 = -\left(\omega'' \sin(\theta'_{\text{cm}}) \cos(\phi'_{\text{cm}}) - k_{\text{T}} \omega' \cos(\theta'_{\text{cm}}) \right) \quad , \tag{A.4d}$$

$$v_3 = -\left(\omega'' \sin(\theta'_{\text{cm}}) \cos(\theta'_{\text{cm}}) \cos(\phi'_{\text{cm}}) - k_{\text{T}} \omega' \left(1 - \sin^2(\theta'_{\text{cm}}) \cos^2(\phi'_{\text{cm}}) \right) \right) \quad , \tag{A.4e}$$

$$k_{\text{T}} = \tilde{Q} \sqrt{\frac{\epsilon}{2(1-\epsilon)}} \quad , \tag{A.4f}$$

$$\omega = \left[-\mathrm{q}'_{\text{cm}} \left(\frac{1}{p \cdot q'} + \frac{1}{k \cdot q'} \right) \right]_{\mathrm{q}'_{\text{cm}}=0} \quad , \tag{A.4g}$$

$$\omega' = \left[\mathrm{q}'_{\text{cm}} \left(\frac{1}{k' \cdot q'} + \frac{1}{k \cdot q'} \right) \right]_{\mathrm{q}'_{\text{cm}}=0} \quad , \tag{A.4h}$$

$$\omega'' = \omega \mathrm{q}_{\text{cm}} - \omega' \sqrt{\tilde{k'}^2 - k_{\text{T}}^2} \quad . \tag{A.4i}$$

The factors v_{LL} and v_{LT} are functions of four variables, but in this experiment two of them, $(q_{\text{cm}}, \epsilon)$, were kept constant.

Appendix B

Fitting functions

This appendix describes non standard functions I used for fitting experimental spectra.

B.1 Fitting of target z

The calibration of the Y_{0000} transfer coefficient (see Section 5.6.2) and beam position (see Section 5.6.4) required a precise determination of target center along the beamline. For this I used a nine-parameter model to fit the target spectrum and then calculate the center from two of the fitted parameters.

The target model can be described by the next function:

$$\mathrm{f}_{\text{target}}(z; k, n, A_\mathrm{u}, A_\mathrm{d}, r_\mathrm{A}, \mu_\mathrm{u}, \mu_\mathrm{d}, \sigma_\mathrm{w}, \sigma_\mathrm{i}) = \mathrm{f}_{\text{hydrogen}} + \mathrm{f}_{\text{walls}} \quad , \tag{B.1a}$$

$$\mathrm{f}_{\text{hydrogen}} = \begin{cases} \mathrm{g}(z; A^\mathrm{i}_\mathrm{u}, \mu_\mathrm{u}, \sigma_\mathrm{i}) + \mathrm{g}(z; A^\mathrm{i}_\mathrm{u} \cdot r_\mathrm{A}, \mu_\mathrm{u}, \sigma_\mathrm{w}) & \text{if} \quad z < \mu_\mathrm{u} \\ \mathrm{l}(z; k, n) & \text{if} \quad \mu_\mathrm{u} \leq z \leq \mu_\mathrm{d} \\ \mathrm{g}(z; A^\mathrm{i}_\mathrm{d}, \mu_\mathrm{d}, \sigma_\mathrm{i}) + \mathrm{g}(z; A^\mathrm{i}_\mathrm{d} \cdot r_\mathrm{A}, \mu_\mathrm{d}, \sigma_\mathrm{w}) & \text{if} \quad \mu_\mathrm{d} < z \end{cases} \quad , \tag{B.1b}$$

$$\begin{aligned} \mathrm{f}_{\text{walls}} = {} & \mathrm{g}(z; A_\mathrm{d}, \mu_\mathrm{d}, \sigma_\mathrm{w}) + \mathrm{g}(z; A_\mathrm{d} \cdot r_\mathrm{A}, \mu_\mathrm{d}, \sigma_\mathrm{i}) \\ & + \mathrm{g}(z; A_\mathrm{u}, \mu_\mathrm{u}, \sigma_\mathrm{w}) + \mathrm{g}(z; A_\mathrm{u} \cdot r_\mathrm{A}, \mu_\mathrm{u}, \sigma_\mathrm{i}) \quad , \end{aligned} \tag{B.1c}$$

$$\mathrm{l}(z; k, n) = k \cdot z + n \quad , \tag{B.1d}$$

$$\mathrm{g}(z; A, \mu, \sigma) = A \cdot \exp\left(\frac{(z-\mu)^2}{2\sigma^2}\right) \quad , \tag{B.1e}$$

$$A^\mathrm{i}_{\mathrm{u,d}} = \frac{l(\mu_{\mathrm{u,d}}, k, n)}{1 + r_\mathrm{A}} \quad . \tag{B.1f}$$

The target function is a sum of a hydrogen and wall part. The hydrogen part has a linear function between target walls and a sum of two Gaussians at each end to describe the smearing because of finite resolution. The $A^\mathrm{i}_{\mathrm{u,d}}$ is the height of one of the Gaussians calculated such that the whole function is continuous. The walls are modelled as a sum of two Gaussians that

describe thin walls with deposit on them smeared because of finite resolution. The parameters k and n describe the central part of the hydrogen, $A_{\mathrm{u,d}}$ are heights of one of the wall Gaussians, r_{A} is the ratio between the two Gaussians, $\mu_{\mathrm{u,d}}$ are the positions of target walls and $\sigma_{\mathrm{w,i}}$ are widths of the Gaussians. The subscripts u, d mark the upstream and downstream side. An example of the fit is shown on Figure B.1.

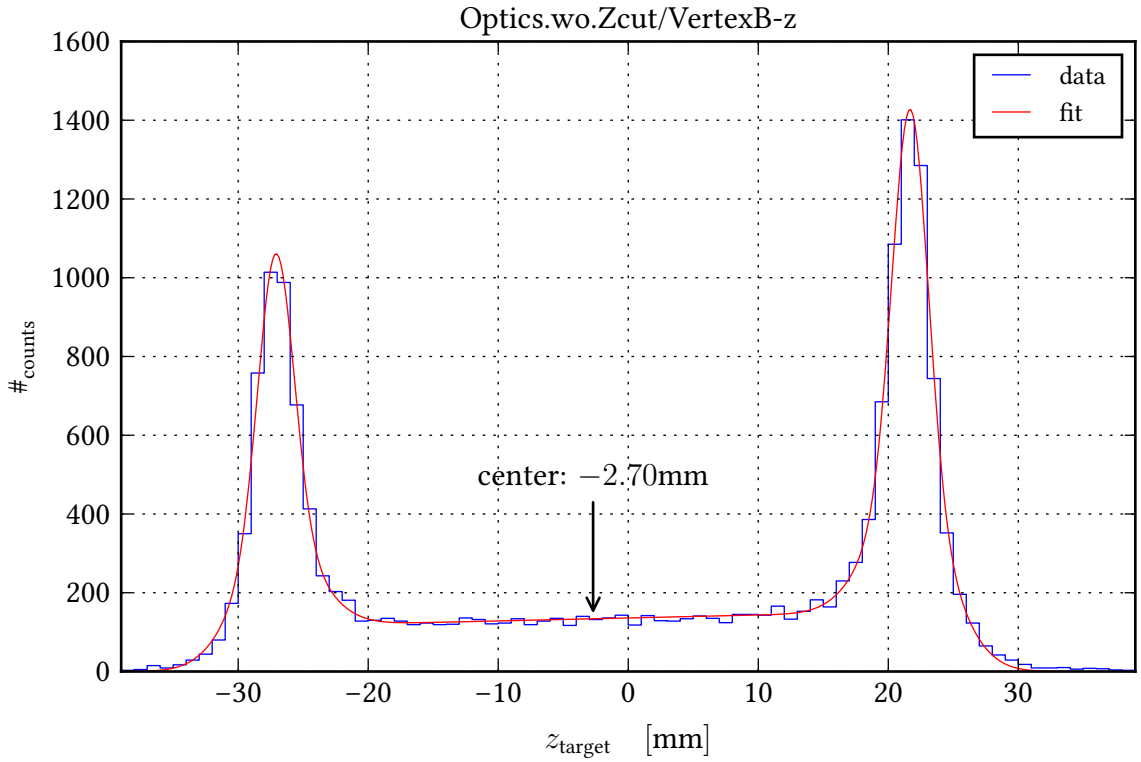

Figure B.1: This plot shows a sample result of a fit described in the Equation B.1 to an experimental spectrum.

The target center is calculated as arithmetic center of both peak positions:

$$z_{\mathrm{target}}^{\mathrm{center}} = \frac{\mu_{\mathrm{d}} + \mu_{\mathrm{u}}}{2} \tag{B.2}$$

B.2 Fitting of VCS missing mass squared peak

Among other parts, the calibration of snow thickness and spectrometer B momentum (see Section 5.12) depend on the width and position of the VCS missing mass squared peak. To get the best results, I used a model to fit the spectra and then determine the width and position from fitted curve. I tried several different models to see which works best. Plots of all models are shown on Figure B.2.

Gaussian function

The first model I tried was a simple Gaussian fit:

$$\text{gauss}(x; A, \mu, \sigma) = \text{g}(x; A, \mu, \sigma), \tag{B.3}$$

with function g defined in Equation B.1e. The problem with this model is that it is symmetric, while the missing mass squared peak is not. So in order to get a good value for peak width and position, it needs to be fitted only on a narrow range around the center of the peak.

Double Gaussian function

The second model was a sum of two Gaussian functions with different centers and widths:

$$\text{gauss\_d}(x; A_1, \mu_1, \sigma_1, A_2, \mu_2, \sigma_2) = \text{g}(x; A_1, \mu_1, \sigma_1) + \text{g}(x; A_2, \mu_2, \sigma_2). \tag{B.4}$$

While this model proved to be a good match for experimental spectrum, it sometimes produced weird results for low statistics spectra or wide peaks.

Asymmetric Gaussian function

This model uses two Gaussian functions with different widths to describe left and right part from the center of the peak:

$$\text{gauss\_d}(x; A, \mu, \sigma_1, \mu, \sigma_2) = \begin{cases} \text{g}(x; A, \mu, \sigma_1) & x \leq \mu \\ \text{g}(x; A, \mu, \sigma_2) & \mu < x \end{cases} \quad . \tag{B.5}$$

It turns out, that this model is not very good.

Mirrored Crystal Ball function

The Crystal Ball function [112, 113] is named after the SLAC Crystal Ball collaboration. It is usually written as a probability density function used to describe lossy processes in high energy physics. To model the missing mass squared peak I needed to change the normalization and mirror the function about the central value, so that it has a Gaussian core and and power-law high-end tail instead of low-end tail:

$$\text{cb\_m}(x; A, \mu, \sigma, n, \alpha) = \begin{cases} \text{g}(x; A, \mu, \sigma) & \frac{x-\mu}{\sigma} \leq \alpha \\ A_\text{f} \cdot \left(B_\text{f} + \frac{x-\mu}{\sigma}\right)^{-n} & \alpha < \frac{x-\mu}{\sigma} \end{cases} \quad , \tag{B.6a}$$

$$A_\text{f} = \left(\frac{\alpha}{n}\right)^n \cdot \exp\left(-\frac{\alpha^2}{2}\right) \quad , \tag{B.6b}$$

$$B_\text{f} = \frac{n}{\alpha} - \alpha \quad . \tag{B.6c}$$

This model work very well across different conditions and this is the one I used in the calibration.

Convoluted Landau and Gaussian function

To describe an energy loss of particles a convolution of Landau and Gauss distributions is sometime used. Since the shape of energy loss and VCS missing mass squared peak spectra are similar, I tried to use it as a model of this peak.

$$\text{langauss}(x; A, \mu, c, \sigma) = (\text{landau}(\mu, c) * \text{g}(A, 0, \sigma))\,(x) \quad . \tag{B.7}$$

I followed the ROOT implementation [114] and used the Landau distribution of [115]. This model gives results very similar to the mirrored Crystal Ball model but is much slower to compute.

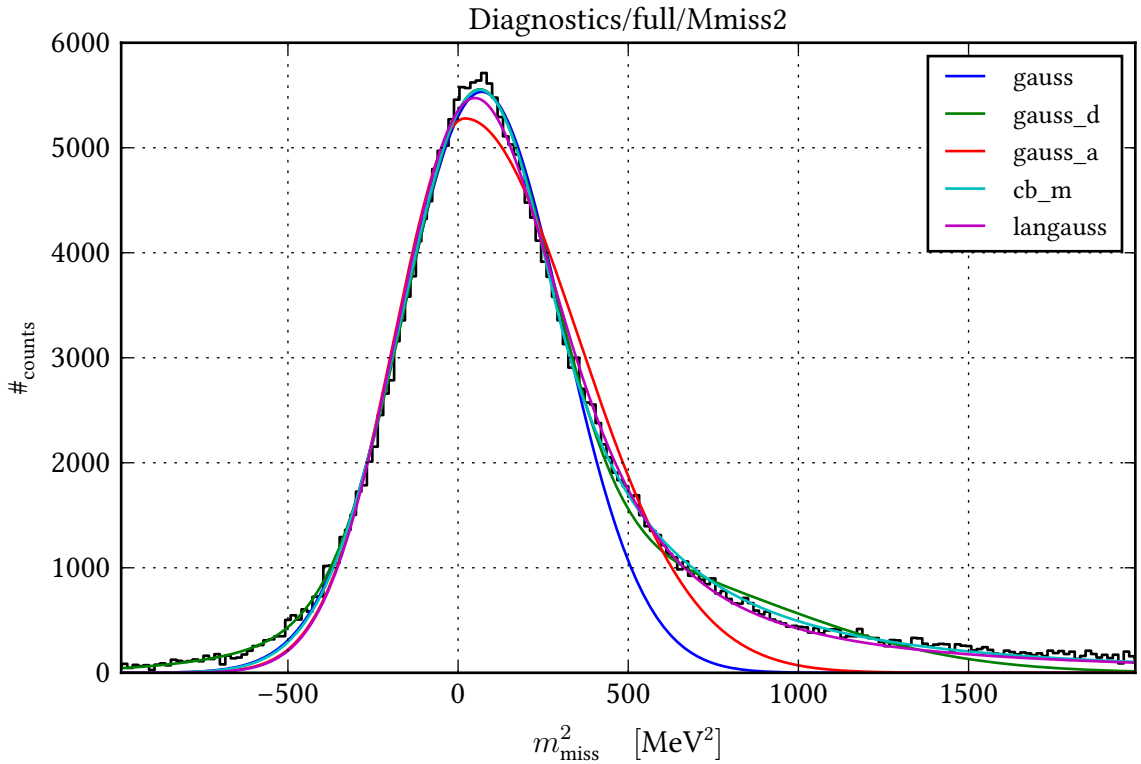

Figure B.2: This plot shows a sample fit of all models from Appendix B.2. to an experimental VCS missing mass squared peak spectrum.

B.3 Fitting of χ^2 grid

The precision in on-grid-minimization is defined by the distance between grid points. The minimum can be found only on grid points, not between them. This is the situation in the

on-grid-minimization of χ^2 in the DR analysis, as described in Section 6.5.2. Increasing the density of the grid helps, but here was also another solution. Since the χ^2 between calculated and experimental cross sections as the function of chosen α_{E} and β_{M} shows paraboloidal dependency, I decided to make a fit near the minimum. The fit function is as follows:

$$\chi^2{}_{\mathrm{fit}}(\alpha_{\mathrm{E}}, \beta_{\mathrm{M}}) = \chi^2_{\mathrm{min}} + a_\alpha \cdot (\alpha_{\mathrm{E}} - \alpha_0)^2 + a_\beta \cdot (\beta_{\mathrm{M}} - \beta_0)^2 + a_{\alpha\beta} \cdot (\alpha_{\mathrm{E}} - \alpha_0)(\beta_{\mathrm{M}} - \beta_0) \quad , \tag{B.8}$$

with six parameters:

- α_0: optimal value for α_{E},
- β_0: optimal value for β_{M},
- χ^2_{min}: minimal value of χ^2,
- a_α: steepness of parabola in α_{E} direction,
- a_β: steepness of parabola in β_{M} direction and
- $a_{\alpha\beta}$: measure of correlation between α_{E} and β_{M}.

This fit does not only increase the precision determined minimum, but also the smoothness of the contours, most importantly the contour at $\chi^2_{\mathrm{min}} + 1$ which measures the uncertainty of the polarizability extraction. An example of this fit is shown on Figure B.3.

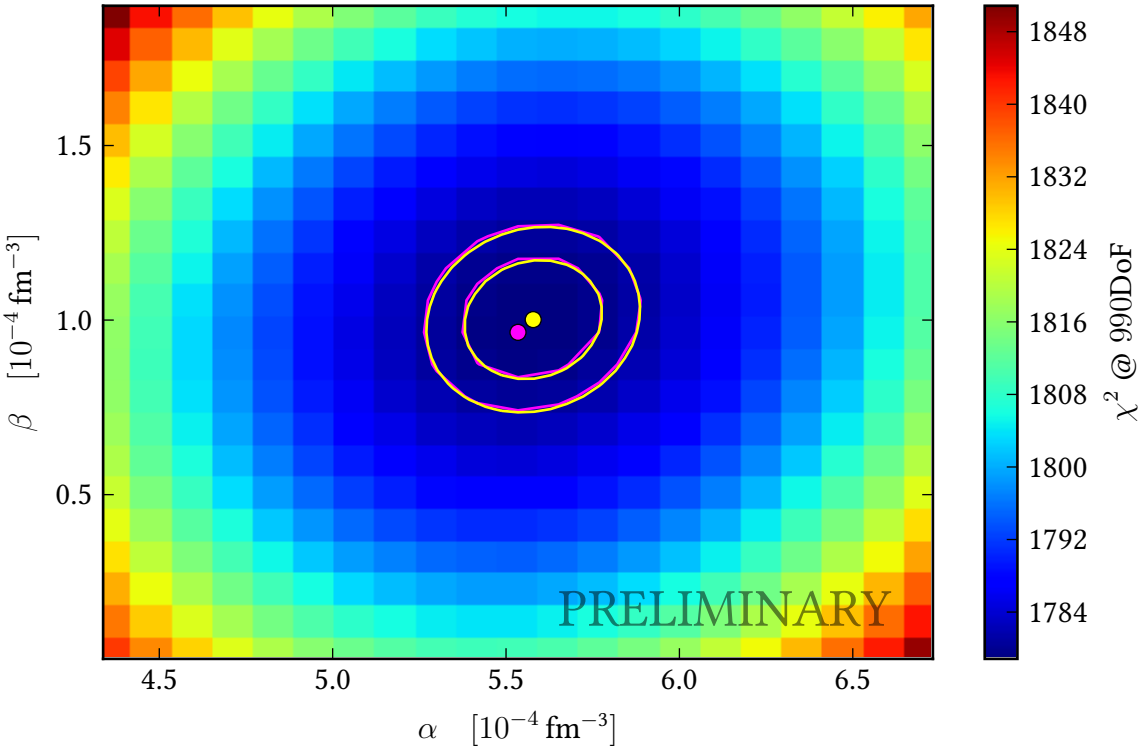

Figure B.3: This figure shows an example of extraction of generalized polarizabilities α_{E} and β_{M} by the on-grid-minimization. Purple color marks the extraction directly from grid and yellow the extraction by fitting the grid with function shown in Equation B.8. The points mark the position of minimum and the lines are contours at $\chi^2_{\mathrm{min}} + 1$ and $\chi^2_{\mathrm{min}} + 2.41$. Both sets of contours match, with the yellow ones being smoother. More difference is for position of minimum. The purple point is on the grid point and it does not match the center of the contours. The yellow point is not constrained to grid points and shows better position and value of the χ^2_{min} and also lies in the center of the contours.

Appendix C

Coordinate systems

This appendix gives a short overview of coordinate systems used to describe the experiment.

C.1 Target coordinate system

The target coordinate system is typically used to measure the position of the target and the position of the beam on the target. The z_{tg} is directed along the beam direction with positive values towards the beam dump. The y_{tg} has the direction of gravity, i.e. toward the hall floors. The orientation of x_{tg} is such, that the axes form a right-handed system.

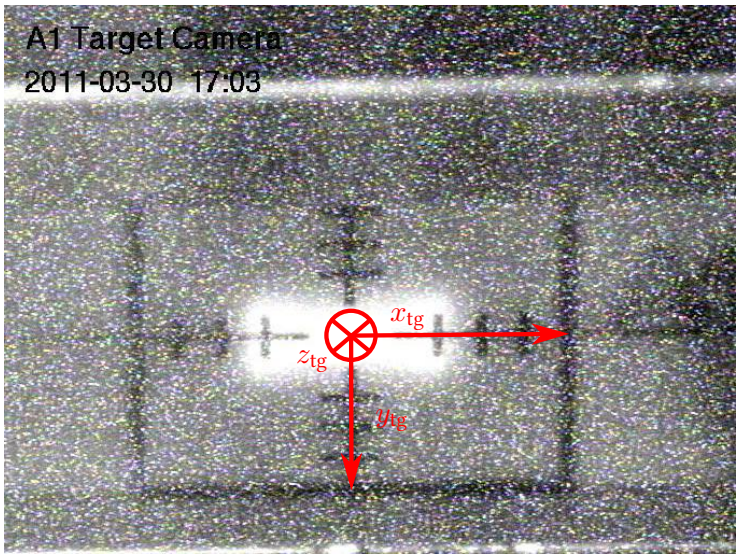

Figure C.1: Target coordinate system shown on target snapshot.

C.2 Laboratory coordinate system

The laboratory system is centered on the scattering chamber. The z_{lab} shows along the beam direction and the y_{lab} is oriented toward the hall ceiling (see Figure C.2). The x_{lab} is oriented such, that the axes form a right-handed system.

The orientation of particle track in this system is usually given by two spherical angles θ and ϕ such that the direction vector is:

$$\hat{n} = (\sin(\theta)\cos(\phi), \sin(\theta)\sin(\phi), \cos(\theta)) \tag{C.1}$$

C.3 Spectrometer systems

A spectrometer coordinate system is defined for each spectrometer. The origin of the system is set on the scattering chamber and the z_{s} axis points towards the center of the spectrometer's collimator. The transformation from laboratory to spectrometer coordinate system is:

$$\hat{x}_{\text{s}} = (\sin(\theta)\sin(\phi), -\cos(\theta), \sin(\theta)\cos(\phi)) \quad , \tag{C.2a}$$
$$\hat{y}_{\text{s}} = (\cos(\phi), 0, -\sin(\phi)) \quad , \tag{C.2b}$$
$$\hat{z}_{\text{s}} = (\cos(\theta)\sin(\phi), \sin(\theta), \cos(\theta)\cos(\phi)) \quad . \tag{C.2c}$$

The angles θ and ϕ are Cartesian angles, where θ is the out-of-plane angle of the spectrometer and ϕ is the angle of the spectrometer in the $z_{\text{lab}} - x_{\text{lab}}$ plane (see Figure C.2).

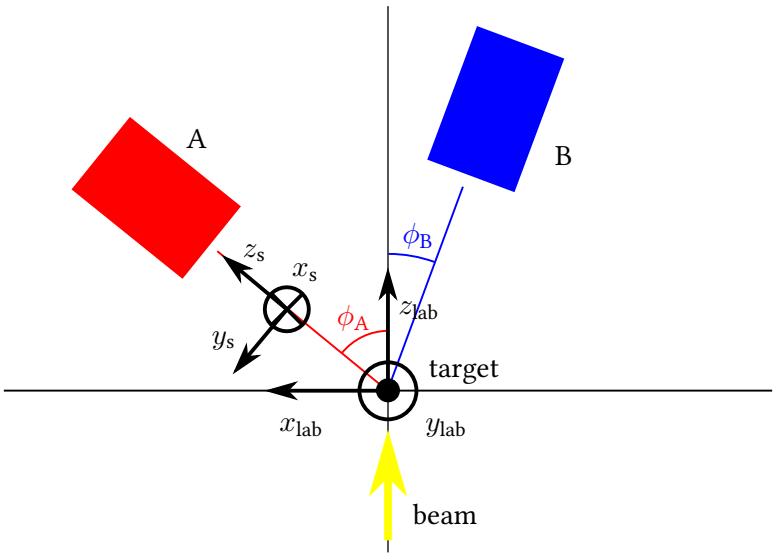

Figure C.2: Laboratory and spectrometer coordinate systems shown on top-down view of the hall.

C.4 Focal plane coordinate system

The particle track is measured in the spectrometer focal plane by four VDC planes. Onto this plane a focal plane coordinate system is attached. The x VDC planes measure the x_{fp} coordinate and the s planes measure the s_{fp} coordinate which is then recalculated into y_{fp}. The s_{fp} axis is rotated for angle $\Gamma = 40^\circ$ with respect to the x_{fp} axis (see Figure C.3). Along with two coordinates $(x_{\text{fp}}, y_{\text{fp}})$ also two angles θ_{fp} and ϕ_{fp} are measured [116]:

$$\tan(\theta_{\text{fp}}) = \frac{\Delta x}{\Delta z} \quad , \tag{C.3a}$$

$$\tan(\phi_{\text{fp}}) = \frac{\Delta y}{\Delta z} \quad . \tag{C.3b}$$

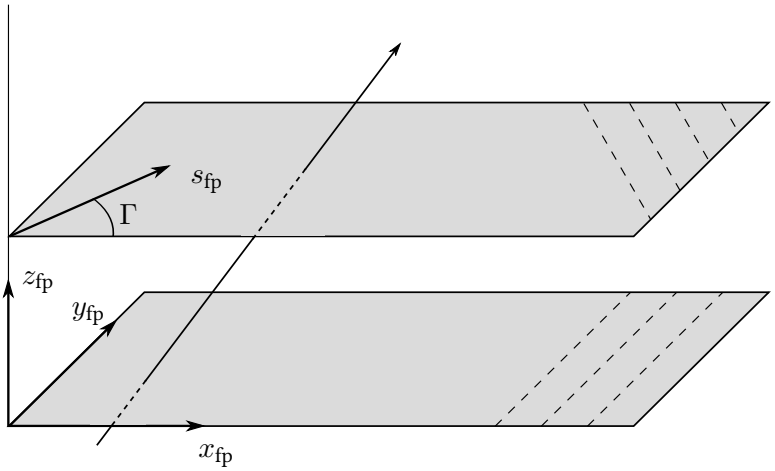

Figure C.3: Focal plane coordinate system shown on a pair of x1-s1 VDC planes. The dashed lines symbolize the signal wires in both planes.

Razširjeni povzetek v slovenskem jeziku

Uvod

Obstoj protona je dokazal Rutherford že leta 1919, vendar do danes njegova struktura še vedno ni zadovoljivo poznana. Natančno poznavanje strukture protona je povezano z natančnim poznavanjem kvantne kromodinamike. Proton je namreč sestavljen iz treh valenčnih kvarkov uud, katerih masa znaša le okoli 1% celotne mase protona. Ostalo maso prispeva energija gluonov, ki povezujejo kvarke. Interakcijo gluonov s kvarki in z drugimi gluoni pa opišemo ravno s kvantno kromodinamiko.

Proton je moč opisati tudi s strukturnimi konstantami in funkcijami. Kot osnovne informacije lahko podamo njegovo maso, električni naboj in magnetni moment. Opis lahko izboljšamo s poznavanjem oblikovnih faktorjev protona, ki predstavljajo prostorsko porazdelitev električnega naboja in magnetnega momenta, oziroma njuno Fourierevo transformacijo. Odziv protona kot celote na zunanjo motnjo opišemo s polarizirnostmi. Prostorsko porazdelitev teh polarizirnosti pa lahko podamo s posplošenimi polarizirnostmi, ki so tudi glavna tema tega dela.

Posplošene polarizirnosti so zanimive iz več razlogov. Ker jih lahko razumemo kot Fourierevе transformacije prostorske porazdelitve polarizirnosti v protonu, nam nudijo dodaten vpogled v strukturo protona. S tem dobimo tudi dodatne informacije o kvantni kromodinamiki v ne-perturbativnem režimu. Posplošene polarizirnosti potrebujejo pri računu Lambovega premika, preko katerega lahko določijo polmer protona. Poznavanje razlike med magnetnimi poslošenimi polarizirnostmi protona in nevtrona pa je pomembno za sodobne izračune masne razlike protona in nevtrona.

Posplošene polarizirnosti protona lahko določimo z virtualnim comptonskim sipanjem, to je sipanje virtualnega fotona na protonu. Eksperimentalno je ta reakcija dosegljiva preko elektroprodukcije fotona. Tu gre za sipanje elektrona na protonu, pri čemer je v končnem stanju prisoten realni foton. Elektron in proton si pri tem izmenjata virtualen foton. Če pogledamo le hadronsko stran te reakcije, je to ravno virtualno comptonsko sipanje. Naivno lahko na elektroprodukcijo fotona gledamo kot na elastično sipanje elektrona, pri čemer se proton nahaja v elektromagnetnem polju končnega fotona. Proton se v tem polju deformira in to deformacijo lahko opišemo s posplošenimi polarizirnostmi.

Teoretično zanimanje za virtualno comptonsko sipanje se je začelo že leta 1958 [18], vendar prvi poskusi niso bili mogoči vse do prihoda sodobnih pospeševalnikov z zveznim žarkom in visokoločljivih spektrometrov. Prvi poskus namenjen meritvam virtualnega comptonskega sipanja so tako naredili šele med letoma 1996 in 1997 [19] v kolaboraciji A1 na pospeševalniku MAMI. Takrat so izmerili sipalni presek za nepolarizirano elektroprodukcijo fotona pri specifični vrednosti kvadrata prenosa štiri-vektorja gibalne količine (Q^2). Iz izmerjenih presekov so nato določili vrednosti dveh strukturnih funkcij $(P_{\mathrm{LL}} - P_{\mathrm{TT}}/\epsilon)$ in P_{LT}, ki sta kombinaciji posplošenih polarizirnosti.

Temu je sledilo še nekaj podobnih poskusov [77, 84, 86]. Tako sta sedaj omenjeni strukturni funkciji poznani pri štirih vrednostih Q^2, vendar do sedaj noben teoretični model ni sposoben zadovoljivo opisati vseh točk. Zato smo izvedli dodaten poskus na pospeševalniku MAMI [71]. Cilj tega poskusa je določiti vrednosti strukturnih funkcij pri treh novih vrednostih Q^2, $0.1\,\mathrm{GeV}^2$, $0.2\,\mathrm{GeV}^2$ in $0.5\,\mathrm{GeV}^2$, s čimer bomo dobili boljši pregled. V tem delu opisujem analizo dela podatkov pri $Q^2 = 0.1\,\mathrm{GeV}^2$.

Virtualno comptonsko sipanje

Elektromagnetna interakcija je idealna za raziskavo strukture protona. Opis te interakcije v okviru kvantne elektrodinamike je izjemno natančen. Je tudi relativno šibka interakcija, kar nam omogoči, da jo obravnavamo perturbativno. Kot sondo lahko uporabimo elektron ali foton. Oba sta točkasta delca, kar pomeni, da v poskusu dobimo informacije o strukturi tarče brez vpliva sondine lastne strukture.

Elektromagnetno interakcijo lahko uporabimo na več različnih načinov in s tem izvemo različne informacije. Z elastičnim sipanjem lahko določimo potek dveh oblikovnih faktorjev protona, ki opisujeta prostorsko porazdelitev naboja in magnetizacije. Realno comptonsko sipanje lahko uporabimo, da določimo šest statičnih polarizirnosti protona, ki opisujejo, kako se proton kot celota prilagodi na zunanje elektromagnetno polje. Dve izmed polarizirnosti sta električna in magnetna ter ju lahko določimo pri nepolariziranemu poskusu. Za določitev preostalih štirih spinskih polarizirnosti potrebujemo polariziran poskus. Z virtualnim comptonskim sipanjem pa lahko določimo potek posplošenih polarizirnosti, ki opisujejo prostorsko porazdelitev polarizirnosti iz realnega comptonskega sipanja.

Virtualno comptonsko sipanje je proces

$$\gamma^* + \mathrm{p} \longrightarrow \mathrm{p}' + \gamma \quad ,$$

pri katerem proton absorbira virtualen foton in izseva realen foton. Ekperimentalno to reakcijo opazujemo preko elektroprodukcije fotona:

$$\mathrm{e} + \mathrm{p} \longrightarrow \mathrm{e}' + \gamma + \mathrm{p}' \quad .$$

Tu lahko končni foton izsevata tako elektron kot proton. Bethe-Heitlerjeva (BH) amplituda opisuje proces, ko končni foton izseva elektron. Ta amplituda je izračunljiva v okviru

kvantne elektrodinamike. Če pa končni foton izseva proton, govorimo o polnem virtualnem comptonskem sipanju (FVCS).

V nadaljevanju se bom omejil na primer nepolariziranega sipanja pod pragom za nastanek piona in sledil izpeljavi v [42].

Kinematiko, kot je elektroprodukcija fotona, lahko opišemo s petimi neodvisnimi količinami. V mirovnem sistemu so to: velikosti gibalne količine virtualnega in končnega fotona $\mathrm{q_{cm}}$ ter $\mathrm{q'_{cm}}$, polarizacija virtualnega fotona ϵ, kot med virtualnim in končnim fotonom θ'_{cm} ter kot ϕ'_{cm} med ravnino, ki jo določata elektrona, ter ravnino, ki jo določata fotona. Mirovni sistem je definiran z $\vec{p}_{\mathrm{cm}} + \vec{q}_{\mathrm{cm}} = 0$, kjer je $\mathrm{p_{cm}}$ vektor gibalne količine protona. Obstaja bijektivna preslikava med tem naborom količin ter naborom količin v laboratorijskem sistemu in naborom invariantnih spremenljivk (glej enačbi (2.22) in (2.23)).

Sipalni presek za nepolarizirano reakcijo elektroprodukcije fotona v laboratorijskem sistemu lahko zapišemo kot:

$$\frac{\mathrm{d}^5\sigma_{\mathrm{lab}}}{\mathrm{dk'_{lab}}\mathrm{d}\hat{k}'_{\mathrm{lab}}\mathrm{d}\hat{p'}_{\mathrm{cm}}} = \frac{(2\pi)^{-5}}{64m_{\mathrm{p}}}\frac{\mathrm{k'_{lab}}}{\mathrm{k_{lab}}}\frac{2\mathrm{q'}_{\mathrm{cm}}}{\sqrt{s}}\,\mathcal{M} = \frac{(2\pi)^{-5}}{64m_{\mathrm{p}}}\frac{\mathrm{k'_{lab}}}{\mathrm{k_{lab}}}\frac{2\mathrm{q'}_{\mathrm{cm}}}{\sqrt{s}}\frac{1}{4}\sum_{\sigma,\sigma',h',\lambda'}\left|T^{\mathrm{ee'}\gamma}\right| \quad ,$$

kjer smo povprečili po vseh spinskih stanjih delcev. Sipalno matriko T lahko razdelimo na dva dela, BH del in FVCS del. FVCS del pa lahko še naprej razdelimo v tako imenovani Bornov del (B) in ne-Bornov del (NB). Bornova amplituda opisuje izsevanje fotona preko lokalne sklopitve s protonom, ne-Bornova amplituda pa izsevanje fotona preko nelokalne dvofotonske interakcije s protonom (glej sliko 2.7).

Sipalne amplitude lahko razvijemo po potencah $\mathrm{q'}_{\mathrm{cm}}$. Amplitudi za procesa BH in B vsebujeta singularnost, zato se njun razvoj prične s členom $\mathrm{q'}_{\mathrm{cm}}^{-1}$. Za proces NB pa velja nizkoenergijski izrek [46], ki nam pove, da se razvoj prične šele s členom $\mathrm{q'}_{\mathrm{cm}}$. Tako lahko zapišemo:

$$\begin{aligned} T^{\mathrm{ee'}\gamma} &= T^{\mathrm{BH}} + T_{\mathrm{B}}^{\mathrm{FVCS}} + T_{\mathrm{NB}}^{\mathrm{FVCS}} \\ &= \frac{a_{-1}^{\mathrm{BH+B}}}{\mathrm{q'}_{\mathrm{cm}}} + a_0^{\mathrm{BH+B}} + (a_1^{\mathrm{BH+B}} + a_1^{\mathrm{NB}})\mathrm{q'}_{\mathrm{cm}} + \mathcal{O}(\mathrm{q'}_{\mathrm{cm}}^2) \quad , \end{aligned}$$

pri čemer so a_i funkcije preostalih štirih kinematskih spremenljivk $(\mathrm{q_{cm}}, \epsilon, \theta'_{\mathrm{cm}}, \phi'_{\mathrm{cm}})$. Členi v razvoju BH in B amplitude so odvisni le od globalnih lastnosti protona, njegove mase, naboja, anomalnega magnetnega momenta in elastičnih oblikovnih faktorjev ter so popolnoma izračunljivi v kvantni elektrodinamiki. Nova informacija o strukturi protona se skriva v členu a_1^{NB}, ki nastopi šele v tretjem redu razvoja. To je tudi faktor, ki ga lahko opišemo s šestimi posplošenimi polarizirnostmi.

Sipalni presek za elektro.produkcijo fotona lahko prepišemo kot:

$$\frac{\mathrm{d}^5\sigma}{\mathrm{d}\Omega^5} = (\phi\mathrm{q'}_{\mathrm{cm}})\,\mathcal{M} \quad ,$$

kjer je $(\phi \mathrm{q}'_{\mathrm{cm}})$ kinematični faktor in $\mathcal{M}$ je Lorentzovo invariantna verjetnost za interakcijo. Podobno kot sipalno amplitudo, lahko tudi $\mathcal{M}$ razvijemo po potencah $\mathrm{q}'_{\mathrm{cm}}$. Naredimo to posebej za eksperimentalno in teoretično verjetnost:

$$\mathcal{M}^{\mathrm{exp}} = \frac{\mathcal{M}^{\mathrm{exp}}_{-2}}{\mathrm{q}'^{2}_{\mathrm{cm}}} + \frac{\mathcal{M}^{\mathrm{exp}}_{-1}}{\mathrm{q}'_{\mathrm{cm}}} + \mathcal{M}^{\mathrm{exp}}_{0} + \mathcal{O}(\mathrm{q}'_{\mathrm{cm}}) \quad ,$$
$$\mathcal{M}^{\mathrm{the}} = \frac{\mathcal{M}^{\mathrm{BH+B}}_{-1}}{\mathrm{q}'^{2}_{\mathrm{cm}}} + \frac{\mathcal{M}^{\mathrm{BH+B}}_{-1}}{\mathrm{q}'_{\mathrm{cm}}} + \mathcal{M}^{\mathrm{BH+B}}_{0} + \mathcal{M}^{\mathrm{NB}}_{0} + \mathcal{O}(\mathrm{q}'_{\mathrm{cm}}) \quad .$$

Člena $\mathcal{M}^{\mathrm{exp}}_{-2}$ in $\mathcal{M}^{\mathrm{exp}}_{-1}$ sta enaka členoma $\mathcal{M}^{\mathrm{BH+B}}_{-2}$ in $\mathcal{M}^{\mathrm{BH+B}}_{-1}$ in sta izračunljiva za dane vrednosti $(\mathrm{q}_{\mathrm{cm}}, \epsilon, \theta'_{\mathrm{cm}}, \phi'_{\mathrm{cm}})$ ob poznavanju elastičnih oblikovnih faktorjev. Informacije o posplošenih polarizirnostih se skrivajo v členu $\mathcal{M}^{\mathrm{exp}}_{0}$. Do njih lahko dostopamo preko primerjave med eksperimentalno verjetnostjo, $\mathcal{M}^{\mathrm{exp}}$ in verjetnostjo za proces BH in B, $\mathcal{M}^{\mathrm{BH+B}}$, pri majhnih vrednostih $\mathrm{q}'_{\mathrm{cm}}$, ko lahko zanemarimo nadaljnje člene razvoja.

Pri poskusu lahko izmerimo sipalni presek za elektroprodukcijo fotona, zato je prikladneje zgornje razmišljanje prepisati v naslednjo obliko:

$$\frac{\mathrm{d}^5\sigma^{\mathrm{exp}}}{\mathrm{d}\Omega^5} = \frac{\mathrm{d}^5\sigma^{\mathrm{BH+B}}}{\mathrm{d}\Omega^5} + (\phi \mathrm{q}'_{\mathrm{cm}}) \left[v_{\mathrm{LL}} \left(P_{\mathrm{LL}}(\mathrm{q}_{\mathrm{cm}}) - \frac{P_{\mathrm{TT}}}{\epsilon} \right) + v_{\mathrm{LT}} P_{\mathrm{LT}}(\mathrm{q}_{\mathrm{cm}}) \right] \quad .$$

Tu je prvi člen na desni strani sipalni presek za proces BH in B, ki je natančno izračunljiv. Drugi del pa predstavlja parametrizacijo neznanega dela, ki ustreza $\mathcal{M}^{\mathrm{NB}}_{0}$, z dvema strukturnima funkcijama $(P_{\mathrm{LL}}(\mathrm{q}_{\mathrm{cm}}) - P_{\mathrm{TT}}/\epsilon)$ in P_{LT}. Ti dve strukturni funkciji sta kombinaciji posplošenih polarizirnosti (glej enačbo 2.69). Funkciji v_{LL} in v_{LT} sta odvisni le od kotov $(\phi'_{\mathrm{cm}}, \theta'_{\mathrm{cm}})$, njuna funkcijska odvisnost pa je podana v dodatku A.

Eksperimentalna določitev strukturnih funkcij $(P_{\mathrm{LL}}(\mathrm{q}_{\mathrm{cm}}) - P_{\mathrm{TT}}/\epsilon)$ in P_{LT} poteka preko separacije med različnimi kombinacijami P_{LL} in P_{LT} - analiza LEX. Sipalni presek za elektroprodukcijo fotona je potrebno izmeriti pri različnih vrednostih $(\phi'_{\mathrm{cm}}, \theta'_{\mathrm{cm}})$ in fiksnih $(q'_{\mathrm{cm}}, \epsilon)$. Določitev vrednosti teh dveh strukturnih funkcij za $Q^2 = 0.1\,\mathrm{GeV}^2$ je cilj tega doktorskega dela.

Teoretične in eksperimentalne študije virtualnega comptonskega sipanja

Prvi izračun posplošenih polarizirnosti so opravil Guichon et al. [41] v okviru nerelativističnega kvarkovskega modela (ang. *non-relativistic quark model*). Ta model je nerelativističen, krši umeritveno invarianco in ne upošteva kiralne simetrije. Zaradi tega rezultati niso najbolj verodostojni, vendar podajo red velikosti prispevkov jedrskih resonanc.

Kasneje so bile polarizirnosti izračunane še v mnogo drugih modelih, kot na primer v linearnem σ modelu [59] (ang. *linear* σ *model*), v kiralni perturbacijski teoriji težkih barionov [56]

(ang. *heavy baryon chiral perturbation theory*) in v modelu efektivnega Lagrangeove gostote [52] (ang. *effective Lagrangian model*).

Pri svojem delu sem za določitev strukturnih funkcij iz izmerjenih sipalnih presekov uporabil dve metodi: analizo LEX in primerjava z modelom disperzijskih zvez ali modelom DR (ang. *dispersion relation model*). Model DR za virtualno comptonsko sipanje na protonu so razvili Pasquini et al. [50], v katerem so tudi izračunali posplošene polarizirnosti. V nasprotju z analizo LEX je ta model veljaven tudi preko meje za produkcijo piona, do resonance $\Delta(1232)$.

V modelu DR virtualno comptonsko sipanje opisujejo neodvisne spremenljivke Q^2, t in $\nu = (s-u)/4M_{\mathrm{p}}$. Tu so s, t in u Mandelstamove spremenljivke (glej enačbo 3.2). Sipalni tenzor za virtualno comptonsko sipanje je parametriziran z dvanajstimi amplitudami $F_i(Q^2, \nu, t)$. Posplošene polarizirnosti so definirane v limiti $\mathrm{q}'_{\mathrm{cm}} \to 0$ pri končni vrednosti q_{cm}. Ta limita ustreza $\nu \to 0$ in $t \to Q^2$. Polarizirnosti lahko izrazimo z ne-Bornovim delom zgornjih amplitud v tej isti limiti. Polarizirnosti tako ostanejo funkcije zgolj Q^2. Če so amplitude analitične in če imajo ustrezno visokoenergijsko obnašanje, jih je moč izračunati v okviru neodštetih disperzijskih zvez (glej enačbo 3.5), pri čemer se upoštevajo glavni prispevki stanj πN. Izračuni uporabljajo analizo MAID [51] za ovrednotenje multipolov foto- in elektroprodukcije piona.

Izkaže se, da dve amplitudi, $\bar{F}_1$ in $\bar{F}_5$, nimata ustreznega obnašanja pri visokih energijah [50], zato dveh od šestih posplošenih polarizirnosti ni mogoče neposredno ovrednotiti. Ti dve amplitudi razdelimo v dva dela, integralni in asimptotični del. Integralni del je omejen na $-\nu_{\mathrm{max}} < \nu < \nu_{\mathrm{max}}$ in je končen pri ustrezni izbiri mej. Asimptotični del amplitude $\bar{F}_5$ je večinoma posledica izmenjave π^0 v kanalu t in ga je možno oceniti. Amplitudo $\bar{F}_1$ pa lahko izrazimo z magnetno posplošeno polarizirnostjo. Prikladna parametrizacija neznanega dela ima obliko:

$$\beta_{\mathrm{M}}(Q^2) - \beta^{\pi\mathrm{N}}(Q^2) = \frac{\beta_{\mathrm{M}} - \beta^{\pi\mathrm{N}}}{\left(1 + Q^2/\Lambda_\beta^2\right)^2} \quad ,$$

ki fiksira vrednost posplošene polarizirnosti pri $Q^2 = 0$ na vrednost statične magnetne polarizirnosti iz realnega comptonskega sipanja. Amplitudo $\bar{F}_2$ lahko povežemo z električno posplošeno polarizirnostjo. Navkljub ustrezni visokoenergijski limiti, tu ponovimo isti postopek kot za $\bar{F}_1$. S tem podaljšamo veljavnost izraza do resonance $\Delta(1232)$. Parametrizacija je analogna:

$$\alpha_{\mathrm{E}}(Q^2) - \alpha^{\pi\mathrm{N}}(Q^2) = \frac{\alpha_{\mathrm{E}} - \alpha^{\pi\mathrm{N}}}{\left(1 + Q^2/\Lambda_\alpha^2\right)^2} \quad .$$

Parametra $\Lambda_{\alpha,\beta}$ sta edina prosta parametra modela DR in ju je potrebno eksperimentalno določiti.

Prvi poskus, namenjem meritvam virtualnega comptonskega sipanja, so izvedli v kolaboraciji A1 na pospeševalniku MAMI med letoma 1996 in 1997 [19]. Izmerili so sipalni presek za elektro-produkcijo fotona pri $Q^2 = 0.33\,\mathrm{GeV}^2$ in $\epsilon = 0.62$. Gibalna količina končnega fotona $\mathrm{q}'_{\mathrm{cm}}$ je obsegala pet vrednosti 33.6, 45.0, 67.5, 90.0 in 111.5 MeV. Razpon kota ϕ'_{cm} je bil določen s spektrometersko sprejemljivostjo okoli centralne vrednosti 0° in 180°, kot θ'_{cm} pa je pokril območje od -141° do 6°. Za detekcijo elektrona in protona so uporabili par visokoločljivih spektrometrov. Dogodki, ki ustrezajo elektroprodukciji fotona, so bili določeni

na podlagi manjkajoče mase. Uporabljena tarča je bila $49.5\,\mathrm{mm}$ dolga celica iz havarja napolnjena s tekočim vodikom. Iz izmerjenih presekov so določili vrednosti strukturnih funkcij $(P_{\mathrm{LL}} - P_{\mathrm{TT}}/\epsilon)$ in P_{LT} z analizo LEX.

Naslednje meritve virtualnega comptonskega sipanja so opravili v kolaboraciji Hall A na Thomas Jefferson National Accelerator Facility [19]. Tu so izmerili sipalni presek kot funkcijo $\mathrm{q}'_{\mathrm{cm}}$, θ'_{cm} in ϕ'_{cm} pri dveh vrednostih Q^2, $0.92\,\mathrm{GeV}^2$ in $1.76\,\mathrm{GeV}^2$, ter dveh vrednostih ϵ, 0.95 in 0.88. Iz teh podatkov so z analizo LEX in DR določili vrednosti dveh strukturnih funkcij ter električne in magnetne posplošene polarizirnosti za obe vrednosti Q^2.

Na MIT-Bates [84] pa so izmerili sipalni presek pri majhni vrednosti $Q^2 = 0.06\,\mathrm{GeV}^2$ in pri $\epsilon = 0.9$. Merili so sočasno pri vrednostih kota $\phi'_{\mathrm{cm}} = 90°$, $180°$ in $270°$. Uporabili so analizo LEX in DR za določitev strukturnih funkcij $(P_{\mathrm{LL}} - P_{\mathrm{TT}}/\epsilon)$ in P_{LT}. Dobljeni vrednosti za $(P_{\mathrm{LL}} - P_{\mathrm{TT}}/\epsilon)$ po obeh metodah sta se ujemali, vrednosti za P_{LT} pa sta se močno razlikovali. To so razložili s skoraj popolnim krajšanjem odziva zaradi električne in magnetne polarizirnosti v redu $\mathcal{O}(\mathrm{q}'_{\mathrm{cm}})$. To pomeni, da je glavni prispevek šele naslednjega reda, ki ni vsebovan v LEX, je pa prisoten v DR modelu. Z uporabo kiralne perturbacijske teorije težkih barionov so določili tudi povprečen polarizacijski polmer protona $\langle r_\alpha^2 \rangle = (2.16 \pm 0.31)\,\mathrm{fm}^3$. Dobljena vrednost je dosti večja kot nabojni radij protona, kar nakazuje pomembno vlogo mezonskih efektov za električno polarizirnost.

V okviru poskusa, namenjenega meritvam polariziranega virtualnega comptonskega sipanja, so med letoma 2005 in 2006 v kolaboraciji A1 na pospeševalniku MAMI ponovili [86] prejšnjo nepolarizirano meritev pri $Q^2 = 0.33\,\mathrm{GeV}^2$. Tudi tokrat so uporabili LEX analizo za določitev dveh strukturnih funkcij. Dobljeni rezultati so potrdili prejšnjo meritev.

Opisani poskusi predstavljajo vse dokončane meritve nepolarizirane virtualnega comptonskega sipanja do sedaj. Navkljub malemu številu meritev, trenutno teoretični modeli ne morejo opisati vseh izmerjenih točk (glej sliko 3.8). To je bil tudi razlog, da smo naredili nov poskus [71], katerega cilj je določiti strukturni funkciji $(P_{\mathrm{LL}} - P_{\mathrm{TT}}/\epsilon)$ in P_{LT} pri treh vrednostih Q^2, $0.1\,\mathrm{GeV}^2$ (opisano v tem delu), $0.2\,\mathrm{GeV}^2$ ter $0.5\,\mathrm{GeV}^2$. S temi meritvami bomo lahko natančneje določili potek strukturnih funkcij in posplošenih polarizirnosti.

Postavitev poskusa

Poskus, ki je opisan v tem doktorskem delu, smo izvedli v okviru kolaboracije A1 na Institut für Kernphysik, ki je del Johannes Gutenberg Universität v Mainzu v Nemčiji. V okviru inštituta deluje pospeševalnik elektronov MAMI [91, 92], ki je zaradi svojega zveznega žarka in velike intenzitete izredno primeren za meritve virtualnega comptonskega sipanja. Pospeševalnik ima nepolariziran (do $100\,\mu\mathrm{A}$) in polariziran (do $20\,\mu\mathrm{A}$) izvor elektronov ter več pospeševalnih stopenj, ki lahko elektrone pospešijo do največje energije $1604\,\mathrm{MeV}$.

Meritve smo izvajali v eksperimentalni hali kolaboracije A1. V hali se nahajajo trije stalni, visokoločljivi spektrometri [95], poimenovani preprosto A, B in C. Spektrometra A in C imata

enako magnetno optiko (kvadrupolni, sekstupolni ter dva dipolna magneta), le da je C manjši. Spektrometer B pa ima le en velik dipolni magnet. Zaradi tega pokrije manjši obseg gibalnih količin in kotov, vendar omogoča boljšo ločljivost na tarči kot spekrometra A in C. Spektrometer B je mogoče tudi nagniti in s tem meriti kinematike izven sipalne ravnine. Pri našem poskusu smo uporabili spektrometra A in B za zaznavanje elektronov in protonov.

Vsi trije spektrometri imajo podoben standardni detektorski paket. Prvi del tega paketa sta dva para vertikalnih potovalnih komor. Dva para komor sta potrebna za dovolj natančno določitev pozicije in kota preleta delca na fokalni ravnini. Iz teh koordinat je potem mogoče rekonstruirati dogodek na tarči. Naslednji detektorski del sta dve ravnini plastičnih scintilacijskih detektorjev. Prva ravnina je debela 3 mm in se imenuje dE, druga je pa debelejša, 1 cm in se imenuje ToF. Ti scintilacijski detektorji se uporabljajo kot prožilec za sistem za zajem podatkov, določijo čas preleta delca in izmerijo njegovo energijsko izgubo. Zadnji standardni del je pragovni detektor sevanja Čerenkova, ki se uporablja za ločevanje med elektroni (pozitroni) in težjimi delci (večinoma pioni).

Na sredini med spektrometri se nahaja sipalna komora. V njej je več različnih tarč. Pri našem poskusu smo uporabljali tri tarče, ogljikovo ploščico za kalibracijo, ploščico iz aluminijevega oksida za merjenje pozicije žarka in kriogensko celico za meritve virtualnega comptonskega sipanja. Kriogenska celica je 49.5 mm dolga in 11.5 mm široka celica s stenami iz havarja, v kateri je tekoči vodik. Tipična temperatura vodika je 21 K in tipičen tlak je 2 bar.

Cilj našega poskusa je bil izmeriti vpliv posplošenih polarizirnosti pri treh vrednostih Q^2: 0.1, 0.2 in 0.5 GeV^2, pri čemer se to delo osredotoča na analizo dela podatkov pri $Q^2 = 0.1$ GeV^2. Pri vsaki vrednosti Q^2 smo izmerili vsaj tri različne postavitve: v ravnini, izven ravnine in "nizko" postavitev. Nizka postavitev je zasnovana tako, da omogoča merjenje pri nizkih vrednostih $\mathrm{q'_{cm}}$ okoli 37.5 GeV/c. Tu je vpliv polarizirnosti zmanjšan, zato lahko te meritve uporabimo za normalizacijo. Ostali dve postavitvi pokrivata višje vrednosti $\mathrm{q'_{cm}}$ in sta zasnovani tako, da ustvarita veliko ročico v v_{LL} in v_{LT}, s čimer izboljšamo občutljivost na polarizirnosti. Pri postavitvi izven ravnine, je spektrometer B nagnjen izven sipalne ravnine, po čemer je dobila tudi ime. Pregled vseh izmerjenih postavitev se nahaja v tabeli 4.2.

Kalibracija

Preden sem se lotil analize podatkov, sem moral kalibrirati programsko opremo. Pri kalibraciji nastavimo parametre programske opreme tako, da ti čim boljše opisujejo dejansko stanje med samim zajemom podatkov. Od kalibracije je tako odvisna rekonstrukcija fizikalnih procesov iz zajetih surovih podatkov.

Najprej sem nastavil parametre vertikalnih potovalnih komor. Tu je recimo potrebno izključiti mrtve in vroče žice, ki bi drugače lahko vplivale na rekonstrukcijo poti delca skozi spektrometer. Poleg tega je potrebno še precizno nastaviti potovalno hitrost (ang. *drift velocity*) elektronov v plinu ter odmike pretvornikov čas-v-digitalno.

Nadaljeval sem s kalibracijo scintilacijskih detektorjev. Da lahko ločimo med pravimi in naključnimi koincidenčnimi dogodki, je potrebno uskladiti časovne zamike med foto-pomnoževalkami in upoštevati efekt časovnega zamika zaradi različnih amplitud signalov (ang. *time walk*). Scintilatorji se uporabljajo tudi za merjenje energijskih izgub delcev, kar lahko uporabimo za identifikacijo delcev. V mojem primeru lahko sem lahko ločil med protoni in pioni (ter ostalimi minimalno ionizirajočimi delci). To delitev sem izboljšal s tem, da sem reskaliral odziv posameznih foto-pomnoževalk tako, da imajo vse enak odziv za pione in enak za protone. Ker moja analiza temelji na meritvi absolutnih sipalnih presekov, sem moral določiti tudi izkoristek scintilatorjev za detekcijo elektronov in protonov.

Naslednja na vrsti je bila kalibracija položaja tarče in žarka na tarči. Iz drugih meritev vemo, da je tarča premaknjena vzdolž smeri žarka in to je potrebno pravilno upoštevati. Prečna pozicija žarka na tarči se lahko s časom malo spreminja in to spreminjanje je potrebno upoštevati pri kalibraciji. Ponavadi se za to uporablja posnetke žarka na tarči iz aluminijevega oksida. Med meritvami leta 2012 pa to ni bilo mogoče, zato sem moral ta popravek dobiti iz prečne odvisnosti med pozicijo žarka in rekonstruiranim centrom tarče.

Iz koordinat delca v fokalni ravnini se koordinate na tarči izračunajo preko tako imenovane prenosne matrike (ang. *transfer matrix*) (glej enačbo 4.1). Pri svojem delu sem uporabil prenosne matrike, ki so že bile optimizirane za mojo kinematiko. Zaradi tega so bili potrebni le manjši popravki nekaterih elementov, ki sem jih določil na podlagi primerjave med meritvami in simulacijo ter glede na vpliv na rekonstruirano manjkajočo maso reakcije.

Primerjava histogramov med meritvami in simulacijo je pokazala, da se spektra kota ϕ'_{cm} ne ujemata. Za kinematiko v ravnini se pričakuje, da je ta histogram simetričen okoli kota $0°$, kot je kazala simulacija, ne pa podatki. To neskladje med simulacijo in podatki sem rešil z nastavitvijo kota nagiba spektrometra B izven sipalne ravnine.

Ker je tarčna celica ohlajena na okoli $22\,\mathrm{K}$, se na njen nabira sneg, čeprav je postavljena v vakuumu. Ta sneg je potrebno upoštevati zaradi dodatnih energijskih izgub delcev. Centralni moment spektrometrov se določi z meritvami magnetnega polja magnetov. Za te meritve se ponavadi uporabi NMR sondo, vendar v našem primer ni dobro delala v spektrometru B, zato smo uporabili Hallovo sondo, ki je manj natančna. Zato centralni moment spektrometra ni točno določen in ga je možno malce popraviti. Nastavitev snega in centralnega momenta pa sta povezana, saj oba spreminjata pozicijo vrha kvadrata manjkajoče mase. Ta pozicija pa je določena s pozicijo vrha v simulaciji. Zato sem moral ta dva popravka narediti usklajeno.

Analiza podatkov

Prva stopnja analize podatkov je bila določitev sipalnega preseka za elektroprodukcijo fotona. Sipalni presek za to reakcijo je odvisen od petih neodvisnih spremenljivk, vendar sta bili dve, q_{cm} in ϵ, kinematično omejeni na majhen interval. Čez ostale tri spremenljivke, $\mathrm{q}'_{\mathrm{cm}}$, $\cos(\theta'_{\mathrm{cm}})$ in ϕ'_{cm}, sem napel tri-dimenzionalno mrežo. Sipalni presek sem določil na točkah te mreže s

primerjavo števila izmerjenih in simuliranih dogodkov:

$$\left(\frac{\mathrm{d}^5\sigma}{\mathrm{d}\Omega^5}\right)_{\mathrm{exp}} = \left(\frac{\mathrm{d}^5\sigma}{\mathrm{d}\Omega^5}\right)_{\mathrm{sim}} \frac{N_{\mathrm{exp}}}{N_{\mathrm{sim}}} \frac{\mathcal{L}_{\mathrm{sim}}}{\mathcal{L}_{\mathrm{exp}}} \quad .$$

Tu je $(\mathrm{d}^5\sigma/\mathrm{d}\Omega^5)_{\mathrm{sim}}$ sipalni presek, kot ga uporablja simulacija, $\mathcal{L}_{\mathrm{exp,sim}}$ pa sta eksperimentalna in simulirana svetlost (ang. *luminosity*). Pri tem je potrebno upoštevati, da izmerjeno število dogodkov vključuje tudi naključne koincidence, ki jih je potrebno odšteti: $N_{\mathrm{exp}} = N_{\mathrm{TT}} - \eta N_{\mathrm{TB}}$, kjer je η skalirni faktor, ki predstavlja razmerje med širinama intervalov za prave in naključne koincidence (glej sliko 6.1).

Tako izračunane preseke je potrebno popraviti zaradi treh efektov, neučinkovitosti detektorjev, nepopolno poznavanje sevalnih popravkov in vpliv parametrizacije oblikovnih faktorjev protona na dobljene vrednosti strukturnih funkcij (parametrizacija strukturnih funkcij ne vpliva na izmerjen sipalni presek). Neučinkovitost detektorjev je možno izmeriti. Za določitev ostalih dveh efektov sem vzel izmerjene preseke, popravljene za neučinkovitosti detektorjev, pri najnižji vrednosti $\mathrm{q'_{cm}}$, kjer je vpliv polarizirnosti najmanjši. Te preseke sem primerjal s preseki, izračunanimi po metodi LEX. Korekcijski faktor sem izbral tako, da sta se nabora presekov med seboj kar najbolj ujemala.

Popravljene sipalne preseke sem nato analiziral v okviru dveh metod, LEX in DR. Metoda LEX, kot pove že ime, temelji na nizkoenergijskem razvoju sipalnega preseka. Sipalni presek za elektroprodukcijo fotona je v prvem približku enak Bethe-Hitlerjevemu in Bornovemu preseku. Vpliv polarizirnosti nastopi kot popravek prvega reda in ga lahko zapišemo kot linearno kombinacijo dveh strukturnih funkcij $(P_{\mathrm{LL}}(\mathrm{q_{cm}}) - P_{\mathrm{TT}}/\epsilon)$ in P_{LT}. V primeru, ko lahko zanemarimo popravke višjega reda, lahko vrednost strukturnih funkcij določimo s postopkom separacije med različnimi kombinacijami P_{LL} in P_{LT}.

Metoda DR omogoča direktno določitev posplošenih polarizirnosti α_{E} in β_{M}. V okviru disperzijskih relacij sta vrednosti α_{E} in β_{M} omejeni. Zato sem naredil dvodimenzionalno mrežo, ki je pokrila celoten fazni prostor za DR. Na vsaki točki te mreže sem izračunal sipalni presek za dana α_{E} in β_{M} za vsako točko kinematične mreže. Za izračun sem uporabil program, ki ga je napisala Barbara Pasquini [105]. Izračunane sipalne preseke sem primerjal z izmerjenimi tako, da sem izračunal vrednost χ^2 (glej enačbo 6.16). Par $(\alpha_{\mathrm{E}}, \beta_{\mathrm{M}})$, za katerega je vrednost χ^2 minimalna, tako ustreza optimalni vrednosti za posplošeni polarizirnosti.

Rezultati

Na dobljene vrednosti strukturnih funkcij in posplošenih polarizirnosti močno vpliva skupna normalizacija izmerjenih sipalnih presekov. To je bil tudi razlog za uvedbo normalizacijskega faktorja F_{norm}. Pričakovana relativna velikost tega popravka je bila okoli 4%, medtem ko so dobljene vrednosti okoli 10% (glej tabelo 7.1). Natančna določitev izvora te neskladnosti je cilj nadaljnjega dela.

Vpliv normalizacijskega faktorja na dobljene vrednosti se kaže na dva načina (glej sliki 7.1): absolutni premik vrednosti in relativno ujemanje za različne parametrizacije oblikovnih faktorjev protona. Trenutne napovedi modela DR in že obstoječih meritev se bolj ujemajo z neuporabo normalizacijskega faktorja ($F_{\text{norm}} = 1$). Na drugi strani pa uporaba normalizacijskega faktorja kompenzira vpliv uporabe različnih oblikovnih faktorjev tako, da so dobljene vrednosti enake v okviru statistične negotovosti.

Vrednosti strukturnih funkcij dobljenih po metodi LEX za različne oblikovne faktorje protona [25, 90, 85]. Prva napisana napaka je statistična in druga je sistematična.

strukturni faktorji	F_{norm}	$P_{\text{LL}} - P_{\text{TT}}/\epsilon$ $[\text{GeV}^{-2}]$	P_{LT} $[\text{GeV}^{-2}]$	χ^2 (276 NDoF)
Bernauer	0.896	$64.8 \pm 1.5 \pm 8.5$	$2.65 \pm 0.56 \pm 3.21$	452
Kelly	0.885	$63.6 \pm 1.5 \pm 8.5$	$2.37 \pm 0.55 \pm 3.21$	452
Friedrich-Walcher	0.889	$64.2 \pm 1.5 \pm 8.5$	$2.38 \pm 0.55 \pm 3.21$	452
Bernauer	1	$35.2 \pm 1.7 \pm 8.5$	$-8.47 \pm 0.62 \pm 3.21$	467
Kelly	1	$31.0 \pm 1.7 \pm 8.5$	$-9.89 \pm 0.62 \pm 3.21$	473
Friedrich-Walcher	1	$32.6 \pm 1.7 \pm 8.5$	$-9.47 \pm 0.62 \pm 3.21$	472

V nasprotju z metodo LEX, model DR ne more opisati poljubno velikega vpliva polarizirnosti. Zaradi tega nisem mogel določiti vrednosti posplošenih polarizirnosti v primeru optimalne vrednosti za F_{norm} (glej sliko 7.3 zgoraj). Minimum za χ^2 se nahaja v spodnjem desnem kotu, ki nakazuje intrinzično mejo modela DR, kar nakazuje, da se pravi minimum nahaja izven tega območja. To je konsistentno z izmerjenimi vrednostmi po metodi LEX. Za primer $F_{\text{norm}} = 1$ sem dobil naslednje rezultate:

$$\alpha_{\text{E}} = (5.58 \pm 0.20) \cdot 10^{-4}\,\text{fm}^3 \quad ,$$
$$\beta_{\text{M}} = (1.00 \pm 0.17) \cdot 10^{-4}\,\text{fm}^3 \quad ,$$

s $\chi^2 = 1779$ pri 990 prostostnih stopnjah. Primerjava z rezultati po metodi LEX je prikazana na sliki 7.4 in kaže konsistentne rezultate, vendar dokaj veliko odstopanje za P_{LT}.

Zaključek

Trenutni podatki kažejo na povečan vpliv električne polarizirnosti v območju okoli dveh MAMI točk [19, 86] pri $Q^2 = 0.33\,\text{GeV}^2$. Da bi dobili boljši pregled v tem območju, smo na pospeševalniku MAMI opravili nove meritve virtualnega comptonskega sipanja, s ciljem določitve vrednosti strukturnih funkcij $(P_{\text{LL}} - P_{\text{TT}}/\epsilon)$ in P_{LT} ter posplošenih polarizirnosti α_{E} in β_{M} pri treh vrednostih Q^2: 0.1, 0.2 in $0.5\,\text{GeV}^2$.

V tem delu sem opisal postopke kalibracije detektorjev in analize podatkov, ki sem jih uporabil za določitev strukturnih funkcij in posplošenih polarizirnosti iz podatkov pri $Q^2 = 0.1\,\text{GeV}^2$.

Polarizirnosti sem določil iz meritev sipalnega preseka, zato sem moral natančno kalibrirati detektorje in precizno določiti eksperimentalno svetlost. To je ključno za takšne natančne meritve sipalnega preseka (glej na primer [110]). Za potrebe kalibracije smo razvili do sedaj najbolj sofisticiran postopek za razločevanje ozadja pri uporabi kriogenske tarče. Ker smo potrebovali visoko natančnost, sem moral posebno pozornost nameniti navidez nepomembnim odmikom pri simulaciji, kar je vodilo v dolgotrajno optimizacijo tarčnih parametrov in rekonstrukcijskih algoritmov. Podatke sem moral sistematično analizirati, da sem zagotovil konsistentnost med analizama LEX in DR.

Primerjava preliminarnih rezultatov, skupaj s preliminarnimi rezultati ločene analize podatkov pri $Q^2 = 0.2$ in $0.5\,\mathrm{GeV}^2$ s strani skupine v Clermont-Ferrandu, z ostalimi rezultati je prikazana na sliki na koncu poglavja. Dosežena statistična natančnost je dosti boljša kot v eksperimentu v MIT-Bates [84] in prejšnjih dveh v Mainzu [19, 86]. To je tudi prva meritev virtualnega comptonskega sipanja, kjer smo zahtevali strogo ujemanje med LEX in DR med analizo. Trenutno se naši rezultati dobro ujemajo s prejšnjo prilagoditvijo modela DR. To je v neskladju z dvema točkama pri $Q^2 = 0.33\,\mathrm{GeV}^2$, ki nakazujeta strukturo v tem območju.

Dodaten vpogled v strukturo protona ponuja tudi zadnja meritev strukturnih faktorjev protona [25]. Ko so primerjali njihove rezultate s standardno dipolno parametrizacijo, so odkrili veliko spremembo naklona G_E okoli $Q^2 = 0.1\,\mathrm{GeV}^2$ in padec v G_M okoli $Q^2 = 0.2\,\mathrm{GeV}^2$. Ta sprememba električne in magnetne strukture protona bi lahko vplivala tudi na porazdelitev polarizirnosti v protonu.

Nadaljnje delo bo usmerjeno v reševanje problema z normalizacijami faktorjem F_norm in v zbližanje rezultatov analiz posameznih postavitev $q2\_01\_inp$ in $q2\_01\_oop$ ter združene analize, kjer trenutno dobim dokaj različne rezultate (glej sliko 7.2). Primerjava dveh sofisticiranih simulacij je pokazala dobro ujemanje v večini primerov, razen v delu histograma za kot ϕ_0 (in v nekaterih povezanih histogramih). Test je pokazal, da omejitev analize le na območje v katerem se simulaciji ujemata, prinese manjše povečanje normalizacijskega faktorja, boljše ujemanje med posameznimi postavitvami in nižjo vrednost reduciranega χ^2.

Poleg rezultatov iz našega eksperimenta čakamo še na analizo meritve virtualnega comptonskega sipanja v območju resonance delta [72]. Pred kratkim so objavili tudi končne rezultate dvojno polarizirane meritve [68], kje so uspeli prvič izmeriti vrednost strukturne funkcije $P_\mathrm{LT}^\perp$. Nadaljnje meritve virtualnega comptonskega sipanja pa načrtujejo v JLab-u [111].

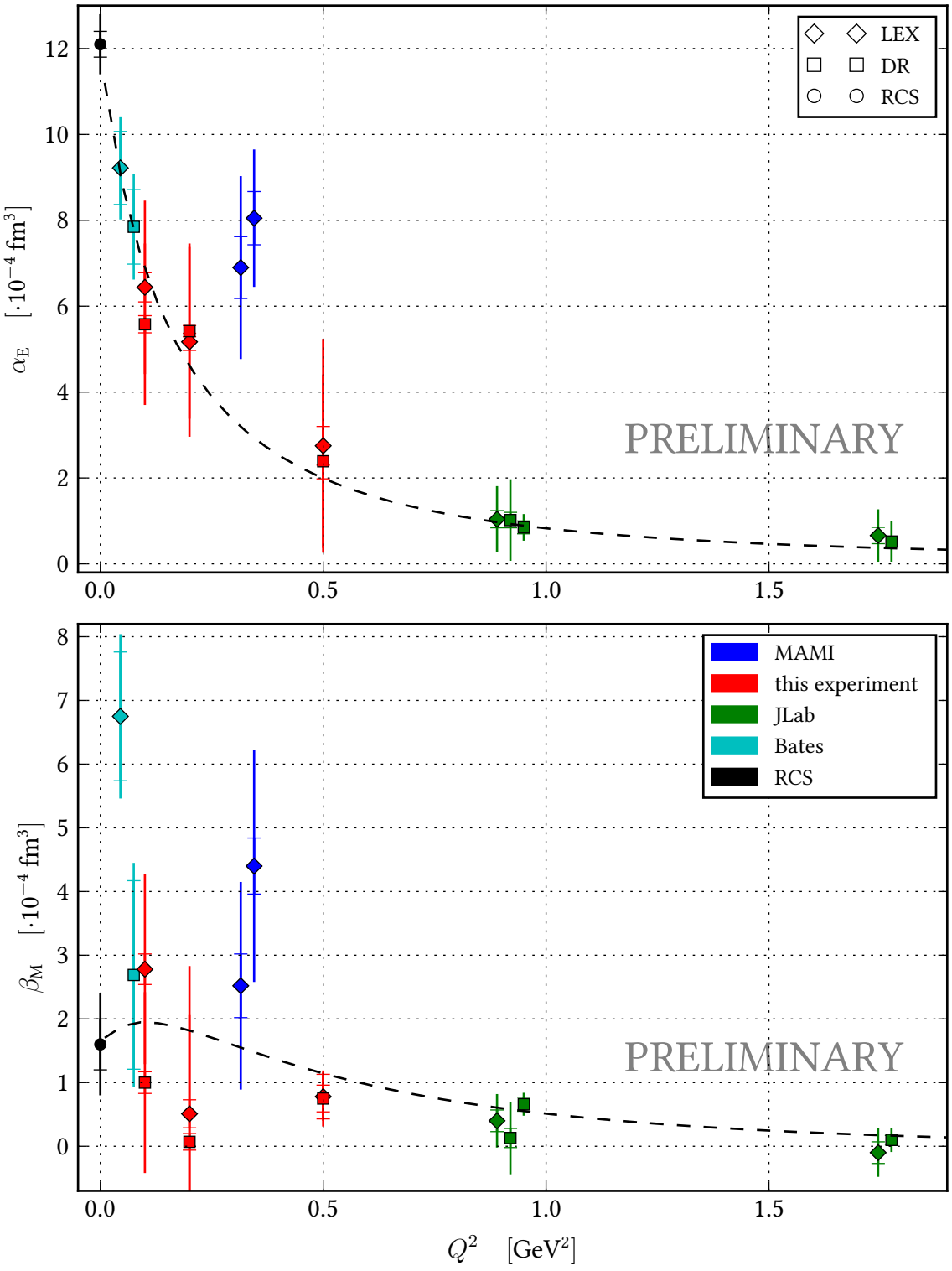

Trenutni podatki o pospešenih polarizirnostih α_E in β_M za virtualno comptonsko sipanje, skupaj z rezultati tega dela. Podatki za ostale točke so bili dobljeni v [30, 84, 19, 86, 77]. Črtkana črta prikazuje prilagoditev DR modela na točke RCS in JLab s parametri $\Lambda_\alpha = 0.7$, $\Lambda_\beta = 0.63$ in $\epsilon = 0.645$. Točke pri isti vrednosti Q^2 so razmaknjene za večjo preglednost.